TOWARDS ULTRAFAST QUANTUM PROCESSING: GENERATION AND STORAGE OF ULTRAFAST PHOTONIC QUANTUM STATES

BY

KAI SHINBROUGH

DISSERTATION

Submitted in partial fulfillment of the requirements
for the degree of Doctor of Philosophy in Physics
in the Graduate College of the
University of Illinois Urbana-Champaign, 2024

Urbana, Illinois

Doctoral Committee:

Professor Paul G. Kwiat, Chair
Professor Virginia O. Lorenz, Director of Research
Emeritus Professor J. Gary Eden
Assistant Professor Kejie Fang
Dr. Offir Cohen

Abstract

This thesis is divided into five parts, each with an accompanying publication. In Chapter 1, I motivate the broad scientific pursuit that underlies this thesis: the quest to build universal, fault-tolerant technology that operates on the principles of quantum mechanics and quantum information theory. I motivate the use of single photons as the quantum particles of choice for this task, and I describe the open challenges facing the field of researchers embarking on this quest. This motivation pervades each subsequent chapter of this thesis, which focus in turn on overcoming four distinct technological and scientific hurdles related to these open challenges.

The first of these open challenges is to demonstrate experimentally a *useful* single-photon source. This source of single photons ought to release just one photon at a time, in an on-demand fashion, with high-rate, low-latency, and high quantum-state purity and indistinguishability, in a single spatial mode, at the right wavelengths for a given application, and ought to satisfy certain practical constraints on size, weight, power, and sensitivity to environmental noise and perturbation. This is a long list of performance metrics, some of which are orthogonal, some not, and non-trivial tradeoffs often exist between metrics. While in this thesis we do not present a solution to this general open problem, we modestly expand scientific knowledge of one of the fundamental mechanisms behind single-photon generation. In particular, we present a new formalism for describing the quantum properties of spontaneous Stokes scattering in the Raman interaction, and we probe its effects on the quantum state purity of resulting Stokes photons both experimentally and theoretically. This is the focus of Chapter 2.

Another open challenge to universal, fault-tolerant photonic quantum processing is the experimental demonstration of a *useful* photonic quantum memory—a device that is capable of storing and releasing single photons in a quantum-information-conserving manner, and which possesses sufficiently high performance across, again, a large set of non-orthogonal metrics. On this challenge, we have made several substantial contributions. Chapter 3 describes a novel approach to optimizing the efficiency of photonic quantum memories in atomic ensembles possessing a three-level Λ-type energy level structure, in an experimentally friendly fashion. Chapter 4 discusses the practical side of implementing robust quantum memory in these atomic systems, where we carefully consider the theoretical sensitivity of these systems to experimental noise and perturbation. These two Chapters lead up to the experimental work described in Chapter 5, where we experimentally demonstrate a state-of-the-art and best-in-class photonic quantum memory in neutral barium vapor that possesses simultaneously high efficiency, broad bandwidth, and low noise. Our experimental demonstration features >95% storage efficiency at roughly 3 orders of magnitude larger bandwidth (higher speed) than the previous state of the art, as well as record-low noise for Λ-type atomic memories. The noise is so low, and the bandwidth so large, that we are able to perform a novel characterization experiment to extract the temporal amplitude and phase of the photons retrieved from our memory, based on spectral interferometry with a known reference. This is the most demanding possible characterization of one of these

memories, and has direct implications for using this type of memory in quantum processing tasks that require temporally indistinguishable photons.

In Chapter 6 I do the requisite summing up of the thesis, and discuss ongoing and future work on the memory project.

In the various and sundry appendices I include information that will chiefly be useful for my successors in the lab, but may be of passing interest to other readers.

To my grandmother Elaine and my friend Ted, both passed during the execution of this PhD, both inspirational intellects and compassionate iconoclasts...

Acknowledgments

It takes a village.

There are many people and institutions who made this work possible:

My advisor Gina, without whose meticulous example of a dedicated, honest, fastidious scientist, this PhD would not exist. Thank you for leading the village.

My chair Paul, who sets an inimitable example of a dedicated scientist and lover of life, and who was kind enough to humor a certain industrial project related to this thesis. Thank you for leading an adjacent village, and making frequent visits to our own.

J. Gary Eden, Kejie Fang, and Offir Cohen, without whose time, teaching, and leadership I would not have learned nearly as much as I have. Thank you for being the wise elders of the village.

S. Lance Cooper, who has offered support, congratulations, and commiserations to me, and countless other Illinois graduate students. I never dreamed I would meet an administrator who so clearly, sincerely, and selflessly loves his students. Thank you for administrating the village.

Yujie Zhang, who started the PhD at the same time as me, and, as ever, finished more quickly and accomplished more than me. Thank you for your companionship.

Benjamin D. Hunt, who grew and is growing in a parallel academic journey. Thank you for your assistance and for the occasionally cheerful reunions.

Tegan Loveridge, who is taking on the helm. Thank you for your good nature, and your willingness to learn from my mistakes.

Everyone in the group, old and new, direct and honorary members, in no particular order: Bin Fang, Wenrui Wang, Daniel Inafuku, Michael O'Boyle, Yanting Teng, Rodrigo Bravo, Simon Hu, Xinan Chen, Ryan Spiniolas, Kevin Ly, Kathleen Oolman, Junyi Wu, Dong Beom Kim, Sam Cieszynski, Keshav Kapoor, Soroush Hoseini, Jaehoon Choi, Yunkai Wang, Mengdi Zhao, Sehyun Park, Elizabeth Goldschmidt, Brian DeMarco, Donny Pearson, Ashwith Prabhu, Safura Sharifi, Priyash Barya, Ogulcan Orsel, Michael Highman, Shraddha Agrawal, Sai Paladugu, Garrett Williams, Jackson Ang'ong'a, Nathan Arnold, Colin Lualdi, Kelsey Ortiz, Benjamin Nussbaum, Ujaan Purakayastha, Andrey Mironov, Kavita Kabelitz, Thomas Reboli, and everyone else I have hastily and foolishly forgotten (if this describes you: it is my error, not yours).

My compatriots in the Graduate Employees' Organization, and others around the world: Andrea Herrera, Natalie Nagel, Emily Wros, Ellie Fujimoto, Shubhang Goswami, Jessica Montone, Roshni Bano, Ryan Levy, Jackie Acres, and many others.

And last but not least, the cherished members of my personal village: My wife Anaeli, my parents, my sibling, and my extended family. Thank you for your unending love and support.

Table of contents

Chapter 1

Introduction and background

1.1 Motivation

1.1.1 Why quantum information?

This thesis describes several theoretical and experimental results in the study of quantum optics and quantum information science. This is, admittedly, a somewhat esoteric subject, but one which possesses great promise to drive forward the technological prowess of our species, positively impact the everyday lives of millions of people, and generally revolutionize society. The actual results of the collective scientific study of quantum information science, say, 50 year from now, will likely be much more modest, but the promise does exist, and in the meantime the subject allows fortunate graduate students such as myself to probe some of the most fundamental and beautiful aspects of our universe. Here I hope to motivate this study of quantum information from first principles in a way that is suitable for a lay audience.

Quantum information science is best understood in contrast with "normal" information science, or "classical" information science. The fundamental unit of classical information is the bit—an information-theoretic object that can be in one of two states, 0 or 1. The physical manifestation of classical bits are all around us, as a bit is instantiated in any switch. Anything that can be in one of two positions ("states"), like a light switch, or a railroad turnout, or, importantly, a transistor in a classical computer, can be considered to encode one bit of classical information.

By comparison, the fundamental unit of quantum information is the qubit—an information-theoretic object that can be in a complex superposition of two states, that, for historical and technical reasons, we write as $|0\rangle$ and $|1\rangle$. What does it mean for a qubit to exist in a complex superposition? The best way to explain this is by way of an example: The state

$$\frac{1}{\sqrt{2}}|0\rangle + \frac{i}{\sqrt{2}}|1\rangle = |+i\rangle \tag{1.1}$$

is a complex superposition of $|0\rangle$ and $|1\rangle$. This state is complex because it possesses an i in the prefactor of $|1\rangle$ (but not the prefactor of $|0\rangle$), and it is a superposition because it is neither $|0\rangle$ nor $|1\rangle$, but a sum of the two. Note that the state

$$\frac{1}{\sqrt{2}}|0\rangle + \frac{1}{\sqrt{2}}|1\rangle = |+\rangle \tag{1.2}$$

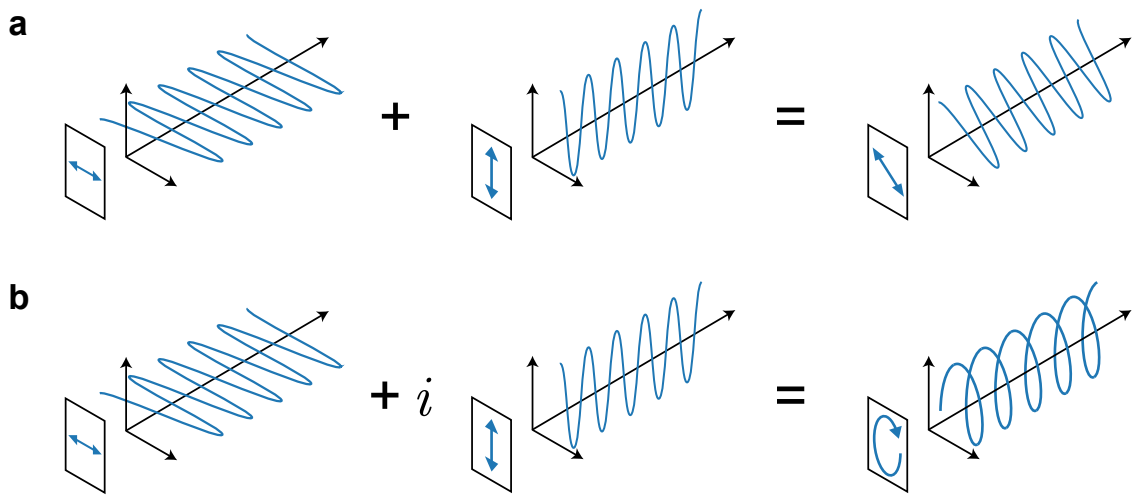

Figure 1.1: **Polarization states of light and their superpositions. a** Horizontal and vertical polarization in equal additive superposition form diagonal polarization. **b** The same two polarizations in equal complex additive superposition form circular polarization.

is also a perfectly valid superposition state, though not complex (there are no i's in the prefactors). Quantum superposition states need not be complex (nor complicated!), but they can be.

The states in Eqs. (1.1) and (1.2) are completely unlike the possible states of a classical bit. Consider crudely using the same notation such that $|0\rangle$ and $|1\rangle$ represent the states of classical bits. One would never come across a classical bit in a state like in Eq. (1.2)—it doesn't make any sense to talk about something like a light switch neither being in the state $|0\rangle$ (off), nor in the state $|1\rangle$ (on), but instead being in some additive combination of the two. Sure, ok, with real light switches that have friction you might be able to balance the switch between the on and off positions, and that's sort of similar (though not *really* the same as an equal superposition), but we're not concerned with real lightswtiches here—we're concerned with information-theoretic light switches that are only ever on or off, never anything in between. One would never find an information-theoretic light switch in the state of Eq. (1.2), and a state like Eq. (1.1) is even less comprehensible.

A qubit is different from a classical bit insofar as it can be in complex superpositions of $|0\rangle$ and $|1\rangle$ instead of just one state or the other, but what does this mean physically? Consider the polarization state of a single photon (a single particle of light). Photons can be polarized horizontally or vertically, relative to some reference like a laboratory bench (or relative to a patch of the surface of the earth, in the case of reflection of the suns rays from the ocean, which you can block almost completely with a pair of polarized sunglasses). However, photons can also be polarized in complex superpositions of horizontal and vertical. Identifying $|0\rangle$ with the horizontally polarized state of light, $|H\rangle$, and $|1\rangle$ with vertical, $|V\rangle$, the equal additive superposition state in Eq. (1.2) is, it turns out, just diagonally polarized light (relative to the same reference; see Fig. 1.1a):

$$\frac{1}{\sqrt{2}}|H\rangle + \frac{1}{\sqrt{2}}|V\rangle = |D\rangle. \tag{1.3}$$

And what about the complex superposition in Eq. (1.1)? This corresponds to light that is "circularly" polarized, which means that the polarization of the light rotates as it moves, shown schematically in Fig. 1.1b. The polarization of circularly polarized light can rotate in one of two directions, leading to so-called right-circular and left-circularly polarized light. The superposition in Eq. (1.1) is leads to right-circularly polarized light,

$$\frac{1}{\sqrt{2}}|H\rangle + \frac{i}{\sqrt{2}}|V\rangle = |R\rangle. \tag{1.4}$$

(Left-circularly polarized light corresponds to a subtractive, not additive, complex superposition.)

Another key difference between the description of classical and quantum bits is found in the prefactors of Eqs. (1.1)-(1.2), which are always $1/\sqrt{2}$, instead of $1/2$ as one might expect. The explanation here is that superposition states refer to superpositions of the *amplitudes* of certain states, not their *probabilities*. If one wants to find the probability of a certain state occurring (i.e., how likely is it that I will measure the qubit in state $|0\rangle$), one has to calculate the modulus squared of the prefactor (e.g., $\left|1/\sqrt{2}\right|^2 = 1/2$).

And this leads us to another curious fact about quantum bits: there are special rules that govern the measurement of qubits. When we measure classical bits, we simply look at the physical system in question (in the case of light switches, railroad turnouts), or we measure a voltage (in the case of transistors), and what you see is what you get—the bit is either 0 or 1, depending on what state it was last set to. Quantum measurements are different. In order to measure a quantum mechanical object, one first has to decide on the "basis" of the measurement. In some sense a measurement basis is like the type of question one is asking about the state of a qubit. One can ask "Is the qubit in state $|0\rangle$ or $|1\rangle$?", or one can ask "Is the qubit in state $|+\rangle$ or $|-\rangle$?" [where $|-\rangle = (|0\rangle - |1\rangle)/\sqrt{2}$], but one cannot ask "Is the qubit in state $|0\rangle$ or $|1\rangle$ or $|+\rangle$ or $|-\rangle$?" One is only allowed to ask about the results of a measurement in one basis at a time—that's the rule. If a qubit is in a superposition state like Eq. (1.1) or (1.2), measuring in the $\{|0\rangle, |1\rangle\}$ basis results in a 50% probability of measuring $|0\rangle$, and a 50% probability of measuring $|1\rangle$. [And this is true for both Eq. (1.1) and (1.2), as the modulus squared is actually a complex operation that results in, e.g., $\left|i/\sqrt{2}\right|^2 = 1/2$.] If instead one measures in the $\{|+\rangle, |-\rangle\}$ basis, measurement of the qubit state in Eq. (1.2) results in a 100% probability of measuring $|+\rangle$, and a 0% probability of measuring $|-\rangle$. [This same measurement on the qubit state in Eq. (1.1) results in 50% probability of measuring $|+\rangle$, and 50% probability of measuring $|-\rangle$.]

As if this wasn't enough, there exists another rule governing quantum measurements. The state of a qubit after a measurement is often different than before the measurement. If one starts with a qubit in the state $|+\rangle$, one measures in the $\{|0\rangle, |1\rangle\}$ basis, and one receives, say, a measurement result of $|0\rangle$ (which will occur 50% of the time), the new state of the qubit is $|0\rangle$. The qubit does not return to the $|+\rangle$ state after the measurement. In fact, if one begins with a qubit in $|+\rangle$, measures in the $\{|0\rangle, |1\rangle\}$ basis, and then measures again in the $\{|+\rangle, |-\rangle\}$, basis, one will find with 50% probability that the qubit returns its original state $|+\rangle$, and, with 50% probability, that the qubit ends up in $|-\rangle$. After two measurements, the qubit has 50% probability of ending up in state $|-\rangle$ even though the probability of measuring the qubit in state $|-\rangle$ was 0% when the qubit was originally in $|+\rangle$! This strange behavior has been the topic of many interesting philosophical arguments (under the umbrella of the "measurement problem").

With the above pieces in place, one can now understand another strange feature of quantum mechanics and an important resource for quantum information processing: entanglement. This time, consider a quantum state of two qubits A and B like

$$\frac{1}{\sqrt{2}}|0\rangle_A|0\rangle_B + \frac{1}{\sqrt{2}}|1\rangle_A|1\rangle_B = \left|\Phi^+\right\rangle. \tag{1.5}$$

This is a perfectly reasonable superposition state, and when we write two state vectors next to each other, like $|0\rangle_A|0\rangle_B$, we are imagining a state of the whole system where the first qubit is in state $|0\rangle_A$ and the

second qubit is in state $|0\rangle_B$.[1] The strange part about this kind of state is that when one measures either particle individually, one has a 50:50 shot of finding it in the state $|0\rangle$ or $|1\rangle$, just like before, and after the measurement the particle 'sticks' in the state it was measured in, just like before, but now the second particle, which one didn't measure, also 'sticks' to the corresponding state in the product [i.e., for the state in Eq. (1.5), if one measures qubit A to be in $|0\rangle_A$, even though one didn't measure qubit B, one can have 100% certainty that it is in state $|0\rangle_B$]. This behavior is sometimes referred to as 'spooky action at a distance' [1], and is one more thing that separates quantum information from classical information.

At this point, if you have made it this far, you might rightly think to yourself, "hang on a second—I thought we were supposed to be motivating the use of quantum information for building new technology that can revolutionize society, but so far all we've talked about is how quantum information is different from classical information." Let's get to that first part now. In essence, the strongest argument I can make on this point is one that I first heard from an certain well-renowned professor in quantum information science when I politely pressed him on the subject, essentially asking whether there was any point to studying this quantum stuff other than for fun. The argument goes that this is a fundamentally new way of processing information, of building computers, of communicating between people, and of interrogating our universe, and it's hard to imagine how that *could not* be useful. That was convincing enough for me, but it may also be helpful to discuss briefly two of the complimentary landmark prospective applications of quantum information science that have been developed over the past several decades, and which motivate much of the commercial interest in quantum technology today:

- **Shor's Algorithm.** A quantum algorithm (i.e., an algorithm run on a quantum computer; a computer that uses qubits instead of bits) for finding the prime factors of (potentially large) numbers [2]. On a quantum computer, Shor's algorithm can in principle factor an integer N in $m_Q \sim \mathcal{O}[(\log N)^2 \log\log N]$ algorithmic steps (i.e., the algorithm requires serial computation of m_Q quantum gates). This is significantly faster than the fastest-known classical algorithm [3], which requires $m_C \sim \mathcal{O}(e^{1.9\sqrt[3]{\log N(\log\log N)^2}})$ steps to factor the same integer. In practice, Shor's algorithm will require significantly more quantum gates for correcting errors that accumulate during the computation time, but there is such a large gap in the algorithmic runtime between the two ($m_C \gg m_Q$), particularly as N becomes large, that this is unlikely to sully the speedup.

  Why should one care about prime factorization of large numbers? The RSA public-key encryption scheme [4] is a widely used scheme for transmitting data in a secure fashion (e.g., a scheme for encrypting text messages or emails sent between two people), and, by a cruel twist of fortune, turns out to rely on the practical mathematical difficulty of prime factorization. In principle, with a sufficiently large and fast quantum computer, any secure data encrypted via RSA could be intercepted, decrypted, and read.

  "What is the current state of prime factorization on quantum computers?", one might ask. To date, the largest integer factored on a quantum computer is 21 (with prime factors 3 and 7) [5]. Some ambitious experimentalists have tried to factor 35 on a quantum computer, but only received the correct answer (5 and 7) about 14% of the time [6]. In binary, the number 35 is 6 bits long. As of the time of this writing, most RSA encryption keys are 2,048 to 4,096 bits long. Nevertheless, this task is not as far out of reach as it may seem [7, 8].

[1] A note on lazy notation: Often times you will find the state in Eq. (1.5) written without the subscripts A and B, and often the two states are written together like $|00\rangle$ and $|11\rangle$, and sometimes we drop the prefactors of $1/\sqrt{2}$. All of these are implied in a state like $|00\rangle + |11\rangle$ or $|HH\rangle + |VV\rangle$.

- **Quantum Key Distribution (QKD).** Shor's algorithm renders some very popular encryption schemes vulnerable to decryption attacks, if one can build a sufficiently large fault-tolerant quantum computer. Does this spell the end for all secret data transmission for the remainder of human history? Well, no, for at least two different reasons—for one thing, there exist classical encryption schemes that do not rely on the hardness of prime factorization, and which have been specifically designed to thwart quantum attacks: so-called post-quantum cryptographic schemes. We have good reason to believe that these classical encryption schemes are not vulnerable to quantum attacks, at least not in the same way that RSA is, but, at the end of the day, there is no law of nature that guarantees the cryptographic security of these schemes. Amazingly, however, quantum mechanics does provide such a guarantee, in the form of quantum cryptography. Quantum key distribution is the most well known branch of quantum cryptography, and employs a scheme based on the sharing of (typically) single photons between a sender and receiver. It turns out we can leverage the measurement problem discussed above in this scheme to guarantee that, if there is an eavesdropper intercepting the photons in transit, the sender and receiver will know about it. Now, this isn't very useful if one is sending an actual message using single photons—you will know when someone has intercepted your message, but that's not nearly as good as preventing someone from intercepting it in the first place. Hence this protocol is typically used only to distribute encryption keys, not the actual messages themselves. If one detects an eavesdropper has intercepted a certain encryption key, one doesn't have to use it; one can throw the intercepted key away and choose a key that hasn't been intercepted to encrypt a message. Once the message is encrypted, the idea is that one can send it along to the receiver using any normal classical communication device (email, text, etc.). It's the security of the encryption key that is guaranteed by quantum mechanics, not the message directly.

It is hopefully easy to see why there is so much commercial interest in quantum technology, from these two applications alone. Adversaries want a quantum computer so that they can use Shor's algorithm to decrypt any secret messages sent by their competitors, and those with sensitive data and information want the quantum technology necessary to implement QKD to shield their data from quantum attacks. Whether either side of this battle wants the outcome enough to fork over the billions of dollars in research funding needed to make real-world quantum devices remains to be seen. In any case, it is not a bad investment, as there exist plenty of other applications as well, from drug and fertilizer discovery via quantum chemistry simulation to financial optimization via quantum annealing and hybrid quantum-classical optimization [9–13].

1.1.2 Why photons?

In the quest to demonstrate universal, fault-tolerant quantum technology, one must pick a particular physical platform (or a set of complimentary physical platforms, in so-called hybrid quantum schemes) to manifest quantum information. There are several leading candidates, and novel qubit platforms emerge every so often. In this work, we will focus only on single photons as our carriers of quantum information—a choice that I motivate in this section.

Photons make excellent qubits for a few different reasons:

- **Decoherence.** As Pieter Kok, *et al.*, state in Ref. [14], "[t]he quantum information stored in a photon *tends* to stay there." This noise-robustness stems from the fact the photons do not interact very strongly with their environment. Consider the polarization of a single photon, as described in Sec. 1.1.1, for example; if that photon propagates in free space it will maintain that same polarization forever, or, at

least, until it is absorbed or enters a material. The answer to the question, "how long will one have to wait for a vertically polarized photon to decay into a horizontally polarized photon?" is, in principle, infinite time. This is in stark contrast to almost every other qubit platform, which possess both this kind of population decay from $|1\rangle$ to $|0\rangle$ (parameterized by the T_1 time of the qubit), and the more parasitic processes of dephasing and decoherence (parameterized by T_2 and T_2^*).

- **Ultra-high fidelity, ultra-fast single qubit gates.** A quantum gate on a single photonic qubit is, in most encoding schemes, almost trivial. In the case of polarization encoding, a single qubit rotation corresponds to the action of quarter- and half-wave plates that apply arbitrary polarization rotations depending only on the rotation of these glass plates about the optic axis. The fidelity of this kind of operation is near unity—in practice, if we wanted to characterize the fidelity of rotating the polarization of a single photon from, say, $|H\rangle$ to $|V\rangle$, we would send it through a polarization analyzing device like a polarizing beamsplitter, and our measured fidelity would be limited by the extinction ratio of the beamsplitter (often to better than 1 part in 10,000); in fact, this is precisely how we measure the beamsplitter's extinction ratio, just with many more photons. That's how confident we are in our single-qubit rotations. And if one calculates the photon-transit-time limited speed of one of these gates, assuming reasonable values for the thickness of glass in quarter- and half-wave plates (t_G) and their indices of refraction (n_G), one finds gate times on the order of $t_G n_G/c \sim \mathcal{O}(10\text{ ps})$ (where c is the speed of light). This is at least three orders of magnitude faster than typical gate speeds in superconducting and trapped-ion qubit platforms, which tend to be of order $\mathcal{O}(10\text{ ns})$ [15] and $\mathcal{O}(1\ \mu\text{s})$ [16], respectively.[2]

- **Room temperature, ambient pressure operation.** Most photonic components, from lasers to photonic sources to detectors, operate or can be made to operate at room temperature and atmospheric pressure, and this is in stark contrast to most other qubit platforms that require cryogenic temperatures and ultra-high vacuum environments. It turns out that for some of the best photonic sources and detectors, cryogenic temperatures are also required, but the path toward practical, wide-spread deployment of quantum photonic technology is nevertheless much clearer than for other platforms.

These advantages constitute the siren song of the quantum photonic platform. There are several disadvantages, however, which we discuss in the next subsection.

1.1.3 Open challenges

There are several open challenges for the quantum photonic platform that stand between the scientific pursuits of the field today and the goal of large-scale, universal, fault-tolerant quantum photonic devices. These are:

- **Deterministic generation.** A natural prerequisite to large-scale quantum processing with single photons is the ability to create a single photon on demand, with all the right properties. The "right properties" include things like high brightness, low latency, high yield, low multi-photon component, high spectral purity, high indistinguishability, clean spatial mode, single polarization, and appropriate wavelength (typically 1550 nm) and bandwidth (typically ∼GHz) for the desired application. Ensuring

[2] I have occasionally advertised this back-of-the-envelope calculation and faced the criticism that this gate time is not really relevant, because what matters is how quickly one can reconfigure a single-qubit gate. In the case of bulk waveplates, this is indeed slow, on the order of $\mathcal{O}$(ms) at best. But, for one thing, the photonic platform need not be limited to bulk optics, and for another, no other qubit platform is subject to this criticism. In all other platforms, the gate time is reported as the time it takes to enact the gate, not the reconfiguration time (see, e.g., [15–17])—the reconfiguration time for any qubit platform tends to be limited by electronic switching, and is thus roughly the same across all platforms.

all of these criteria simultaneously in a room-temperature, ambient pressure device with low size, weight, and power is a difficult thing to do.

- **Two-qubit gates.** Conditional two-qubit gates, i.e., entangling gates, are a necessary component for universal quantum computation [18]. In Sec. 1.1.2, we saw that the decoupling of a single photon from its environment renders it nearly decoherence-free. This is a double-edged sword, however, as it also means that photon-photon interactions are extremely weak and linear-optical two-qubit gates are inefficient. The original linear-optical two-qubit gate has a success probability of 1/16 [19].

- **Photon synchronization.** Before one attempts to implement a two-qubit photonic gate, one must ensure that two photonic qubits arrive at the apparatus implementing the gate at the same time. This kind of photon synchronization is trivial for an experimental apparatus with fixed, short path lengths, but when the path a certain photonic qubit takes in a quantum photonic device is dynamically switched, or very long (as in a metropolitan-scale quantum network), synchronization becomes significantly more difficult.

These are three important disadvantages of the quantum photonic platform, and may spell the end for photonics in the competition between qubit platforms, but it is much too early to determine a winner in that competition (or a set of winners) today, and there is still much hope for, and commercial interest in, the photonic platform. Photonic quantum memory, which is the focus of the bulk of this thesis (Chapters 3-5), can aid in the solution of all three of these open problems. Further details on the kinds of quantum memories we have in mind are provided in Sec. 1.3. It is straightforward to see how these memories could help with photon synchronization. However, it is also the case that an array of quantum memories (in time, space, frequency, etc.) can make probabilistic photon sources deterministic [20], and thereby solve the deterministic generation problem. And once photonic qubits are loaded into a quantum memory as spin-waves, one can, in principle, implement universal quantum computation with these spin waves, including the implementation of two-qubit gates [21].

1.2 How to generate long-distance entanglement and on-demand single photons using spontaneous Raman scattering: the DLCZ protocol

Chapter 2 of this thesis concerns experimental and theoretical work aimed at alleviating the first of the challenges described in the previous section: deterministic photon generation. Here we spell out the general idea and physical intuition behind this work before diving into the technical description contained in the Chapter.

The most common approach to single-photon generation is through the generation of a photon pair, and the detection of one photon out of the pair that heralds the presence of the other (see, e.g., Refs. [22–24]). The problem with this approach is that the generation of photon-pairs in this way is non-deterministic—in a given time bin, a photon (or pair of photons) is either created with some small probability or not created at all. One will receive a herald when a photon pair is created, but heralding efficiencies tend to be only around 50% [25–27] (up to 83% has been reported, with significant tradeoffs [28]), and this can only get quantum photonic applications so far. (A heralding efficiency of 50% means that when one receives a click on a heralding detector, only half of the time does that click mean that another photon is available in the

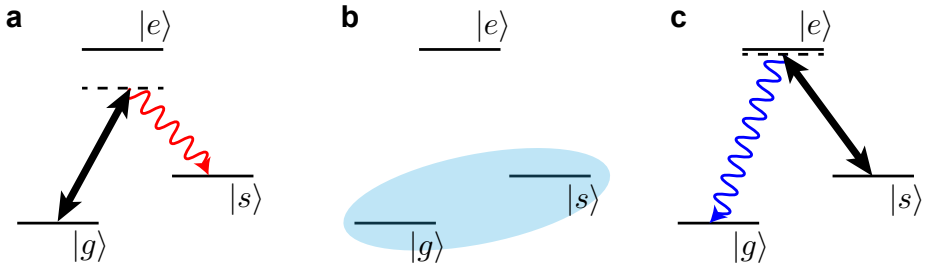

Figure 1.2: **Delayed-choice single photon generation.** **a** The Stokes scattering process involves absorption of a pump photon (black) and emission of a Stokes photon (red), along with **b** a material excitation that persists in the medium for a characteristic lifetime determined by the decay mechanisms in the medium. Within that lifetime, **c** the anti-Stokes scattering process can occur, involving the absorption of a second pump photon and the emission of an anti-Stokes photon (blue).

undetected arm of the experiment; the other half of the time, there is no photon in the undetected arm.) One possible solution to this problem can be found in the protocol of Duan, Lukin, Cirac, and Zoller (DLCZ) [29], which was originally a scheme for remote entanglement preparation for long distance quantum communication, but can be rephrased in a single-photon generation framework: If we consider the Raman interaction shown in Figure 1.2a, wherein a pump photon from a strong, classical laser pulse is annihilated and a single Stokes photon and collective excitation in the Raman medium are spontaneously created, the detection of the Stokes photon heralds the presence of the excitation in the medium. Once the excitation is heralded, it can be read out from the medium deterministically as an anti-Stokes photon with close to unit efficiency, with the application of a second strong laser pulse [30]. In order for this process to provide on-demand single photons useful for synchronization of multiple sources, the lifetime of the excitation needs to be much longer than the "attempt rate" or repetition rate of the generation process. If the lifetime does not meet this threshold, the source can serve as a photon-pair source with controllable delay, for use as a photonic buffer, for example. We call this only "quasi-on-demand" or "delayed-choice" single photon generation, as it is only on-demand as long as there exists an excitation in the medium to read out. Although the DLCZ protocol has been demonstrated in this way before, the correlations and entanglement between Stokes photon and excitation, excitation and anti-Stokes photon, and Stokes and anti-Stokes photons have not been carefully or fully explored. The first set of correlations (between Stokes photon and excitation) are the subject of Chapter 2.

1.3 Broadband quantum memory in atomic ensembles

Chapters 3-5 of this thesis pertain to the task of photonic quantum memory, which, in principle, addresses all of the key open challenges in quantum photonics enumerated in Sec. 1.1.3. Here we provide some introductory information about atomic-ensemble-based photonic quantum memory and review the underpining theoretical principles and the state of the art. The content of this section was published in Ref. [31], and is reproduced here with only minor formatting changes.[3] One should note that the figures presented here are identical to those in Ref. [31]; a more up-to-date version of Fig. 1.11 can be found in Chapter 5.

[3]Previously published material appears in this section. Bibliographic information for this material is as follows: K. Shinbrough, D. R. Pearson Jr., B. Fang, E. A. Goldschmidt, and V. O. Lorenz, "Broadband Quantum Memory in Atomic Ensembles," Adv. At. Mol. Opt. Phys. **72**, 297 (2023). Invited Chapter. The copyright owner, Elsevier, has provided permission to reprint. I gratefully acknowledge the coauthors listed above for their contributions to the text, and Donny R. Pearson Jr. for creation of the cartoons in Figures 1.3, 1.4, 1.6, 1.7, and 1.8.

1.3.1 Introduction

1.3.1.1 Motivation

The fundamental challenges behind distributing quantum information using light are light's fixed speed and ubiquitous propagation losses in optical fiber. Given the inability to copy quantum states [32], this means that, in order to engage in quantum information processing using systems in separate locations, one must find a way to store the quantum information contained in an optical field for a time commensurate with the travel time between locations. This holds for long-distance operations where ms-scale storage is required for round-trip communication [30, 33] as well as on-chip or integrated devices where ns-scale delays allow more complex quantum logic [34–39]. Such a quantum memory must store an incoming photonic quantum state, with quantum information encoded in one (or more) of its degrees of freedom, and faithfully retrieve that photonic state without altering its quantum information or adding noise. The most intuitive application of this primitive operation relates to photon synchronization: two photons arriving at, for example, a node in a quantum network [40], may have traveled long and disparate distances to the node and require some form of quantum memory if they are both to impinge on a beamsplitter at the same time and affect a Bell state measurement [41], entanglement swapping [42], quantum teleportation [43], or almost any other quantum networking protocol. This is perhaps the most straightforward application of quantum memory; however, quantum memory is also of critical importance for all-optical quantum computing [14], quantum communication [44], enhanced measurement and sensing [45], and local quantum gates [46].

There are many potential architectures for implementing quantum memory effectively. Here we focus on the storage of quantum states of light in collective states of atomic ensembles. This general class of schemes is widely applicable across different wavelength and bandwidth regimes, and is only fundamentally limited by the coherence and optical depth of the atomic system, which can be chosen or engineered to be suitable for applications, albeit typically at the expense of other important parameters. In this work, we focus specifically on implementations of atomic ensemble quantum memory in the broadband regime, which we consider to be photon bandwidths greater than 10 MHz. Broadband memory operation is of unique importance for the implementation of quantum photonic applications at high speeds, as high clock rates and processing speeds imply the use of photons that are short in duration and therefore broad in bandwidth.

This chapter concerns the use of both atomic or atom-like ensemble systems for broadband optical quantum memory. Atom-like systems include rare-earth ions doped in solids, molecular gases, phonons in solids, and any platform in which there exists an ensemble of particles with at least three energy levels on which the memory interaction can be based. For ease of notation we refer to both atomic and atom-like systems as "atomic." Note that in this work we do not consider "atomic-ensemble quantum memories" to include the creation of single photons entangled with long-lived matter excitations [29], long-lived excitations in single atoms or ions [47, 48], or other means of transducing photonic quantum information into a material platform [49, 50]. For more information on these alternative mechanisms for engineered atom-photon interactions, we refer the reader to the reviews of Refs. [30, 51].

Even within the relatively narrow scope of broadband quantum memory using collective atomic states, there exist many physically distinct quantum memory protocols and many distinct hardware implementations. Each protocol and hardware implementation possesses particular advantages and disadvantages. We provide some context for these relative advantages and disadvantages by first introducing the fundamentals and the merits of atomic ensembles as quantum memories in Sec. 1.3.1.2. We then discuss a critical problem for atomic ensemble quantum memory in Sec. 1.3.1.3, the linewidth-bandwidth mismatch problem. We present

the metrics used to quantify memory performance in Sec. 1.3.1.4, before launching into a comprehensive discussion of atomic memory protocols and hardware implementations and their respective advantages in Sec. 1.3.2. In Sec. 1.3.3, we review the theory of atomic ensemble quantum memory, including the various forms of the equations of motion in the presence of homogeneous and inhomogeneous broadening and the mathematical approximations that lead to each physical protocol. With these theoretical foundations in mind, we then discuss the theoretical tools developed for the optimization of memory efficiency and the recently developed theoretical tools for investigating memory sensitivity [52], which describes the behavior of atomic ensemble quantum memory in the presence of experimental fluctuations and drift. Finally, in Sec. 1.3.4, we turn to the state-of-the-art performance of broadband atomic-ensemble quantum memories in the literature, providing empirical evidence for the advantages and disadvantages discussed in Sec. 1.3.2. We focus on three metrics of particular importance to broadband atomic ensemble quantum memory: efficiency (Sec. 1.3.4.1), memory lifetime (Sec. 1.3.4.2), and noise (Sec. 1.3.4.3).

1.3.1.2 Ensemble Atomic Systems

Ensemble atomic systems are well-suited for quantum memory as they possess high optical depths, controllable frequency (based in part on atomic species, in part on the chosen detuning from atomic transitions), long-lived atomic superposition states, low sensitivity to experimental noise, and arbitrary storage time. As discussed below, however, atomic systems often suffer from linewidth-bandwidth mismatch, noise from the necessary optical control fields, and undesirable broadening mechanisms. Different atomic level structures have been employed experimentally for atomic ensemble quantum memory, including ladder-type [53–57], M-type [58, 59], and others [60–62]; however, the atomic Λ-type level structure is the most common, and all level structures typically obey the same underlying atom-photon interaction physics (see Fig. 1.3 for the Λ-type and ladder-type structures).

In the memory interaction, the 'signal' field of interest, which possesses some quantum information encoded in one of its degrees of freedom, is tuned on, near, or off resonance with the ground-to-excited-state transition ($|g\rangle \leftrightarrow |e\rangle$ in Fig. 1.3) of the atoms. We note that this signal field may be a single photon, or a more general photonic quantum state, with either discrete or continuous variable quantum information encoded in its degrees of freedom (though typically more care must be taken when using continuous variables [63]). For the remainder of this chapter, we typically focus on the case of single-photon signal fields. The classical 'control' field, possessing many photons, is tuned to the excited-to-storage-state transition ($|e\rangle \leftrightarrow |s\rangle$). These two atomic transitions are typically assumed to be dipole allowed, and the $|s\rangle \leftrightarrow |g\rangle$ transition is assumed to be forbidden. Atoms entering the $|s\rangle$ state are thus metastable. In this typical situation, the time-domain Maxwell-Bloch equations describing the memory interaction are [64–69]:

$$\partial_z A(z,\tau) = -\sqrt{d}P(z,\tau) \tag{1.6}$$

$$\partial_\tau P(z,\tau) = -\bar{\gamma}P(z,\tau) + \sqrt{d}A(z,\tau) - i\frac{\Omega(\tau)}{2}B(z,\tau) \tag{1.7}$$

$$\partial_\tau B(z,\tau) = -\gamma_B B(z,\tau) - i\frac{\Omega^*(\tau)}{2}P(z,\tau), \tag{1.8}$$

where z represents the one-dimensional spatial dimension of the atomic ensemble normalized to the ensemble length [i.e., $z = 0$ ($z = 1$) represents the beginning (end) of the ensemble]; $\tau = t - z/c$ represents time measured in the comoving frame of the photon (t represents time in the lab frame) normalized to the

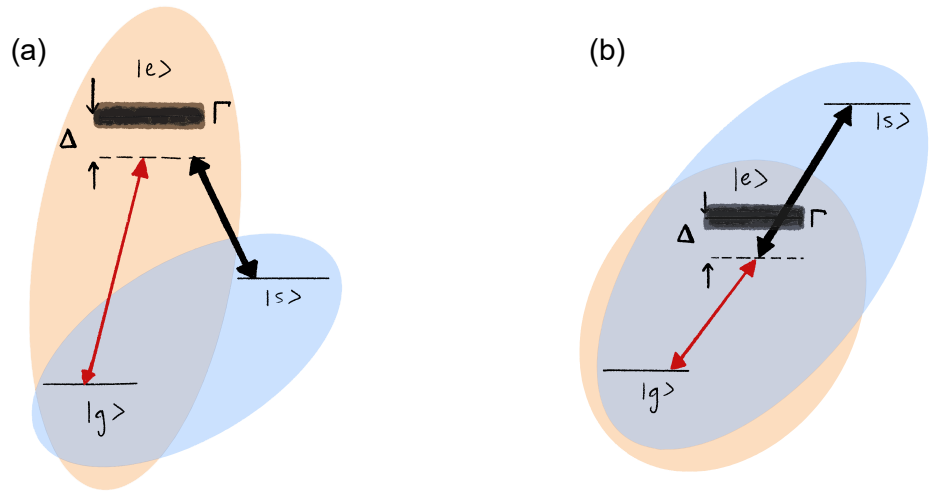

Figure 1.3: **Schematic of the atomic level structures** for (a) Λ-type and (b) ladder-type ensemble quantum memory. Each structure possesses a ground state $|g\rangle$, intermediate excited state $|e\rangle$ (with population decay rate $\Gamma = 2\gamma$), and metastable storage state $|s\rangle$. The signal field (red) and control field (black) are typically kept in two-photon resonance with detuning Δ from the excited state. Orange and blue shaded regions correspond to atomic polarization and spin wave coherences, respectively.

excited-state coherence decay rate $\gamma = \Gamma/2$ (Γ is the total excited-state population decay rate, or the linewidth of the $|g\rangle \leftrightarrow |e\rangle$ transition); $A(z,\tau)$ is the spatially and temporally dependent signal photon field; $P(z,\tau)$ and $B(z,\tau)$, referred to as the atomic polarization and spin wave fields, respectively, are macroscopic field operators representing the atomic coherences $|g\rangle \leftrightarrow |e\rangle$ and $|g\rangle \leftrightarrow |s\rangle$, which are delocalized across the length of the medium and are shown in Fig. 1.3 as orange and blue shaded regions; d is the resonant optical depth of the memory; $\bar{\gamma} = (\gamma - i\Delta)/\gamma$ is the normalized complex detuning, where the two-photon detuning Δ is shown schematically in Fig. 1.3; and $\Omega(\tau)$ is the control field Rabi frequency coupling the $|e\rangle$ and $|s\rangle$ states. All atomic population is assumed to start in the ground state, and the metastable storage state is assumed to have a coherence decay rate γ_B that is much smaller than the excited state decay rate ($\gamma_B \ll 1$, in normalized units).

By inspection of Eqs. (1.6)-(1.8), we note that the photon field acts as a source for the atomic polarization with coupling constant $\sqrt{d}$, which then decays and accumulates temporal phase according to $\bar{\gamma}$. The atomic polarization then acts as a source for the spin wave field with coupling constant $\Omega(\tau)/2$, which then decays exponentially at a rate of γ_B. Depending on the sign of each of the fields, the roles of source and sink can be reversed, allowing for reversible mapping of population ultimately from the photon field to the spin wave and back.

Options other than atomic ensemble systems exist for optical quantum memory, including notably the use of optical delay lines, free-space optical cavities [23, 70–76], optical fibers [73, 77, 78], and optical fiber cavities [79]. These quantum memories take the simplest approach to photon storage by merely increasing the path length traveled by the photon instead of transducing the photon into a material excitation. As such, these delay-based optical quantum memories provide an important point of comparison for atomic ensemble quantum memories. Delay-based memories possess their own disadvantages, however, including fixed-increment delay times, unavoidable optical losses, slow switching speed (∼MHz), and high sensitivity to thermal fluctuations and air currents. Nevertheless, delay-based quantum memories are in principle agnostic to photon bandwidth and exhibit some of the highest efficiencies and longest memory lifetimes in

the broadband regime (see Sec. 1.3.4), limited only by losses in the optical path. Delay-based memories additionally typically exhibit ultra-low-noise operation. As shown in Ref. [80], only a few atomic ensemble quantum memories can currently outperform fiber delay lines in terms of memory efficiency and lifetime, where the total memory efficiency for fiber delay lines is taken as $\eta(\tau) = 10^{-\varepsilon c_n \tau/10}$ for a fiber with loss ε (typically given in units of dB/km) and a speed of light in the fiber of c_n (the necessary length of fiber is therefore $L = c_n\tau$). This calculation ignores coupling losses into and out of the fiber, but serves as an important point of comparison. For particularly long-lived storage, matter-based systems are likely the only option given the sub-ms limits of propagation delay techniques. In the case of fiber-based delay lines, for example, assuming state-of-the-art 0.2 dB/km loss [81], the $1/e$ lifetime of a single fiber loop memory (without switchable delay, which introduces additional loss) is only ∼100 ns. Similar constraints on memory lifetime exist for free-space delay line memories as well, in which case the most optimistic memory lifetime is ∼10 μs [23, 70–76].

Another important point of comparison between fiber-based and atomic-ensemble quantum memory concerns the distortion of broadband pulses of light in fiber due to group velocity dispersion. As the different frequencies of light in broadband photons propagate in fiber at different velocities, broadband photons experience temporal stretching and distortion described in the frequency domain by $A_{\text{out}}(\omega) = A_{\text{in}}(\omega)e^{i\beta(\omega-\omega_0)^2 L/2}$, where β is the second-order group velocity dispersion of the fiber (typically given in units of fs^2/mm) evaluated at the center frequency ω_0, and L is the fiber length. By assuming an initially Gaussian input pulse with angular $1/e^2$ frequency bandwidth $\sigma_\omega = \pi BW/\sqrt{2\ln 2}$ (where BW is the full-width at half-maximum bandwidth; see Sec. 1.3.1.4), Fourier transforming into the temporal domain, and applying Eq. (1.15), one can calculate the fidelity of a fiber-based memory as a function of storage time t and photon bandwidth. Inverting this relationship and considering a fixed target memory fidelity $\mathcal{F}_0$, one can derive the following tradeoff between storage time and fiber memory bandwidth:

$$t = \frac{\sqrt{1-\mathcal{F}_0^2}}{\mathcal{F}_0 \sigma_\omega^2 \beta c_n}, \tag{1.9}$$

which demonstrates that either high-fidelity, large-bandwidth memory is possible at short storage times, or high-fidelity, long-storage-time memory is possible at narrow bandwidths, but all three (high-fidelity, large-bandwidth, long-storage-time) are not possible simultaneously in standard fiber. This tradeoff can be alleviated if an appropriate length of dispersion-compensating fiber is spliced onto the end of standard fiber; whether this is necessary or not for a given storage time, bandwidth, and target fidelity can be derived from Eq. (1.9).

While today ensemble-based quantum memories compare mostly poorly to delay lines in terms of efficiency, bandwidth, lifetime, and noise, there is substantial room for improvement and reason to believe that further work will lead to important advances. In particular, the extremely high losses in on-chip waveguides make integrated photonic systems a place where ensemble memories may be able to make a major difference in the near term. In on-chip photonic devices, coupling on- and off-chip to fiber may introduce more loss than even low-efficiency, evanescently coupled atomic memory, and certainly more loss than chip-integrated rare-earth memories. Attempts to integrate atomic ensembles on chip and in fiber have met with some success to date [36–39, 82–88] and there is hope for improvement. Atomic ensemble memories also possess the capacity for some basic quantum optical processing that is absent among delay-based memories. These include the capacity for built-in mode conversion, shaping, and sorting, multiphoton quantum state preparation [20, 53], local quantum processing [46], arbitrary spectral-temporal and polarization mode conversion, and preparation

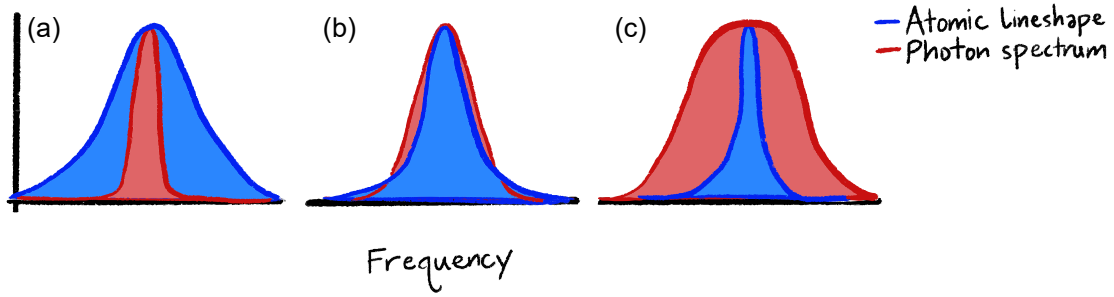

Figure 1.4: **Schematic of linewidth-bandwidth mismatch.** In atomic ensemble quantum memories, the photon spectrum (bandwidth) may be (a) smaller than the atomic lineshape (linewidth), (b) matched, or (c) mismatched.

of arbitrary superposition states that are either not possible through other means or not possible at the same rate or bandwidth [89–91].

Mode shaping and conversion are processing tasks particularly well-researched in atomic ensemble memories. In the broadband regime, this typically focuses on shaping and conversion in the temporal and frequency domains, although polarization conversion has also been demonstrated [92]. Demonstrations to date include frequency and bandwidth conversion in a Raman memory in room-temperature diamond [93]; frequency conversion in room-temperature molecular hydrogen [94]; temporal and frequency multiplexing, arbitrary temporal shaping, and temporal stretching and compression in an AFC memory in cryogenic Tm:$LiNbO_3$ [95]; temporal beamsplitting in a warm cesium Raman memory [89]; temporal beamsplitting and temporal stretching and compression in a laser-cooled rubidium ATS memory [90]; and temporal compression, stretching, and beamsplitting in a laser-cooled rubidium Raman memory [91]. Taken together, these demonstrations show the capacity for temporal, frequency, duration, and bandwidth conversion of atomic-ensemble memories, which may be of practical application in developing quantum networks and quantum information processors. We note, however, that additional work is needed to demonstrate this utility and to extend the characterization of atomic ensembles as mode converters to include phase as well as amplitude manipulation.

A problem is posed for broadband atomic ensembles beyond roughly MHz bandwidths, which is the lack of sufficiently fast classical electronic switches to effectively make use of the broad optical bandwidths demonstrated. Fortunately, ongoing work toward GHz and THz optical switches shows promise toward alleviating this concern [96–107].

1.3.1.3 Linewidth-Bandwidth Mismatch

Broad spectral bandwidth is of particular importance for quantum applications, and we highlight this aspect of quantum memory performance in this chapter. Quantum memory operation with broadband photons, corresponding to short photon durations, enables the use of large clock and qubit processing rates. Broadband operation presents a natural problem for standard atomic ensemble quantum memory, however, as the linewidths involved in atomic ensembles are typically narrow, and narrow storage-to-ground-state-transition linewidths are desirable for long memory lifetimes. We refer to the problem of storing broadband photons with high efficiency in typically narrowband atomic ensemble quantum memories as the 'linewidth-bandwidth mismatch' problem. Figure 1.4 shows a schematic of the different situations possible for broadband photons; high memory efficiency is, in general, more easily achievable for the cases of photon bandwidths smaller than the atomic excited state linewidth [Fig. 1.4a] or when the photon bandwidth is matched to the atomic linewidth

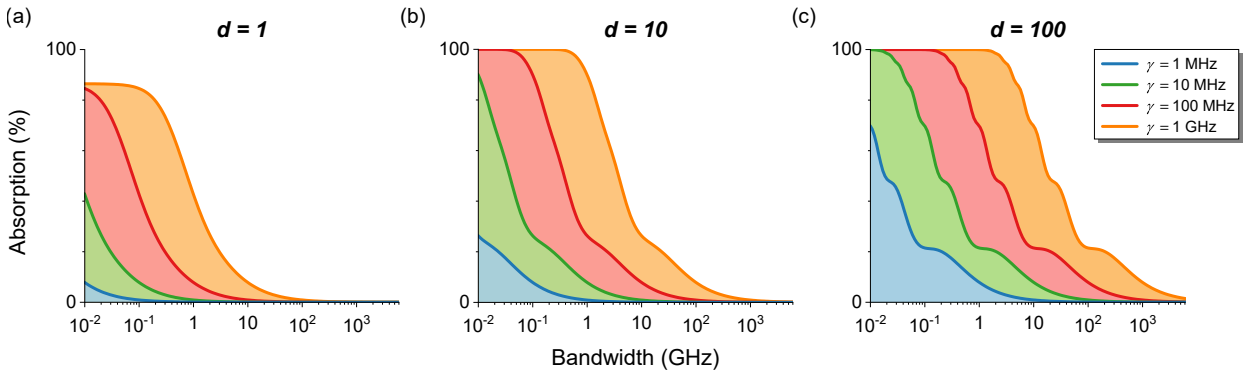

Figure 1.5: **Linear absorption and memory resources.** Calculated upper bounds on memory efficiency based on linear absorption, demonstrating the linewidth-bandwidth mismatch problem for photon bandwidths between 10 MHz and 1 THz, assuming excited state linewidths of 1, 10, 100 MHz, and 1 GHz, and peak optical depths of (a) $d = 1$, (b) $d = 10$, and (c) $d = 100$.

[Fig. 1.4b], compared to the case when the two are mismatched [Fig. 1.4c]. More specifically, we consider the linewidth-bandwidth mismatch problem to encapsulate the empirical trend of decreasing memory efficiency with increasing photon bandwidth; evidence for this trend is presented in Sec. 1.3.4. This trend is physically a result of the difficulty of absorbing broadband photons along a narrowband transition — if a broadband photon cannot be absorbed along the $|g\rangle \rightarrow |e\rangle$ transition, it is difficult to affect the memory operation described by the equations in Sec. 1.3.1.2. This is easiest to see in the case of the absorb-then-transfer protocol (discussed more in Sec. 1.3.2.1), which explicitly relies on linear absorption of the signal field. The overall memory efficiency cannot be high without high-efficiency absorption.

We can model this phenomenon heuristically by considering the efficiency of linear absorption in a dense atomic ensemble. Linear absorption can be modeled by Eqs. (1.6)-(1.8) of Sec. 1.3.1.2 in the absence of a control field [$\Omega(\tau) = 0$]:

$$\partial_z A(z,\tau) = -\sqrt{d} P(z,\tau) \tag{1.10}$$

$$\partial_\tau P(z,\tau) = -\bar{\gamma} P(z,\tau) + \sqrt{d} A(z,\tau), \tag{1.11}$$

where we define absorption as $\int_{-\infty}^{\infty} d\tau |A_{\text{out}}(\tau)|^2 / |A_{\text{in}}(\tau)|^2$ for a Gaussian-shaped input temporal distribution $A_{\text{in}}(\tau)$ and an output distribution $A_{\text{out}}(\tau) = A(\tau, z = 1)$. This absorption is plotted in Fig. 1.5 for photon bandwidths between 10 MHz and 1 THz, assuming excited state linewidths of 1, 10, 100 MHz, and 1 GHz. Figure 1.5a-c show absorption for optical depths of $d = 1$, 10, 100, respectively. In general, the larger excited state linewidths are able to absorb broadband photons with higher efficiency as they have lesser linewidth-bandwidth mismatch. Absorption can also be increased by increasing optical depth, but this is typically a less effective strategy for increasing efficiency than increasing atomic linewidth at the same optical depth. The oscillations that appear in Fig. 1.5b-c are due to periodic backaction of the atomic ensemble onto the photon temporal distribution and the formation of zero-area photon pulses [108]. The takeaway from Fig. 1.5 is that high efficiency at broad photon bandwidths is difficult to achieve with (relatively) narrowband atomic transitions, and this is due to linewidth-bandwidth mismatch. This issue introduces a trade-off between efficiency and lifetime, since narrowband atomic transitions are useful for preserving the coherence of collective atomic states for long timescales, but lead to lower memory efficiency for broadband pulses.

One resolution to the linewidth-bandwidth mismatch problem has been demonstrated in recent work in hot atomic barium [109, 110]. This approach relies on large, tunable modification of the homogeneous excited state linewidth to better match broadband photons, where the linewidth modification is mediated by the intentional and controllable introduction of collisional dephasing. This technique creates broad homogeneous excitation linewidths that allow for complete absorption and storage of broadband photonic quantum states in a system that would otherwise exhibit relatively narrowband transitions. This approach yields a demonstrated storage efficiency of 95.6±0.3% for ultrashort photons (500 fs), which to our knowledge is the highest measured storage efficiency to date for any atomic-ensemble memory with bandwidth >10 MHz, and rivals the efficiencies demonstrated in delay-line and fiber-based memories, as is discussed further in Sec. 1.3.4.

The controlled homogeneous broadening approach described in Refs. [109, 110] constitutes a novel technique for alleviating the linewidth-bandwidth mismatch problem, but it is not the only technique. In particular, the use of far-off-resonant schemes for quantum memory in atomic ensembles is well known, and similarly alleviates the linewidth-bandwidth mismatch problem, albeit through a different mechanism. In far-off-resonant memory protocols, memory bandwidth is not limited by the narrowband atomic transitions, as the large detuning adiabatically eliminates the excited state. This elimination of the excited state also eliminates the restriction on memory bandwidth posed by the excited state linewidth; however, this advantage comes at the cost of large control field power necessary to drive the off-resonant two-photon transition. This requirement of large control field powers can be difficult to satisfy in experiment, and also tends to lead to low efficiency at broad photon bandwidths (see Sec. 1.3.4). By contrast, the technique of Refs. [109, 110] can be applied on or near resonance, and therefore requires significantly less control field power than the far-off-resonant schemes, and can achieve similar memory bandwidths. A third technique for alleviating linewidth-bandwidth mismatch relies on inhomogeneous broadening of the otherwise narrowband atomic transitions, either in a controlled fashion (i.e., in the CRIB protocol; see Sec. 1.3.2.1) or by the choice of hardware that intrinsically possesses inhomogeneity (i.e., rare-earth ions doped in solids; see Sec. 1.3.2.2). This technique can in principle be used to create inhomogeneous linewidths that match broad photon bandwidths, and therefore allow for high-efficiency, broadband quantum memory; however, the external fields necessary in the controllable case tend to be large and experimentally challenging to generate, and in the intrinsic case the inhomogeneity introduces dephasing during the storage operation that tends to lead to lower efficiencies upon retrieval when compared to the homogeneous case.

Regardless of efficiency, broadband atomic ensemble quantum memories tend to possess short memory lifetimes, mostly for technical (rather than fundamental) reasons. Narrowband atomic $|s\rangle \rightarrow |g\rangle$ transitions are desirable and necessary for achieving long memory lifetimes, but in practice in the broadband regime either inhomogeneous broadening (e.g., motional dephasing) or intrinsic material constraints (e.g., phonon lifetimes) tend to limit memory lifetime. That said, recent techniques have been developed to alleviate inhomogeneous broadening of the storage state (see Ref. [56] and Sec. 1.3.2.2), which may allow for simultaneous high-efficiency, broadband, and long-lived quantum memory operation. Even short-lived photonic quantum memories are useful, however, for such applications as quasi-on-demand single-photon generation and multiphoton quantum-state preparation [20, 53], short-timescale synchronization, mode conversion [93, 95], and local quantum processing [46], among others. Each quantum application employing quantum memory places different constraints on acceptable memory performance, and for some applications short memory lifetime is not prohibitive.

1.3.1.4 Metrics

In what follows we give a brief description of the relevant metrics for quantum memory performance that have been developed in the literature:

Efficiency – Quantum memory efficiency describes the integrated intensity ratio of photons sent in to the memory, and those retrieved from it:

$$\eta = \frac{\int_{-\infty}^{\infty} d\tau |A_{\text{out}}(\tau)|^2}{\int_{-\infty}^{\infty} d\tau |A_{\text{in}}(\tau)|^2} = \frac{\int_{-\infty}^{\infty} d\omega |A_{\text{out}}(\omega)|^2}{\int_{-\infty}^{\infty} d\omega |A_{\text{in}}(\omega)|^2}, \tag{1.12}$$

where $A_{\text{in}}(\tau)$ $[A_{\text{in}}(\omega)]$ and $A_{\text{out}}(\tau)$ $[A_{\text{out}}(\omega)]$ describe the incident and retrieved photon amplitude in the temporal (spectral) domain, respectively.

Memory efficiency in atomic ensembles is determined by two processes, storage (or read-in) and retrieval (or read-out), which each have independent efficiencies η_{stor} and η_{ret}, respectively, where $\eta = \eta_{\text{stor}}\eta_{\text{ret}}$. These efficiencies correspond to the integrated intensity ratio of photons sent in to the memory and the population entering the collective atomic storage state, $|B_{\text{out}}(z)|^2$, and the integrated intensity ratio of photons retrieved from the memory and the same collective atomic state:

$$\eta_{\text{stor}} = \frac{\int_0^1 dz |B_{\text{out}}(z)|^2}{\int_{-\infty}^{\infty} d\tau |A_{\text{in}}(\tau)|^2}, \qquad \eta_{\text{ret}} = \frac{\int_{-\infty}^{\infty} d\tau |A_{\text{out}}(\tau)|^2}{\int_0^1 dz |B_{\text{out}}(z)|^2}, \tag{1.13}$$

where $z = 1$ in normalized units refers to the full length of the atomic ensemble, and where again spectral derivatives may be substituted for the temporal derivatives with impunity.

An important figure of comparison for memory efficiency is the optimal efficiency at a given optical depth, d. Described in Refs. [66, 68, 69], available atom number and optical depth of an atomic ensemble impose an upper limit on the achievable memory efficiency of a given system. The optimal bound on storage efficiency, η_{opt}, is calculated by finding the largest eigenvalue of the antinormally ordered storage kernel

$$K(z, z') = \frac{d}{2} e^{-d(z+z')/2} I_0(d\sqrt{zz'}), \tag{1.14}$$

where $I_0(x)$ is the zeroth order modified Bessel function of the first kind. The optimal bound on retrieval efficiency is also η_{opt}. Typically, optimal retrieval is only achievable for backward retrieval of the signal field [68]; forward retrieval of the signal field typically suffers from reabsorption loss, as the signal field is reabsorbed by the atoms as it propagates through the ensemble after retrieval [69]. The optimal bound on total memory efficiency is $\eta_{\text{opt}}^2 \geq \eta$.

Bandwidth – Memory bandwidth corresponds to the full width at half maximum of the signal photon spectral intensity stored and retrieved in the memory. For a Gaussian-shaped signal field amplitude $A_{\text{in}}(\tau) \propto e^{-\tau^2/4\sigma^2}$, where $\sigma = \tau_{\text{FWHM}}/(2\sqrt{2\ln 2})$ in terms of the signal temporal intensity full width at half maximum (τ_{FWHM}), the Fourier-transform-limited photon bandwidth is $BW = 2\ln 2/(\pi\tau_{\text{FWHM}})$. The bandwidth of a quantum memory determines the memory's compatibility with short-duration pulses, which is of critical importance to real-world quantum applications that benefit from large clock rates and high processing speeds [111, 112].

Memory Lifetime – The lifetime of an atomic ensemble quantum memory, T, typically corresponds to the time it takes for the retrieved photon population $[\langle A_{\text{out}}\rangle \propto \int_{-\infty}^{\infty} d\tau |A_{\text{out}}(\tau)|^2]$ to reach $1/e$ of its maximum value. Assuming the retrieval control field pulse remains unchanged aside from its arrival time in the atomic ensemble, this is equivalent to the time it takes for the the collective atomic state population

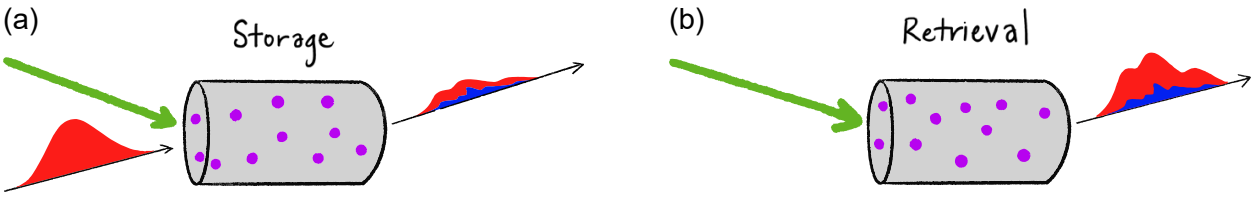

Figure 1.6: **Schematic of atomic ensemble quantum memory** during the (a) storage and (b) retrieval stages. The classical control field is shown in green, the quantum signal field in red, and the noise field in blue.

$[\langle B_{\text{out}}\rangle \propto \int_0^1 dz |B_{\text{out}}(z)|^2]$ to reach $1/e$ of its maximum value. Occasionally, the $1/2$ lifetime of a memory is given instead of the $1/e$ lifetime and a conversion factor depending on the decay model must be used to compare memories (e.g., for exponential decay, the $1/e$ lifetime T and $1/2$ lifetime $T_{1/2}$ are related by $T_{1/2} = T\ln 2$; for Gaussian decay, $T_{1/2} = T\sqrt{\ln 2}$).

Time-Bandwidth Product – A relevant figure of merit for most quantum protocols is the time-bandwidth product, defined as the product of memory lifetime and spectral bandwidth, $\text{TBP} = T \times BW\pi/(2\ln 2)$. This figure provides a metric for the fractional delay produced by the memory in units of the photon duration, $\text{TBP} = T/\tau_{\text{FWHM}}$. Broadband quantum memories may have equivalent or even larger time-bandwidth product at short storage times compared to narrowband quantum memories with long storage times.

Noise – Noise is a critical figure of merit for determining the performance of a quantum memory. Even if the photon retrieved from a quantum memory is retrieved in the same quantum state as the input with unit efficiency, the presence of noise photons in addition to the retrieved signal renders such a memory useless for almost every quantum application. This importance of noise relates to whether a memory qualifies as 'quantum'—true 'quantum' memories must demonstrate below (ideally far below) 1 noise photon per retrieved signal photon, such that they do not contaminate the quantum states they store.

The noise performance of quantum memory can be quantified several different ways. The most popular metrics for determining noise performance are: $\langle n_{\text{noise}}\rangle$, the average number of noise photons produced per pulse that overlap with the retrieved signal field; signal-to-noise ratio at 1 input photon/pulse (SNR), which is the signal-to-noise-ratio of the retrieved signal population to the average number of noise photons [$\text{SNR} = \langle A_{\text{out}}\rangle/\langle n_{\text{noise}}\rangle = \eta\langle A_{\text{in}}\rangle/\langle n_{\text{noise}}\rangle = \eta/\langle n_{\text{noise}}\rangle$], evaluated when on average 1 photon per pulse is sent into the memory ($\langle A_{\text{in}}\rangle = 1$); $\mathcal{F}_{\text{noise}}$, the single-photon fidelity of the memory, defined as $\mathcal{F}_{\text{noise}} = 1 - 1/(\text{SNR}+1)$, which is a measure of the fidelity of retrieving the stored signal photon rather than a noise photon, and which may be approximated as $\mathcal{F}_{\text{noise}} = 1 - 1/\text{SNR}$ in the limit of large SNR; and μ_1, which is the ratio of the average number of noise photons per pulse to the memory efficiency, $\mu_1 = \langle n_{\text{noise}}\rangle/\eta = 1/\text{SNR}$.

Some caution must be exercised in using each of these metrics, as ambiguity exists in the definition of SNR. As shown in Fig. 1.6b, the total photon field retrieved from a memory is made up of two contributions, which we call the signal (shown in red) and the noise (blue). Occasionally, the *total* photon field retrieved (signal and noise) is referred to as the "signal," in which case the signal-to-noise ratio is reported as what we would consider the 'total-to-noise' ratio (TNR). The two are related by $\text{TNR} = \text{SNR} + 1$.

Fidelity – Independent from the noise performance of a memory, one can consider the overlap of the retrieved photon quantum state with the quantum state of the photon before it was sent into the memory. The definition of this fidelity typically depends on the degree of freedom of interest where quantum information is encoded, as in the case of quantum process tomography for polarization-encoded photonic qubits [113], and can be performed for a single input state or averaged over multiple input states [114]. Typically, fidelity is

defined in terms of a state overlap $\mathcal{F} = |\langle\Psi_{\text{out}}|\Psi_{\text{in}}\rangle|^2$ for pure states or $\mathcal{F} = \langle\Psi_{\text{in}}|\rho_{\text{out}}|\Psi_{\text{in}}\rangle$ for mixed states, which, in the temporal domain, can be expanded as

$$\mathcal{F} = \frac{\left|\int_{-\infty}^{\infty} d\tau\, A^*_{\text{out}}(\tau - \tau_d) A_{\text{in}}(\tau)\right|^2}{\int_{-\infty}^{\infty} d\tau\, |A_{\text{in}}(\tau)|^2 \int_{-\infty}^{\infty} d\tau\, |A_{\text{out}}(\tau)|^2}, \tag{1.15}$$

where τ_d is the time delay between incident and retrieved pulses. This definition of fidelity is sometimes called the "waveform likeness" [115–117], as it compares the likeness of the incident and outgoing temporal waveforms, where the outgoing waveform typically encounters some distortion [see Fig. 1.6a and b]. In experiment, this is typically measured via intensity interferometry, where a reference pulse identical to the incident signal field is interfered with the retrieved pulse. Often in this case the interferometric visibility is reported in place of fidelity [90, 111].

Fidelity is a critical figure of merit as it relates to the degree of phase- and entanglement-preservation of a memory. Phase- and entanglement-preservation are critical to the use of quantum memories in quantum repeaters [30], for example, among other applications.

Adiabaticity – The adiabaticity of a free-space atomic ensemble quantum memory is given by $d\tau_{\text{FWHM}}\gamma$, where d and τ_{FWHM} are as defined above, and γ is the coherence decay rate of the intermediate excited atomic state of the three-level atomic system ($\Gamma = 2\gamma$ is the population decay rate). Described in detail in [65, 66, 68], quantum memories which satisfy $d\tau_{\text{FWHM}}\gamma \gg 1$ are considered adiabatic, and memories with $d\tau_{\text{FWHM}}\gamma \sim 1$ are typically considered non-adiabatic. The adiabatic condition $d\tau_{\text{FWHM}}\gamma \gg 1$ ensures that for efficient memory operation the signal field bandwidth ($\propto 1/\tau_{\text{FWHM}}$) will be smaller than, or a similar order to, the excited state linewidth. It also ensures that the control field used to mediate the memory operation will be weak and long in duration relative to the timescale of evolution of the atomic states. All of these conditions together allow for adiabatic elimination of the atomic polarization in the equations of motion described in Sec. 1.3.1.2.

Multimode Capacity – A quantum memory capable of storing and retrieving multiple photonic qubits independently at overlapping times is considered multimode, as opposed to a single-mode memory, which must store and retrieve a given photon and reinitialize before it is prepared to store and retrieve another. Atomic ensembles may demonstrate multimode capacity in a number of different degrees of freedom, including temporal mode [118], angular wavevector [119], three-dimensional spatial position [120], time bin [121], and frequency bin [122].

Multimode capacity is typically defined relative to a reference efficiency, η_{ref}. The multimode capacity N of a quantum memory corresponds to the largest number of independent modes that can each be stored with at least η_{ref} efficiency.

Sensitivity – The sensitivity of atomic ensemble quantum memory is a metric that has been discussed only recently [52, 123]. Memory sensitivity relates to a memory's performance in the presence of experimental noise, including fluctuations and drift in memory parameters such as optical depth and atomic transition linewidth as well as in the optical control field parameters used in the memory interaction. A memory that is less sensitive is more robust to experimental noise, and vice versa.

Memory sensitivity may be quantified in a number of different ways, and memory sensitivity may in principle refer to the sensitivity of any of the metrics of this section in the presence of experimental noise. The typical case, however, concerns changes in memory efficiency in the presence of noise. When short-timescale fluctuations lead to changes in memory efficiency, the memory sensitivity is given in terms of the variance of memory efficiency in the presence of fluctuations ζ in parameters $\mathcal{X}$

$$V_\eta^{\text{fluc}}\left(\overline{\mathcal{X}}\right) = V_\zeta[\eta(\overline{\mathcal{X}}+\zeta)], \tag{1.16}$$

where $\overline{\mathcal{X}}$ is the mean parameter value averaged over a large number of fluctuations, and where $V_x[y(x)] = \int dx\, y^2(x)P(x) - [\int dx\, y(x)P(x)]^2$ is the unconditional variance of y obtained when x fluctuates with some probability distribution $P(x)$. The resulting standard deviation in memory efficiency can then be reported as $\sigma_\eta^{\text{fluc}}(\overline{\mathcal{X}}) = \sqrt{V_\eta^{\text{fluc}}(\overline{\mathcal{X}})}$.

When long timescale drift in experimental conditions lead to changes in memory efficiency, and only one parameter of the system drifts, the memory sensitivity can be calculated via the one-at-a-time (OAT) variance

$$V_\eta^{\text{OAT}}(\overline{\mathcal{X}}) = V_{\mathcal{X}}[\eta(\mathcal{X})], \tag{1.17}$$

where $\mathcal{X}$ varies uniformly over a finite range, $\mathcal{X} \in [\mathcal{X}^{\min}, \mathcal{X}^{\max}]$ centered on $\overline{\mathcal{X}}$. Again, the standard deviation $\sigma_\eta^{\text{OAT}}(\overline{\mathcal{X}}) = \sqrt{V_\eta^{\text{OAT}}(\overline{\mathcal{X}})}$ may be used to quantify the change in memory efficiency due to changes in $\mathcal{X}$. In the case where multiple experimental parameters $\mathcal{X} = (x_1, ..., x_N)$ drift simultaneously, a *global* variance-based sensitivity analysis is required, wherein the most prevalent sensitivity measure is the first-order Sobol' variance [124–126]

$$V_i = V_{x_i}\{E[\eta(\mathcal{X})|x_i]\}, \tag{1.18}$$

where the inner expectation value, $E[\cdot]$, corresponds to the mean of $\eta(\mathcal{X})$ when $\mathcal{X}$ is varied over all possible values in a finite range at fixed x_i. The outer variance then measures the variance of this mean with respect to changes in x_i. The first-order Sobol' sensitivity index for parameter x_i can then be calculated as

$$S_i = V_i/V_{\text{tot}}, \tag{1.19}$$

where V_{tot} is the total variance $V_{\mathcal{X}}[\eta(\mathcal{X})]$ observed over the range of interest.

Telecom Compatibility – Quantum memories are often proposed for use before, after, or inside networks of optical fiber. As linear absorption in standard silica optical fiber reaches a minimum at 1310 and 1550 nm [127], the telecom O- and C-band, respectively, a quantum memory compatible with these wavelengths is desirable. If 1310 or 1550 nm operation is not possible, other less-standard telecommunications bands exist in the range of 1260-1675 nm, and wavelength compatibility within this range is more desirable than outside this range. Telcom compatibility is therefore typically a binary metric, designating whether or not a quantum memory is capable of storage and retrieval of photons between 1260 and 1675 nm center wavelengths, where special attention is given to 1310 nm and 1550 nm operation.

Latency – As with any technical device, latency describes the amount of time required by a quantum memory for initialization and preparation before storage and retrieval of photonic quantum states is possible. A useful figure of merit for this aspect of quantum memory operation is the memory's duty cycle, defined as the ratio of the amount of time the memory is capable of storage and retrieval to the total cycle time necessary for initialization and subsequent memory operation [128]. In general, a memory with a larger duty cycle (ideally 100%) is preferable to a memory with a smaller duty cycle.

Size, Weight, and Power (SWaP) – Of practical importance to the use of quantum memories in real-world quantum applications is the size, weight, and power consumption of the memory. Typically these metrics are not reported exactly in the scientific literature, and may be hard to estimate, but general trends

can be intuited (such as, for example, that an atomic vapor cell held at a higher temperature will have a higher power consumption than a cooler one, and memories requiring high control field optical powers will have higher power consumption than those with low powers). In general, a memory with a smaller SWaP is preferable to a memory with a larger SWaP.

Device Lifetime – The lifetime of a quantum memory device is also of practical importance. In the limiting case, a quantum memory that is single-use — only capable of storing and retrieving one photonic quantum state before the device needs to be replaced — has virtually no practical application. All quantum memories in the literature exceed this limit; however, some platforms tend to demonstrate longer device lifetimes than others and again general trends can be intuited based on the required temperatures, pressures, and experimental components.

1.3.2 Protocols and Hardware

1.3.2.1 Atomic Quantum Memory Protocols

Many protocols for quantum memory operation in atomic ensembles exist based on distinct and quite disparate physical mechanisms. This section provides a brief review of the ensemble memory protocols found in the literature to date. We comment on the advantages of each memory in terms of the metrics described above in Sec. 1.3.1.4, focusing in particular on the bandwidth limitations of each protocol.

Electromagnetically Induced Transparency (EIT)

Electromagnetically induced transparency (EIT) in atomic ensembles is a phenomenon characterized by optical transparency at wavelengths resonant with the $|g\rangle \rightarrow |e\rangle$ atomic transition (see Fig. 1.3), which normally exhibits significant attenuation, and an associated reduction in group velocity of the incident signal field [129]. This transparency and slowed group velocity is due to the presence of a second, strong optical control field which couples the excited and metastable atomic states ($|e\rangle \leftrightarrow |s\rangle$), where the $|e\rangle \rightarrow |s\rangle$ transition is dipole allowed but the $|s\rangle \rightarrow |g\rangle$ tranistion is forbidden. This is a quite general phenomenon; for the purposes of this work we focus on EIT harnessed for quantum memory, where the 'slow light' of general EIT is transformed into 'stopped light' via adiabatic attenuation of the control field [130].

The pulse sequence for this protocol is as follows: A control field of duration longer than the signal field ($\tau_{\mathrm{FWHM}}^{\mathrm{ctrl}} > \tau_{\mathrm{FWHM}}$) enters the medium ahead of the signal field in time ($\Delta\tau^{\mathrm{ctrl}} < 0$). This opens a spectral transparency window at the signal frequency. This window is then slowly closed after the signal field enters the medium via attenuation of the control field. The signal field is thereby compressed and trapped in the medium in a superposition of the metastable and ground states of the atoms. This protocol is described in the narrowband regime in Refs. [66, 129–133], and in the broadband regime in Refs. [117, 134].

Numerous experimental implementations of the EIT protocol for quantum memory exist (a review of most EIT quantum memory implementations can be found in Refs. [87, 133, 135–137]). Efficiencies as high as 92% have been demonstrated [138], as well as—separately—memory lifetimes verging on 1 minute [139, 140]. As EIT memory requires adiabatic elimination of the excited state however, either large optical depths or narrow bandwidths (relative to the excited state linewidth) are required to fulfill the adiabaticity criterion $d\tau_{\mathrm{FWHM}}\gamma \gg 1$ [134, 141]. To date this has limited operation of EIT-based quantum memory to bandwidths of 170 MHz [142] or less.

Noise operation in EIT systems tends to be limited by either four-wave-mixing (FWM) or control field noise. FWM noise occurs when the strong control field operates off-resonantly along the $|g\rangle \rightarrow |e\rangle$ transition,

generating a spontaneous Stokes or idler photon along $|e\rangle \rightarrow |s\rangle$, before operating again along the $|s\rangle \rightarrow |e\rangle$ transition, generating an anti-Stokes or 'spurious signal' photon along $|e\rangle \rightarrow |g\rangle$, which overlaps with the retrieved signal photon in all degrees of freedom. Control field noise occurs when there is a small frequency difference between signal and control field, and thus spectral isolation of the signal field is difficult to attain. Compared to ATS and SR memory protocols (discussed below) at the same bandwidth, EIT exhibits larger FWM noise due to its comparatively larger requirements on optical depth and control field Rabi frequency [143, 144]. FWM noise in EIT is very well characterized [145–147] and many technical solutions to both control field and FWM noise exist [92, 148–152].

In ladder systems, the EIT protocol is often referred to as fast ladder memory (FLAME), and may include a small detuning from resonance [53, 56, 57].

Autler-Townes Splitting (ATS)

The Autler-Townes Splitting (ATS) memory protocol is closely related to the EIT protocol [134, 141], but typically operates most efficiently at lower optical depths and broader photon bandwidths, placing it in the non-adiabatic class of quantum memories ($d\tau_{\mathrm{FWHM}}\gamma \sim 1$). The physical mechanism of ATS quantum storage relies on dynamic control of the Autler-Townes doublet created in the $|g\rangle \rightarrow |e\rangle$ absorption profile in the presence of a strong control field. By generating a dynamic Autler-Townes doublet that scans across the full bandwidth of the signal field (which is typically of the same order as the excited state linewidth, Γ) as it propagates through the atomic ensemble, uniform attenuation of the signal field in frequency can be achieved that ensures coherent population transfer to the spin wave state [90].

The pulse sequence used to generate the appropriate dynamical Autler-Townes splitting consists of a control field pulse of similar duration to the signal field ($\tau^{\mathrm{ctrl}}_{\mathrm{FWHM}} \sim \tau_{\mathrm{FWHM}}$) that arrives at the atomic ensemble contemporaneously with the signal field ($\Delta\tau^{\mathrm{ctrl}} \sim 0$) and possesses net control field pulse area (overlapping with the signal field) of 2π.

As the bandwidth of the signal field increases, the effective optical depth of the $|g\rangle \rightarrow |e\rangle$ transition decreases due to increasing necessary Autler-Townes splitting, and as the bandwidth of the signal field decreases, population in the atomic polarization state experiences increased decoherence due to the increased duration of the protocol [90]. Both of these effects lead to decreased memory efficiency, and therefore lead to an optimal photon bandwidth for a given ATS memory that is typically of order $BW \sim \Gamma$ [90, 134, 141]. This leads to favorable memory bandwidth compared to the EIT protocol in the same memory; however, to date ATS memories have been limited experimentally to bandwidths of 20 MHz [134] and below.

Superradiance (SR) Mediated Memory

Superradiance (SR) mediated memory is another on-resonant non-adiabatic protocol, similar to the ATS protocol, but with distinct characteristics. The protocol [143] relies on the effect of superradiance [153], which is characterized by cooperative spontaneous emission in atomic ensembles. The superradiant quantum memory protocol has three stages: absorption, writing, and retrieval. In the absorption stage, the signal photon is absorbed linearly along the $|g\rangle \rightarrow |e\rangle$ transition of the ensemble and thereby prepares the ensemble in a timed-Dicke state [154] with a decay time shorter than the bare atomic excited state lifetime, as the induced ordered spatial phase distribution encourages the coherent enhancement of radiation in the direction of the absorbed photon. This short decay time makes SR memory compatible with photons with bandwidth greater than the bare excited state linewidth, $BW > \Gamma$. To suppress superradiant emission of the absorbed photon and realize photon storage, the writing stage starts directly after the absorption stage, within the

superradiant decay time T_{SR}. This process is accomplished by sending in a control field with π pulse area and duration $\tau_{\mathrm{FWHM}}^{\mathrm{ctrl}} \ll T_{SR}$, which maps the generated atomic polarization to a collective spin excitation. During the retrieval process, another π-pulse control field is applied and the photon is superradiantly emitted.

Optimizing the absorption process in SR memory requires shaping the temporal profile of the signal photon to match the time-reversed superradiant decay. The optimal shape of the photon is therefore exponentially rising with time constant inversely proportional to the linewidth Γ and the optical depth d. Currently, the first demonstration of SR memory has achieved storage of signal photons with time constants down to 10ns and 3% memory efficiency [143]. The lower-than-expected efficiency is due to a long experimental control pulse duration $\tau_{\mathrm{FWHM}}^{\mathrm{ctrl}}$ that does not completely satistfy the condition $\tau_{\mathrm{FWHM}}^{\mathrm{ctrl}} \ll T_{SR}$. When compared with EIT and ATS protocols, the SR protocol requires less optical depth for the same memory efficiency at the cost of higher control power. Four-wave mixing noise in SR memory appears to be on par with EIT but much higher than ATS memory.

Absorb-then-Transfer (ATT)

Similar to SR memory, the absorb-then-transfer (ATT) memory protocol [66, 155–157] occurs in three physically distinct stages. As the name suggests, the first two stages correspond to linear absorption along the $|g\rangle \rightarrow |e\rangle$ transition in the absence of the control field, then a short delay later the application of a π-pulse control field along the $|e\rangle \rightarrow |s\rangle$ transition that transfers population from the atomic polarization coherence ($|g\rangle \leftrightarrow |e\rangle$) to the spin wave coherence ($|g\rangle \leftrightarrow |s\rangle$). These two stages implement the storage operation. When retrieval is desired, another control field pulse with π pulse area is applied to the atomic ensemble, transferring population back to the atomic polarization coherence, which then emits the stored signal field through dipolar radiation. This memory protocol is distinct from the photon-echo protocols discussed below as it relies on homogeneous broadening of the intermediate excited state rather than (reversible or structured) inhomogeneous broadening.

In order to optimize storage efficiency in the ATT protocol, the storage control field arrival should be synchronized in time with the first zero of the complex signal field amplitude evaluated at the middle of the ensemble ($L/2$) [157]. This protocol can implement optimal photon storage (i.e., $\eta_{\mathrm{stor}} = \eta_{\mathrm{opt}}$) for large optical depths, when the adiabaticity criterion $d\tau_{\mathrm{FWHM}}\gamma \gg 1$ is satisfied [156]. As this protocol is typically employed when $\tau_{\mathrm{FWHM}}\gamma < 1$, this implies $d \gg 1/(\tau_{\mathrm{FWHM}}\gamma)$.

Near-off-resonant memory (NORM) operation of ATT was introduced in Ref. [109] as a means to achieve higher efficiency than resonant ATT when control field power is constrained. NORM balances reabsorption loss, which is worst on resonance at large optical depths, and finite available control field power, which leads to lower efficiency at larger detuning. NORM operation is not necessary in the ideal case, for example, investigated in Ref. [141], when all parameters of the control field are optimized to improve memory efficiency. NORM operation only appears to help in the case when one parameter of the control field is constrained, as is frequently the case experimentally. Future work is needed to investigate this behavior theoretically.

The NORM ATT protocol is well-suited for broadband operation, as was recently demonstrated in Refs. [109] and [110] in atomic barium vapor. A storage efficiency of 95.6±0.3% was reached for ultrashort photons (500 fs), which, as noted in Sec. 1.3.1.3, is the highest attained for bandwidths >10 MHz (see Fig. 1.11 in Sec. 1.3.4.1). The total efficiency was measured to be 31±1% at 900 °C, limited by control field power. The lifetime of this memory was measured to be 0.49(1) ns at 900 °C, which, while not long in absolute terms, is significantly better than the ∼ps level lifetimes that are typical of solid-state THz memories (see Sec. 1.3.4.2), which are usually assumed to be population-lifetime limited; the bare atomic

0.25 sec population lifetime of the storage state used in atomic barium leaves large room for improvement. This lifetime corresponds to a time-bandwidth product of TBP $= 980 \pm 20$. In terms of noise performance, a signal-to-noise ratio of SNR $=(8.2\pm1.3)\times10^3$ is measured for an input of 1 photon per pulse, leading to a single photon fidelity of $F = 0.99988(2)$. This noise performance is on par with the lowest noise ladder-type atomic ensemble memory systems [53–55, 57], as shown in Sec. 1.3.4.3. The exceptional noise performance of this memory is explained by the ultra-large ground-storage state splitting, which is so large (∼340 THz) that it eclipses the excited-storage state splitting (∼200 THz), the transition operated along by the control field. This means that, to first order, the control field frequency is insufficient to excite four-wave mixing noise, which is the dominant noise contribution in almost all other Λ-type memories. This large ground-storage state splitting also virtually eliminates noise from thermal population of the storage state, and furthermore allows for near complete spectral suppression of control field leakage noise into the signal path.

Off-Resonant Raman

The off-resonant Raman memory protocol [158] is well-suited for storage and retrieval of broadband photons. In a typical Λ-type or ladder system, the strong control field, which is off-resonant from the excited state $|e\rangle$ by a detuning Δ (see Fig. 1.3), enables a two-photon transition between the ground state $|g\rangle$ and storage state $|s\rangle$. In the storage process, the signal photon, which is also detuned by Δ from the $|g\rangle \rightarrow |e\rangle$ transition, is spatially and temporally overlapped with the control field and is thereby mapped onto a collective spin-wave excitation. A subsequent retrieval field (typically the same as the storage field) is then applied to the atomic ensemble and the stored photon is deterministically released, completing the retrieval process.

In the off-resonant Raman limit, the detuning is much greater than the excited state linewidth, the bandwidths of signal and control fields, and the control field Rabi frequency $|\Delta| \gg \Gamma, BW, |\Omega(\tau)|$. This allows the off-resonant Raman protocol to operate in the adiabatic regime where the excited state is eliminated. In principle, this may also allow for the storage and retrieval of photons with arbitrary temporal shapes, and for arbitrary temporal shaping upon retrieval, depending on the shape of the control field. The memory efficiency for this protocol is proportional to the optical depth and control pulse energy and is inversely proportional to the detuning. The bandwidth of storage is typically only limited by the energy splitting between ground and storage states, and has therefore exceeded 1 THz in experiment [92, 159–161]. Due to the large detuning, four-wave mixing noise is typically dominant over control field leakage noise and other noise contributions.

In ladder systems, the off-resonant Raman protocol with few modifications is referred to as off-resonant cascaded absorption (ORCA) [54, 55].

Controlled Reversible Inhomogeneous Broadening (CRIB)

In atomic ensembles that exhibit inhomogeneous broadening of the optical transition, the atomic coherence generated by the absorption of the incoming signal will begin to rapidly dephase. Controlled reversal of the inhomogeneous broadening at a time t following absorption leads to time-reversal of this dephasing and the subsequent re-emission of the signal field at time $2t$ [133, 155, 162–165]. A review of the equations of motion governing this process can be found in Sec. 1.3.3.1 of this chapter and in the proposal of this protocol, Ref. [163]. This memory protocol is commonly referred to as controlled reversible inhomogeneous broadening (CRIB). The bandwidth for this protocol is set by the inhomogeneous broadening of $|g\rangle \rightarrow |e\rangle$ transition [162, 166]. A subset of these protocols are the gradient echo memories (GEM) in which the controlled inhomogeneous broadening is given by a spatial electric or magnetic field gradient [162].

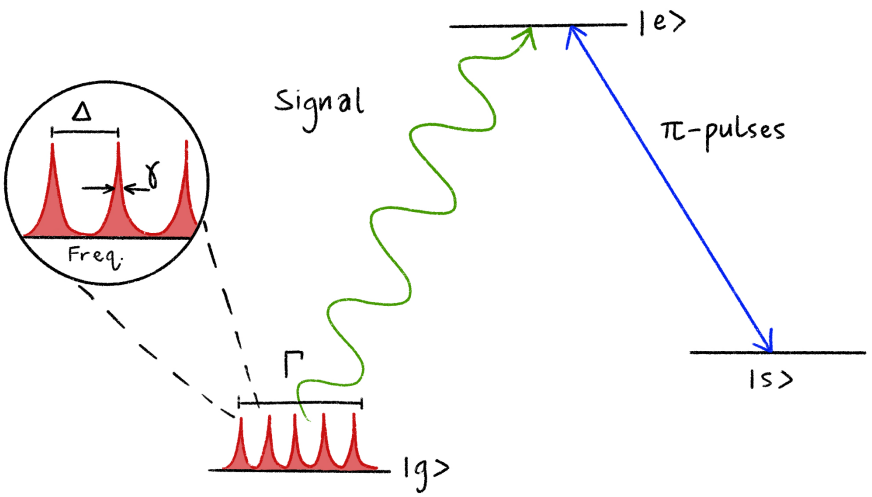

Figure 1.7: **Schematic of the atomic frequency comb (AFC) quantum memory protocol.** A periodic comb structure of total width Γ is formed in the inhomogeneous line. The comb teeth have linewidth γ and are evenly spaced by Δ. More details can be found in Ref. [121].

The efficiency of CRIB is derived in Refs. [163, 165]. For a narrow absorption feature of initial linewidth γ_0 that has been inhomogeneously broadened to γ, the efficiency of CRIB is given by:

$$\eta_{\text{CRIB}} = (1 - e^{-d\gamma_0/\gamma})^2 \tag{1.20}$$

where d is the optical depth of the unbroadened line. The efficiency goes as the square of the probability of absorption, as the retrieval process is given by time-reversed absorption [165, 167]. Additional considerations and expressions for the efficiency are discussed in Refs. [133, 168]. To date, the bandwidth and efficiency of experimental implementations of the CRIB protocol have been limited to ~ 0.7 MHz and 69%, respectively [169].

Gradient Echo Memory (GEM)

Gradient echo memories (GEM) are an implementation of the CRIB protocol in which the inhomogeneous broadening is given by a (typically spatial) electric or magnetic field gradient [133, 162, 165]. In these schemes, the spatial gradient gives rise to a spatially dependent detuning that can be reversed by changing the sign of the gradient. The GEM protocol consequently does not require backward propagation of the signal for high efficiency [162]. GEM was first implemented at the few-photon level over a decade ago using light in the telecommunications C-band, at a bandwidth of 5 MHz, with a storage time of several hundred nanoseconds [170]. Implementations in cold atomic ensembles have also been demonstrated over the last decade [171–173], however the bandwidths demonstrated (sub-MHz) tend to be small due to the difficulty in generating GHz-THz inhomogeneous linewidths.

Atomic Frequency Comb (AFC)

The atomic frequency comb (AFC) protocol is an inherently multimode photon echo memory that utilizes many narrow, periodically spaced absorption features created in a broad inhomogeneous $|g\rangle \rightarrow |e\rangle$ line by optical pumping [87, 121, 133, 162, 165, 174]. Contrary to the CRIB and GEM protocols, the periodic

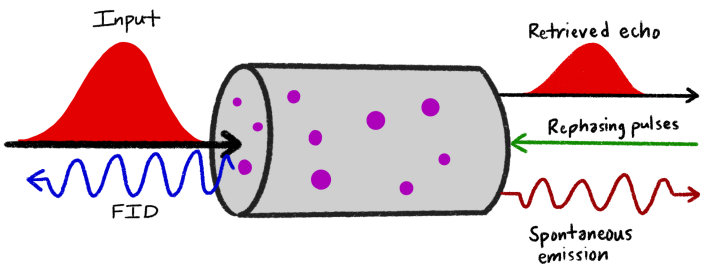

Figure 1.8: **Schematic of the ROSE protocol.** The rephasing pulses (green) are counterpropagating relative to the input signal. In this geometry, the free induction decay (blue) will be emitted in the same direction as the rephasing beams. Spontaneous emission noise (thin red) will still be present and pollute the retrieved echo emitted in the forward direction. More detail can be found in Ref. [176].

structure of this frequency comb itself leads to periodic rephasing, without the need for external fields to reverse the inhomogeneity. The periodic structure has total width Γ, and is composed of narrow comb teeth of linewidth γ evenly spaced in frequency by Δ. The finesse of the comb teeth is then $\mathscr{F} = \Delta/\gamma$. Since atoms are selectively removed from the inhomogeneous line to form the comb structure, the optical depth of the transition has been reduced approximately by a factor of $\mathscr{F}$ [121, 174].

Signal bandwidths compatible with the AFC protocol must satisfy $\Delta < BW \lesssim \Gamma$. Upon absorption of the signal field, the periodic structure of the frequency comb causes the atomic coherence to rephase after a time $2\pi/\Delta$, leading to subsequent reemission of the signal field. The AFC protocol thus possesses a fixed, predetermined storage time set by the spacing of the comb teeth; however, prolonged and arbitrary storage times can be achieved by mapping the coherence to a third metastable state, $|s\rangle$, via optical π-pulses [121, 133, 162], as shown in Fig. 1.7.

Retrieval of the signal field in the forward direction is limited to a maximum efficiency of 54% due to reabsorption of the signal field by the medium [121, 133, 162], and is given by the closed form $\eta_{\text{AFC}} \approx (d/\mathscr{F})^2 e^{-7/\mathscr{F}^2} e^{-d/\mathscr{F}}$. Retrieval of the signal field in the backward direction is not subject to this constraint, and is given by $\eta_{\text{AFC}} \approx (1 - e^{-d/\mathscr{F}})^2 e^{-7/\mathscr{F}^2}$ [121].

A distinct advantage of the AFC protocol is that the total number of temporal modes that can be stored does not depend on the optical depth of the medium, but rather the total number of comb teeth that are prepared [165]. In contrast, the capacity of the EIT protocol to store N modes scales as $\sqrt{d}$, and for the CRIB protocol, for sufficiently large optical depth, the number of modes N scales linearly with d [121, 133, 165].

Out of those protocols employing an inhomogeneously broadened $|g\rangle \rightarrow |e\rangle$ transition, the AFC protocol tends to be the most broadband, where bandwidths up to 50 GHz at an efficiency of 1.8% have been demonstrated in the literature [175].

Revival of Silenced Echo (ROSE)

The two-pulse photon echo is a natural candidate for quantum memory in inhomogeneously broadened media [177]. In principle, two-pulse photon echoes do not require any state preparation, and may utilize the entire inhomogenous linewidth and optical depth, which may improve the multimode capacity of such a memory compared to the AFC protocol [177–179]. Such a protocol can in principle also be extended to a three-level system to transfer the inhomogeneous atomic coherence to a longer-lived spin state [179]. A two-photon echo

on its own is not suitable for quantum memory, however, as population inversion from the strong rephasing pulse creates significant and unavoidable spontaneous emission and free induction decay (FID) noise [177, 179].

A modification to the two-pulse photon echo protocol, the revival of silenced echo (ROSE) protocol, is able to suppress some of these inherent noise sources and provide quantum operation. This protocol relies on phase-mismatching of the incoming signal and the first rephasing pulse. The atomic polarization in the medium persists regardless of the phasematching between these two fields, and phasematching with a second rephasing pulse enables coherent emission of a second photon in the absence of FID noise. The total storage time for this process is $2(t_2 - t_1)$, where t_1 and t_2 are the arrival times of the first and second rephasing pulses, respectively [176, 179, 180]. The geometry of this scheme is described in Refs. [176, 179, 180] and illustrated in Fig. 1.8. If both rephasing pulses are co-linear and counterpropagating relative to the incoming signal, FID will be emitted in the direction of the rephasing pulses and not the retrieved echo. Spontaneous emission noise cannot be eliminated and remains a limitation to the noise performance of this protocol.

In the limit of an infinite T_2 coherence time, and assuming forward emission of the second echo, the efficiency of ROSE depends solely on the optical depth as $\eta_{\mathrm{ROSE}} = d^2 e^{-d}$. For a finite T_2, the efficiency also depends on T_2 and the time difference between the two rephasing pulses as $\eta_{\mathrm{ROSE}} = d^2 e^{-d} e^{-4(t_2-t_1)/T_2}$ [176, 179].

In the proposal for the ROSE scheme, the authors note that π-pulses are not optimal for the population inversion [179]; adiabatic passage with chirped pulses is preferable and has been used in several experimental implementations of ROSE [176, 178, 179, 181]. To date, the ROSE protocol has been exclusively implemented in rare-earth ion-doped solids at cryogenic temperatures: Tm^{3+}:YAG [176, 180, 182, 183], Er^{3+}:YSO, [178, 181], and Tm^{3+}:YSO [184]. Efficiencies as high as 44% have demonstrated in 0.005% $^{167}Er^{3+}$:YSO, as well as storage times of up to 16 μs, though memory bandwidths are typically limited to below 1 MHz [178, 181].

Hybrid Photon-Echo Rephasing (HYPER)

Hybrid photon-echo rephasing (HYPER) is a protocol that combines the concepts of CRIB with a two-photon echo, thus avoiding the optical pumping step required for protocols like CRIB and AFC, and reducing the noise associated with the naïve two-pulse photon echo protocol. In HYPER, an inhomogeneously broadened atomic ensemble is further inhomogeneously broadened in a controllable fashion after absorption of the signal field. The controllable broadening is then turned off, a π-pulse typical of the two-pulse photon echo scheme is applied, and the controllable broadening is turned back on. By introducing this controllable broadening, the standard two-pulse echo is silenced, and after turning off the controllable broadening a second time, and applying a second π-pulse, finally the atomic polarization rephases and the signal field is reemitted. This scheme ultimately reduces the number of atoms that would experience gain and undergo spontaneous emission, thus reducing the noise inherent to two-photon echoes [166]. Analytical treatment of the protocol, and the first experimental implementation with 0.2 MHz bandwidth and ~10% efficiency, can be found in Ref. [166].

1.3.2.2 Hardware

We now move on to discuss the various types of hardware used for atomic ensemble quantum memory. Each type possesses unique advantages and disadvantages, and may place limits on the memory protocols that are possible to implement in each system (e.g., rare-earth ions doped in solids with intrinsic inhomogeneous broadening).

Hot Atoms

Hot atomic ensembles have been widely used to establish different quantum memory schemes, thanks to their advantages of room (or near-room) temperature operation and reduced experimental complexity. Due to their relatively simple electronic structure, high vapor pressure, and long-lived spin states, the alkali metals rubidium and cesium have been the atomic species most widely used for hot atomic ensemble quantum memory. The recently demonstrated barium memory is an exception, where instead of spin states, electronic orbitals were used for the memory interaction to enable THz-bandwidth storage [109, 110]. In addition to hot atomic species, molecular species in room-temperature gas cells have also been used for ensemble quantum memory [94, 161], where a phononic storage state is used instead of a hyperfine spin level as is the case for the alkali atoms.

Glass vapor cells have the advantage of widespread commercial availability, and are thus one of the most frequently used hardware implementations for hot atomic ensemble quantum memory. These cells are prepared using precision scientific glassblowing techniques, in which the atoms are introduced to the glass cell under vacuum conditions. One disadvantage of glass vapor cells are the inelastic collisions between atoms inside the cell and the cell walls, which can limit memory lifetimes in the narrowband regime [185] or when the atoms are optically pumped into the metastable spin state [186]. These collisions occur on the microsecond timescale for a typical, centimeter-size cell, and can further induce spin depolarization, thus reducing the lifetime of any collective spin state, including those used in ensemble quantum memory. Buffer gases such as Ar, Ne or N_2 are commonly loaded into the vapor cell along with the atomic species of choice to increase the lifetime of collective spin states and to reduce the broadening of certain transitions due to inelastic collisions [187]. As it slows atomic diffusion and limits the absorption of atoms onto the cell walls, the presence of a buffer gas may also increase the device lifetime of glass vapor cells. Unfortunately, the presence of buffer gas can also induce additional spin depolarization and quenching due to collisions between the atoms and buffer gas [188]. An optimal buffer gas pressure can be found that balances mitigation of wall collisions and the increase in atom–buffer-gas collisions [189]. Paraffin-coated vapor cells have also been studied as an alternative method to increase collective spin state lifetimes by inducing elastic instead of inelastic wall collisions [185, 190]. A disadvantage of paraffin-coated or similar vapor cells is their complex fabrication process, as well as the fact that the coating material may be incompatible with elevated temperatures. Collisions between atoms and buffer gas can also be a source of noise due to collision-induced fluorescence [188, 191]. This noise source limits the fidelity of quantum memory, particularly at or near resonance, and is greatly reduced when the quantum memory is operated off resonance and optical filtering is applied. Buffer-gas free vapor cells naturally suppress collision-induced fluorescence noise [185].

The lifetime of collective spin states is not only influenced by collisions. Broadband quantum memories using hot atomic ensembles may also suffer from spin-wave dephasing arising from thermal atomic motion [192]. This atomic motion may result in atoms wandering out of the effective interaction region defined by the laser fields, or it may result in scrambling of the spin-wave phase as the constituent atoms move within the interaction region. The rate of this latter dephasing process is proportional to $\Delta\vec{k} \cdot \vec{v}$ with $\Delta\vec{k} = \vec{k}_s - \vec{k}_c$ representing the wavevector of the spin wave, where $\vec{k}_s$ and $\vec{k}_c$ are the wavevectors of signal and control fields, respectively, and $\vec{v}$ representing the thermal velocity of the atoms. In general, it is desirable generate a spin wave with long wavelength in order to maintain spin-wave coherence. This can be modified somewhat through experimental design [185], but in many cases the spin-wave wavelength is limited by the large detuning of the signal and control fields. One scheme [56] has demonstrated elimination of motional dephasing through dressing of the collective spin state to an auxiliary 'sensor' state. A sensor state corresponds to a state

that, when coupled via an optical field to the storage state, exhibits opposing energy shifts under the same broadening mechanism. First demonstrated experimentally in a Doppler-broadened system [56], off-resonant fields couple the storage state to the sensor state, dressing the collective excitation such that the frequency shifts due to the dephasing mechanism cancel out. Thus, the dephasing of the spin wave is protected at the price of one or two additional dressing fields. Another scheme using velocity-selective optical pumping [193] has been proposed and proved to be effective against motional dephasing at the cost of reduced optical depth. In this scheme the atoms are pumped out from ground state to an auxiliary state and then pumped back to the ground state using a narrowband laser, which selectively narrows the motional distribution of the atoms. The rate of dephasing is therefore reduced owing to the small $\Delta\vec{v}$ of the atoms. Other mechanisms that induce spin wave dephasing include spatial and temporal variation of longitudinal magnetic field. Note that this is not unique to hot atomic ensembles and experiments have been performed to show prolonged spin-wave coherence using hot atomic vapors through magnetic shielding [194] or applying a strong guiding magnetic field [195, 196].

The heat-pipe oven is an alternative to glass vapor cells, and represents a more robust, higher-temperature, customizable vapor cell [197–199]. Typically heat-pipe ovens are comprised of a stainless-steel tube covered by a heater with water cooling at both ends. Inside the tube, the wall is covered by mesh that acts as wick. Upon heating, atoms from liquid metal evaporate, form a dense vapor, and diffuse toward both ends of the oven until they condense in the water-cooled region and return to the center through the wick due to the capillary effect. The heat-pipe oven can be used to establish a homogeneous temperature and density distribution oven for a long period of time. It can handle high temperatures, which is suitable for low-vapor-pressure atomic species or high-vapor-pressure species at much higher optical depth. The design of the oven can prevent vapor from condensing on the cell windows, and thus the windows tend to become opaque more slowly than in equivalent glass vapor cells. The species of atoms and buffer gas can also be changed more readily than in sealed glass vapor cells.

Many efforts have been made to miniaturize the hot atomic vapor cell in order to achieve chip-scale operation, enabling compact design and lower necessary optical power [34]. Early attempts to integrate hot atoms with optical fibers and silicon platforms include loading hot atomic vapor near tapered fibers [200], into hollow-core fibers [201], or near waveguides [202]. These approaches in principle allow long interaction length while maintaining tight confinement, although to-date only quantum memory in hollow-core fibers has been implemented experimentally [83]. The large core size of kagome fiber (26 μm) allows for a large optical depth compared to other approaches [200]. The achieved memory lifetime of 100 ns could be further extended using buffer gas or a spin-preserving coating. Light-induced atomic desorption (LIAD) [203, 204] has been found effective in increasing optical depth without heating in miniaturized vapor cells and in kagome fiber [83, 201, 205].

Cold Atoms

Similar to the case in hot atoms, the alkali metals are the species most commonly used for cold atomic ensemble quantum memory. Storage times in hot atomic vapors are limited by various mechanisms, including Doppler broadening and transit-time broadening, which are effectively eliminated in laser-cooled atomic ensembles. However, laser cooling tends to require large ultra-high vacuum chambers, multiple stabilized lasers for cooling and trapping, and typically imposes large latency and a non-unity duty cycle in order to re-cool atoms between shots. The colder the atoms are, the denser the cloud and the further the reduction in motion-related broadening and dephasing. However, the maximum length of the ensemble is typically

reduced for colder temperatures due to practicalities of the various laser fields used for cooling and trapping and the process of evaporative cooling. As a result, there continue to be quantum memory demonstrations in cold atomic gasses in magneto-optical traps at $\sim \mu$K temperatures and in Bose-Einstein condensates at $\sim$ nK temperatures. Optical depths as high as $\sim$ 1000 can be achieved [138]. We note that for very long-lived storage, an optical lattice along the k-vector of the stored spin wave is required to eliminate residual motional effects, which substantially reduces the available optical depth and largely precludes broadband storage.

Solids

Optical phonon modes and optically active point defects in diamond

Over the last 10 years the use of optical phonon modes in bulk diamond has emerged as a platform for fast, broadband quantum memory. Such memories are attractive due to their THz bandwidth operation across the visible and near infrared due to the large bandgap of diamond, and room temperature operation [92, 159, 160, 206–208]. A Λ-system consisting of the ground state of diamond, an optical phonon mode storage state, and the conduction band as the excited state provides a storage bandwidth of up to 40 THz, limited only by the splitting between the ground state and the optical phonon mode. The memory lifetime in this platform is ultimately limited to 3.5 ps by the decay of the phonon mode [160, 208].

The first proof-of-principle experiment to demonstrate the suitability of diamond as a quantum memory yielded a noise floor well below 1 photon per pulse [160]. The primary noise source was FWM noise intrinsic to most Λ-type memory schemes, though the authors highlight that FWM is suppressed due to the large dispersion in diamond [160]. Other sources of noise, such as resonant fluorescence, are greatly suppressed by operating with a detuning of $\sim$950 THz from the conduction band [92, 159, 160].

True single-photon storage was first demonstrated with THz-bandwidth (260 fs) photons produced from a heralded spontaneous parametric down conversion (SPDC) source [92]. The preservation of nonclassicality in the retrieved photons was determined by measuring the second-order correlation function using Hanbury-Brown Twiss interferometry [92, 160]. Storage of polarization qubits and of a single photon from a polarization-entangled pair has been demonstrated with a fidelity of 76% for picosecond-long storage [159].

Optically active point defects in diamond have also been proposed for broadband optical quantum memory [209–211]. Experiments to-date have focused on storage or transduction of photonic quantum information into single diamond color centers [49, 50] and color center ensembles [212], generally through mechanisms outside of those described in Secs. 1.3.1.2 and 1.3.3. Broadband single photon storage and retrieval in diamond color center ensembles has yet to be demonstrated.

Rare-earth ions

Trivalent rare-earth ions doped in solids at cryogenic temperatures have many properties that make them a promising platform for quantum memory devices, including long-lived coherence, compatibility with integrated photonics, lack of motional dephasing, high density of ions, moderate optical depths, and telecommunications wavelength compatibility [213–221]. Optical coherence times can exceed milliseconds [222, 223] and, to date, the longest spin coherence time observed is 6 hours [224].

The long optical and spin coherence properties afforded to the rare earths is due to their unique electronic structure. The optical transitions of interest are between their 4f-4f valence electronic levels, which are dipole-forbidden in the free ion. The 4f valence shell is electronically shielded by filled 5s and 5p orbitals, which renders the 4f levels largely insensitive to their environment. Incorporation of the rare-earth ion in a

solid introduces a crystal electric field which acts as a perturbation to the free-ion states. For sufficiently low site-symmetry of the rare-earth ion, the crystal electric field mixes in additional states, which weakly allows electronic transitions [220, 225].

The electronic states of the free ion are labeled by Russell-Saunders term symbols where the electronic spin J and projection m_j are considered good quantum numbers [220, 225, 226]. These states are $(2J+1)$-degenerate, known as Kramer's degeneracy. The addition of the crystal electric field either partially or completely lifts the degeneracy of these states. For sufficiently low site symmetry and ions with an even number of electrons—the non-Kramer's ions—the degeneracy can be lifted completely. The species with an odd number of electrons—the Kramer's ions—require an external field to fully break this degeneracy. Rare-earth ions can have further splittings of their crystal field levels from hyperfine structure, the Zeeman effect, and higher order moments [220, 225].

While these electronic levels are largely insensitive to their environment, it is residual environmental effects that broaden the optical and spin transitions. Homogeneous broadening is largely due to dynamical processes within the solid and can be sorted broadly into four categories: ion-phonon interactions, ion-ion interactions, ion-host lattice interactions, and pure dephasing. Optical phonons are suppressed at or below 4 K [220, 225, 227]. Microwave phonons can couple the spin transitions and primarily interact with the ion via multiphonon processes that scale nonlinearly with temperature [222, 225, 228]. Ion-ion interactions account for a number of interactions such as instantaneous spectral diffusion, in which the excitation of one ion shifts the electric dipole of a neighboring ion [220, 225, 227, 229, 230]. The dominant source of dephasing below 4 K is interactions between the ion and the host lattice, which acts as a spin bath [220]. For example, fluctuating magnetic fields due to nuclear spin flips of Y^{3+} are the dominant source of dephasing in YSO [231]. This dephasing can be suppressed to extend the coherence times by application of a moderate external magnetic field to polarize the spin bath, as well as finding spin transitions that have zero effective first-order Zeeman shift [224, 232–234], and employing rephasing techniques like dynamical decoupling [235–239].

Defects and strain in the crystalline host result in inhomogeneous broadening of both the optical and spin transitions. The local crystal field seen by the ions varies site-to-site, resulting in a static inhomogeneous shift to their transition energy. In commercially doped rare-earth materials, the inhomogeneous broadening of the optical transition can be on the order of 10's of MHz to 100's of GHz depending on factors such as (but not limited to) the host material, doping concentration, and isotopic purity. The inhomogeneous broadening is always many orders of magnitude larger than the homogeneous linewidth [220, 225, 227, 240–246]. In the case of rare-earth doped solids, where the ions themselves are substitutional dopants, they may be the primary source of this inhomogeneous broadening [162, 220, 226, 247].

Ions with an even number of electrons—the non-Kramer's ions (Eu^{3+}, Pr^{3+}, Tm^{3+})—have a quenched electronic spin and consequently are more insensitive to their environment and have longer coherence properties. The nuclear spin state splittings in these ions are between 10-100 MHz—too narrow to be optically resolved in many host materials due to the large inhomogeneous linewidth [233, 245, 248–253]. The spin coherence properties of the non-Kramer's ions can be exploited for long storage times by utilizing techniques such as spectral holeburning to resolve the nuclear spin states; however, this comes at the expense of sacrificing optical depth—and therefore the storage efficiency—by only using a small subset of the atoms in the inhomogeneous line [162].

In the Kramer's ions (Er^{3+},Yb^{3+}, Nd^{3+})—the paramagnetic species—application of an external magnetic field can yield Zeeman splittings large enough for the Zeeman sublevels to to be resolvable in the inhomogeneous line. These species are of particular interest due to their larger bandwidths, on the order of hundreds of MHz

to GHz, and potential for interfacing with platforms such as superconducting qubits [254–257]. While their Zeeman states can be accessible and have the potential for larger memory bandwidths than the non-Kramer's ions, with state splittings of several hundred MHz to GHz, their electronic spin has stronger coupling to the environment due to its larger magnetic moment and thus is more susceptible to fluctuations and exhibits shorter coherence times. A challenge of utilizing the Kramers species is the ability to efficiently optically pump them [258, 259], which is a prerequisite of many quantum memory protocols such as AFC and CRIB [121, 133, 162]. Erbium is one of the most attractive rare-earths due to its telecom C-band transition at 1.5 μm; however erbium can be difficult to optically pump since the lifetime of its Zeeman sublevels is only about an order of magnitude slower than the excited state lifetime [228, 260]. However, using Kramers isotopes with nuclear spin helps substantially and spin coherence times as long as 1 second have been achieved in $^{167}Er^{3+}$:YSO [261]. Progress has been made recently to overcome the limitations of optical pumping in both Yb^{3+} and Nd^{3+} [221, 258, 262].

There have been many proof-of-principle light storage experiments with both classical light and weak coherent states that show these systems can operate with the proper SNR to store single photons [263–266]. Storing single-photon states in a rare-earth-ion-based quantum memory has also been achieved [267–279].

To date, the longest storage time of a bright classical pulse was 53 minutes and for weak coherent states exceeding 1.0 second [236, 280]; however, both were acheived with low storage efficiencies. On-chip storage of telecommunications C-band light at the few-photon level has also been demonstrated in a photonic nanoresonator with isotopically purified Er-167:YSO [281]. Rare-earth ions have demonstrated quantum memory protocols with bandwidths exceeding a GHz [267, 275, 282, 283].

1.3.3 Theory

1.3.3.1 Maxwell-Bloch Equations

In this section, we expand upon the three-level Maxwell-Bloch equations described in Sec. 1.3.1.2. Section 1.3.3.1 provides several approximations to the Maxwell-Bloch equations relevant for the memory protocols discussed in Sec. 1.3.2.1 that rely on homogeneous broadening, while Sec. 1.3.3.1 provides more information on the Maxwell-Bloch equations in the presence of inhomogeneous broadening.

Each of the protocols in Sec. 1.3.2.1 requires or permits a certain type of line broadening for the intermediate excited state shown in Fig. 1.3, and the type of broadening present in a given system limits the possible memory protocols that can be implemented in that system. The types of excited-state line broadening are broadly categorized into those with homogeneous and inhomogeneous mechanisms. Homogeneous broadening mechanisms affect each atom in the system equally, whereas inhomogeneous mechanisms affect different classes of atoms differently. These classes of atoms may be distinguished in frequency, spatial position, momentum, or any other degree of freedom. Homogeneous broadening mechanisms, which typically apply to cold atoms—but, importantly for broadband operation, are not restricted to cold atoms—include effects such as natural or lifetime broadening, resonance broadening, collisional broadening (which is separated into impact and quasi-static regimes, depending on the timescale of collisions [284]), and phonon broadening in solids. Inhomogeneous broadening mechanisms include Zeeman and Stark broadening (these are typically considered inhomogeneous due to spatial or temporal non-uniformity in the magnetic and electric fields, respectively), Doppler broadening, and crystal-field or impurity-based broadening in solids [225].

Homogeneous

Several approximations to Eqs. (1.6)-(1.8) from Sec. 1.3.1.2 lead to the mathematical descriptions of EIT, ATS, ATT, SR, and Raman protocols, which we compile here. In addition, we provide representations of the Maxwell-Bloch equations in the spectral domain and in the temporal domain split into amplitude and phase. These different forms of the Maxwell-Bloch equations are useful for both analytical and numerical investigation of quantum memory behavior.

In the case of EIT, the approximations $\Delta = 0$ (i.e., $\bar{\gamma} = 1$) and $BW \ll \gamma$ (or $\tau_{\mathrm{FWHM}}\gamma \gg 1$) for both the signal and control fields implies that the time evolution of the atomic polarization in Eq. (1.7) may be adiabatically eliminated, and a reduced set of partial differential equations can be found:

$$\partial_z A(z,\tau) = -dA(z,\tau) + i\sqrt{d}\frac{\Omega(\tau)}{2}B(z,\tau) \tag{1.21}$$

$$\partial_\tau B(z,\tau) = -i\sqrt{d}\frac{\Omega^*(\tau)}{2}A(z,\tau) - \frac{|\Omega(\tau)|^2}{4}B(z,\tau), \tag{1.22}$$

which are significantly less computationally expensive to simulate.

In the case of ATS, the assumptions $\Delta = 0$, $|\Omega| \gg \bar{\gamma}, \sqrt{d}$ imply the elimination of the first two terms on the right-hand-side of Eq. (1.7), and in the case of a constant control field (which without loss of generality can be assumed to be purely imaginary), the simplified coupled partial differential equations

$$\partial_\tau P(z,\tau) = -i\frac{\Omega(\tau)}{2}B(z,\tau) \tag{1.23}$$

$$\partial_\tau B(z,\tau) = -i\frac{\Omega^*(\tau)}{2}P(z,\tau), \tag{1.24}$$

lead to periodically oscillating atomic polarization and spin wave populations that are $\pi/2$ out of phase:

$$A(z,\tau) \propto P(z,\tau) = \sin\left(\frac{|\Omega(\tau)|}{2}t\right) \tag{1.25}$$

$$B(z,\tau) = \cos\left(\frac{|\Omega(\tau)|}{2}t\right). \tag{1.26}$$

For ATT, the assumptions $\Delta = 0$, $BW \geq \gamma$ (or $\tau_{\mathrm{FWHM}}\gamma \leq 1$), and $d \gg 1$ imply that we can drop the $\bar{\gamma}P(z,\tau)$ term in Eq. (1.7). Further assuming a π-pulse control field that arrives after absorption of the signal field implies the terms involving $\Omega(\tau)$ are eliminated during the initial absorption stage, leaving only the simplified equations:

$$\partial_z A(z,\tau) = -\sqrt{d}P(z,\tau) \tag{1.27}$$

$$\partial_\tau P(z,\tau) = \sqrt{d}A(z,\tau), \tag{1.28}$$

which has exact solution

$$A(z,\tau) = e^{t-dz}[1-\Theta(\Delta\tau^{\text{ctrl}})] \tag{1.29}$$

$$P(z,\tau) = \sqrt{d}e^{t-dz}[1-\Theta(\Delta\tau^{\text{ctrl}})] \tag{1.30}$$

during the absorption stage (until the arrival of the control field, $\tau < \Delta\tau^{\text{ctrl}}$), where $\Theta(\Delta\tau^{\text{ctrl}})$ is the Heaviside step function. The π-pulse control field then in principle transfers $P \to B$ exactly. Applying the definition of storage efficiency, we find $\eta_{\text{stor}} = 1 - e^{-2d}$. The treatment of the SR memory protocol is nearly identical, but operates under the assumption of $BW \gg \gamma$ (or $\tau_{\text{FWHM}}\gamma \ll 1$) and superradiant coupling between atoms in the ensemble. The approximations leading to the Raman protocol are similar to EIT, but in the far-off-resonant limit, i.e., $\Delta \gg \gamma$ (i.e., $\bar{\gamma} \approx -i\Delta/\gamma = -i\bar{\Delta}$) and $BW \ll \Delta$. These conditions also imply the adiabatic elimination of the atomic polarization, leading to the simplified system:

$$\partial_z A(z,\tau) = -i\frac{d}{\bar{\Delta}}A(z,\tau) - \frac{\sqrt{d}}{\bar{\Delta}}\frac{\Omega(\tau)}{2}B(z,\tau) \tag{1.31}$$

$$\partial_\tau B(z,\tau) = \frac{\sqrt{d}}{\bar{\Delta}}\frac{\Omega^*(\tau)}{2}A(z,\tau) - i\frac{|\Omega(\tau)|^2}{4\bar{\Delta}}B(z,\tau). \tag{1.32}$$

Several other forms of the Maxwell-Bloch equations are useful both analytically and numerically. In the spectral domain, we can rewrite the Maxwell-Bloch equations via application of the Fourier transform as:

$$\partial_z \tilde{A}(z,\omega) = -\sqrt{d}\tilde{P}(z,\omega) \tag{1.33}$$

$$i\omega\tilde{P}(z,\omega) = -\bar{\gamma}\tilde{P}(z,\omega) + \sqrt{d}\tilde{A}(z,\omega) - \frac{i}{\sqrt{2\pi}}\frac{\tilde{\Omega}(\omega)}{2} * \tilde{B}(z,\omega) \tag{1.34}$$

$$i\omega\tilde{B}(z,\omega) = -\gamma_B\tilde{B}(z,\omega) - \frac{i}{\sqrt{2\pi}}\frac{\tilde{\Omega}^*(-\omega)}{2} * \tilde{P}(z,\omega). \tag{1.35}$$

Here we have made use of the convolution theorem for Fourier transforms and the fact that the Fourier transform of a conjugated function is the conjugate of the function's Fourier transform reflected about $\omega = 0$. We have used "$*$" to express the convolution of two functions, e.g. $\tilde{\Omega}(\omega) * \tilde{B}(z,\omega) = \int_{-\infty}^{\infty} du\, \tilde{\Omega}(\omega - u)\tilde{B}(z,u)$. Here ω represents the difference from each field's center frequency. This form of the Maxwell-Bloch equations can be particularly useful for simulation of broadband quantum memory. As usual, application of the Fourier transform has converted equations involving temporal derivatives to simple algebraic equations.

Another useful form of the Maxwell-Bloch equations arises from separating the amplitude and phase of each field, leading to the following 6 equations of motion:

$$\partial_z|A(z,\tau)| = -\sqrt{d}|P(z,\tau)|\cos[\phi_P(z,\tau)-\phi_A(z,\tau)] \tag{1.36}$$

$$\partial_z\phi_A(z,\tau) = -\sqrt{d}\frac{|P(z,\tau)|}{|A(z,\tau)|}\sin[\phi_P(z,\tau)-\phi_A(z,\tau)] \tag{1.37}$$

$$\begin{aligned}\partial_\tau|P(z,\tau)| = &-\bar{\gamma}|P(z,\tau)| + \sqrt{d}|A(z,\tau)|\cos[\phi_A(z,\tau)-\phi_P(z,\tau)] \\ &+ \frac{1}{2}\Re[\Omega(\tau)]|B(z,\tau)|\sin[\phi_B(z,\tau)-\phi_P(z,\tau)] \\ &+ \frac{1}{2}\Im[\Omega(\tau)]|B(z,\tau)|\cos[\phi_B(z,\tau)-\phi_P(z,\tau)]\end{aligned} \tag{1.38}$$

$$\begin{aligned}\partial_\tau\phi_P(z,\tau) = \Delta &+ \sqrt{d}\frac{|A(z,\tau)|}{|P(z,\tau)|}\sin[\phi_A(z,\tau)-\phi_P(z,\tau)] \\ &- \frac{1}{2}\Re[\Omega(\tau)]\frac{|B(z,\tau)|}{|P(z,\tau)|}\cos[\phi_B(z,\tau)-\phi_P(z,\tau)] \\ &+ \frac{1}{2}\Im[\Omega(\tau)]\frac{|B(z,\tau)|}{|P(z,\tau)|}\sin[\phi_B(z,\tau)-\phi_P(z,\tau)]\end{aligned} \tag{1.39}$$

$$\begin{aligned}\partial_\tau|B(z,\tau)| = &-\gamma_B|B(z,\tau)| + \frac{1}{2}\Re[\Omega(\tau)]|P(z,\tau)|\sin[\phi_P(z,\tau)-\phi_B(z,\tau)] \\ &- \frac{1}{2}\Im[\Omega(\tau)]|P(z,\tau)|\cos[\phi_P(z,\tau)-\phi_B(z,\tau)]\end{aligned} \tag{1.40}$$

$$\begin{aligned}\partial_\tau\phi_B(z,\tau) = &-\frac{1}{2}\Re[\Omega(\tau)]\frac{|P(z,\tau)|}{|B(z,\tau)|}\cos[\phi_P(z,\tau)-\phi_B(z,\tau)] \\ &- \frac{1}{2}\Im[\Omega(\tau)]\frac{|P(z,\tau)|}{|B(z,\tau)|}\sin[\phi_P(z,\tau)-\phi_B(z,\tau)],\end{aligned} \tag{1.41}$$

where each field is written $X(z,\tau) = |X(z,\tau)|e^{i\phi_X(z,\tau)}$ for $X = A, P$, and B, and where $\Re(\cdot)$ and $\Im(\cdot)$ designate the real and imaginary parts of the enclosed function, respectively. This form of the equations of motion is particularly useful for analysis and simulations involving chirped optical fields or fields with non-trivial temporal/spectral phase.

Inhomogeneous

Inhomogeneous broadening of the intermediate excited state is treated as a coherent sum of homogeneous distributions separated in frequency [67], leading to the following equations of motion:

$$\partial_z A(z,\tau) = -\sqrt{d}P(z,\tau) \tag{1.42}$$

$$\partial_\tau P_\Delta(z,\tau) = -(\bar{\gamma}-i\Delta)P_\Delta(z,\tau) + \sqrt{d}\sqrt{p_\Delta}A(z,\tau) - i\frac{\Omega(\tau)}{2}B_\Delta(z,\tau) \tag{1.43}$$

$$\partial_\tau B_\Delta(z,\tau) = -\gamma_B B_\Delta(z,\tau) - i\frac{\Omega^*(\tau)}{2}P_\Delta(z,\tau), \tag{1.44}$$

where $P(z,\tau) = \int d\Delta\sqrt{p_\Delta}P_\Delta(z,\tau)$ in Eq. (1.42) and p_Δ represents the normalized fraction of atoms with inhomogeneous detuning Δ (i.e., $\int d\Delta\, p_\Delta = 1$). Here we have redefined $\bar{\gamma} = (\gamma - i\Delta_0)/\gamma$ to designate the detuning Δ_0 of the optical fields relative to the atoms with no inhomogeneous shift (i.e., for $\Delta = 0$).

Analytic expressions for memory efficiency and other metrics for each of the protocols discussed in Sec. 1.3.2.1 may be derived from Eqs. (1.42)-(1.44) by assuming the appropriate inhomogeneous spectral profile p_Δ and the appropriate pulse sequence [i.e., for most protocols, during storage the control field is off

and terms involving $\Omega(\tau)$ in Eqs. (1.42)-(1.44) may be neglected].

Again, these equations may be Fourier transformed into the spectral domain or split into amplitude and phase for ease of computation, just as in the homogeneous case described above.

1.3.3.2 Efficiency Optimization

The primary focus of most existing theoretical work dealing with atomic ensemble quantum memory revolves around the goal of increasing memory efficiency. In principle, the same or similar tools that have been developed for efficiency optimization may also be used to improve other metrics, but efficiency is uniquely important for quantum memory applications and has accordingly received the majority of theoretical attention. The techniques described in the following Secs. 1.3.3.2 and 1.3.3.2 are most fully described in Refs. [65–69].

Signal Field Shaping

One particularly powerful tool for increasing memory efficiency is optimization of the temporal profile of the signal field in both amplitude and phase. The idea behind this optimization technique is that every stage of the memory process can be treated as a linear integral mapping with a unique integral kernel fully describing the map. Each kernel can be decomposed into singular vectors and associated singular values that act as a prefactor describing the efficiency for each mapping between singular vectors. For example, the storage process is described by the map

$$B_{\text{out}}(z) = \int_{-\infty}^{\infty} d\tau \, K_{\text{stor}}(z,\tau) A_{\text{in}}(\tau), \tag{1.45}$$

where $A_{\text{in}}(\tau)$ is the incident signal field temporal profile, $K_{\text{stor}}(z,\tau)$ is the integral kernel for the storage operation, and $B_{\text{out}}(z)$ is the long-lived spatially dependent spin wave resulting from the storage process. Singular value decomposition of this storage kernel takes the form

$$K_{\text{stor}}(z,\tau) = \sum_j \lambda_j B_j(z) A_j^*(\tau), \tag{1.46}$$

where $B_j(z)$ and $A_j(\tau)$ are the left-singular and right-singular vectors (sometimes called the 'optimal modes') of $K_{\text{stor}}(z,\tau)$ and λ_j are its singular values. The exact form of the storage kernel $K_{\text{stor}}(z,\tau)$ depends on parameters of the memory such as the optical depth, linewidth, control field shape, etc. Given Eqs. (1.45) and (1.46), it is clear to see that the largest storage efficiency is achieved when $A_{\text{in}}(\tau)$ matches the right-singular vector of the storage kernel with the largest singular value, $A_{\text{opt}}(\tau)$, as any admixture of $A_{\text{in}}(\tau)$ with other modes will imply a component of the mapping with non-optimal λ_j, or non-optimal efficiency. Thus if it is possible to arbitrarily shape the signal field to be stored, one can optimize memory efficiency by shaping $A_{\text{in}}(\tau)$ to match $A_{\text{opt}}(\tau)$. One can determine the exact form of $A_{\text{opt}}(\tau)$ by numerically or analytically constructing $K_{\text{stor}}(z,\tau)$ and computing its singular value decomposition based on the experimental parameters at hand, or by an iterative experimental process based on time-reversal described in Refs. [66, 137, 285, 286].

Control Field Shaping

Shaping of incident single-photon light pulses that contain sensitive encoded quantum information can introduce loss, which is undesirable for almost every application of quantum memory. It is generally more desirable to shape the strong, many-photon control field, where loss can be easily compensated for by

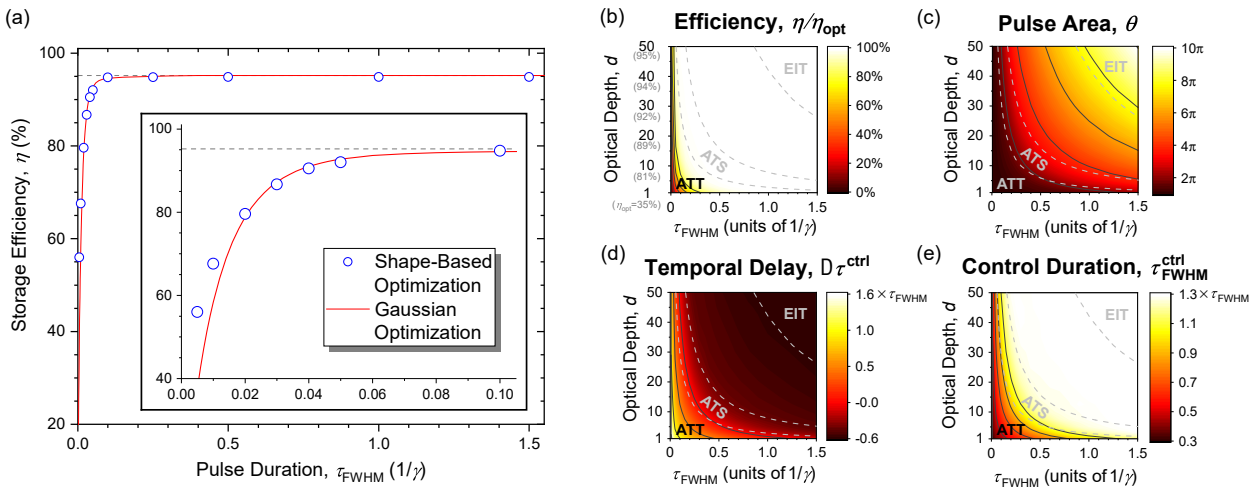

Figure 1.9: **Gaussian optimization of Λ-type quantum memory.** (a) Comparison of signal-field shape-based and Gaussian-pulse-shape optimization techniques for an optical depth of $d = 50$. The dotted line marks the optimal storage efficiency, $\eta_{\text{opt}} \approx 95\%$. (b) Gaussian-optimized memory efficiency and (c)-(e) optimized control field parameters in the broadband regime. Adapted from Ref. [141].

increasing control field power. The approach for optimizing memory efficiency through the temporal shape of the control field then takes on a similar form to the signal-field shaping discussed above. In the case of quantum storage, instead of matching the signal field to the right-singular vector of the storage kernel with the largest singular value, the task becomes to shape the storage kernel itself and thereby shape its right-singular vector with largest eigenvalue to match the input signal field. This can be accomplished analytically in several limiting cases, or, in the general case, this can be accomplished numerically through an iterative process: First, the storage kernel is constructed numerically for an initial guess of the control field shape (amplitude and phase), $\Omega_1(\tau)$, which is discretized along a series of spline points. The optimal mode $A^1_{\text{opt}}(\tau)$ of this initial storage kernel is constructed and compared to the target signal field $A_{\text{in}}(\tau)$. A series of N numeric interpolations between $A^1_{\text{opt}}(\tau)$ and $A_{\text{in}}(\tau)$ are constructed, $A_k(\tau)$, where $A_1(\tau) = A^1_{\text{opt}}(\tau)$ and $A_N(\tau) = A_{\text{in}}(\tau)$. For each $A_k(\tau)$, the control field spline points are optimized, leading to an optimal control field shape $\Omega_k(\tau)$ that maximizes storage efficiency for each $A_k(\tau)$ and provides the initial guess for $\Omega_{k+1}(\tau)$. This optimization at each step can either be implemented by constructing the storage kernel for each guess and comparing the optimal mode from the SVD of the kernel with $A_k(\tau)$, or by numerically integrating the single instance of the Maxwell-Bloch equations with input $A_k(\tau)$ and the control field guess. Assuming a large enough number of interpolations N, this iterative process slowly transforms the storage kernel such that its optimal mode overlaps with the final $A_N(\tau)$ (i.e., $A^N_{\text{opt}}(\tau) = A_N(\tau) = A_{\text{in}}(\tau)$, where the superscript N is just a label, not a multiplicative power).

In practice, this optimization technique tends to produce similar efficiencies compared to the signal-field shaping technique, however the relative strength of each technique for optimizing memory efficiency remains an open question. It is possible that regions of the memory parameter space exist where control field shaping either outperforms or underperforms signal-field shaping, and it is possible that optimization of both fields together may yield higher efficiencies in some regions than optimization of either field shape alone.

Gaussian-Pulse-Shape Optimization

In contrast to the two techniques described above, each of which requires arbitrary shaping of the respective light field temporal envelope, recent work reported in Ref. [141] addresses the question of how far memory efficiency can be optimized using a fixed shape of the temporal envelope, one which is a good approximation for the shape that is natively produced by modelocked lasers and single-photon sources. The shape chosen in Ref. [141] is a Gaussian, such that the signal and control field shapes are

$$A_{\text{in}}(\tau) = e^{-\tau^2/4\sigma^2} \tag{1.47}$$

$$\Omega(\tau) = \Omega_0\, e^{-[(\tau-\Delta\tau^{\text{ctrl}})/2\sigma^{\text{ctrl}}]^2}, \tag{1.48}$$

where again all timescales are normalized by $1/\gamma$, and $\sigma = \tau_{\text{FWHM}}/(2\sqrt{2\ln 2})$, $\Omega_0 = \theta/(2\sqrt{\pi}\sigma^{\text{ctrl}})$, the control-field pulse area is $\theta = \int_{-\infty}^{\infty} d\tau\, \Omega(\tau)$, the temporal delay of the control field relative to the maximum of the signal field is $\Delta\tau^{\text{ctrl}}$, and the duration of the control field is $\tau^{\text{ctrl}}_{\text{FWHM}} = 2\sqrt{2\ln 2}\sigma^{\text{ctrl}}$.

The approach of Gaussian-pulse-shape optimization has three main benefits: First, related to the motivation of using the pulse shapes that are native to many modelocked lasers and single-photon sources, it demonstrates that over a large range of memory parameter space (for a large range of optical depths d and signal durations/linewidths $\tau_{\text{FWHM}}\gamma$) very high storage efficiencies very close to the optimal bound discussed in Sec. 1.3.1.4 can be achieved with only these native Gaussian shaped pulses. This eliminates the need in most quantum memories for experimentally complex and costly pulse shaping methods. Fig. 1.9a shows a comparison of the storage efficiencies achieved using both signal-field, arbitrary shape-based optimization and the optimization of Gaussian-shaped control fields for $d = 50$. Over a wide range of signal-field pulse durations $\tau_{\text{FWHM}}\gamma$, the Gaussian-pulse-shape optimization technique produces the same efficiency as the shape-based technique, within numerical error. For the most broadband photons (smallest $\tau_{\text{FWHM}}\gamma$), the shape-based technique outperforms Gaussian-pulse-shape optimization, but the storage efficiency is far from the optimal bound in both cases. Additionally, the Gaussian-pulse-shape optimization technique is significantly less computationally expensive, allowing for a continuous calculation of optimized storage efficiency as a function of $\tau_{\text{FWHM}}\gamma$, whereas the shape-based optimization method is only computationally tractable in a point-wise fashion.

Second, Gaussian-pulse-shape optimization provides three physically intuitive optimization parameters for the control field — the control-field pulse area, duration, and delay relative to the signal field — whereas the shape-based technique relies on arbitrary pulse shaping that is arguably less physically intuitive. The resulting optimized control field parameters are shown in Fig. 1.9c-e. In addition to providing a convenient lookup table for the optimized control parameters to use experimentally for a quantum memory with a given optical depth, signal duration, and linewidth, Fig. 1.9c-e also agrees with and builds upon the physical intuition for each quantum memory protocol. In the EIT region, Fig. 1.9c-e shows that control fields with large duration and pulse area should be used that arrive before the signal field; control fields of this type open the well-known transparency window of EIT and adiabatically close this window as the signal field enters the medium and is compressed and stored. Similarly the physical intuition holds in the ATS and ATT regions, where control fields of 2π and π pulse area, control durations of τ_{FWHM} and less than τ_{FWHM}, and delays of 0 and positive delays implying a control field that arrives after the signal field are used, respectively, as predicted for both of these protocols. These physically intuitive control field parameters are practically useful when dealing with tunable experiments, but also allow for more sophisticated sensitivity analysis, as

detailed in Ref. [52] and Sec. 1.3.3.3.

Third, Gaussian-pulse-shape optimization reveals a continuous mathematical transformation between the three resonant protocols of EIT, ATS, and ATT. As shown in Fig. 1.9b and c-e, memory efficiency remains at the optimal bound across a continuous range of memory parameters $\mathcal{M} = (d, \tau_{\mathrm{FWHM}}\gamma)$ where the memory protocol behavior changes continuously from EIT to ATS to ATT. As $\mathcal{M}$ varies, the control field parameters $\mathcal{G} = \left(\theta, \Delta\tau^{\mathrm{ctrl}}, \tau^{\mathrm{ctrl}}_{\mathrm{FWHM}}\right)$ also vary continuously and monotonically. Naïvely, one might predict discontinuities in $\mathcal{G}$ as one protocol region changes into another, but Fig. 1.9 shows this is not the case, and a continuous transformation between memory protocols exists and can be exploited to achieve optimal memory efficiency in the regions of memory parameter space between protocols, or in the regions of "mixed" memory behavior.

Inhomogeneous Profile Shaping

While in principle the three optimization techniques above (Sec. 1.3.3.2-1.3.3.2) can be applied to both homogeneous and inhomogeneous systems, they have primarily been applied in the homogeneous case. In the inhomogeneous case another unique degree of freedom is available for optimization, namely the inhomogeneous broadening profile, which can be straightforwardly manipulated via spectral hole burning and related experimental techniques.

In Ref. [67], the authors consider several inhomogeneous profile shapes, including a delta function (identical to the homogeneous case), a Lorentzian distributed inhomogeneous profile, and a Gaussian distributed inhomogeneous profile typical of Doppler-broadened gases. The efficiencies resulting from the three inhomogeneous are compared (where, unsurprisingly, the delta function profile leads to the highest efficiency), and a general procedure for calculating the efficiency for different inhomogeneous profile shapes is developed. In Ref. [287], a similar analysis is carried out assuming a periodic inhomogeneous frequency profile characteristic of the AFC protocol. The authors show that in this case, the optimal inhomogeneous profile shape is a square-toothed frequency comb with an analytically calculable tooth width depending on the achievable peak optical depth. In addition to these techniques, one can imagine implementing a similar procedure to Sec. 1.3.3.2 to calculate the optimal inhomogeneous profile shape in the absence of the assumptions made in the AFC protocol. Ref. [253], for example, has examined the EIT visibilities resulting from different inhomogeneous shapes, which may lead to the discovery of an optimal inhomogeneous shape for the EIT protocol in inhomogeneously broadened media.

1.3.3.3 Sensitivity Analysis

Although efficiency optimization has received the lion's share of theoretical attention related to atomic ensemble quantum memory, recent work reported in Ref. [52] introduces theoretical tools aimed at the distinct task of characterizing and comparing the *sensitivity* of different quantum memory protocols to external perturbations.

Figure 1.10 shows a few selected results from Ref. [52], considering the case of short-timescale, shot-to-shot fluctuations $\zeta = (\zeta_d, \zeta_g)$ in memory parameters $\mathcal{M}$ drawn from a normal distribution $P(\zeta) \sim e^{-(\zeta_d^2 g^2 + \zeta_g^2 d^2)/[2(\epsilon_M dg)^2]}$, where $g = \tau_{\mathrm{FWHM}}\gamma$ [Fig. 1.10a-d], and long-timescale drift in control field parameters $\mathcal{G}_s$ for a control field with arbitrary profile defined by spline points $\mathcal{G}_s = (\xi_1, ..., \xi_N)$ [Fig. 1.10e-g]. The situation in mind addressed by Fig. 1.10a-d is frequently encountered in atomic-ensemble quantum memory using hot atoms, wherein the average optical depth and excited state linewidth are fixed with minimal long-timescale drift (typically through setting the vapor cell temperature) but there may be non-negligible shot-to-shot fluctuations in optical depth and linewidth arising from density fluctuations in the interaction

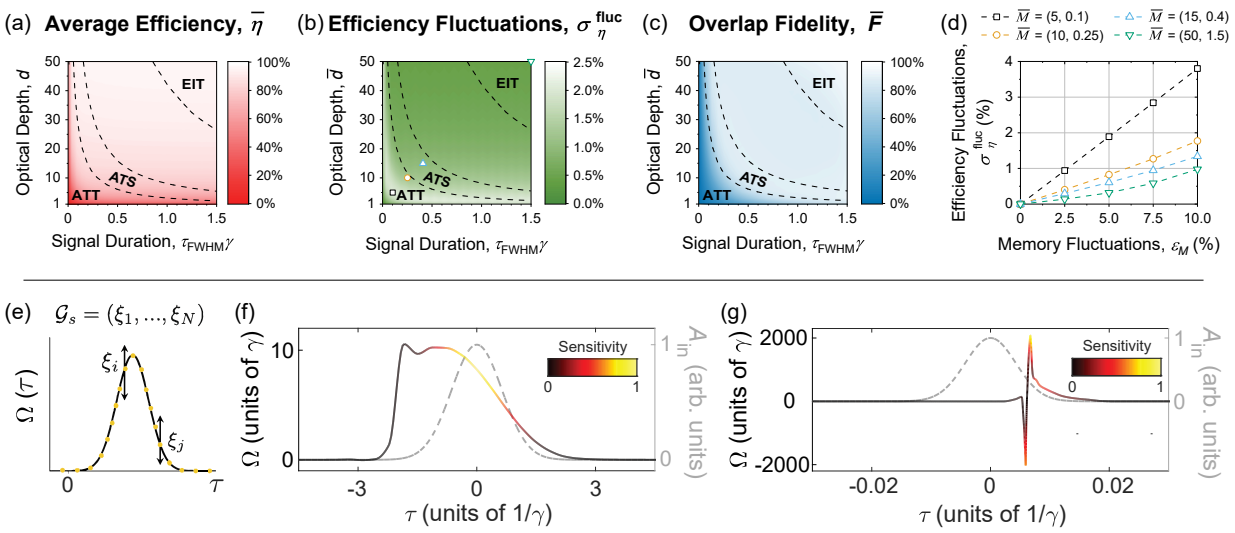

Figure 1.10: **Sensitivity analysis of Λ-type quantum memory.** Select results from sensitivity analysis of Λ-type quantum memory in the presence of (a)-(d) short-timescale fluctuations of the memory parameters (optical depth, d, and linewidth, γ), and (e)-(g) long-timescale drift in control field parameters.

volume defined by the optical modes. With this situation in mind, Fig. 1.10a shows average memory efficiency in the presence of memory parameter fluctuations $\epsilon_M = 5\%$, and Fig. 1.10b shows the magnitude of the fluctuations in memory efficiency arising from $\epsilon_M = 5\%$. First, the average memory efficiency drops slightly from the case without fluctuations [e.g., compared to Fig. 1.9b], as expected. Second, we find that the absorb-then-transfer (ATT) region is most sensitive to these memory parameter fluctuations, as it is this region that possesses the largest fluctuations in memory efficiency (for the same fluctuations in memory parameters) shown in Fig. 1.10b. The relatively large sensitivity of the ATT protocol compared to the other resonant memory protocols (i.e., ATS and EIT) is explained by the overlap fidelity of optimal control fields neighboring any given point in $\mathcal{M} = (d, \tau_{\text{FWHM}}\gamma)$, shown in Fig. 1.10c. Where the overlap fidelity is low, one expects a significant mismatch between the control field used (which corresponds to the average optical depth and linewidth) and the optimal control field (corresponding to the optical depth and linewidth modified by a given shot-to-shot fluctuation), which should result in lower average efficiency and larger efficiency fluctuations. When the overlap fidelity is high, one expects (and we observe) high average efficiency and lower efficiency fluctuations. Across several points in the memory parameter space shown by the markers in Fig. 1.10b, sampling over all three resonant memory protocols, we measure efficiency fluctuations as a function of the memory parameter fluctuation magnitude, ϵ_M, and plot the results in Fig. 1.10d. First, we observe efficiency fluctuations that are smaller, as a percentage, than the memory parameter fluctuations that cause them (i.e., memory parameter fluctuations of magnitude $\epsilon_M = 5\%$ cause at most memory efficiency fluctuations of 2.5%). This behavior persists over all reasonable magnitudes of memory parameter fluctuations, shown in Fig. 1.10d, which implies that all three resonant memory protocols are 'stable.' We also note that the EIT and ATS protocols are significantly less sensitive to memory parameter fluctuations than the ATT protocol (by about a factor of 3), across all memory parameter fluctuation magnitudes.

In addition to deviations in memory parameters, we can also consider the effect of deviations in control field parameters within the same general mathematical framework. Typically memory parameters fluctuate over a short timescale around a fixed center point; control field parameters may also fluctuate in this manner, but a

more common problem experimentally is long timescale drift from an initially optimal setpoint. Investigating the sensitivity of a memory to this long timescale drift is, coincidentally, equivalent to probing the difficulty of finding the optimal setpoint for that memory. Memory protocols that allow for a larger region of control field parameter space with optimal efficiency, and which therefore lead to less difficulty in finding the optimal control field setpoint, are less sensitive to control field drift out of that optimal region. The converse is also true—memory protocols that permit only a small region of control field parameter space with optimal efficiency lead to more difficulty in finding the optimal control field setpoint and are more sensitive to control field drift. This situation is explored in Fig. 1.10e-g for optimal arbitrary control field shapes. Fig. 1.10e shows the general approach; the optimal control field shape for a certain memory protocol is found by the procedure described in Sec. 1.3.3.2, and each spline point parameterizing the control field shape is allowed to drift by $\epsilon_G = 5\%$ of its optimum. The resulting change in memory efficiency is recorded and is used to compute a normalized sensitivity relative to the rest of the points along the control field shape. The results of this procedure are shown for two optimal control fields in Fig. 1.10f and g, in the adiabatic [EIT-like, $\mathcal{M} = (50, 1.5)$] and non-adiabatic [ATT-like, $\mathcal{M} = (50, 0.01)$] regimes, respectively. Fig. 1.10f shows that EIT-like control field shapes are most sensitive to drift along the trailing edge of the control field shape, which overlaps with the signal field in time and adiabatically closes the transparency window. Importantly, this result is in agreement with the experimental determination of Ref. [186]. For ATT-like control field shapes, Fig. 1.10g shows that the most sensitive regions of the control field are those with the largest Rabi frequency. This agrees with physical intuition for the ATT protocol (see Sec. 1.3.2.1 for a review), as it is these regions of the control field that have the largest effect on its net pulse area, and therefore have the largest effect on the efficiency of the atomic-polarization–to–spin-wave transfer process. The same one-at-a-time sensitivity analysis is performed for Gaussian control fields in Ref. [52], as well as a more sophisticated and computationally expensive Sobol' analysis that probes correlations between Gaussian control field parameters.

We stress here that the sensitivity analysis performed in Ref. [52] represents only a small subset of all sensitivity calculations that can be performed, and which may be relevant and useful for quantum memory experiments. The general framework developed in Ref. [52] may also be applied to characterize the sensitivity of off-resonant memory protocols, or those protocols that make use of inhomogeneously broadened ensembles. Moreover, Ref. [52] considers only the case of 'efficiency sensitivity,' or how fluctuations and drift in certain parameters affect memory efficiency. The same approach may straightforwardly be repurposed to evaluate such metrics as fidelity sensitivity, bandwidth sensitivity, or lifetime sensitivity, to name only a few. This may be the subject of future work.

1.3.4 State of the Art

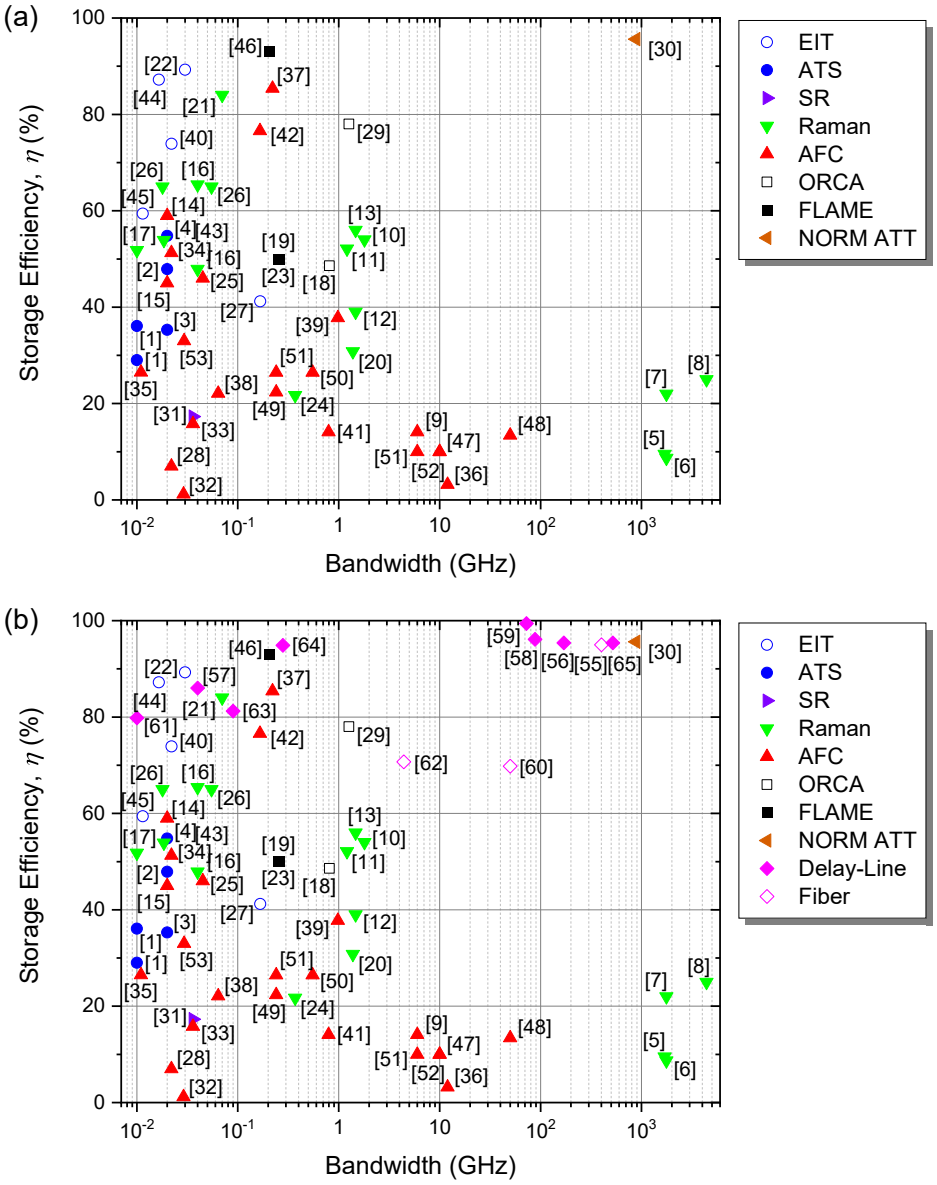

Figure 1.11: State of the art storage efficiencies for (a) atomic ensemble and (b) all quantum memories (including delay-based) in the broadband regime. Delay-line and fiber memories tend to have high efficiency independent of bandwidth. Citation numbers appear in Ref. [288]. Adapted from Ref. [109].

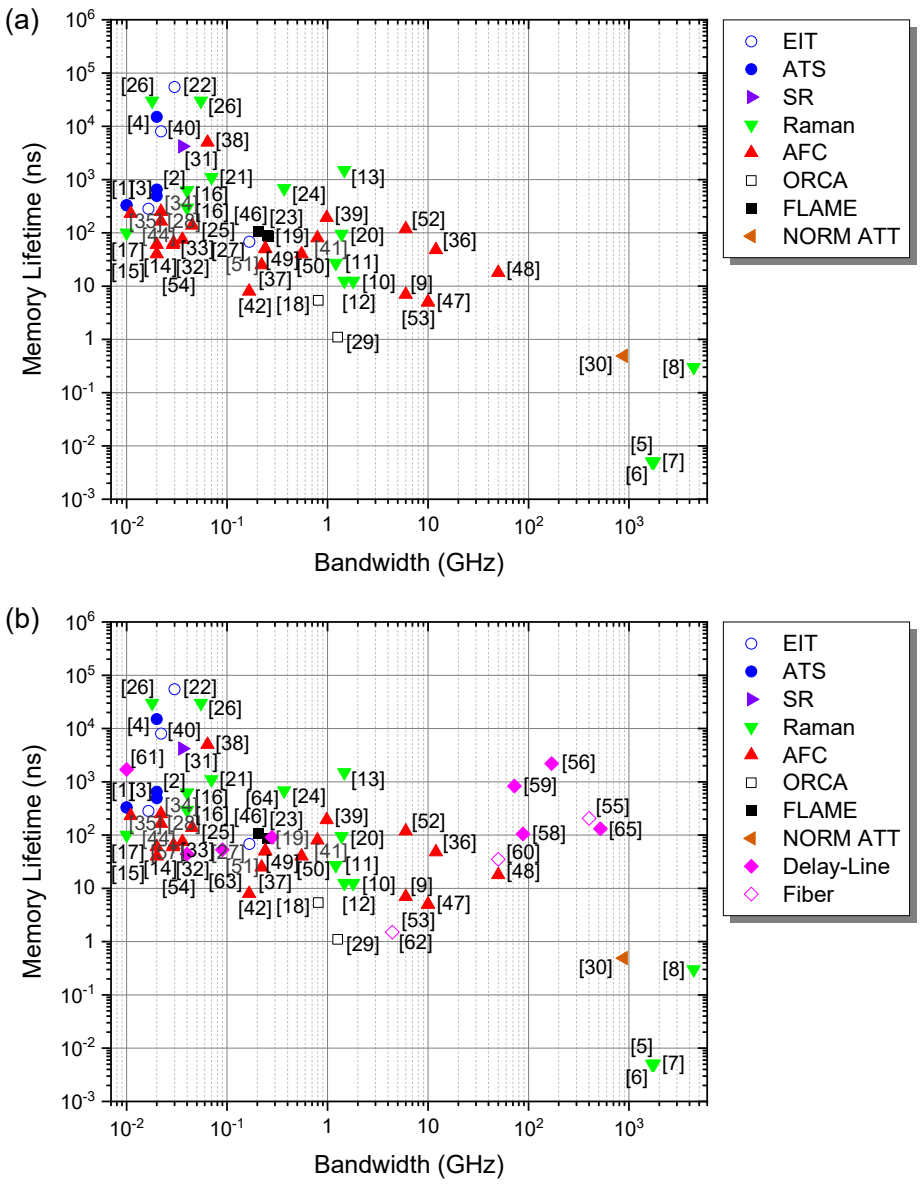

Figure 1.12: State of the art memory lifetimes for (a) atomic ensemble and (b) all quantum memories (including delay-based) in the broadband regime. Citation numbers appear in Ref. [288]. Adapted from Ref. [110].

1.3.4.1 Efficiency

With the foundation for the quantum memory protocols and theory laid above, in this section we move on to discuss the state of the art for experimental quantum memory performance in the broadband regime, which we consider to be memory bandwidths greater than 10 MHz (defined as the full width at half-maximum of the signal frequency intensity distribution, see Sec. 1.3.1.4).

Figure 1.11a shows the state-of-the-art storage efficiencies for atomic ensemble quantum memories in the broadband regime, as of the writing of this chapter. Each memory protocol is given a different marker type. As can be seen, Raman and AFC memories are the most popular types in the broadband regime, and Raman memories are the only type used in the THz-bandwidth regime except for Ref. [30], which most closely resembles the absorb-then-transfer protocol. Resonant, homogeneous atomic ensemble protocols (e.g., EIT, ATS, SR, FLAME) tend to be limited to bandwidths below 1 GHz, with the exception of Ref. [30], due to linewidth-bandwidth mismatch. More details on how Ref. [30] alleviates the linewidth-bandwidth mismatch problem can be found in Sec. 1.3.1.3. Fig. 1.11b shows the performance of all quantum memories in the broadband regime, as of the writing of this chapter, including delay-line and fiber memories, which tend to have high efficiency independent of bandwidth.

In Fig. 1.11, we show state-of-the-art storage efficiencies; total efficiency follows a similar trend, but is always significantly lower, and the trend is complicated by non-optimal phasematching and reabsorption loss during retrieval, as well as spin wave decay, which vary depending on the reference and reduce total efficiency non-uniformly across the bandwidths shown.

1.3.4.2 Memory Lifetime

Figure 1.12 shows the state-of-the-art memory lifetimes for atomic ensemble quantum memories [Fig. 1.12a] and all quantum memories [Fig. 1.12b] in the broadband regime. An empirical tradeoff exists between memory lifetime and bandwidth. We believe this trend primarily arises from technical considerations, rather than fundamental physical ones — in the THz-bandwidth regime, for example, the Raman memories shown suffer from low memory lifetime not due to a fundamental aspect of the Raman protocol, but because the hardware employed (solids and molecular gases) have inherently limited storage state lifetimes. Ref. [30] represents a unique case in this regard, where the lifetime is instead limited by atomic motion (sometimes called Doppler broadening) due to the high temperatures used, yet the inherent storage state lifetime is long, of order 0.1 seconds [289]. The delay-based memories shown in Fig. 1.12b break this trend, and all tend to have nanosecond to microsecond delay times.

1.3.4.3 Noise

We plot the state-of-the-art noise performance for broadband atomic ensemble quantum memories in Figure 1.13. We plot the signal-to-noise ratio as defined in Sec. 1.3.1.4 for each broadband memory found in the literature. The dark, medium, and light red regions represent the signal to noise ratios for <90%, <99%, and <99.9% single-photon fidelities. Across all bandwidths shown, only a few quantum memories exceed an SNR of 10^3; most memories in this region employ a ladder-type energy level system (ORCA and FLAME memories, specifically) that is in principle noise-free. Ref. [30] is the only atomic ensemble memory in this regime that employs a Λ-type level structure, and is also in principle noise-free to first order due to a large ground-state–storage-state splitting compared to the storage-state–excited-state splitting.

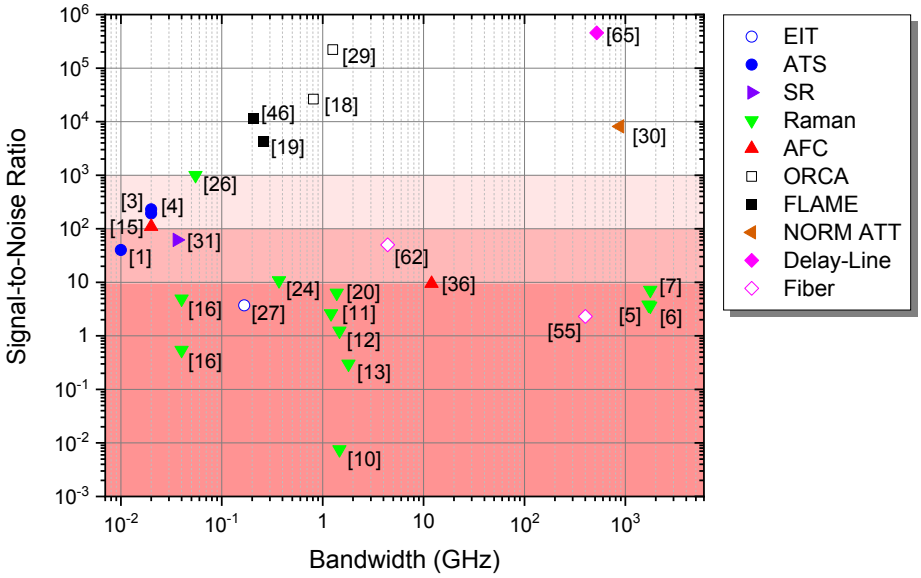

Figure 1.13: State-of-the-art noise performance for atomic ensemble and delay-based quantum memories in the broadband regime. Dark, medium, and light red regions correspond to the signal to noise ratios necessary for <90%, <99%, and <99.9% single-photon fidelities. Note that many fiber and delay-line memories do not report a figure of merit for noise performance, and are therefore not plotted here, as the added noise is virtually zero; some of those presented here are fiber memories that rely on nonlinear optical interaction with strong laser light, which imparts added noise, and are not representative of all fiber or delay-line memories. Citation numbers appear in Ref. [288].

1.3.5 Conclusion

In this work we have comprehensively reviewed broadband quantum memory in atomic ensembles, including its motivation, the challenge posed by linewidth-bandwidth mismatch, the physical protocols applicable to atomic ensembles, the underlying theory for homogeneous and inhomogeneous systems and application of the theory for efficiency optimization and sensitivity analysis, and the current state-of-the-art performance of broadband atomic ensembles relative to delay-line and fiber memories. We hope this chapter serves as a useful guide to and reference for broadband atomic ensemble quantum memory.

Acknowledgements

This work was funded in part by NSF grant Nos. 1640968, 1806572, 1839177, 1936321, and 2207822; and NSF Award DMR1747426. This material is based upon work supported by the U.S. Department of Energy Office of Science National Quantum Information Science Research Centers. We thank J. Gary Eden, Benjamin D. Hunt, Sehyun Park, Andrey Mironov, Thomas Reboli, Kathleen Oolman, Yujie Zhang, Dongbeom Kim, Yunkai Wang, Colin Lualdi, Tegan Loveridge, and Ujaan Purakayastha for helpful discussion.

Chapter 2

Photon-matter quantum correlations in spontaneous Raman scattering

This chapter pertains to the task of delayed-choice single-photon generation, as described in Sec. 1.2. The content of this chapter was published in Ref. [290], and is reproduced here with only minor formatting changes.[1]

2.1 Introduction

Raman scattering is one of the most fundamental light-matter interactions: an incident photon scatters inelastically in a medium, transferring energy to, or gaining energy from, a specific excited state. The lifetime of this excited state, which is finite due to interaction with the environment, dictates the Raman gain spectrum and affects the spatio-temporal structure of the Raman-generated optical field [291–294] as well as its intensity and fluctuations [291, 295–298]. The equations of motion for the optical field and medium excitation generated in the Raman interaction have traditionally been solved in the Heisenberg picture, where the temporal decay of the material excitation is taken into account through a dissipation-fluctuation mechanism [291, 292, 298, 299]. Using this formalism an extensive body of work has formed around exploration of the quantum properties of the spontaneously-initiated optical field, including the decomposition of the field into independent temporal coherence modes [291, 293] and decomposition of the excitation field into corresponding orthonormal spatial modes [294, 300]. Here we investigate the quantum correlations (entanglement) between modes of a single Stokes photon and its single material excitation counterpart in the Schrödinger picture, focusing instead on the spectral representation of these modes. Motivating this work is the necessity of pure, uncorrelated photonic quantum states for many quantum applications, which, in the case of Raman scattering [301–303], occurs when no correlations exist between the Stokes photon and medium excitation, apart from their coexistence.

We begin by incorporating the environment degrees of freedom into the system Hamiltonian, and writing the Raman interaction in terms of the eigenmodes of the medium, which includes the environment. Our approach then provides an intuitive understanding of photon–matter correlations arising due to energy and

[1] Previously published material appears in this section. Bibliographic information for this material is as follows: K. Shinbrough, Y. Teng, B. Fang, V. O. Lorenz, and O. Cohen, "Photon-matter quantum correlations in spontaneous Raman scattering," Phys. Rev. A **101**, 013415 (2020). The copyright owner, the American Physical Society, has provided permission to reprint. I gratefully acknowledge the coauthors listed above for their contributions to the text.

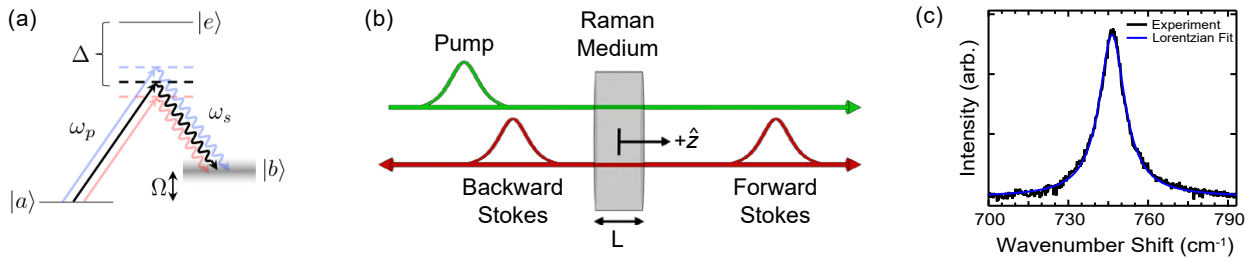

Figure 2.1: (a) Relevant level structure of the Raman-active medium, where from ground state $|a\rangle$ a pump photon (of angular frequency ω_p) creates a single excitation (Ω) in the medium through far-detuned (Δ) intermediate state $|e\rangle$, leading to collective state $|b\rangle$ and an emitted Stokes photon (ω_s). (b) Schematic of one-dimensional propagation of Stokes photons, emitted forward or backward relative to the pump. (c) Measured gain spectrum of our Raman medium (Al_2O_3), with a Lorentzian fit.

momentum conservation in the same way those correlations arise in the photon–photon pairs created in spontaneous parametric down-conversion (SPDC) [304] or spontaneous four-wave mixing (SFWM) [305]. Our state formalism reveals photon–matter correlations that have a critical effect on the quantum state of the photon and consequently on its quantum-state purity and the photon statistics of the Raman scattering.

We present one- and three-dimensional models of the Raman interaction, corresponding respectively to flat-phase-front (e.g. waveguided) and free-space propagation of pump and Stokes pulses. We then present experimental data on the degree of photon–matter correlation as a function of pump bandwidth, as measured through second-order coherence of the optical field. Our analysis predicts further correlations due to collection geometry of the broadband Stokes photons, and we confirm experimentally the generation of highly correlated photon–excitation pairs produced when the photons are emitted counter-propagating with the pump. Understanding these correlations and the properties of the joint photon–excitation state, especially in the low gain regime as studied here, is key to controlling Raman emission and enabling new applications for quantum communication, computation, and sensing. We anticipate this work to inform Raman scattering at the quantum level in solid-state systems [306, 307] as well as atomic vapors [308, 309], and thence on the implementation of quantum protocols such as the Duan-Lukin-Cirac-Zoller protocol [301] and Raman-based quantum memories [306, 310–318].

2.2 One-Dimensional Model

The Raman interaction that we consider in this work is shown in the three-level Λ-system in Fig. 2.1(a). Given a laser pump pulse traveling through a Raman-active medium along the $\hat{z}$-axis [Fig. 2.1(b)], the Hamiltonian of the system is given by

$$\hat{H}(t) = \hat{H}_O + \hat{H}_M + \hat{V}(t), \tag{2.1}$$

where

$$\hat{H}_O = \int d\omega_s \, \hbar\omega_s \hat{a}^\dagger(\omega_s)\hat{a}(\omega_s) \tag{2.2}$$

is the free Hamiltonian of the Stokes optical field generated in the Raman interaction, and $\hat{a}^\dagger(\omega_s)$ ($\hat{a}(\omega_s)$) is the creation (annihilation) operator for a photon of that field with angular frequency ω_s. We assume that the medium's excited states form a bosonic field (Q-field) of collective excitations (CEs) [292] with associated creation and annihilation operators $\hat{Q}^\dagger(z)$ and $\hat{Q}(z)$, respectively, that obey the commutation

relations $[\hat{Q}(z),\hat{Q}(z')]=[\hat{Q}^\dagger(z),\hat{Q}^\dagger(z')]=0$ and $[\hat{Q}(z),\hat{Q}^\dagger(z')]=\delta(z-z')$. $\hat{H}_M$ is the matter Hamiltonian that describes the energy of the Q-field, the environment, and the interaction between the two, which we assume takes form [299, 319]

$$\begin{aligned}\hat{H}_M = \hbar\Omega_0 \int_{-L/2}^{L/2} dz\, \hat{Q}^\dagger(z)\hat{Q}(z) \\ + \int d\Omega \int_{-L/2}^{L/2} dz\, \hbar\Omega \hat{R}^\dagger(\Omega,z)\hat{R}(\Omega,z) \\ + \int d\Omega \int_{-L/2}^{L/2} dz\, v(\Omega)\Big[\hat{R}^\dagger(\Omega,z)\hat{Q}(z) \\ + \hat{R}(\Omega,z)\hat{Q}^\dagger(z)\Big],\end{aligned} \tag{2.3}$$

where Ω_0 is the angular frequency of the Q-field and the environment is treated as a reservoir comprised of a spectral continuum of localized harmonic oscillators with creation (annihilation) operators $\hat{R}^\dagger(\Omega,z)$ ($\hat{R}(\Omega,z)$) for an oscillator with angular frequency Ω at point z, where $v(\Omega)$ is the frequency-dependent coupling between the Q-field and the reservoir, which we take to be real for convenience, and is responsible for the decay of the Q-field and its finite lifetime. The three-wave mixing Raman interaction between the pump, Stokes field, and the medium is given by

$$\hat{V}(t) = \gamma \int d\omega_s \int_{-L/2}^{L/2} dz\, E_p(z,t)\hat{a}^\dagger(\omega_s)e^{-ik(\omega_s)z}\hat{Q}^\dagger(z) + \text{h.c.}, \tag{2.4}$$

where γ is a coupling constant dependent on the properties of the Raman medium and the frequency of the Raman emission [320], $E_p(z,t)$ is the electric field amplitude of the strong pump pulse at time t and point z along the medium, which we treat classically, and $k(\omega_s)$ is the wavevector of the Stokes photon. In Eqs. (2.2)-(2.4) we consider one-dimensional propagation of the optical fields, which is valid when the interaction medium is a waveguide as well as in various bulk experimental geometries with Fresnel number $\mathscr{F}=A/\lambda L \gg 1$, where A is the cross-sectional area of a pencil-shaped beam of wavelength λ incident on a Raman medium of length L [291, 292, 295, 321]. In Section 2.3 we consider correlations within photon–CE pairs, in both the forward- and backward-scattering one-dimensional geometries shown in Fig. 2.1(b). In Section 2.4 we take into account the spatial modes of the optical fields and verify the limit on $\mathscr{F}$ under which this one-dimensional approximation holds, in addition to considering off-axis emission and collection of the Stokes field.

We begin by examining the medium Hamiltonian in Eq. (2.3); using the procedure in Ref. [322], one can write it in terms of decoupled oscillators [319]

$$\hat{H}_M = \int d\Omega\ \hbar\Omega \int_{-L/2}^{L/2} dz\, \hat{B}^\dagger(\Omega,z)\hat{B}(\Omega,z), \tag{2.5}$$

where $\hat{B}(\Omega,z)$ ($\hat{B}^\dagger(\Omega,z)$) is the annihilation (creation) operator associated with a CE (B-field) at point z along the medium with angular frequency Ω, and obeys boson commutation relations. It is given by a linear combination of the Q- and reservoir-fields as $\hat{B}(\Omega,z)=g(\Omega)\hat{Q}(z)+\int d\Omega'\, h(\Omega,\Omega')\hat{R}(\Omega',z)$, where the general solutions for $g(\Omega)$ and $h(\Omega,\Omega')$ can be found in Ref. [319]. For this work it is only important to notice that,

inversely, we can express the Q-field operators in terms of B-field operators as [319]

$$\hat{Q}(z) = \int d\Omega\, g^*(\Omega)\hat{B}(\Omega, z), \tag{2.6a}$$

$$\hat{Q}^\dagger(z) = \int d\Omega\, g(\Omega)\hat{B}^\dagger(\Omega, z), \tag{2.6b}$$

and that $g(\Omega)$ is a normalized function ($\int d\Omega\, |g(\Omega)|^2 = 1$). In the case where the coupling in Eq. (2.3) is frequency independent (i.e. $v(\Omega) = v_0$ where v_0 is a constant), the Raman gain is homogeneously broadened and

$$g(\Omega) = \sqrt{\frac{\Gamma/2\pi}{(\Omega - \Omega_0)^2 + (\Gamma/2)^2}} \tag{2.7}$$

takes the form of a Lorentzian lineshape [319], where $\Gamma = 2\pi|v_0|^2$ is the full width at half maximum bandwidth of the Raman-gain spectral intensity. In the eigenbasis of $\hat{H}_M$ [Eq. (2.5)], the interaction term in Eq. (2.4) is written as

$$\begin{aligned}\hat{V}(t) = \gamma \int d\Omega d\omega_s \int_{-L/2}^{L/2} dz\, E_p(z,t)\hat{a}^\dagger(\omega_s)e^{-ik(\omega_s)z} \\ \times g(\Omega)\hat{B}^\dagger(\Omega, z) + \text{h.c.},\end{aligned} \tag{2.8}$$

which couples the Stokes field to a spectral continuum of distinct oscillators (B-field), with coupling amplitude $\gamma g(\Omega)$. In effect, Eq. (2.8) mathematically treats homogeneous broadening as inhomogeneous broadening with a Lorentzian lineshape; such equivalence has been found empirically in the analysis of the statistical properties of the optical field operators as derived in the fluctuation-dissipation approach (that is, writing the Heisenberg equations of motion with the Q-field operators) in Ref. [323]. We note, however, that unlike the case of inhomogeneous broadening where the lineshape is dictated by the (Gaussian) distribution of the density of states, here the spectral distribution of the density of states is uniform, while the coupling strength ($|\gamma g(\Omega)|^2$) is responsible for the lineshape.

Transforming Eq. (2.8) into the interaction picture, after the rotating wave approximation we arrive at the interaction Hamiltonian

$$\begin{aligned}\hat{H}_I(t) = \gamma \int d\omega_p d\omega_s d\Omega \int_{-L/2}^{L/2} dz \Big[\mathcal{E}(\omega_p)g(\Omega) \\ e^{i[k(\omega_p)-k(\omega_s)]z}e^{-i\Delta\omega t}\hat{a}^\dagger(\omega_s)\hat{B}^\dagger(\Omega, z)\Big] + \text{h.c.},\end{aligned} \tag{2.9}$$

where we have written the classical pump field in the spectral domain as $E_p(z,t) = \int d\omega_p\, \mathcal{E}(\omega_p)e^{i[k(\omega_p)z-\omega_p t]} +$ h.c. with the spectral amplitude $\mathcal{E}(\omega_p)$ and wavenumber $k(\omega_p)$. The frequency mismatch of the three fields is $\Delta\omega = \omega_p - \omega_s - \Omega$, and for simplicity we assume the pump and Stokes modes have the same dispersion relation; it is straightforward to expand our treatment when this is not the case.

2.3 Photon–CE Pair State

We assume that prior to the pump pulse entering the medium the Stokes and CE fields are both in their respective vacuum states, which we write in the combined Stokes–CE system as $|\text{vac}\rangle$. In this work we restrict our discussion to the low-gain limit, assuming that the interaction is weak and perturbative expansion of the

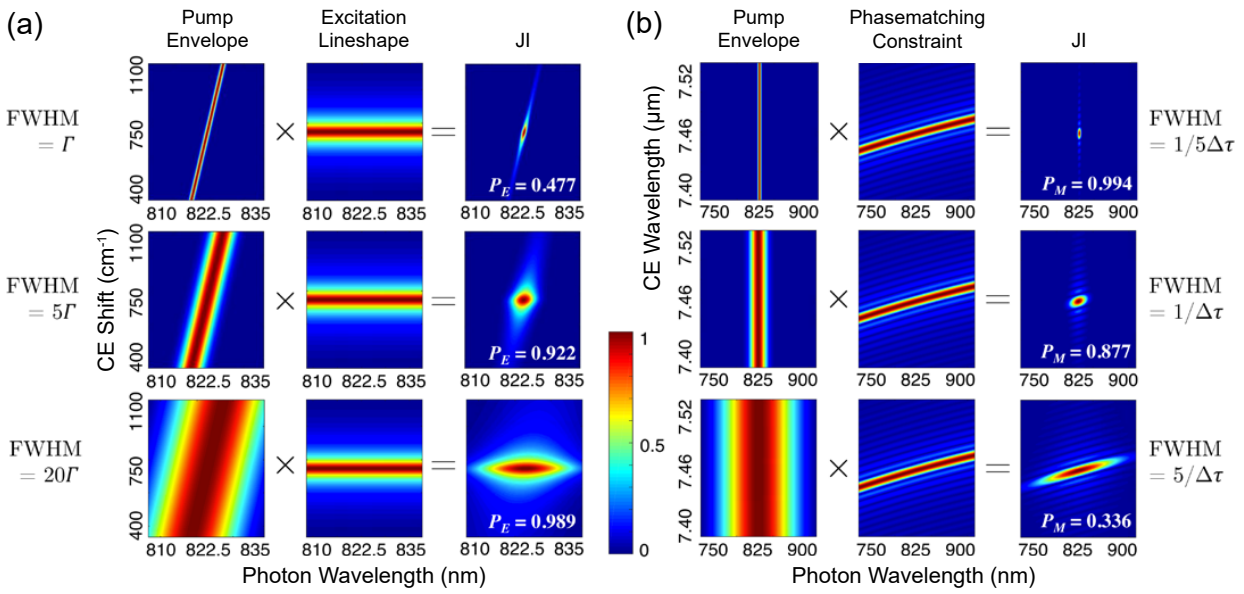

Figure 2.2: Joint intensity (JI) of photon–CE pairs in the one-dimensional regime for (a) fixed position, showing the effect of excitation linewidth, and (b) fixed collective excitation (CE) frequency, showing the effect of chromatic dispersion; FWHM is the pump spectral full width at half maximum, Γ the linewidth of the relevant excitation, $\Delta\tau$ the group delay between Stokes and pump pulses for a bulk Al_2O_3 Raman medium, and P_E and P_M the frequency (energy)- and momentum-state purities corresponding to each joint intensity, respectively.

resulting state is allowed. Once the interaction ceases, the lowest order non-vacuum state of this system [304] $|\Psi\rangle = \mathcal{N}\int_{-\infty}^{+\infty} dt\, \hat{H}_I(t)|\text{vac}\rangle$ describes a joint quantum state of a single Stokes photon and collective excitation, where $\mathcal{N}$ is a normalization factor. In the one-dimensional case, the resulting photon–CE pair state is $|\Psi\rangle = \mathcal{N}\int d\omega_s d\Omega \int_{-L/2}^{L/2} dz\, f_{1\text{D}}(\omega_s, \Omega, z)|\omega_s; \Omega, z\rangle$, where the joint amplitude (JA) for the photon–CE pair is given by

$$f_{1\text{D}}(\omega_s, \Omega, z) = \mathcal{E}(\omega_s + \Omega) g(\Omega) e^{i[k(\omega_s+\Omega)-k(\omega_s)]z} \tag{2.10}$$

$$\approx \mathcal{E}(\omega_p^0 + \nu + \delta) g(\Omega^0 + \delta) e^{i(\Delta\tau/L)\nu z} \times e^{i\beta_p \delta z} e^{i\left[k(\omega_p^0)-k(\omega_s^0)\right]z}, \tag{2.11}$$

and $|\omega_s; \Omega, z\rangle = \hat{a}_s^\dagger(\omega_s)\hat{B}^\dagger(\Omega, z)|\text{vac}\rangle$ represents a photon–CE pair state with Stokes photon angular frequency ω_s and CE with angular frequency Ω created at point z along the interaction medium. Here we define the center frequency of the pumping light ω_p^0, which is set by experiment, and the center frequency of the CE mode Ω^0, which is determined by the properties of the Raman medium and in turn defines the center frequency of the Stokes light $\omega_s^0 = \omega_p^0 - \Omega^0$ through energy conservation. The variations about the center frequencies $\nu = \omega_s - \omega_s^0$, $\delta = \Omega - \Omega^0$, and linear expansions $k(\omega_s + \Omega) - k(\omega_s^0 + \Omega^0) \approx \beta_p(\nu + \delta)$ and $k(\omega_s) - k(\omega_s^0) \approx \beta_s \nu$, where $\beta_{p(s)} = \partial k/\partial\omega|_{\omega_{p(s)}^0}$ is the inverse group velocity of the pump (Stokes) pulse lead to the approximate form in Eq. (2.11), where $\Delta\tau = (\beta_p - \beta_s)L$ is the group delay between pump and Stokes pulses acquired during propagation in a dispersive medium.

We have decomposed Eq. (2.11) into terms with different physical roles: the $\mathcal{E}(\omega_p^0 + \nu + \delta)$ term manifests energy conservation via the pump spectral envelope, the lineshape $g(\Omega^0 + \delta)$ puts constraints on the value of

the CE energy, $e^{i(\Delta\tau/L)\nu z}$ is responsible for correlations between the point at which the CE is created and the arrival time of the Stokes photon [294], and the $e^{i\beta_p\delta z}$ term describes correlations due to the fact that a CE created at one point in the medium has evolved and decayed more than those created later. This latter term raises correlations between the position and energy of the CE and thus affects the CE internal state, but has no effect on the state of the Stokes photon. The term $e^{i\left[k(\omega_p^0)-k(\omega_s^0)\right]z}$ represents a global phase accumulation and does not possess any correlations.

With the Fourier transform of the CE creation operator $\hat{b}^\dagger(\Omega, k_{\rm CE}) = (2\pi)^{-1}\int dz\, \hat{B}^\dagger(\Omega, z)e^{ik_{\rm CE}z}$, where $k_{\rm CE} = k_{\rm CE}^0 + \kappa$ is the CE wavevector with variation κ about its center $k_{\rm CE}^0 = k(\omega_p^0) - k(\omega_s^0)$, the k-space JA is given by

$$\begin{aligned}
&\widetilde{f}_{\rm 1D}(\omega_s, \Omega, k_{\rm CE}) \\
&= \mathcal{E}(\omega_s+\Omega)g(\Omega){\rm sinc}\left[\frac{L}{2}\big(k(\omega_s+\Omega) - k(\omega_s) - k_{\rm CE}\big)\right] &(2.12)\\
&\approx \mathcal{E}(\omega_p^0+\nu+\delta)g(\Omega^0+\delta){\rm sinc}\left[\frac{\Delta\tau}{2}\nu + \frac{L}{2}\big(\beta_p\delta-\kappa\big)\right]. &(2.13)
\end{aligned}$$

The joint amplitudes in Eqs. (2.10)-(2.13) capture the spectral and momentum correlations between spontaneous Stokes photon and CE in one dimension, including those arising from the CE linewidth and group velocity dispersion in the medium.

The quantum state of the Stokes photon created in this interaction is given by the reduced density matrix

$$\begin{aligned}
\hat{\rho}_s &= {\rm Tr}_{\rm CE}|\Psi\rangle\langle\Psi| \\
&= \mathcal{N}^2\int d\omega_s d\omega_s' d\Omega dz\, f_{\rm 1D}(\omega_s,\Omega,z)f_{\rm 1D}^*(\omega_s',\Omega,z) \\
&\qquad\qquad \times |\omega_s;\Omega,z\rangle\langle\omega_s';\Omega,z|, &(2.14)
\end{aligned}$$

where ${\rm Tr}_{\rm CE}$ represents the partial trace over the CE degrees of freedom, Ω and z. The quantum state purity of the Stokes photon $P = {\rm Tr}\hat{\rho}_s^2$ amounts to the degree to which the photon and CE are in pure rather than mixed states, and is a critical figure of merit in quantum protocols that rely on two-photon interference [324]. In particular, the photon–CE pair state that leads to unit purity of the Stokes photon is the factorable state, where the JA can be written as independent functions of the Stokes and CE degrees of freedom: $f(\omega_s,\Omega,z) = f_s(\omega_s)f_{\rm CE}(\Omega,z)$. Conversely, when the photon and CE are spectrally entangled, $f(\omega_s,\Omega,z)$ is not factorable, $P<1$, and the photon and CE are individually in mixed states.

In general, all three degrees of freedom of the photon–CE pair are entangled. In order to characterize this entanglement, we consider correlations between the photon frequency and each degree of freedom of the CE in turn. These two forms of entanglement arise mainly from two separate physical effects, which we explore in the following subsections. To enumerate these correlations, unless otherwise stated we consider a single-crystal, c-axis, bulk sapphire (Al_2O_3) Raman medium of length $L = 8$ mm, with measured 746.6 cm^{-1} Raman shift and Lorentzian lineshape with full width at half maximum (FWHM) $\Gamma = 11.0$ cm^{-1} [see Fig. 2.1(c)] corresponding to $(2\bar{1}\bar{1}0)E_g$ optical phonon creation in the medium [325, 326]. We consider pump pulses centered at 775 nm and approximate chromatic dispersion in the bulk with the Sellmeier equation of Ref. [327].

2.3.1 Effect of Excitation Linewidth

To isolate the effect of a finite CE linewidth on spectral correlations between photon and excitation, which exist on the local level of the CE (i.e. for each fixed location $z = z^0$), we write the components of the JA that capture these energy correlations as

$$f_{1D}^{E}(\omega_s, \Omega) = \mathcal{E}(\omega_s + \Omega) g(\Omega). \tag{2.15}$$

Figure 2.2(a) shows the components of the photon–CE joint intensities (JIs) $\left|f_{1D}^{E}(\omega_s, \Omega)\right|^2$ for pump pulses around the intermediate regime FWHM $\sim \Gamma$, where FWHM is the spectral intensity full width at half maximum of a Gaussian pump envelope. We plot these JIs with respect to photon wavelength $\lambda_s = 2\pi c/\omega_s$ and CE shift $\nu_{CE} = \Omega/(2\pi c)$, where c is the speed of light. The results of Fig. 2.2(a) show an increase in pair correlations with decreasing pump spectral width. Physically this indicates energy entanglement between photon and CE: in the limit of a monochromatic pump, the linewidth of the CE allows for a distribution of Stokes photons in frequency, with each frequency entangled with an excitation through energy conservation. For larger bandwidths or narrower CE linewidths this entanglement is diminished. As a figure of merit, we also include in Fig. 2.2(a) the energy state purity $P_E = \mathrm{Tr}\hat{\rho}_{s,E}^2$ (where $\hat{\rho}_{s,E}$ is the reduced energy state density matrix of the Stokes photon, given by the trace of $\hat{\rho}_s$ only over CE frequency Ω at fixed z^0) corresponding to each JI and calculated photon–CE state. In the absence of further momentum state correlations, $P_E = P$ is the quantum state purity of the Stokes photon.

2.3.2 Effect of Chromatic Dispersion

As derived in previous work in the time-domain [294], chromatic dispersion leads to entanglement between the Stokes frequency and the location or momentum of the CE in the Raman medium. Figure 2.2(b) shows the JI components in k-space for pump pulse durations varying about the group delay between Stokes and pump pulses, which is $\Delta\tau \approx 32$ fs for the medium considered here. To isolate the correlations between photon frequency and CE momentum (k_{CE}), we write the JA at fixed CE frequency

$$\tilde{f}_{1D}^{M}(\omega_s, k_{CE}) = \mathcal{E}(\omega_s + \Omega^0)\mathrm{sinc}\left[\frac{L}{2}\left(k(\omega_s + \Omega^0) - k(\omega_s) - k_{CE}\right)\right]. \tag{2.16}$$

In Fig. 2.2(b) $\left|f_{1D}^{M}(\omega_s, k_{CE})\right|^2$ is plotted against photon and CE wavelength ($2\pi/k_{CE}$), showing the effect of chromatic dispersion in the absence of those correlations considered in Fig. 2.2(a). For a given interaction length, the group-delay between pump and Stokes pulses leads to momentum correlations between photon and CE, due to the temporal walkoff between pulses that serves to distinguish the spatial location of photon–CE pair creation. For larger pump bandwidths (shorter coherence-lengths) the distinguishability of Stokes pulses increases, increasing the photon–CE correlations. Conversely, for smaller medium lengths the accumulated group delay between Stokes and pump pulses and the resulting correlations decrease. We include in Fig. 2.2(b) the momentum state purity ($P_M = \mathrm{Tr}\hat{\rho}_{s,M}^2$, where $\hat{\rho}_{s,M}$ is given by the trace of $\hat{\rho}_s$ only over CE position z at fixed Ω^0) corresponding to each pair state.

The competing effects of excitation linewidth and chromatic dispersion in general lead to a maximum Stokes photon purity (minimum photon–CE entanglement) at finite pump bandwidth. Within this one-dimensional model, the magnitude of this maximum purity along with the corresponding pump settings are dependent only on three parameters: the dispersion relation in the medium, the linewidth of the excitation,

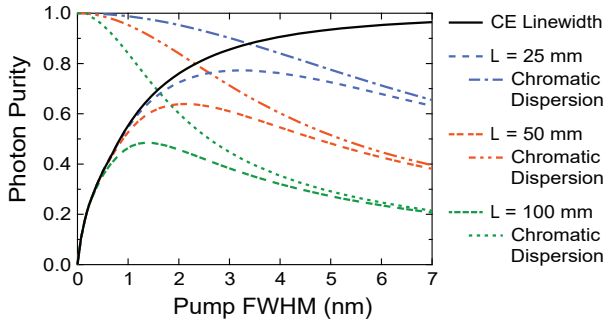

Figure 2.3: Stokes photon purities calculated within a one-dimensional model (see text) as a function of pumping spectral full width at half maximum (FWHM) for varying interaction lengths of a bulk Al_2O_3 Raman medium. Effects on the photon purity due to the collective excitation (CE) linewidth (solid) and chromatic dispersion (dotted) are isolated for a given length, showing their contribution to each convolution (dash-dot) representing the total photon purity.

and the interaction length. In practice, while the dispersion relation and linewidth of an excitation are not easily modified parameters for a given Raman medium, the interaction length is. In Fig. 2.3 then, we show the dependence of the spontaneous Stokes photon purity on pump spectral bandwidth for varying interaction length, along with the isolated effects of finite excitation linewidth and chromatic dispersion, to show the general behavior of the photon purity.

2.3.3 Backward Collection

As spontaneous Stokes scattering is generally emitted over solid angle 4π, we extend our one-dimensional treatment to backward-emission of spontaneous Stokes photons [Fig. 2.1(b)]. We find the pair state joint amplitude:

$$f_{\mathrm{1D}}^{\leftarrow}(\omega_s, \Omega, z) = \mathcal{E}(\omega_s + \Omega) g(\Omega) e^{i[k(\omega_s+\Omega)+k(\omega_s)]z}. \tag{2.17}$$

In general this modification serves to increase photon–CE correlations via temporal walkoff by an argument analogous to that of chromatic dispersion in the previous subsection, though they are, to be clear, independent effects: Even in the absence of dispersion, the temporal delay between Stokes photons generated at the input versus the output face of the medium under consideration is $\Delta\tau^{\leftarrow} \approx 26$ ps. This timing information serves to distinguish photon–CE pairs and decrease the state purity of the photon, and normally has a significantly stronger effect on the photon purity than chromatic dispersion. Here we note that whereas for Raman-active atomic vapors the effect of excitation linewidth and chromatic dispersion may be negligible, for the same media collection in the backwards direction [309, 328] can strongly affect the correlations between broadband photon and excitation.

2.4 Three-Dimensional Model: Free-Space Propagation

In the case of bulk optics and free-space propagation of the optical fields, we consider a TEM_{00} Gaussian pump beam focused into the Raman medium that reaches its minimal beam waist radius w_p at the center of the medium (see Fig. 2.4). While the subsequently generated Stokes field is generally emitted in all directions,

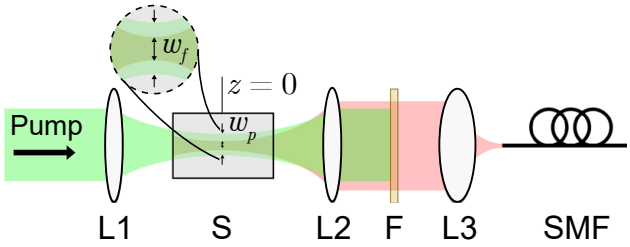

Figure 2.4: Configuration assumed for collinear three-dimensional calculations. A pump beam (green) is focused by a lens (L1) into the Raman medium (S). Stokes photons are generated, collected by a lens (L2), pass through a spectral filter (F) that removes the pump light, and are coupled by a coupling lens (L3) to single mode fiber (SMF), projecting the photons onto an approximately Gaussian collection mode (red).

here we consider the quantum state of only the fraction of photons that are collected by a lens and coupled into a single-mode fiber. In this three-dimensional case we cannot neglect correlations in the transverse degrees of freedom of photon and CE [329, 330]. To include these correlations we rewrite the pump, CE, and Stokes fields with the additional cylindrically symmetric degree of freedom $\boldsymbol{\rho} = (x, y)$: The Q-field operators take the form

$$\hat{Q}^\dagger(\boldsymbol{\rho}, z) = \int d\Omega d^2\mathbf{q}_{\mathrm{CE}}\, g(\Omega) e^{-i\mathbf{q}_{\mathrm{CE}}\cdot\boldsymbol{\rho}} \hat{B}^\dagger(\Omega, \boldsymbol{q}_{\mathrm{CE}}, z), \tag{2.18}$$

where the CE field with creation operator $\hat{B}^\dagger(\Omega, \boldsymbol{q}_{\mathrm{CE}}, z)$ now also includes the CE transverse wavevector ($\boldsymbol{q}_{\mathrm{CE}}$) as an additional degree of freedom. We assume that the spatial mode supported by the single-mode fiber (into which the Stokes photons are collected) can also be well approximated by a TEM_{00} Gaussian mode such that the Stokes collection configuration of Fig. 2.4 projects the optical field onto the Gaussian state $|u_f(\omega_s)\rangle = \hat{A}^\dagger(\omega_s)|\mathrm{vac}\rangle$ with beam waist w_f, which we assume to also occur at the center of the Raman medium, where

$$\hat{A}^\dagger(\omega_s) = (4\pi/w_f^2) \int d^2\mathbf{q}_s\, e^{-w_f^2|\mathbf{q}_s|^2/4} \hat{a}^\dagger_{\mathbf{q}_s}(\omega_s) \tag{2.19}$$

and $\hat{a}^\dagger_{\mathbf{q}_s}(\omega_s)$ is the creation operator of a Stokes photon with transverse wavevector $\mathbf{q}_s$ and angular frequency ω_s. The resulting projected state is then given by $|\Psi\rangle^{\mathrm{proj.}}_{\mathrm{3D}} = \mathcal{N}_{\mathrm{3D}} \int d\omega_s d\Omega d^2\mathbf{q}_{\mathrm{CE}} \int_{-L/2}^{L/2} dz\, f_{\mathrm{3D}}(\omega_s, \Omega, z, \mathbf{q}_{\mathrm{CE}}) \hat{A}^\dagger_s(\omega_s)$ $\hat{B}^\dagger(\Omega, \mathbf{q}_{\mathrm{CE}}, z)|\mathrm{vac}\rangle$ (for a more detailed calculation, see Appendix). Here $\mathcal{N}_{\mathrm{3D}}$ is the appropriate normalization factor and we find the three-dimensional JA can be expressed in terms of the one-dimensional JA [Eq. (2.10)] as

$$f_{\mathrm{3D}}(\omega_s, \Omega, z, \mathbf{q}_{\mathrm{CE}}) = \beta(\mathbf{q}_{\mathrm{CE}}, z) f_{\mathrm{1D}}(\omega_s, \Omega, z), \tag{2.20}$$

where

$$\beta(\mathbf{q}_{\mathrm{CE}}, z) = \frac{\exp\left[-i\frac{C_p(z)C_s^*(z)}{2(C_p(z)-C_s^*(z))}|\mathbf{q}_{\mathrm{CE}}|^2\right]}{C_p(z) - C_s^*(z)} \tag{2.21}$$

and $C_p(z) = (z + iz_{R,p})/k(\omega_p^0)$ and $C_s(z) = (z + iz_{R,f})/k(\omega_s^0)$ for pump and fiber collection modes with Rayleigh ranges $z_{R,p} = k(\omega_p^0)w_p^2/2$ and $z_{R,f} = k(\omega_f^0)w_f^2/2$, respectively. We ignore the slow spectral dependence of $\beta(\mathbf{q}_{\mathrm{CE}}, z)$ in considering only central wavevectors $k(\omega_s^0)$ and $k(\omega_p^0) = k(\omega_s^0 + \Omega^0)$. We define the Fresnel numbers of the pump and fiber modes in terms of their respective Rayleigh ranges as $\mathscr{F}_p = 2z_{R,p}/L$ and $\mathscr{F}_f = 2z_{R,f}/L$, respectively. As expected, for interaction lengths much smaller than the Rayleigh ranges, i.e. $\mathscr{F}_p, \mathscr{F}_f \gg 1$, the correction in Eq. (2.21) reduces to a constant and the one-dimensional calculations

hold. In the three-dimensional case, the reduced density matrix of the Stokes photon is then given by

$$\hat{\rho}_s = \mathcal{N}_{3\mathrm{D}}^2 \int d\omega_s d\omega_s' d\Omega dz\, \alpha(z) f_{1\mathrm{D}}(\omega_s, \Omega, z) f_{1\mathrm{D}}^*(\omega_s', \Omega, z) |\omega_s; \Omega, z\rangle\langle\omega_s'; \Omega, z|, \tag{2.22}$$

where

$$\begin{aligned}\alpha(z) &= \int d^2\mathbf{q}_{\mathrm{CE}}\, |\beta(\mathbf{q}_{\mathrm{CE}}, z)|^2 \\ &= \frac{8\pi^3}{w_p^2 w_f^2} \left(\frac{z^2 + z_{R,f}^2}{\left[w_f k(\omega_s^0)\right]^2} + \frac{z^2 + z_{R,p}^2}{\left[w_p k(\omega_p^0)\right]^2} \right)^{-1}\end{aligned} \tag{2.23}$$

is a Lorentzian function along z that manifests an effective apodization of the interaction length and therefore has the effect of decreasing correlations between the Stokes photon and the spatial (or momentum) degree of freedom of the CE (in comparison to the 1D case).

2.4.1 Off-Axis Collection of Stokes Photons

We now generalize the above treatment to include off-axis collection of Stokes photons at angle φ from the z-axis within the free-space model. We assume that the dispersion relation is independent of propagation angle, a condition that is satisfied for isotropic media such as atomic vapors, or for uniaxial crystalline media with pump and Stokes polarizations along the ordinary axis. It is straightforward to include emission modes with different dispersion relations when this condition is not met. We further assume that the collection and pumping modes share a focal point. Under these assumptions, the photon–CE JA is given by Eq. (2.20) with a generalized form of Eq. (2.21):

$$\begin{aligned}&\beta(\mathbf{q}_{\mathrm{CE}}, z, \varphi) = \\ &\exp\left[i \frac{C_p(z)}{2} \left(|\mathbf{q}_{\mathrm{CE}}|^2 - k(\omega_s^0)^2 \sin^2\varphi - 2k(\omega_s^0) q_{\mathrm{CE}}^y \sin\varphi \right) \right] \\ &\quad \times \frac{\exp\left[i \frac{(C_p(z)\cos\varphi(q_{\mathrm{CE}}^y - k(\omega_s^0)\sin\varphi) + z\sin\varphi)^2}{2\left(C_s'^*(z) - C_p(z)(2\cos^2\varphi - 1)\right)} \right]}{\sqrt{C_s'^*(z) - C_p(z)(2\cos^2\varphi - 1)}} \\ &\quad \times \frac{\exp\left[i \frac{(C_p(z) q_{\mathrm{CE}}^x)^2}{2\left(C_s'^*(z) - C_p(z)\cos^2\varphi\right)} \right]}{\sqrt{C_s'^*(z) - C_p(z)\cos^2\varphi}},\end{aligned} \tag{2.24}$$

where $C_s'(z) = (z\cos\varphi + iz_{R,f})/k(\omega_s^0)$ and q_{CE}^x (q_{CE}^y) is the transverse momentum component of the CE along the x- (y-) axis. Similarly, the Stokes photon density matrix takes the same form as Eq. (2.22) with the generalized apodization function [Eq. (2.23)]

$$\begin{aligned}\alpha(z, \varphi) = \exp&\left[- \frac{2z^2 \sin^2\varphi}{w_f^2 + \left(\varpi_f^2(z) + \varpi_p^2(z) + w_p^2\right)\cos^2\varphi} \right] \\ &\times \left\{ \left[(\varpi_f^2(z) + \varpi_p^2(z) + w_p^2)\cos^2\varphi + w_f^2 \right] \right. \\ &\left. \left[\varpi_f^2(z)\cos^2\varphi + \varpi_p^2(z) + w_p^2 + w_f^2 \right] \right\}^{-1/2},\end{aligned} \tag{2.25}$$

where $\varpi_f(z) = w_f z / z_{R,f}$ and $\varpi_p(z) = w_p z / z_{R,p}$.

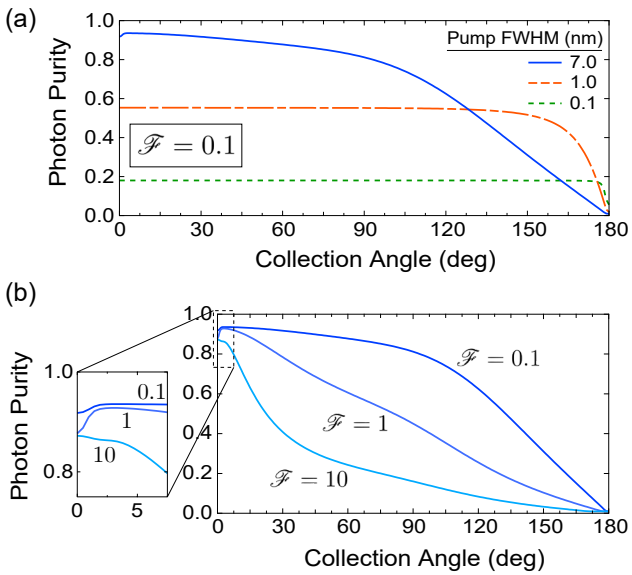

Figure 2.5: Stokes photon purity (a) as a function of collection angle for varying pump bandwidth at Fresnel number $\mathscr{F} = 0.1$, and (b) for varying Fresnel number at fixed pump FWHM = 7 nm. All calculations are performed within a three-dimensional model (see text).

Equation (2.25) has a Lorentzian form in the co-propagating case ($\varphi = 0$) and approaches a Gaussian as φ approaches 90°. The FWHM of the apodization function—the effective length from which photons are collected—decreases considerably with increasing collection angle up to collection perpendicular to the pump ($\varphi = 90°$), after which it increases symmetrically until the counter-propagating case ($\varphi = 180°$) when again the form is Lorentzian (see Appendix). In general, for a fixed medium length and collection angle, a more tightly focused pump beam will generate a narrower apodization function. The effect of this apodization function on the photon purity is shown in Fig. 2.5(a) as a function of collection angle for varying pump bandwidths, plotted for Fresnel number $\mathscr{F} = \mathscr{F}_p = \mathscr{F}_f = 0.1$. We note that in this case, for tightly focused beams, the photon purity is robust to small changes in collection angle about $\varphi = 0$. In Fig. 2.5(b) however, we plot the photon purity for varying Fresnel number at fixed pump bandwidth FWHM = 7 nm, and note that for loosely focused beams the purity becomes more sensitive to changes in collection angle. For some media (including bulk Al_2O_3 presented here) and Fresnel numbers, this interaction length apodization can lead to a maximal photon state purity at nonzero collection angle, as shown in the inset of Fig. 2.5(b).

2.5 Experimental Results

In its simplest form the interaction in Eq. (2.4) describes a two-mode squeezing operation of the Stokes and Q-fields, which leads to thermal photon-number statistics of the Stokes field created spontaneously through the Raman interaction [331]. It was found previously that correlations due to chromatic dispersion in the Raman medium and correlations due to the finite lifetime of the Q-field excitations both independently lead to a multimode-nature of this squeezing [291, 294], affecting the photon-number statistics which become more Poissonian as the number of squeezed modes increases [331, 332]. As we have derived, collection geometry and pump focusing also affect the entanglement of photon and CE and thence the photon purity, multimode nature of the squeezing, and the photon statistics.

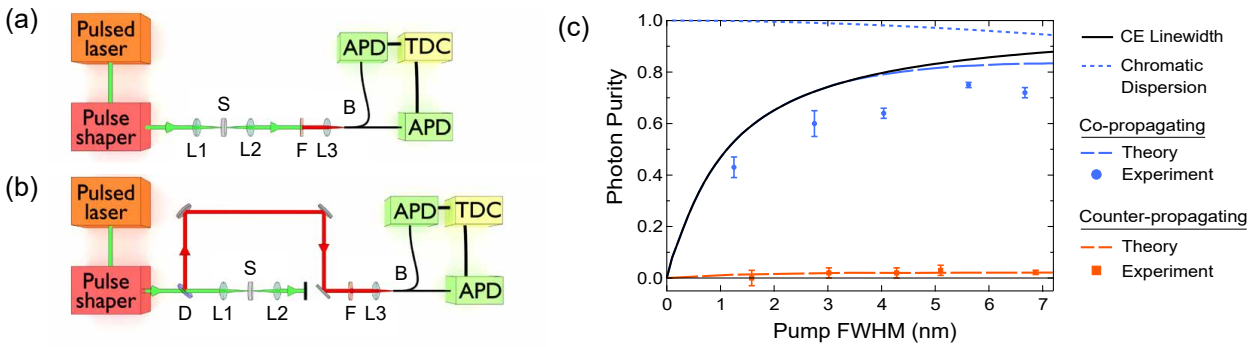

Figure 2.6: Experimental diagrams of (a) co- and (b) counter-propagating collection of Stokes photons; L1-L3: lenses, S: Raman sample, F: spectral filter, B: fiber beam-splitter, APD: avalanche photodiode, TDC: time-to-digital converter, D: dichroic. (c) Stokes photon purity measurements and theory for the two collection geometries at varying pump bandwidth.

Stokes photon second-order coherence $g^{(2)}$ measurements are performed with the Hanbury-Brown–Twiss interferometers shown in Figs. 2.6(a) and (b), for which $g^{(2)} = N_{12}R/N_1N_2$, where N_{12} represents coincident detection of two Stokes photons in both arms of the interferometer, R the number of pump pulses over which the counts are taken, and N_1 (N_2) the counts in arm 1 (2). In the multimode squeezing process as described, the $g^{(2)}$ autocorrelation function takes the form $g^{(2)} = 1 + 1/K$, where K is the effective number of squeezed modes and is related to the purity of the photons by $P = 1/K$ [331, 332].

In our experiments, pump pulses of duration 100 fs from a mode-locked Ti:Sapphire laser at 80 MHz repetition rate pass through a $4f$ spectral pulse shaper before they are focused by a lens of focal length 5 cm, generating spontaneous Stokes photons from a room-temperature, single-crystal, bulk sapphire medium (Ted Pella, Inc.) of length 8 mm centered on the beam waist. The Stokes photons are collected by another (the same) 5 cm focal length lens in the co-(counter-)propagating configuration, and are coupled into a single-mode fiber. The beam waist of our pumping light is 9.5 μm, and the waist of our collection mode is 9 μm, corresponding to Fresnel numbers of the pump and collection modes $\mathscr{F}$ $(= \mathscr{F}_p, \mathscr{F}_f) = 0.1$. The scattered photons are registered by Excelitas SPCM-AQ4C avalanche photodiodes and an IDQuantique time-to-digital converter. Figure 2.6(c) shows the results of Stokes photon purity measurements $P = g^{(2)} - 1$ and our theoretical predictions for two collection schemes: co-propagating [with setup depicted in Fig. 2.6(a)] and counter-propagating [Fig. 2.6(b)] Stokes and pump pulses. We attribute the source of the discrepancy between our theoretical predictions and experimental data to collection of fluorescent photons in the measurement process, which arise from defects in the crystal lattice and whose emission mode overlaps with the Stokes mode. Stokes photons collected counter-propagating from the pump have almost zero purity, indicating strong correlations and spatial entanglement with their corresponding excitations, in agreement with the predictions of our model.

Figure 2.7 shows the results of our photon purity measurements as a function of collection angle for 7 nm pump spectral FWHM. Again the deviation from theoretical prediction is attributed to background fluorescent photons, which are also emitted over solid angle 4π. Error bars in Fig. 2.7 and in Fig. 2.6(c) are calculated assuming Poissonian photon counting statistics.

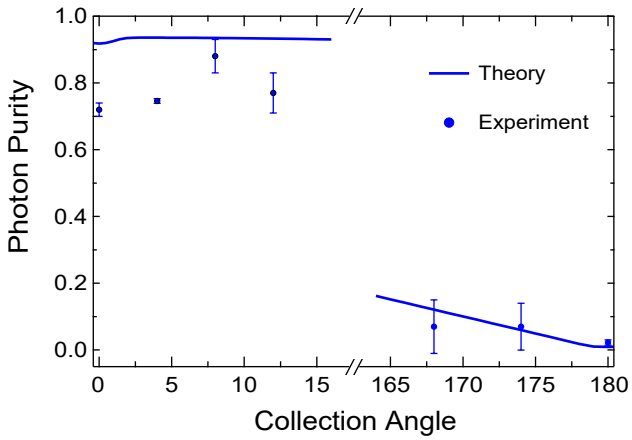

Figure 2.7: Stokes photon purity measurements for varying collection angle at pump FWHM = 7 nm, along with predictions of the three-dimensional off-axis theory (see text) for pump and collection mode Fresnel numbers $\mathscr{F} = 0.1$ corresponding to the experimental parameters.

2.6 Conclusions

We have developed a Hamiltonian formalism to describe the interaction between a pump laser pulse, Stokes field and collective excitations in Raman media. Using a one-dimensional model we have derived the general form of joint photon–CE states created in the low-gain regime of spontaneous Raman scattering. We have found that the CE linewidth creates energy entanglement between the daughter bosons of the pair and through a separate physical mechanism group delay between pump and Stokes pulses (due to chromatic dispersion in the medium) creates momentum/spatial entanglement; together these two effects lead in general to a maximal photon state purity at finite pumping bandwidth. This one-dimensional model is expanded to include the collection of Stokes photons counter-propagating with the pump, in which case we find timing information is available that has a much more substantial effect than does chromatic dispersion, and results in stronger photon–CE spatial entanglement and degradation of the photon purity. We have extended our theory to include photon–CE pair creation in three dimensions with arbitrary Fresnel numbers of the pump and collected Stokes beams, where we find the Stokes photon quantum state differs from the one-dimensional case only by an effective z-dependent correction that serves to apodize the interaction length. Finally, we have derived the correlations between photon and CE in the case of off-axis collection of Stokes photons, revealing non-trivial dependence of the photon purity on both collection angle and the focusing of the pump beam. The theory we have developed in this paper has important consequences for Raman-based quantum protocols that rely on spontaneous scattering and two-photon interference [301, 324, 333].

We compare the predictions of our model with experiment and confirm the presence of non-negligible correlations between photon and CE due to a finite excitation linewidth, and strong dependence of the scattered photon purity on collection angle, where photons collected counter-propagating with the pump are found in nearly completely mixed states.

Acknowledgments

This work is supported in part by NSF Grant Nos. 1521110, 1640968 and 1806572 and NSF award DMR-1747426. The authors thank Michael Raymer for useful comments, Lance Cooper and Astha Sethi for

measuring the Raman spectrum of the sapphire crystal used in the experiment, and Yujie Zhang for helpful discussion.

Supplemental: Photon-Excitation Pair Generation in Three Dimensions

In our three-dimensional treatment, we consider a focused classical pump beam with Gaussian paraxial field given by a collection of plane-waves with transverse wavevector $\mathbf{q}_p = (q_p^x, q_p^y)$ as

$$E_p(\boldsymbol{\rho}, z, t) = \frac{4\pi}{w_p^2} \int d\omega_p d^2\mathbf{q}_p \left[\mathcal{E}(\omega_p) e^{-w_p^2 |\mathbf{q}_p|^2/4} e^{i\mathbf{q}_p\cdot\boldsymbol{\rho}} e^{i\left[k(\omega_p) - |\mathbf{q}_p|^2/2k(\omega_p)\right]z} e^{-i\omega_p t} \right] + \text{h.c.}, \tag{2.26}$$

for Gaussian beam waist w_p.

While the Stokes field propagates in all directions, we consider the physical case of collection of photons emitted only around a small range of angles about the axis $\hat{z}_s$, where we use the following coordinate transformation relative to the $\hat{z}$ axis defined by the pump:

$$x_s = x \tag{2.27}$$

$$y_s = y\cos\varphi + z\sin\varphi \tag{2.28}$$

$$z_s = z\cos\varphi - y\sin\varphi, \tag{2.29}$$

shown schematically in Fig. 2.8(a), where $\boldsymbol{\rho_s} = (x_s, y_s)$, and the transverse photon wavevector in the off-axis coordinate system is $\mathbf{q}_s = (q_s^x, q_s^y)$. In order to develop the three-dimensional theory, instead of the Stokes photon creation operator considered in the text here we consider the negative frequency component of the paraxial Stokes field operator, defined as

$$\begin{aligned} &\hat{E}_s^{(-)}(\boldsymbol{\rho_s}, z_s) = \\ &-i\sqrt{\hbar\omega_s/2\mathcal{V}\varepsilon_0} \int d\omega_s d^2\mathbf{q}_s\, \hat{a}_{\mathbf{q}_s}^\dagger(\omega_s) e^{-i\mathbf{q}_s\cdot\boldsymbol{\rho}_s} \\ &\qquad\qquad \times e^{-i\left[k(\omega_s) - |\mathbf{q}_s|^2/2k(\omega_s)\right]z_s}, \end{aligned} \tag{2.30}$$

for quantization volume $\mathcal{V}$ and vacuum permittivity ε_0. Then using the transformation in Eqs. (2.27)-(2.29), we rewrite the Stokes field operator in the original basis as $\hat{E}_s^{(-)}(\boldsymbol{\rho}, z)$.

We write the interaction term in Eq. (2.4), including the transverse degrees of freedom, as:

$$\hat{V}_{3D}(t) = \gamma_{3D} \int d^2\boldsymbol{\rho} \int_{-L/2}^{L/2} dz\, E_p(\boldsymbol{\rho}, z, t) \hat{E}_s^{(-)}(\boldsymbol{\rho}, z) \hat{Q}^\dagger(\boldsymbol{\rho}, z) + \text{h.c.}, \tag{2.31}$$

with the coupling constant γ_{3D} associated with the amplitude of the interaction locally, and $\hat{Q}^\dagger(\boldsymbol{\rho}, z)$ given by Eq. (2.18) with transverse wavevector $\mathbf{q}_{CE} = (q_{CE}^x, q_{CE}^y)$. We apply this interaction perturbatively to the vacuum state to find the photon–CE joint state in the paraxial approximation

$$|\Psi\rangle_{par} = \mathcal{N}_{par} \int_{-L/2}^{L/2} dz \int d\omega_s d^2\mathbf{q}_s d\Omega d^2\mathbf{q}_{CE}\, f_{par}(\omega_s, \mathbf{q}_s, \Omega, \mathbf{q}_{CE}, z) \hat{a}_{\mathbf{q}_s}^\dagger(\omega_s) \hat{B}^\dagger(\Omega, \mathbf{q}_{CE}, z) |\text{vac}\rangle, \tag{2.32}$$

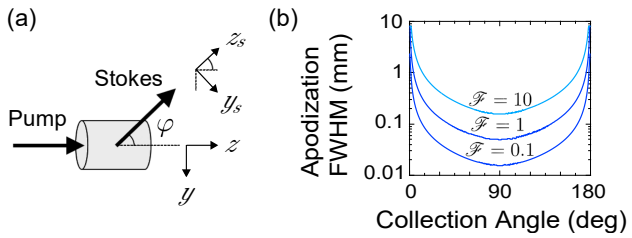

Figure 2.8: (a) Coordinate system for off-axis collection of Stokes photons. (b) Interaction length apodization function full width at half maximum (FWHM) for varying collection angle, evaluated at pump and collection mode Fresnel numbers $\mathscr{F} = 0.1, 1, 10$ for Gaussian beams described in the text.

where we have assumed that the transverse extent of the Raman medium is much larger than the transverse extent of the focused pump beam, thus recovering the transverse momentum conserving relations $q_p^x = q_s^x + q_{\mathrm{CE}}^x$ and $q_p^y = q_s^y \cos\varphi - [k(\omega_s) - |\mathbf{q}_s|^2/2k(\omega_s)]\sin\varphi + q_{\mathrm{CE}}^y$. Here $\mathcal{N}_{\mathrm{par}}$ is a normalization factor. Keeping terms of $\mathcal{O}\left(|\mathbf{q}_s|^2/k(\omega_s)^2\right)$ consistent with the paraxial approximation, the JA is given by

$$f_{\mathrm{par}}(\omega_s, \mathbf{q}_s, \Omega, \mathbf{q}_{\mathrm{CE}}, z) = \mu(\omega_s, \mathbf{q}_s, \Omega, \mathbf{q}_{\mathrm{CE}}, z) f_{1\mathrm{D}}(\omega_s, \Omega, z) \tag{2.33}$$

where

$$\begin{aligned}
&\mu(\omega_s, \mathbf{q}_s, \Omega, \mathbf{q}_{\mathrm{CE}}, z) = \\
&\exp\left[\frac{-w_p^2}{4}\left(q_s^x + q_{\mathrm{CE}}^x\right)^2\right] \exp\left[\frac{-w_p^2}{4}(q_s^y \cos\varphi + q_{\mathrm{CE}}^y)^2\right] \\
&\times \exp\left[\frac{-w_p^2}{4}(k(\omega_s)^2 - |\mathbf{q}_s|^2)\sin^2\varphi\right] \\
&\times \exp\left[\frac{w_p^2}{2}k(\omega_s)(q_s^y \cos\varphi + q_{\mathrm{CE}}^y)\sin\varphi\right] \\
&\times \exp\left[-i\frac{(q_s^x + q_{\mathrm{CE}}^x)^2}{2k(\omega_s + \Omega)}z\right] \exp\left[-i\frac{(q_s^y \cos\varphi + q_{\mathrm{CE}}^y)^2}{2k(\omega_s + \Omega)}z\right] \\
&\times \exp\left[-i\frac{(k(\omega_s)^2 - |\mathbf{q}_s|^2)\sin^2\varphi}{2k(\omega_s + \Omega)}z\right] \\
&\times \exp\left[i\frac{k(\omega_s)(q_s^y \cos\varphi + q_{\mathrm{CE}}^y)\sin\varphi}{k(\omega_s + \Omega)}z\right] \\
&\times \exp\left[i\left(\frac{|\mathbf{q}_s|^2\cos\varphi}{2k(\omega_s)} - q_s^y \sin\varphi\right)z\right] \\
&\times \exp\left[i(k(\omega_s) - k(\omega_s)\cos\varphi)z\right]
\end{aligned} \tag{2.34}$$

and $f_{1\mathrm{D}}(\omega_s, \Omega, z)$ is given by Eq. (2.10) for the one-dimensional case. Considering the physical case of Stokes photons collected by a lens and coupled to a single-mode fiber, assuming that the projection of the spatial mode supported by the fiber onto free space by the lens can be well approximated by a Gaussian, this configuration projects the scattered Stokes photons onto a state with creation operator $\hat{A}_s^\dagger(\omega_s)$ given in Eq. (2.19). Letting $|u_f(\omega_s)\rangle = \hat{A}_s^\dagger(\omega_s)|\mathrm{vac}\rangle$, the projection of the emitted state onto this concentric collection

mode, given by normalizing the state $\int d\omega_s \, |u_f(\omega_s)\rangle\langle u_f(\omega_s)|\Psi\rangle_{\text{par}}$, results in a state with the joint amplitudes given by Eqs. (2.20) and (2.24).

In the three-dimensional case this collection scheme leads to the apodization function in the reduced density matrix of the Stokes photon $\alpha(z, \varphi)$ given in Eq. (2.25). The behavior of the apodization function FWHM for varying Fresnel number is shown in Fig. 2.8(b) for the same bulk Al_2O_3 medium considered in the text. For a fixed medium length and collection angle, a more tightly focused pump beam will generate a narrower apodization function, resulting in the increase of the collected photon purity.

Chapter 3

Optimization of broadband Λ-type quantum memory using Gaussian pulses

This chapter encompasses the first of three projects (with several more to come) focused on the task of single-photon-level quantum memory, as described in Sec. 1.3. In particular, this chapter focuses on improving the efficiency of these memories via numerical optimization of the parameters of the control field pulse. Along the way, we reveal a continuous transformation between three well-known resonant quantum memory protocols that is of general theoretical interest. The content of this chapter was published in Ref. [141], and is reproduced here with only minor formatting changes.[1]

3.1 Introduction

Efficient photonic quantum state generation and synchronization [334, 335], metropolitan-scale quantum networking and entanglement distribution [301, 336], and linear-optical quantum computing [337] all rely on efficient optical quantum memory. In order for these emerging applications to operate at high speed they must be compatible with broadband photonic quantum states [313, 314, 338], ideally with minimal experimental complexity. In quantum memories based on atomic ensembles, a significant body of theoretical [339–344] and experimental [345–347] work has been dedicated to improving quantum memory efficiency by temporal shaping of the optical signal field to be stored or the control field used to mediate the interaction. However, these techniques have largely only been applied for signal bandwidths smaller than the linewidths of the excited states participating in the memory interaction, in part due to the technological complexity of shaping intense broadband fields. In effect, ensemble quantum memories to date have been limited to efficient narrowband operation [348–352] or inefficient broadband operation [313, 353–362], with only a few notable exceptions [338, 363–366].

[1] Previously published material appears in this section. Bibliographic information for this material is as follows: K. Shinbrough, B. D. Hunt, and V. O. Lorenz, "Optimization of broadband Λ-type quantum memory using Gaussian pulses," Phys. Rev. A **103**, 062418 (2021). The copyright owner, the American Physical Society, has provided permission to reprint. I gratefully acknowledge the coauthors listed above for their contributions to the text.

In this work, we provide a quantitative performance analysis of resonant Λ-type quantum memories, shown in Fig. 5.1, with a specific focus on signal bandwidths larger than the memory's intermediate state linewidth (Γ in Fig. 5.1), which we consider broadband. While a variety of other level systems are employed for quantum memory (ladder-type, etc.), Λ-type level systems are currently the most common, and our analysis is readily generalizable to other level systems.

In the broadband regime, far off-resonant quantum memory protocols are well-established, but require significantly more control field power than resonant protocols and suffer from low efficiency due to the experimental difficulty in satisfying this requirement [313, 353–356, 359, 361, 362]. In this work, we restrict our discussion to the use of resonant and near-resonant optical fields with Gaussian temporal envelopes in order to avoid the experimental complexities of large pulse energies and shaping of the optical fields. Despite these restrictions, we find that through optimization of the native parameters of Gaussian control fields (i.e., optical power, arrival time, and duration)—which are simple to fine-tune experimentally—we can still achieve high-efficiency memory operation, including in the broadband regime.

Whereas most work aimed at optimizing quantum memory efficiency focuses on a particular physical quantum memory protocol and leverages physical understanding of the storage mechanism to solve a generic, unconstrained optimization problem [338–341, 344, 363, 364, 367], herein we take a physically agnostic approach where we aim to optimize the memory efficiency through a highly constrained set of experimental parameters, initially without regard for the physical storage protocols. While the protocol-based approach facilitates understanding the underlying physics of the quantum memory interaction, practically one is often presented with a set of experimental parameters and resources which are limited, may drift over time, and which in general are not guaranteed to align neatly with a particular storage protocol. Between these physical regimes and storage protocols, it is useful to fine-tune the experimental parameters at hand in order to maximize memory efficiency.

After numerically calculating the optimal Gaussian control field parameters for a broad range of experimental conditions, we return to examine the physical storage mechanisms and identify the regions of high-efficiency memory operation. We provide physical explanation for the optimized control field parameters in terms of three established memory protocols: those of Refs. [341, 367–369] that we summarize with the phrase 'absorb-then-transfer,' the recently proposed Autler-Townes splitting (ATS) protocol [363–366], and the electromagnetically induced transparency (EIT) protocol [341, 370–372]. As we show, our optimization procedure connects these three physically distinct quantum memory protocols through continuous transformation of the control field parameters (extending the results of Ref. [364]), and allows for high-efficiency operation in the transition regions between physical protocols. In particular, we report optimized Gaussian control field parameters that allow for optimal memory operation for bandwidths broader than those used in the ATS protocol, and for bandwidths between the ATS and EIT protocols.

This article is organized as follows: After providing details on our numerical analysis of the equations of motion describing the quantum memory interaction and the optimal efficiency bound for a given optical depth (Section 3.2), in Section 3.3 we consider resonant (Sec. 3.3.1) and near-resonant (Sec. 3.3.2) Gaussian control field optimization. In Section 3.4 we compare the efficiencies generated with the Gaussian optimization described in Sec. 3.3 and the standard shape-based optimization method described in Refs. [339, 340, 342–344]. We find that the Gaussian optimization procedure achieves memory efficiencies comparable to the shape-based method in all but the most broadband cases. In the appendices we provide physical descriptions of the three resonant storage protocols and details on the conditions we use to calculate ATS and EIT regions.

Throughout this work we assume 'backward retrieval' of the signal field (Fig. 5.1) such that the atomic

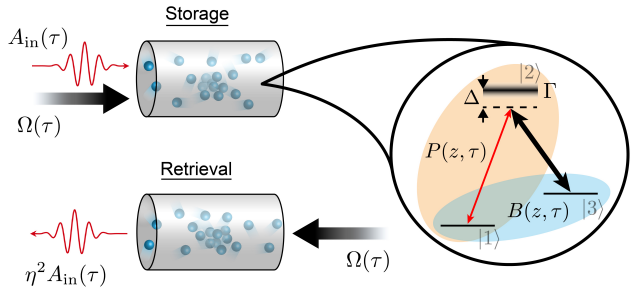

Figure 3.1: 'Backward retrieval' quantum memory scheme, wherein a weak signal field [$A_{\rm in}(\tau)$, red thin line] and strong control field [$\Omega(\tau)$, black thick line] enter an atomic medium, generating atomic polarization [$P(z,\tau)$, orange ellipse] and spin wave [$B(z,\tau)$, blue ellipse] fields according to the Λ-type level scheme shown on the right, with excited-state linewidth Γ and two-photon detuning Δ. After a controllable delay, the signal field is retrieved with total efficiency η^2 via the application of another strong control field that propagates antiparallel to the first control field.

dynamics during retrieval are the time reverse of those during the storage process, which holds for near-degenerate ground and storage states ($|1\rangle$ and $|3\rangle$ in Fig. 5.1) [340–342]. In this case, the retrieval efficiency is identical to the storage efficiency, η, and the total memory efficiency is η^2. Thus, in order to fully characterize the memory efficiency, we need only compute η. Since the Gaussian fields we consider are intrinsically time-reversal symmetric, under these assumptions no additional experimental measures need to be taken in order to ensure optimization of retrieval beyond routing the retrieval control pulse to the output facet of the atomic ensemble.

3.2 Numerical Solution of Maxwell-Bloch Equations

The Λ-type level structure shown in Fig. 5.1 includes two stable or meta-stable ground states, $|1\rangle$ and $|3\rangle$, and an intermediate excited state $|2\rangle$ that decays to the ground states with the coherence decay rate $\gamma = \Gamma/2$, where Γ is the population decay rate of the $|2\rangle$ state. All temporal dynamics are considered in the co-moving frame defined by $\tau = t - z/c$, where t is the time measured in the lab frame, z is the one-dimensional spatial coordinate—defined as $z = 0(L)$ at the input (output) face of the medium, where L is the medium length—and c is the speed of light. We assume that a control field with frequency near the $|2\rangle \leftrightarrow |3\rangle$ transition, Rabi frequency $\Omega(\tau)$, and duration $\tau_{\rm FWHM}^{\rm ctrl}$ enters the medium with a Gaussian temporal envelope and does not undergo significant absorption or distortion as it propagates [$\Omega(z,\tau) = \Omega(\tau)$]. We assume that before the signal field enters the medium, it has a Gaussian temporal envelope $A_{\rm in}(\tau) = e^{-\tau^2/4\sigma^2}$, where $\sigma = \tau_{\rm FWHM}/(2\sqrt{2\ln 2})$, for the signal duration $\tau_{\rm FWHM}$ [temporal full width at half maximum (FWHM)]. There exists also the possibility to temporally chirp the optical field and optimize separately over control pulse bandwidth, but in this work we consider only Fourier-transform-limited pulses such that, e.g., the signal field spectral intensity bandwidth δ and duration $\tau_{\rm FWHM}$ are related by $\delta = 2\pi \times 2\ln 2/(\pi\tau_{\rm FWHM})$.

We further assume that all atoms initially populate the $|1\rangle$ state, which is a valid approximation for atomic populations after optical pumping, or for atomic species with sufficient energy separation between the $|1\rangle$ state and other low-lying states. In general, the signal field undergoes spatial and temporal deformation as it propagates through the medium and is absorbed along the $|1\rangle \rightarrow |2\rangle$ transition, described by $A(z,\tau)$. The atomic dynamics in the presence of these two optical fields are described by the resonant, normalized Maxwell-Bloch equations [340, 344, 363, 373]:

$$\partial_z A(z,\tau) = -\sqrt{d}P(z,\tau) \tag{3.1}$$

$$\partial_\tau P(z,\tau) = -\bar{\gamma}P(z,\tau) + \sqrt{d}A(z,\tau) - i\frac{\Omega(\tau)}{2}B(z,\tau) \tag{3.2}$$

$$\partial_\tau B(z,\tau) = -\gamma_B B(z,\tau) - i\frac{\Omega^*(\tau)}{2}P(z,\tau), \tag{3.3}$$

where d is the resonant optical depth of the memory, $\bar{\gamma} = (\gamma - i\Delta)/\gamma$ is the normalized complex detuning, and $P(z,\tau)$ and $B(z,\tau)$ are macroscopic field operators representing the atomic coherences $|1\rangle \leftrightarrow |2\rangle$ and $|1\rangle \leftrightarrow |3\rangle$, respectively, which are delocalized across the length of the medium. In Eqs. (5.1)-(5.3), all frequency (time) scales are normalized by γ ($1/\gamma$), and all length scales are normalized by L. We assume that the coherence decay rate corresponding to the $|3\rangle \rightarrow |1\rangle$ transition, γ_B, is negligible during the storage and retrieval operations: $\gamma_B \ll 1$.

We iteratively solve these equations of motion using Ralston's method for evaluating the τ-derivatives and Chebyshev spectral differentiation for the z-derivatives. After integration, we compare the population in B to the population in A_{in} in order to calculate the storage efficiency for a particular choice of $\Omega(\tau)$, as:

$$\eta = \frac{\int_0^1 dz\, |B(z,\tau\rightarrow\infty)|^2}{\int_{-\infty}^{\infty} d\tau\, |A_{\text{in}}(\tau)|^2}, \tag{3.4}$$

where in practice we truncate $A_{\text{in}}(\tau)$ and $B(z,\tau)$ at $\tau^{\text{end}} = 4\tau_{\text{FWHM}}$, where $A_{\text{in}}(\tau^{\text{end}})$ has dropped to $\mathcal{O}(10^{-10})$ of its maximum value. Thus Eqs. (5.1)-(5.3) in combination with Eq. (3.4) define an objective function that can be maximized with respect to the free parameters of $\Omega(\tau)$. We parameterize the control field Rabi frequency—which we take to be real for simplicity—in terms of its pulse area $\theta = \int_{-\infty}^{\infty} d\tau\, \Omega(\tau)$, temporal delay $\Delta\tau^{\text{ctrl}}$ relative to the arrival of the signal field, and duration $\tau^{\text{ctrl}}_{\text{FWHM}} = 2\sqrt{2\ln 2}\sigma^{\text{ctrl}}$ as:

$$\Omega(\tau) = \Omega_0\, e^{-[(\tau-\Delta\tau^{\text{ctrl}})/2\sigma^{\text{ctrl}}]^2}, \tag{3.5}$$

where $\Omega_0 = \theta/(2\sqrt{\pi}\sigma^{\text{ctrl}})$, and we optimize over the parameter space vector $\mathcal{G} \equiv \left(\theta, \Delta\tau^{\text{ctrl}}, \tau^{\text{ctrl}}_{\text{FWHM}}\right)$ using a Nelder-Mead simplex method, which rapidly identifies the efficiency maxima under these constraints, as verified by deterministic searches of the same parameter space. We define $\tau = 0$ at the maximum of the signal field.

Throughout this work we normalize the efficiencies calculated via the method above by the protocol-independent efficiency bound for a fixed optical depth, η_{opt}, described in Refs. [340, 341, 344, 346] and elsewhere. In brief, we calculate this efficiency bound by finding the eigenvalues of the anti-normally ordered storage kernel

$$K(z,z') = \frac{d}{2}e^{-d(z+z')/2} I_0(d\sqrt{zz'}), \tag{3.6}$$

where $I_0(x)$ is the zeroth-order modified Bessel function of the first kind, and we discretize $K(z,z')$ on a 5000×5000 point grid. For fixed d, the largest eigenvalue λ_0 of this kernel represents the maximum achievable storage efficiency at that optical depth, $\eta_{\text{opt}} = \lambda_0$. By performing this normalization, we aim to compare the efficiencies of particular memory implementations independent of the limitation imposed by finite optical depth.

3.3 Results of Gaussian Optimization

3.3.1 On Resonance ($\Delta = 0$)

We first consider the case of resonant interaction of the optical fields with the atomic Λ system (i.e., $\Delta = 0$). At each optical depth and signal bandwidth, we optimize over the control field parameters $\mathcal{G} = \left(\theta, \Delta\tau^{\text{ctrl}}, \tau^{\text{ctrl}}_{\text{FWHM}}\right)$, which fully define any Gaussian control field through Eq. (3.5). This allows us to show that the three known, physically distinct quantum storage protocols for resonant storage (see Appendix 3.5 for a brief overview of the protocols) are smoothly connected via continuous transformation of the control-field parameters. This result is similar to that in Ref. [364], which demonstrated ATS and EIT quantum memory behavior can be connected through continuous transformation of the control field Rabi frequency for fixed memory parameters, under the condition of either a constant control field or an interrupted control field of varying linear slope. Here we distinguish between the *memory* parameters $\mathcal{M} \equiv (d, \tau_{\text{FWHM}}\gamma)$, which represent the physical characteristics of a particular quantum memory for the chosen signal bandwidth, and the *control field* parameters $\mathcal{G}$. In this formalism, Ref. [364] derived a connection between ATS and EIT storage for fixed $\mathcal{M}$ by varying $\mathcal{G}$ [where, e.g., $\mathcal{G}_c = (\Omega_0)$ is a single-parameter vector in the case of a constant control field, $\Omega(\tau) = \Omega_0$]. Motivated by this observation, we consider the distinct condition of Gaussian-shape control fields, and we show that again ATS and EIT memory behavior can be connected if we consider the transformation as a function of $\mathcal{M}$, where optimization of $\mathcal{G}$ at each point in $\mathcal{M}$ ensures optimal or near-optimal storage efficiency. Further, we show the two protocols can be connected to the 'absorb-then-transfer' protocol through the same continuous transformation. We show each protocol possesses a region of optimality under the restriction of Gaussian pulses and identify two regions where our optimization scheme is most useful: one where the storage mechanism is given by the 'absorb-then-transfer' protocol, but in the largely unexplored non-adiabatic regime, and one between the regions of efficient ATS and EIT memory operation.

Figure 5.2 presents the main results of this section. In Fig. 5.2(a) we show the normalized efficiencies achieved through the optimization procedure described in Sec. 3.2, for memory parameters in the range $d = 1$ to 50 and $\tau_{\text{FWHM}}\gamma = 0$ to 1.5, which we take to be representative of the bulk of experimental broadband quantum memories, though our analysis is easily extended to other regions. The efficiencies shown saturate the optimal efficiency bound ($\eta/\eta_{\text{opt}} = 100\%$) for adiabaticities $d\tau_{\text{FWHM}}\gamma \geq 1$ [see Fig. 5.2(b) for a map of the memory adiabaticity]. This result demonstrates that Gaussian-shape fields are sufficient for high-efficiency, broadband memory operation, without the need for full pulse-shape control.

The first region of the $\mathcal{M}$ parameter space where our optimization is most useful can be highlighted using Fig. 5.2(b), which shows the memory adiabaticity ($d\tau_{\text{FWHM}}\gamma$) as a function of $\mathcal{M}$. For $d\tau_{\text{FWHM}}\gamma < 1$, we observe the expected decay of the storage efficiency [341], shown in Fig. 5.2(a). Between $d\tau_{\text{FWHM}}\gamma = 1$ and the region of efficient ATS operation [delineated with dashed lines in Fig. 5.2(b)—see Appendix 3.5 for derivation], we observe storage efficiencies that approach the optimal bound ($\eta/\eta_{opt} = 100\%$), where the physical storage mechanism is given by the 'absorb-then-transfer' protocol [341, 367–369]. As can be seen in Fig. 5.2(d)-(f), the optimized control field parameters in this region correspond to approximately π-pulse-area control fields that are narrower in duration than the signal fields they store ($\tau^{\text{ctrl}}_{\text{FWHM}} < \tau_{\text{FWHM}}$), and arrive after the signal field ($\Delta\tau^{\text{ctrl}} > 0$). The optimized control fields arrive at the approximate time when the electric field of the signal changes sign (when evaluated at $z = 1/2$), in agreement with the analysis of Refs. [369, 374, 375]. This result demonstrates that the absorb-then-transfer protocol can approach the optimal efficiency bound in the non-adiabatic regime, in addition to the adiabatic regime investigated in

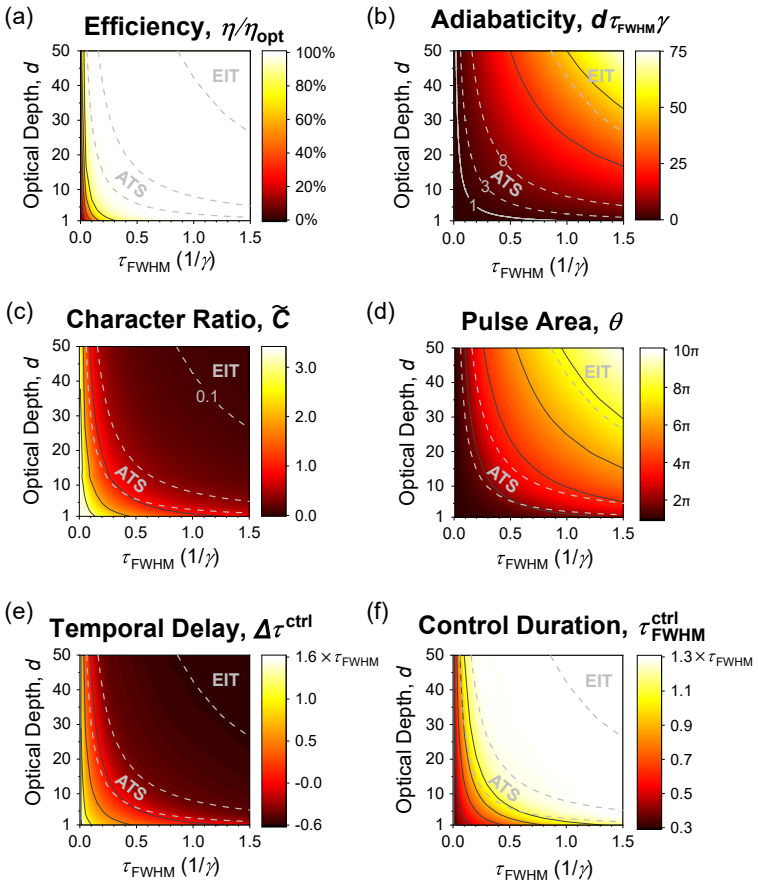

Figure 3.2: (a) Storage efficiencies achieved through optimization of Gaussian-shape control fields, relative to the optimal bound η_{opt} shown in parentheses for each optical depth d; (b) memory adiabaticity, where the region $d\tau_{\text{FWHM}}\gamma = 3$ to 8 corresponds to optimal ATS memory operation (see Appendix B); (c) the memory character ratio, where $\tilde{C} \leq 0.1$ indicates the region of EIT memory operation; and (d)-(f) the optimized control field parameters as a function of optical depth and signal field duration, τ_{FWHM}. Positive (negative) delay, $\Delta\tau^{\text{ctrl}} > 0$ ($\Delta\tau^{\text{ctrl}} < 0$), refers to control fields that arrive after (before) the signal field.

Ref. [367].

The second region of $\mathcal{M}$-space where our optimization procedure is most useful is in the region between the optimal memory conditions for ATS and EIT storage, delineated by the dashed lines in Fig. 5.2 (see Appendix 3.5 for derivation of the boundary of the EIT region). Here the memory is still non-adiabatic ($d\tau_{\text{FWHM}}\gamma \gg 1$ is not satisfied), but the ATS condition $d\tau_{\text{FWHM}}\gamma = 3$ to 8 is exceeded, similar to the broadband-EIT region of Refs. [338, 364]. In this region, fine-tuning of the control field parameters allows for optimal memory efficiency, whereas use of the typical ATS [$\mathcal{G} = (2\pi, 0, \tau_{\text{FWHM}})$] or EIT control field parameters leads to sub-optimal efficiency.

We note that Fig. 5.2(d)-(f) may act as a guide for experimentally simple optimization of broadband quantum memory using Gaussian pulses. For a given set of memory parameters $\mathcal{M}$, the optimal Gaussian control field parameters may be read off directly from Fig. 5.2(d)-(f). In the adiabatic, EIT regime ($d\tau_{\text{FWHM}}\gamma \gg 1$), we find negative temporal delays that asymptote to around $-0.55\tau_{\text{FWHM}}$, and control field durations that asymptote to $\sim 1.33\tau_{\text{FWHM}}$.

Notably, the optimized control field parameters presented in Fig. 5.2 are not mutually independent; for

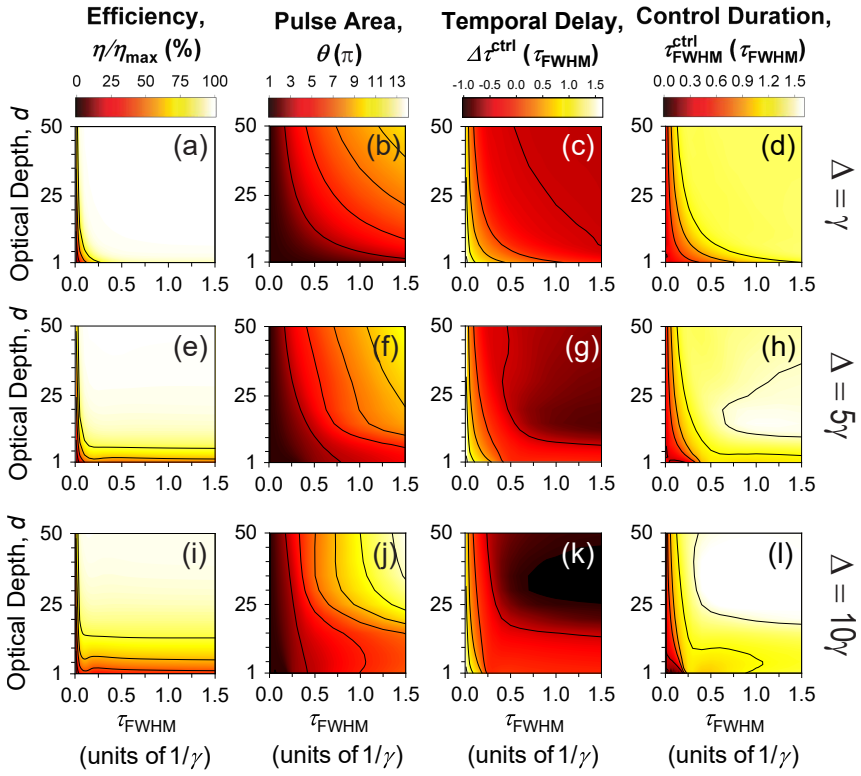

Figure 3.3: Optimized Λ-type quantum memory efficiency and corresponding optimized control field parameters as a function of optical depth, d, and signal field duration, τ_{FWHM}, for varying two-photon detuning, (a)-(d) $\Delta = \gamma$, (e)-(h) $\Delta = 5\gamma$, and (i)-(l) $\Delta = 10\gamma$, for excited state coherence decay rate γ.

example, at fixed $\mathcal{M}$, changes to the control field duration away from the optimal choice shown in Fig. 5.2(f) may be compensated for with changes to the control field delay and pulse area, with only a small decrease in efficiency in some cases. Fig. 5.2(d)-(f) shows only the optimal and mutually dependent choice of control field parameters. The sensitivity or robustness to noise in these optimal parameters may be the subject of future work.

3.3.2 Near Resonance ($\Delta \neq 0$)

The case of resonant signal and control fields considered above has shown optimal storage efficiency to be possible for a wide range of memory parameters using only Gaussian pulses. In this section we continue this analysis for non-zero two-photon detunings in the near-resonant regime, where Δ is of order γ. This analysis differs then from the far-off-resonant Raman regime [344, 353–356, 359], where $\Delta \gg \gamma$. While we nominally only consider positive detunings, the results presented in this section are symmetric about $\Delta = 0$.

Whereas for resonant signal and control fields all optimization parameters $\mathcal{G}$ are smooth, monotonic functions of the memory parameters $\mathcal{M}$, in the near-resonant case we observe more complicated behavior where the optimized parameters are no longer strictly monotonic functions of $\mathcal{M}$. In Fig. 5.3(a)-(d), (e)-(h), and (i)-(l), we consider two-photon detunings $\Delta = \gamma$, $\Delta = 5\gamma$, and $\Delta = 10\gamma$, respectively. As shown in Fig. 5.3(a), (e), and (i), for fixed memory parameters $\mathcal{M}$, larger Δ consistently implies smaller η/η_{max}. It appears this decrease in memory efficiency can be avoided by increasing optical depth, although this comes at the cost of larger control field pulse area and optical power required to implement optimized storage. In

general, as shown in Fig. 5.3(b), (f), and (j), for fixed $\mathcal{M}$ the pulse areas necessary to implement optimized quantum storage with Gaussian pulses tend to increase with increasing Δ. The minimum temporal delay in the region we simulate decreases as a function of Δ, indicating control field pulses in those regions of negative delay that arrive significantly sooner (before the signal field) than their resonant counterparts in the EIT regime. In these same regions [i.e., $\mathcal{M} \approx (20, 1.5)$ for $\Delta = 5\gamma$, $\mathcal{M} \approx (35, 1.5)$ for $\Delta = 10\gamma$], the control field duration is also significantly larger than in the resonant case.

As in Sec. 3.3.1, we note that Fig. 5.3 may serve as an experimental guide for optimized quantum memory implementation with Gaussian-shape signal and control fields at fixed detuning in the near-resonant regime.

3.4 Comparison of Gaussian and Shape-Based Optimization

In the sections above we have introduced an alternative quantum memory optimization scheme that relies only on broadband light pulses with Gaussian temporal envelope. This scheme operates at or near two-photon resonance, and therefore avoids the experimental complexities associated with full pulse-shape control of broadband fields and the use of large pulse energies. In this section, we compare the results of this optimization scheme with the more standard shape-based optimization of Refs. [339, 340, 342–344].

In order to enumerate this comparison, we consider a quantum memory with optical depth $d = 50$, where we calculate via Eq. (3.6) an optimal storage efficiency of $\eta_{\text{opt}} = 95.2\%$ (total efficiency: $\eta_{\text{opt}}^2 = 90.6\%$). We further assume resonant storage of photons such that $\Delta = 0$. To calculate the storage efficiencies achieved via shape-based optimization, we first numerically construct the storage kernel $K(z, \tau)$ defined by the linear integral transform,

$$B_{\text{out}}(z) = B(z, \tau \to \infty) = \int_{-\infty}^{\infty} d\tau\, K(z, \tau) A_{\text{in}}(\tau), \tag{3.7}$$

via the method described in Ref. [344]. The largest singular value of $K(z, \tau)$ and the corresponding right-singular vector represent the optimal storage efficiency and optimal signal mode temporal profile, respectively [341, 344]. Importantly, $K(z, \tau)$ depends both on the chosen optical depth, d, and the control field parameters, $\mathcal{G}$. The optimal signal mode calculated through this method is therefore guaranteed to lead to optimal storage efficiency for the given d and $\mathcal{G}$.

This method relies on signal-field shaping in order to achieve optimal memory efficiency. One can instead optimize the memory efficiency through shaping of the control field with the procedure outlined in Ref. [344]. In short, one interpolates between the optimal signal mode calculated for given d and $\mathcal{G}$ and the desired signal mode (typically a Gaussian, with duration τ_{FWHM}), and at each interpolation step one optimizes $\mathcal{G}_s$, which is a large vector that defines the shape of $\Omega(\tau)$. At each interpolation step, the signal field is deformed away from the optimal shape and the control field shape is optimized in order to compensate for the decrease in memory efficiency. For sufficiently small successive deformations of the signal field, optimality is preserved at each interpolation step and this procedure leads to the optimal control field shape for a Gaussian signal field. We find the final memory efficiency achieved through control-field shaping is typically bounded above by the efficiency achieved through signal-field shaping. For the purposes of this comparison, we compare the results of the Gaussian optimization in Sec. 3.3 with the upper bound achieved via signal-field shaping.

In Fig. 5.4, we calculate the storage efficiency achieved via signal-field shaping alongside the efficiency calculated via the Gaussian optimization scheme presented in this article, for signal durations between 0 and $1.5/\gamma$ in the example case of a Λ-type level system at $d = 50$. We observe saturation of the optimal bound

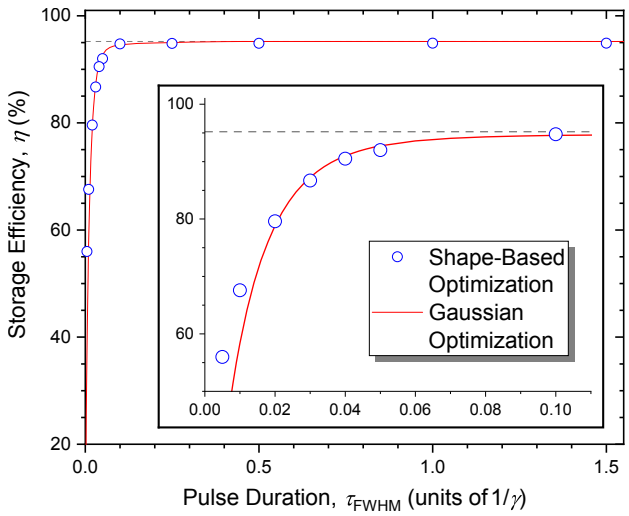

Figure 3.4: Comparison of quantum memory efficiencies achieved using shape-based and Gaussian control field optimization for $d = 50$. Dotted line represents the optimal efficiency bound, $\eta_{\text{opt}} = 95.2\%$.

(dashed line, $\eta = \eta_{\text{opt}} = 95.2\%$) in the region $\tau_{\text{FWHM}} = 0.1/\gamma$ to $1.5/\gamma$ for both optimization schemes, where the optimal storage protocol transitions between all three resonant protocols defined in Appendix 3.5. Below $0.1/\gamma$ signal field duration, we observe decay in the memory efficiency for both schemes, where the Gaussian optimization scheme leads to comparatively lower storage efficiencies for the most broadband pulse durations. Nevertheless, the Gaussian optimization procedure provides comparable memory performance over a wide range of bandwidths.

The main result of this section is as follows: Through the Gaussian optimization procedure described in this article, we achieve storage efficiencies that closely compare with the efficiencies achieved through shape-based optimization, but which (1) require significantly less computational expense to calculate, and (2) physically correspond to quantum memory experiments that are simpler, as they eliminate the need for arbitrary shaping of either intense, broadband fields (control-field shaping) or broadband single-photon level fields (signal-field shaping).

3.5 Conclusions and Future Work

In this work we have presented a quantitative and qualitative exploration of Λ-type quantum memory with Gaussian optical fields that are resonant and near-resonant with an atomic two-photon transition. The restriction to Gaussian fields serves to simplify experimental implementations of optical quantum memory. We have shown that despite this restriction, optimization of the parameters of Gaussian control fields (optical power, arrival time, and duration) can lead to high-efficiency memory operation over a wide range of memory parameters in the broadband regime. We make the distinction between the memory parameters ($\mathcal{M}$) and the control field parameters ($\mathcal{G}$), and in so doing we find that optimization of $\mathcal{G}$ reveals a continuous transition between three physically distinct quantum memory protocols (what we call the 'absorb-then-transfer' protocol, ATS, and EIT) as a function of $\mathcal{M}$. This optimization procedure is most useful in two regions of the memory parameter space. In the region of $\mathcal{M}$ that is more broadband than the optimal ATS region at fixed optical depth, we show that the 'absorb-then-transfer' protocol can operate with near-optimal efficiency, extending

the result investigated previously in the adiabatic ($d\tau_{\mathrm{FWHM}}\gamma \gg 1$) regime [367]. In the region of $\mathcal{M}$ between optimal ATS and EIT operation—the mixed ATS/EIT regime—we also show that optimal memory operation is possible.

In Sec. 3.3.2 we have extended this analysis to the near-resonant regime where the two-photon detuning is of order the excited state linewidth, $\Delta \sim \gamma$. We observe similar qualitative behaviour of the optimal control field parameters $\mathcal{G}$ as a function of $\mathcal{M}$, but in order to achieve the same memory efficiency, a larger optical depth d and control field pulse area θ are required compared to the resonant case.

Finally, in Sec. 3.4 we have provided a numerical comparison of the proposed Gaussian optimization technique with the more common shape-based optimization procedure. We find that Gaussian pulses are suitable for optimal memory operation over a wide range of memory parameters, and only perform significantly worse than arbitrarily shaped pulses in the most broadband cases where the storage efficiency is non-optimal even for shape-based optimization.

In this work we restrict ourselves to the widely available resource of Fourier-transform limited pulses, where pulse duration and bandwidth are Fourier-transform pairs and accordingly only describe one degree of freedom subject to optimization. Future work may consider optimization via chirped optical fields, which expands the toolbox for optimization of Gaussian quantum memory and has been explored in other memory protocols [376–378]. We have also restricted our optimization procedure to the case of homogeneous dephasing of the atomic polarization field. The case of inhomogeneous polarization dephasing, following the approach of [379], may be considered in future work.

Acknowledgements

We gratefully acknowledge helpful discussion provided by Yujie Zhang, Xinan Chen, Sehyun Park, Elizabeth Goldschmidt, Bin Fang, Shuai Dong, Seth Meiselman, and Offir Cohen, as well as support from NSF Grant Nos. 1640968, 1806572, 1839177, and 1936321 and NSF Award DMR-1747426. This work made use of the Illinois Campus Cluster, a computing resource that is operated by the Illinois Campus Cluster Program (ICCP) in conjunction with the National Center for Supercomputing Applications (NCSA) and which is supported by funds from the University of Illinois at Urbana-Champaign.

Supplemental A: Description of Protocols

Here we briefly review the three known resonant quantum memory protocols that make use of a homogeneously broadened excited-state linewidth, and their key features:

(1) 'Absorb-then-transfer.' Described in Refs. [341, 367–369], quantum storage is achieved through linear absorption of the signal field along the $|1\rangle \rightarrow |2\rangle$ transition and coherent population transfer between the atomic polarization and spin-wave field via a π-pulse control field. We distinguish this 'absorb-then-transfer' storage protocol from the related photon-echo protocols [380–383], as photon emission upon retrieval does not depend on dipole rephasing for homogeneously broadened intermediate states. Ref. [369] indicates that in order to optimize storage efficiency the arrival time of the control field should occur near the first zero of the complex signal field amplitude when evaluated at the middle of the ensemble ($z = 1/2$), at least in the weak-absorption regime. Ref. [367] has shown this storage protocol can be optimal (i.e., can achieve $\eta = \eta_{\mathrm{opt}}$) for large optical depths, such that $d\tau_{\mathrm{FWHM}}\gamma \gg 1$.

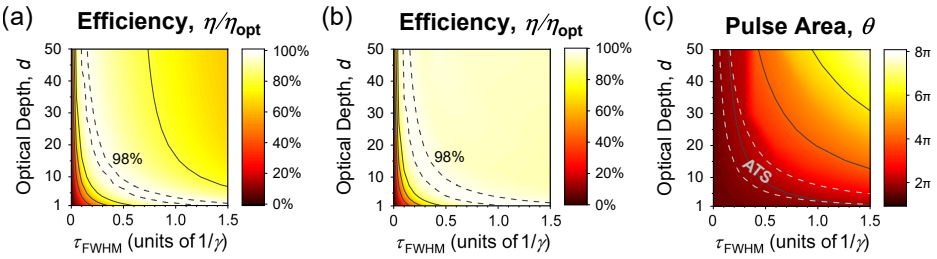

Figure 3.5: Comparison of quantum memory efficiencies achieved using pulse areas of (a) $\theta = 2\pi$, and (b) directly optimized pulse areas shown in (c). Dotted lines in (c) delineate the ATS region $d\tau_{\mathrm{FWHM}}\gamma = 3$ to 8 used in the main text, which captures the region of $\theta \approx 2\pi$ operation.

(2) Autler-Townes Splitting. In the recently proposed Autler-Townes-Splitting (ATS) protocol [363–366], a control field propagates with the signal field at zero delay ($\Delta\tau^{\mathrm{ctrl}} = 0$) with pulse area $\theta = 2\pi$, creating an Autler-Townes doublet in the signal field absorption profile that matches the signal field bandwidth. As shown in Ref. [364], one is free to choose any control-field shape, as long as $\theta = 2\pi$ is fulfilled over the duration of the signal field. As more broadband signal fields experience lesser effective optical depth (due to increasing Autler-Townes splitting), and more narrowband pulses lead to decoherence of the atomic polarization during the storage operation, the ATS protocol is constrained to optimal operation in a narrow bandwidth region around a unique choice of τ_{FWHM} for a given optical depth [363, 364] (see Appendix B).

(3) Electromagnetically Induced Transparency. The well-known Electromagnetically Induced Transparency (EIT) protocol is described in the narrowband regime in Refs. [341, 370–372], and in the broadband regime in Refs. [338, 364]. A control field of duration longer than the signal field ($\tau^{\mathrm{ctrl}}_{\mathrm{FWHM}} > \tau_{\mathrm{FWHM}}$) enters the medium ahead of the signal field in time ($\Delta\tau^{\mathrm{ctrl}} < 0$) and opens a spectral transparency window that is slowly closed after the signal field enters the medium, thereby trapping the signal field in the medium via the slow-light effect.

We note that the key physical features of all three protocols are compatible with the use of Gaussian-shape control fields, which helps to explain why Gaussian-shape fields are sufficient to achieve the high storage efficiencies of Sec. 3.3 and 3.4.

Supplemental B: Derivation of the ATS Region

As stated in Appendix A, at fixed optical depth the ATS protocol is constrained to optimal operation in a narrow region around a unique value of τ_{FWHM} [363, 364]. In this appendix we derive an approximation of this region, for the memory parameters investigated in the text, given by $d\tau_{\mathrm{FWHM}}\gamma = 3$ to 8. Notably, this approximation is dependent on the region of $\mathcal{M}$ chosen, and is not strictly valid for other regions, such as those in Refs. [363–365].

Nominally the ATS protocol requires pulse areas $\theta = 2\pi$ for optimal operation, however, as stated in Ref. [363], this constraint is relaxed in regions of non-optimal effective optical depth $\tilde{d} < 3$, where $\tilde{d} = d\tau_{\mathrm{FWHM}}\gamma\,\pi/(2\theta\ln 2)$ for Gaussian pulses. If the effective optical depth is small—as is frequently the case in the broadband regime considered here—pulses with area $\theta < 2\pi$ yield larger memory efficiency than $\theta = 2\pi$, due to a reduction in Autler-Townes splitting and an increase in the effective optical depth.

In order to accurately capture the ATS region of $\mathcal{M}$ discussed in Section 3.3.1, we do not rely solely on the region of high-efficiency operation with $\theta = 2\pi$ control fields. Instead, we follow a reduced version of

the optimization procedure presented in the main text, wherein we fix $\Delta\tau^{\text{ctrl}} = 0$ and $\tau^{\text{ctrl}}_{\text{FWHM}} = \tau_{\text{FWHM}}$ and optimize over θ. The efficiencies resulting from this optimization procedure, compared to the efficiencies for $\theta = 2\pi$ only, are presented in Fig. 3.5(a)-(b). For purposes of comparison, we plot the boundary of $\eta/\eta_{\text{opt}} = 98\%$ operation, which is increased upon optimization of θ. The optimized pulse areas corresponding to Fig. 3.5(b) are shown in Fig. 3.5(c). The region of $\theta \approx 2\pi$ operation which results in high normalized efficiency is well-captured by the condition $d\tau_{\text{FWHM}}\gamma = 3$ to 8 in this region of $\mathcal{M}$, and accordingly we take this condition to be representative of ATS operation for the memory parameters under consideration.

We note that for extremely low optical depths, $d \sim 1$, the region of high-efficiency ATS operation diverges from the $d\tau_{\text{FWHM}}\gamma = 3$ to 8 condition towards smaller adiabaticity. Other conditions may be used to define the ATS region, for example based on optimal delay (e.g., $\Delta\tau^{\text{ctrl}} = -0.25$ to 0.25) or the character ratio discussed in Appendix 3.5 (e.g., $\tilde{C} = 0.75$ to 1.25), that better capture this region of ATS operation. However, the region given by $d\tau_{\text{FWHM}}\gamma = 3$ to 8 is the largest of these and is consistent with Refs. [363–365].

Supplemental C: Derivation of the EIT Region

We define the boundary of the EIT region via the character ratio

$$C = \frac{1}{\tau_s} \frac{\int_{-\tau_s/2}^{\tau_s/2} d\tau \int_0^1 dz \, |P(z,\tau)|^2}{\int_0^1 dz \, |B(z, \tau \to \infty)|^2} \tag{3.8}$$

introduced in Ref. [364], which gives the ratio of the transient population that enters $P(z,\tau)$ during the storage period $\tau_s = 2.25\tau_{\text{FWHM}}$ to the population that arrives in $B(z,\tau)$ after the storage operation is completed. We consider the normalized character ratio $\tilde{C} = C/C_0$ using the value of C for each optical depth that corresponds to 'pure' ATS operation with $\Delta\tau^{\text{ctrl}} = 0$, which we identify as C_0. Using this normalization, we consider the region of $\mathcal{M}$ where $\tilde{C} \leq 0.1$ to correspond to EIT operation, delineated with dashed lines in Fig. 5.2(c) [364]. In this region, Fig. 5.2(d)-(f) shows the optimal control fields have larger pulse area than in the 'absorb-then-transfer' or ATS regions, the control fields are broader in duration than the accompanying signal field, and the control fields arrive before the signal field. This behavior is a signature of EIT storage, and supports the choice of $\tilde{C} \leq 0.1$ as the threshold for EIT behavior.

Chapter 4

Variance-based sensitivity analysis of Λ-type quantum memory

This chapter builds on the numerical tools developed in the previous chapter. This time, we are focused on the task of numerically estimating the sensitivity of atomic-ensemble-based photonic quantum memories to environmental perturbations. The content of this chapter was published in Ref. [52], and is reproduced here with only minor formatting changes.[1]

4.1 Introduction

In the emerging field of quantum technology, photons play a critical role as carriers of quantum information [301, 336, 384] and as the fundamental qubits for quantum computation and information processing [337, 385]. Photons are, however, difficult to synchronize [334, 335, 386] and are subject to losses in transmission [336, 387–389]. The ability to store and retrieve photonic quantum states on demand—quantum memory—provides a path forward to overcome these challenges, and is therefore a critical enabling technology for future quantum applications [314, 372, 390]. A considerable body of work has been dedicated to quantum memories based on atomic ensembles, where the three-level, resonant, Λ-type atomic system is the most common [314, 363, 367, 368, 370, 372, 390–396].

In the ideal case, an optical quantum memory is capable of storing single-photon quantum states and retrieving them on demand with high efficiency, high fidelity, long storage time, and broad bandwidth [314, 372, 390]. Another critical indicator of quantum memory performance, however—which has largely been neglected until only recently [397, 398]—is a memory's sensitivity to experimental fluctuations and drift. Fluctuations and drift in experimental parameters are invariably present in physical quantum memory implementations, and a memory which is more robust (less sensitive) to experimental noise is more useful for real-world quantum applications. Here we quantitatively address this aspect of Λ-type quantum memory. (For an analysis of other types of memories, we refer the reader to Refs. [397, 398].) We provide a variance-based sensitivity analysis [399–406], which sheds light on not only the sensitivity of an individual quantum memory

[1] Previously published material appears in this section. Bibliographic information for this material is as follows: K. Shinbrough and V. O. Lorenz, "Variance-based sensitivity analysis of Λ-type quantum memory," Phys. Rev. A **107**, 033703 (2022). The copyright owner, the American Physical Society, has provided permission to reprint. I gratefully acknowledge the coauthors listed above for their contributions to the text.

implementation with device-specific fluctuations and drift, but also on the intrinsic sensitivity of different physical Λ-type quantum memory protocols.

We consider quantum memory implementations with memory parameters $\mathcal{M} = (d, \tau_{\mathrm{FWHM}}\gamma)$, where the optical depth d of the atomic ensemble and the intermediate state coherence decay rate γ, scaled by the signal photon duration τ_{FWHM}, are considered to be intrinsic and fixed properties of the memory. We then group the remaining extrinsic, more readily tunable parameters as $\mathcal{G}$, which parameterize the optical control field used in the memory interaction, and which we assume have been optimized in order to maximize memory efficiency. We further partition our analysis according to whether the parameters of the control field define a Gaussian temporal envelope $\mathcal{G}_G = (\theta, \Delta\tau^{\mathrm{ctrl}}, \tau^{\mathrm{ctrl}}_{\mathrm{FWHM}})$ or an arbitrary temporal shape $\mathcal{G}_s = (\xi_1, ..., \xi_N)$, as investigated in Ref. [407] (see Figure 4.1), where θ, $\Delta\tau^{\mathrm{ctrl}}$, and $\tau^{\mathrm{ctrl}}_{\mathrm{FWHM}}$ correspond to the Gaussian control field pulse area, delay relative to the signal field, and duration, respectively, and the points ξ_i, $i = 1, ..., N$ correspond to interpolation points along the temporal envelope of the control field. Details on the numerical calculation of memory efficiency given $\mathcal{M}$ and $\mathcal{G}$ can be found in Ref. [407].

In this work we assume a typical scenario for experimental atomic-ensemble quantum memory, wherein the memory parameters are fixed with minimal long-timescale drift at a given setpoint but may undergo non-negligible shot-to-shot fluctuations. This situation occurs frequently in transient processes for generating dense atomic ensembles, such as in light-induced atomic desorption (LIAD) [408, 409] or laser ablation, but applies to equilibrium systems as well. We assume the optical parameters of the control field possess smaller shot-to-shot fluctuations (e.g., laser fields with locked frequency, power, timing, etc.), but may either drift over time or may not be set precisely for optimal memory performance. We investigate the sensitivity of the memory performance to the setting of these control parameters, including analysis of correlations that exist between parameters, which may allow, for example, for compensating a drop in efficiency due to non-optimal setting of one parameter by modification of the remaining parameters. This latter analysis may be important in situations where one parameter is constrained experimentally, for example in the case of limited laser power, which can often limit memory efficiency [313, 353–356, 359, 361, 362]. This type of memory sensitivity can be interpreted as an indicator of the region of control field phase space where acceptable memory performance can be achieved; low sensitivity implies a large acceptable region of control field phase space, where the control field does not require careful fine-tuning, and where restrictions on one parameter may be compensated for with changes to the remaining parameters. Equivalently, this type of memory sensitivity can be interpreted in terms of the memory's robustness to experimental drift, where low sensitivity implies that, given optimal initial control field settings, the memory will be robust to long-timescale drift in the phase space surrounding the optimal setpoint.

In the following sections, we restrict our discussion to resonant Λ-type memory protocols, but the tools developed in this work are readily applicable to off-resonant protocols, as well as other level systems and a wide range of related techniques [383, 410, 411]. In Section 4.2, we provide definitions for several quantitative aspects of memory sensitivity. In Section 4.3 we use these criteria to analyze the sensitivity of resonant Λ-type quantum memory to fluctuations in memory parameters, and in Section 4.4 we address sensitivity to improper setting of control field parameters or experimental drift.

4.2 Variance-Based Sensitivity Analysis

The sensitivity of classical systems is a much-discussed subject with well-established theoretical and numerical tools [399–406, 412]. In general, the task is to determine the sensitivity of a system with performance criterion

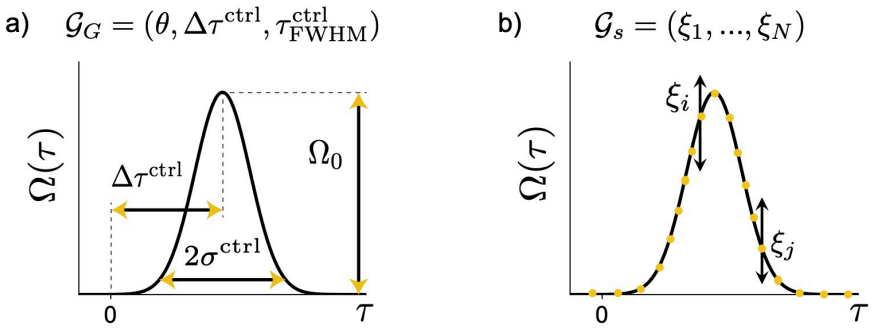

Figure 4.1: Control fields of (a) Gaussian shape, defined by the three parameters $\mathcal{G}_G = (\theta, \Delta\tau^{\rm ctrl}, \tau^{\rm ctrl}_{\rm FWHM})$, where $\Omega_0 = \theta/(2\sqrt{\pi}\sigma^{\rm ctrl})$ and $\sigma^{\rm ctrl} = 2\sqrt{2\ln 2}/\tau^{\rm ctrl}_{\rm FWHM}$, and (b) arbitrary shape, defined by the N interpolation points $\mathcal{G}_s = (\xi_1, ..., \xi_N)$.

$h(\mathcal{X}, \mathcal{A})$ to changes in N input parameters $\mathcal{X} = (x_1, ..., x_N)$ when internal system parameters $\mathcal{A}$ are kept fixed. This performance criterion may correspond to any desired single-valued metric of the system; in the case of quantum memory, this may correspond to memory efficiency, fidelity, storage time, etc. For the sake of brevity, in Sec. 4.3 and Sec. 4.4 we focus on memory efficiency as a key performance criterion, but importantly other criteria may be used and may be the subject of future work. In this section, we provide an outline of the theoretical tools used for a generic criterion h.

The most common method for determining the sensitivity of $h(\mathcal{X}, \mathcal{A})$ to fluctuations in the input parameters proceeds as follows [399, 406]. We define center values for the input parameters $\overline{\mathcal{X}}$, then draw many N-dimensional fluctuations ζ stochastically from a known probability distribution $P(\zeta)$, and average over these fluctuations in order to calculate the mean performance criterion

$$\overline{h}(\overline{\mathcal{X}}) = \int d\zeta\, h(\overline{\mathcal{X}} + \zeta, \mathcal{A}) P(\zeta) \tag{4.1}$$

and the variance in the system performance

$$V_h^{\rm fluc}\left(\overline{\mathcal{X}}\right) = V_\zeta[h(\overline{\mathcal{X}} + \zeta, \mathcal{A})|\mathcal{A}], \tag{4.2}$$

where $V_x[y(x,z)|z] = \int dx\, y^2(x,z)P(x) - [\int dx\, y(x,z)P(x)]^2$ is the unconditional variance of y obtained when x is allowed to vary and z is held constant. In the absence of a tailored noise model, the probability distribution for fluctuations is commonly approximated as an N-dimensional normal distribution $P(\zeta) \sim e^{-|\zeta|^2/(2\epsilon^2)}$ with standard deviation ϵ. In principle, the complete joint distribution $P(\zeta)$ must be measured experimentally in order to implement this form of sensitivity analysis. In practice, this is not always possible or efficient, and instead an estimate of the memory sensitivity can be calculated given only the measured expectation values and variances of each fluctuating experimental parameter. This amounts to approximating the joint distribution $P(\zeta)$ as a factorable distribution of the form $P(\zeta) = P_1(\zeta_1) \times P_2(\zeta_2) \times \ldots \times P_N(\zeta_N)$, where $P_i(\zeta_i) \sim e^{\zeta_i^2/(2\epsilon_i)}$, and each ϵ_i is the measured standard deviation of the ith experimental parameter. The resulting standard deviation in performance criterion h can then be calculated, $\sigma_h^{\rm fluc}(\overline{\mathcal{X}}) = \sqrt{V_h^{\rm fluc}(\overline{\mathcal{X}})}$.

The simple variance-based method above provides useful information on the response of the system to short-timescale, shot-to-shot fluctuations in input parameters around given central values $\overline{\mathcal{X}}$, which typically correspond to the setpoints of the input parameters. $\mathcal{X}$ can also correspond to control parameters, where the setpoint $\overline{\mathcal{X}}$ is assumed to be at or near the optimum values for system performance. The method above does

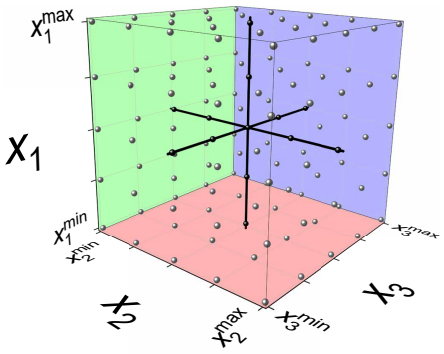

Figure 4.2: Example of 3-dimensional phase space spanned by parameters $\mathcal{X} = (x_1, x_2, x_3)$; the sample points connected by the black lines correspond to one-at-a-time (OAT) analysis of the system sensitivity, which explores only a small fraction of the total phase space.

not provide detailed information on the local environment around the performance optimum, which may be important for long-timescale drift or for determining which parameter is most sensitive to experimental error. The simplest method for determining a system's sensitivity to these long-timescale changes in input parameters $\mathcal{X} = (x_1, ..., x_N)$ is to vary each parameter one-at-a-time (OAT), and to measure the resulting variance in the system's performance. This OAT analysis corresponds to calculating the variances

$$V_i^{\mathrm{OAT}} = V_{x_i}[h(\mathcal{X})|x_{j\neq i}] \tag{4.3}$$

for each parameter x_i, where x_i varies over a finite range, $x_i \in [x_i^{\min}, x_i^{\max}]$. In Eq. (4.3) and in the following discussion, we have suppressed the internal parameters that are always held constant from the notation. We note that Eq. (4.3) is a special case of Eq. (4.2), where $P(\zeta) \sim 1$ and only one parameter x_i is subject to variation. Again, the standard deviation $\sigma_i^{\mathrm{OAT}} = \sqrt{V_i^{\mathrm{OAT}}}$ may be used to quantify the change in system performance due to parameter x_i. The parameter x_i with the largest σ_i^{OAT} has the largest effect on the performance criterion h and therefore the largest sensitivity. In practice, this means stabilizing and optimizing that parameter is the most important for system performance and should receive the largest dedication of resources.

The OAT analysis above provides cross-sectional information on the local environment around a performance optimum, and can be used to rapidly determine if one input parameter is responsible for the majority of observed variance in system performance. As correlations between input parameters arise and the dimensionality of $\mathcal{X}$ increases, however, OAT analysis rapidly becomes insufficient as it ignores control parameter correlations and explores only a small fraction of the input phase space (see Figure 4.2) [405, 406]. When correlations between parameters exist or the dimensionality of $\mathcal{X}$ is large, *global* variance-based sensitivity analysis is required, wherein the most prevalent sensitivity measure is the first-order Sobol' variance [402, 403, 412]

$$V_i = V_{x_i}\{E[h(\mathcal{X})|x_i]\}, \tag{4.4}$$

where the inner expectation value, $E[\cdot]$, corresponds to the mean of $h(\mathcal{X})$ when $\mathcal{X}$ is varied over all possible values in a finite range at fixed x_i. The outer variance then measures the variance of this mean with respect to changes in x_i. For a 3-dimensional parameter space, shown in Fig. 4.2, the variance V_1 in Eq. (4.4)

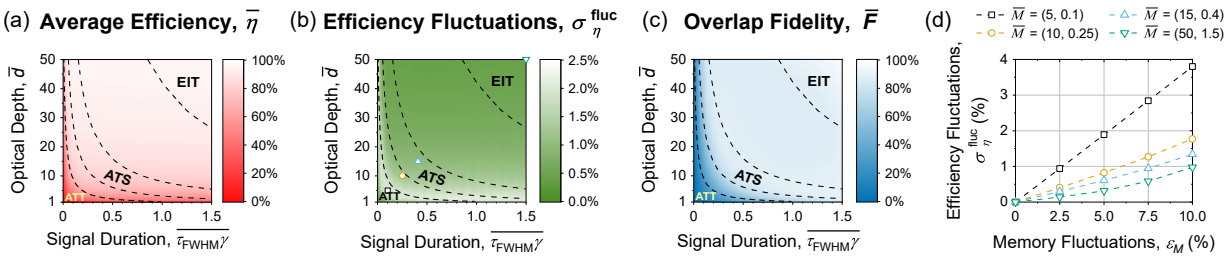

Figure 4.3: Sensitivity of Λ-type quantum memory to fluctuations $\epsilon_{\mathcal{M}}$ in memory parameters around the center points $\overline{\mathcal{M}} = (\overline{d}, \overline{\tau_{\text{FWHM}}\gamma})$. (a) Average efficiency $\overline{\eta}$ and (b) fluctuations in memory efficiency $\sigma_\eta^{\text{fluc}}$ in the presence of fluctuations $\epsilon_{\mathcal{M}} = 5\%$. (c) Average overlap fidelity $\overline{F}$ of optimal Gaussian control field parameters. (d) Fluctuations in memory efficiency as a function of increasing magnitude of fluctuations in memory parameters for selected points shown in (b). Regions for ATT, ATS, and EIT memory protocols are enclosed with dotted lines.

corresponds to calculating the expectation value $E[h(\mathcal{X})|x_1]$ over each red plane where x_1 is fixed and x_2 and x_3 are allowed to vary, and taking the variance of these expectation values. Similarly, V_2 (V_3) corresponds to calculating the variance of expectation values taken over the green (blue) planes. This method fully explores the parameter phase space in Fig. 4.2, whereas OAT analysis only explores the small region of parameter space connected by the black lines. The first-order Sobol' sensitivity index can be calculated as

$$S_i = V_i / V_{\text{tot}}, \tag{4.5}$$

where V_{tot} is the total variance $V_{\mathcal{X}}[h(\mathcal{X})]$ observed over the range of interest. Importantly, this technique also allows for the calculation of higher-order variances and sensitivities:

$$V_{ij} = V_{x_i,x_j}\{E[\eta(\mathcal{X})|x_i, x_j]\} - V_i - V_j, \tag{4.6}$$

$$S_{ij} = V_{ij} / V_{\text{tot}}, \tag{4.7}$$

which are related with Eqs. (4.4) and (4.5) by the conditions

$$V_{\text{tot}} = \sum_i V_i + \sum_i \sum_{j>i} V_{ij} + ... + V_{1...N}, \tag{4.8}$$

$$S_{\text{tot}} = \sum_i S_i + \sum_i \sum_{j>i} S_{ij} + ... + S_{1...N} = 1, \tag{4.9}$$

and which probe correlations between parameters. In 3 dimensions, these higher order variances correspond to the variance of expectation values evaluated along lines in the phase space of Fig. 4.2, instead of planes.

Sobol' variances and sensitivity indices provide a complete picture of the system performance landscape around a central point of input parameters, and allow for identification of which input parameters are most sensitive globally. This analysis also probes whether correlations exist between parameters, which can be leveraged to allow for acceptable system performance at non-optimal parameter values.

4.3 Fluctuations in Resonant Λ-type Quantum Memory

We now apply the general discussion in Sec. 4.2 to the case of resonant, Λ-type quantum memory, beginning with the effect of fluctuating memory parameters on memory efficiency. In the resonant case, there exist three well-known quantum memory protocols: the electromagnetically induced transparency (EIT) [341, 370, 371, 413], Autler-Townes Splitting (ATS) [363–366], and absorb-then-transfer (ATT) [341, 367–369, 407] protocols. A summary of these protocols is given in Ref. [407]; here we provide only the physical information necessary to understand this article: The EIT protocol requires a control field of duration longer than the signal field ($\tau_{\mathrm{FWHM}}^{\mathrm{ctrl}} > \tau_{\mathrm{FWHM}}$), which enters the medium ahead of the signal ($\Delta\tau^{\mathrm{ctrl}} < 0$), opening and slowly closing a transparency window that the signal propagates through. The signal field is thereby trapped via the slow-light effect. The ATS protocol requires a control field that propagates along with the signal field ($\Delta\tau^{\mathrm{ctrl}} = 0$) and possesses pulse area $\theta = 2\pi$. This control field creates an Autler-Townes doublet that matches the signal field bandwidth and transfers it to the long-lived spin state. The ATT protocol has the opposite pulse sequence to EIT, where the necessary control field is shorter than the signal field ($\tau_{\mathrm{FWHM}}^{\mathrm{ctrl}} > \tau_{\mathrm{FWHM}}$) and arrives after it ($\Delta\tau^{\mathrm{ctrl}} > 0$) with $\theta = \pi$ pulse area. This sequence affects linear absorption of the signal field and subsequent transfer of the atomic polarization into the spin-wave state.

Memory efficiency describes the efficiency with which a quantum memory stores and retrieves single-photon-level quantum states. Here, we consider the case where fluctuations in memory efficiency are dominated by fluctuations in the input parameters $\mathcal{M}$, and we assume the control field parameters $\mathcal{G}$ are kept fixed at the optimum values for the average memory parameters $\bar{\mathcal{M}}$ (i.e., the memory parameter setpoints). We assume a generic noise model where fluctuations $\zeta_{\mathcal{M}} = (\zeta_d, \zeta_g)$ are drawn stochastically from the probability distribution $P(\zeta) \sim e^{-(\zeta_d^2 g^2 + \zeta_g^2 d^2)/[2(\epsilon_{\mathcal{M}} dg)^2]}$ using the Mersenne Twister algorithm with seed 0, where $g = \tau_{\mathrm{FWHM}}\gamma$. This implies that, e.g., for $\epsilon_{\mathcal{M}} = 5\%$, both memory parameters vary by 5% of their respective setpoints. We further correlate optical depth and linewidth so as to preserve atom number. We calculate both $\overline{\eta}(\bar{\mathcal{M}})$ and $\sigma_\eta^{\mathrm{fluc}}(\bar{\mathcal{M}})$ following the prescription of Eqs. (4.1) and (4.2), assuming the optimal Gaussian control field values $\mathcal{G}_G(\bar{\mathcal{M}})$ found in Ref. [407]. For each center value $\bar{\mathcal{M}}$ we average over 1000 random fluctuations $\zeta_{\mathcal{M}}$. Physically, the average memory efficiency $\overline{\eta}$ represents the average efficiency of storage and retrieval from the memory in the presence of fluctuations in the memory parameters. One expects that in the presence of fluctuations, the memory efficiency should be, on average, lesser than without fluctuations. Through the procedure described in Sec. 4.2, we can calculate this average memory efficiency. In addition, by keeping track of the shot-to-shot memory efficiencies, we can also calculate the fluctuations in memory efficiency resulting from fluctuations in the memory parameters. In general, a quantum memory with lesser efficiency fluctuations is preferable to a memory with greater efficiency fluctuations, as is a memory with higher average efficiency to a memory with lower average efficiency.

The results of this analysis are shown in Fig. 4.3(a) and (b) for $\epsilon_{\mathcal{M}} = 5\%$, where we have labeled the respective regions of memory parameter space for optimal ATT, ATS, and EIT quantum memory protocols using the same procedure outlined in Ref. [407]. The regions above and below the dotted lines in Fig. 4.3(a)-(c) enclosing each protocol name represent the regions of memory parameter space where each protocol has the highest efficiency. Any protocol may in principle be implemented at any point in memory parameter space, but high-efficiency operation is only possible for each protocol within the bounded region. We find that the largest fluctuations in memory efficiency occur in the region of memory parameter space below the ATS regime, in the ATT regime. The ATS protocol is much less sensitive to memory parameter fluctuations, as $\sigma_\eta^{\mathrm{fluc}}$ is reduced by approximately a factor of 2, but in turn the EIT protocol is approximately a factor of 2

less sensitive to these fluctuations than the ATS protocol.

To explain this behavior physically, we consider the changes in optimized control field parameters $\mathcal{G}_G$ as a function of $\mathcal{M}$. As shown in Ref. [407], the gradient of $\mathcal{G}_G$ with respect to changes in $\mathcal{M}$ is largest in the non-adiabatic ($d\tau_{\mathrm{FWHM}}\gamma \lesssim 1$) regime and becomes smaller as the memory adiabaticity increases. This implies that, if the memory protocol is non-adiabatic, the optimal parameters $\mathcal{G}_G$ change significantly even for small changes in $\mathcal{M}$ and thus these small changes may cause comparatively large changes in memory efficiency compared to the adiabatic regime. This intuition can be evaluated quantitatively by considering the average overlap fidelity of $\mathcal{G} = \mathcal{G}_G(\mathcal{M})$ and $\mathcal{G}' = \mathcal{G}_G(\mathcal{M}')$ at different memory parameters $\mathcal{M}' = \mathcal{M} + m$:

$$\overline{F}(\mathcal{M}) = \frac{1}{A}\int_0^R dm^2\, F(\mathcal{G}, \mathcal{G}'), \tag{4.10}$$

where m varies over a 2D region with radius R and area A, and the overlap fidelity between any two points is

$$F(\mathcal{G}, \mathcal{G}') = \frac{\left|\int_{-\infty}^{\infty} d\tau\, \Omega^*(\mathcal{G})\Omega(\mathcal{G}')\right|^2}{\int_{-\infty}^{\infty} d\tau\, |\Omega(\mathcal{G})|^2 \int_{-\infty}^{\infty} d\tau\, |\Omega(\mathcal{G}')|^2}. \tag{4.11}$$

The control field $\Omega(\mathcal{G})$ is a Gaussian function with area θ, duration $\tau_{\mathrm{FWHM}}^{\mathrm{ctrl}}$, and timing $\Delta\tau^{\mathrm{ctrl}}$. Physically, this overlap fidelity defines how similar a given optimal control field is to the optimal control fields at neighboring points in $\mathcal{M}$. The average overlap fidelity in Eq. (4.10) is shown in Fig. 4.3(c), and confirms the intuition that the region of least overlap corresponds to the absorb-then-transfer protocol, where the memory parameters are most non-adiabatic. It is therefore this region that is most sensitive to fluctuations in $\mathcal{M}$ [as shown in Fig. 4.3(b)].

In addition to the relative sensitivity of the different memory protocols, the magnitude of memory efficiency fluctuations is of practical interest. In Fig. 4.3(d) we plot the dependence of efficiency fluctuations on memory parameter fluctuations for the four points shown in Fig. 4.3(b) spanning all three physical protocols. In each case, $\sigma_\eta^{\mathrm{fluc}}$ is roughly linear in $\epsilon_{\mathcal{M}}$, with proportionality constants $p = 0.38$, 0.13, and 0.09 in the absorb-then-transfer, ATS, and EIT regions, respectively. Insofar as fluctuations in memory parameters are not amplified in the resulting fluctuations in memory efficiency ($p < 1$), it can be said that all three protocols are 'stable.' although the EIT and ATS protocols are significantly more stable than the absorb-then-transfer protocol.

4.4 Drift and Improper Control Field Setting in Resonant Λ-type Quantum Memory

In this section we consider the sensitivity of Λ-type quantum memory to long-timescale drift in control field parameters $\mathcal{G}$ at fixed memory parameters $\mathcal{M}$. The following analysis equivalently provides an indicator of the region of control field phase space where acceptable memory performance is achievable. We perform this analysis on both control fields of Gaussian temporal envelope and control fields with arbitrarily shaped optimal temporal envelope. Analysis of Gaussian control fields is significantly less computationally expensive, and allows for one-at-a-time (OAT) and global sensitivity analysis, whereas it is only computationally feasible to perform OAT sensitivity analysis on arbitrarily shaped control fields.

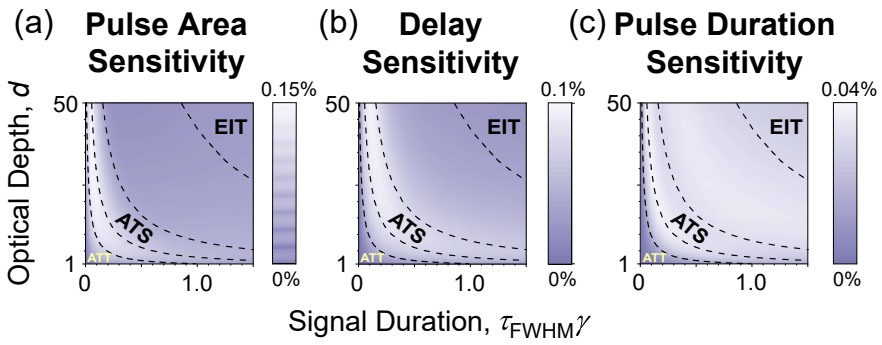

Figure 4.4: One-at-a-time sensitivity of Λ-type quantum memory to drift or improper setting of control field variables $\mathcal{G}_G$ of a Gaussian control field, as a function of memory parameters $\mathcal{M} = (d, \tau_{\mathrm{FWHM}}\gamma)$. Regions for ATT, ATS, and EIT memory protocols are enclosed with dotted lines.

4.4.1 One-at-a-time (OAT) Analysis

We first consider OAT variation of the control field parameters for a Gaussian optimized control field, $\mathcal{G}_G$, following the prescription of Eq. (4.3) and Sec. 4.2. We allow for drift or improper setting of the control field pulse area, delay (relative to the signal field), and pulse duration within $\epsilon_{\mathcal{G}} = 5\%$ of the optimal setpoints for any given memory parameters. These calculations are performed sequentially, which allows us to determine the sensitivity of a given memory (or memory protocol) to each control field parameter independently.

The results are shown in Fig. 4.4(a)-(c). By memory sensitivity, here we mean the standard deviation in memory efficiency due to OAT variation of each parameter, σ_i^{OAT}. In Fig. 4.4, we report this sensitivity as a percent, which represents the standard deviation in memory efficiency that results when each control field parameter is allowed to drift by $\epsilon_{\mathcal{G}}$. We find that sensitivity to drift or improper setting in pulse area [Fig. 4.4(a)] is largest in the region of $\mathcal{M}$-space below the ATS region. As the memory protocol in this region relies on exactly π-pulse control fields to transfer atomic population from the excited to storage state, this result agrees with physical intuition. By contrast, memory sensitivity to drift or improper setting of control field delay is largest in the ATS region [Fig. 4.4(b)]. The ATS protocol relies on signal and control fields that overlap in time in order to implement the requisite dynamically controlled Autler-Townes splitting [363], whereas the absorb-then-transfer and EIT protocols are relatively robust to improper control field delay setting. Again the ATS protocol, and the region of mixed ATS-EIT memory behavior, are most sensitive to variation in control field pulse duration [Fig. 4.4(c)], as changes to control pulse duration affect the dynamical Autler-Townes splitting and the effective pulse area of the control field overlapping with the signal field.

We also perform an OAT sensitivity analysis for arbitrarily shaped optimal control fields. For arbitrarily shaped control fields, given the large number of independent variables used to define the control field shape, computation of the shape sensitivity over a large range of optical depths and signal pulse durations is computationally intractable. Instead, we pick two pulse durations—$\tau_{\mathrm{FWHM}} = 1.5$ and $\tau_{\mathrm{FWHM}} = 0.01$—at an optical depth of $d = 50$, corresponding to adiabatic and non-adiabatic memory conditions, respectively. We parameterize each control field shape, $\Omega(\tau)$, in the temporal (τ) domain with 51 and 135 independent spline points spaced on a Chebyshev grid for $\tau_{\mathrm{FWHM}} = 1.5$ and $\tau_{\mathrm{FWHM}} = 0.01$, respectively. The set of these points, $\mathcal{G}_s$, is drawn schematically in Fig. 4.1(b). Each point along the optimal control field shape is allowed to vary by 5% of its optimal setpoint, as shown in Fig. 4.1(b), and the resulting variance and standard deviation in memory efficiency is recorded. The results of this OAT analysis are shown as a heat map in Fig. 4.5. For $\tau_{\mathrm{FWHM}} = 1.5$ [Fig. 4.5(a)], we find the falling edge of the typical EIT-like control field shape to

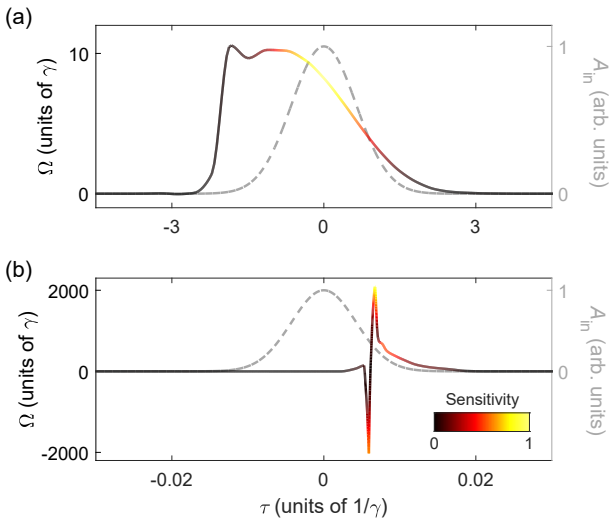

Figure 4.5: One-at-a-time sensitivity of Λ-type quantum memory to drift or improper setting of arbitrary optimized control field shapes $\Omega(\tau)$ in the temporal (τ) domain, described by the control field parameters $\mathcal{G}_s$, for optical depth $d = 50$ in the (a) adiabatic regime, where $\tau_{\mathrm{FWHM}}\gamma = 1.5$, and (b) non-adiabatic regime, where $\tau_{\mathrm{FWHM}}\gamma = 0.01$. The colormap along each $\Omega(\tau)$ shows the sensitivity of that region of the control field to drift. Grey dotted lines show the incident signal field, $A_{\mathrm{in}}(\tau)$.

be most sensitive to drift or improper setting, in agreement with Ref. [347]. Note that larger τ on the x-axis of Fig. 4.5 corresponds to later times in the co-moving frame. For $\tau_{\mathrm{FWHM}} = 0.01$, the optimal control field shape shows characteristic non-adiabatic ringing, and it is the points on the shape with the largest amplitude that show the largest sensitivity, likely due to the fact that changes in these points cause the greatest change in the control field pulse area, which must remain close to π in this regime. For both cases in Fig. 4.5, the input signal field temporal distribution, $A_{\mathrm{in}}(\tau)$, is shown for reference. The storage efficiencies for these two optimized pulse shapes are 95.2% and 58.7%, for $\tau_{\mathrm{FWHM}} = 1.5$ and $\tau_{\mathrm{FWHM}} = 0.01$.

4.4.2 Sobol' Analysis

The OAT analysis above provides rapid cross-sectional information on quantum memory performance around the optimal control field setpoints and ignores any correlations between control field parameters. Given the physical descriptions of the three resonant quantum memory protocols, we expect correlations between control field parameters in both the ATS and EIT regimes. In the ATS regime, quantum storage is accomplished with a 2π pulse-area control field which overlaps in time with the incident signal field; if, for example, the control field pulse duration is erroneously set to be too long, we expect that this error can be compensated for—with minimal effect on storage efficiency—with a larger pulse area, such that the net pulse area over the temporal extent of the signal field remains 2π. In the EIT regime, quantum storage is implemented with a control field that opens a transparency window at the signal wavelength and then slowly closes this transparency window as the signal field is compressed and propagates through the medium [see, e.g., Fig. 4.5(a)]. In the EIT case, we expect correlations between all three Gaussian control field parameters, as it is the slope of the falling edge of the control field which is most important. Errors or drift in control field delay, for example, may be compensated for with larger or smaller pulse area and pulse duration, depending on the sign of the change in delay. (If the change in delay is positive, i.e., the control field shifts closer to the signal field, a reduced pulse area and pulse duration will maintain the same slope of the control field as it closes the transparency window

around the signal field.) We expect no parameter correlations in the absorb-then-transfer regime, as this protocol relies on π pulse-area control fields that arrive after the signal field. Errors or drift in pulse area, for example, cannot be compensated for with changes to control field pulse duration or delay. Note that in the definition of control field pulse area, we account for a given pulse duration; therefore, changes to pulse duration in our model do not directly affect pulse area, and vice versa [407].

In order to probe these correlations, to determine the *global* sensitivity of each regime, and to determine which parameters to tune in order to compensate for drift in a given parameter, we use the first and higher-order Sobol' analysis described in Sec. 4.2. The results of this analysis are shown in Fig. 4.6. Importantly, Sobol' sensitivity analysis also allows for computing single-parameter sensitivities [Eqs. (4.4)-(4.5)], which are shown for Gaussian control field parameters (pulse area, delay, and pulse duration) in Fig. 4.6(a)-(c). Here, sensitivity is a dimensionless number as defined in Eq. (4.5), which physically represents what fraction of the observed variance in memory efficiency is due to each parameter. The results of this single-parameter sensitivity calculation largely agree with the OAT analysis of Sec. 4.4.1 and Fig. 4.4, but are in principle more reliable. The true advantage to this analysis however is in the two- and three-parameter sensitivities shown in Fig. 4.6(d)-(f) and Fig. 4.6(g), respectively, which physically represents what fraction of the observed variance in memory efficiency is due to correlations between parameters [Eq. (4.7)]. In Fig. 4.6(d), we calculate the second-order Sobol' sensitivity index for varying control field delay and pulse duration. We observe the largest sensitivity in the mixed ATS-EIT region, implying that these parameters are tightly correlated in this region of memory parameters. Fig. 4.6(e) shows significant correlations between pulse area and control field delay in the ATS regime, which we can interpret physically as follows: any drift or deviation in control field delay away from 0 in the ATS regime can be compensated for with a larger control field pulse area, such that the effective pulse area overlapping with the temporal extent of the signal field—which controls the dynamical Autler-Townes splitting—is still 2π. Fig. 4.6(f) shows a similar correlation between pulse duration and pulse area in the mixed ATT-ATS region, where presumably it is the effective pulse area overlapping with the signal field that is most important for high efficiency quantum storage. Fig. 4.6(f) also shows some correlation between control pulse duration and pulse area in the EIT regime. A similar behavior can be seen in the three-parameter sensitivities shown in Fig. 4.6(g), although the magnitude of the sensitivity index is smaller. We explain both of these correlations along the same lines discussed in Sec. 4.4.1 for Fig. 4.4(b)—that the physically important part of the control field in the EIT regime is the trailing edge that closes the transparency window around the signal field, and therefore any deviations in pulse area, delay, or duration can be compensated for with the remaining degrees of freedom to ensure that the slope of the falling edge of the control field remains close to the same. The comparison between Fig. 4.6(f) and (g) show however that EIT control pulse duration and pulse area are more tightly correlated than all three parameters together. This means that if there is drift in control field pulse area in the EIT regime, for example, most of the corresponding change in memory efficiency can be compensated for by tuning the the control pulse duration (and vice versa).

The Sobol' analysis performed here reveals which parameters are correlated, and therefore which parameters to adjust when one is non-optimal and constrained, but it does not reveal the direction in which to adjust the remaining parameters. If more detailed, directional information is required, partial derivatives of the memory efficiency with respect to each remaining parameter can be calculated numerically. Nevertheless, the information revealed by the Sobol' analysis is sufficient to develop the physical intuition described above, and, in practice, knowing which parameter to adjust out of many is often useful.

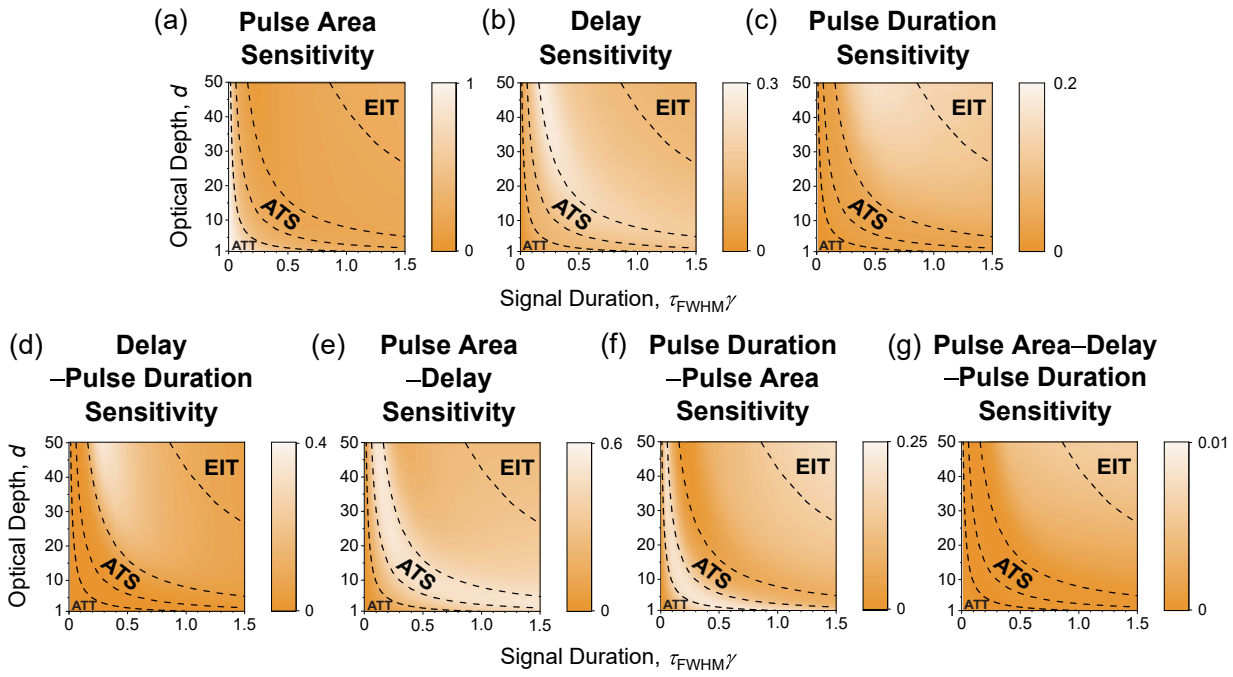

Figure 4.6: Sobol' sensitivity indices for Λ-type quantum memory subject to drift or improper setting of control field variables $\mathcal{G}_G$ of a Gaussian control field, as a function of memory parameters $\mathcal{M} = (d, \tau_{\mathrm{FWHM}}\gamma)$. Regions for ATT, ATS, and EIT memory protocols are enclosed with dotted lines.

4.5 Conclusion

In this work we have presented a general framework for evaluating the sensitivity of Λ-type optical quantum memory to fluctuations and drift (or improper setting) of memory and control field parameters. We have applied this framework for the case of non-negligible memory parameter fluctuations, where we have found that the region of memory parameter space corresponding to the absorb-then-transfer protocol is most sensitive, yet for all memory parameters, Λ-type optical quantum memory is stable insofar as the resulting fluctuations in memory efficiency are always smaller than the magnitude of the fluctuations in memory parameters. Further we have considered the case of drift or improper setting of control field parameters in both the case of Gaussian control fields and arbitrarily shaped control fields. The collapse of the N-dimensional parameter space in the case of full arbitrary shape-based optimization to just 3 physically instructive dimensions in the Gaussian case allows for a physical interpretation of memory sensitivity, as well as a more sophisticated Sobol' analysis of correlations between control field parameters.

The theoretical predictions of this work serve to instruct future and ongoing experiments on optical quantum memory. If average memory efficiency or efficiency fluctuations are of import to an application of quantum memory, Sec. III demonstrates that the EIT protocol is the most robust and provides the smallest efficiency fluctuations out of the three resonant Λ-type memory protocols, and should therefore be used in experiments where fluctuations are important. If instead drift or improper setting of control field parameters is a concern for experimental implementations of Λ-type quantum memory, Sec. 4.4 provides an example for how to calculate these effects on experimental quantum memories. Furthermore, Sec. 4.4 provides information on which parameters are most important to optimize when one control field parameter is constrained or drifts, as is frequently the case in experiment (e.g., constrained or drifting control field power). This information

can serve as a practical guide for making experimental quantum memory more robust to both fluctuations and drift.

To determine which analysis is most relevant for a given quantum memory experiment, the experimentalist must measure or estimate the fluctuations in memory parameters, $\epsilon_{\mathcal{M}}$, and drift in control field parameters, $\epsilon_{\mathcal{G}}$, to determine which contribution dominates. If $\epsilon_{\mathcal{G}}$ is dominant, the experimentalist must then determine if a single control field parameter is drifting, in which case the one-at-a-time (OAT) analysis of Sec. 4.4.1 is sufficient, or if all control field parameters are drifting by close to the same fractional amount, in which case the Sobol' analysis of Sec. 4.4.2 is necessary. If $\epsilon_{\mathcal{M}}$ and $\epsilon_{\mathcal{G}}$ are of similar magnitude, both analyses may be necessary to accurately estimate the memory sensitivity and resulting fluctuations and drift of the memory efficiency.

We note that many alternative calculations to those presented here are also possible. For example, if shot-to-shot fluctuations exist in the control field parameters instead of the memory parameters, the same analysis of Sec. 4.3 may be applied, substituting $\mathcal{G}$ for $\mathcal{M}$. Variations in two-photon or single-photon detuning as well as chirp in the optical fields can also be implemented in a straightforward fashion using the general framework developed in Sec. 4.2. Additionally, the present discussion of sensitivity focuses only on sensitivity with respect to changes in memory efficiency; in principle, other types of sensitivity are possible beyond this 'efficiency sensitivity.' Caution must be observed when applying the framework of Sec. 4.2 to other parameters, however, as experimental considerations beyond those discussed here may come into play. For example, 'fidelity sensitivity' is another possible sensitivity of interest; in this case, however, our analysis can only calculate an upper bound on memory fidelity (or a lower bound on fidelity sensitivity) in the presence of experimental fluctuations and drift.

Acknowledgements

We gratefully acknowledge helpful discussion provided by Yujie Zhang, Kathleen Oolman, Dongbeom Kim, Donny Pearson, and Elizabeth Goldschmidt; support from NSF Grants No. 1640968, No. 1806572, No. 1839177, No. 1936321, and No. 2207822; and support from NSF Award DMR1747426. This work made use of the Illinois Campus Cluster, a computing resource that is operated by the Illinois Campus Cluster Program (ICCP) in conjunction with the National Center for Supercomputing Applications (NCSA) and which is supported by funds from the University of Illinois Urbana-Champaign.

Chapter 5

High-efficiency, broadband, and low-noise photonic quantum memory in barium vapor

With the numerical footing established in Chapters 3 and 4, we now move on to our experimental implementation of high-efficiency, ultra-broadband, and low-noise quantum memory operation in neutral barium vapor. The content of this chapter appears in the preprint Ref. [414], and is reproduced here with only minor formatting changes.[1]

Single photons are excellent carriers of quantum information, and in recent years several important photonic quantum information processing (QIP) tasks have been demonstrated experimentally [415–418]. The principle challenges to implementing more complex, large-scale photonic QIP tasks are high-quality deterministic single photon generation, high-fidelity two-qubit gates, and low-loss photon synchronization. Photonic quantum memory—the elementary operation of converting single photons into stationary qubits and releasing them on demand—provides a path to overcome these challenges [20, 53, 133]. However, high-efficiency, high-fidelity photonic quantum memory in atomic ensembles, the dominant technological approach, has hitherto been limited to bandwidths on the order of single gigahertz [419–421], whereas the bandwidth of high-quality single photon sources tend to be on the order of terahertz [41–43, 422, 423]. Here we propose and demonstrate experimentally a technique to bridge this bandwidth gap, increasing the speed of atomic-ensemble memories by almost three orders of magnitude. This technique relies on controllable collisional dephasing in a warm atomic barium vapor, and results in >95% storage efficiency (>26% total efficiency) and 99.94% noise-limited fidelity for 0.9 THz bandwidth photons. The ultra-broad bandwidth compatibility demonstrated in this work opens the door for high-speed photonic quantum information processing, and contributes to the development of practical quantum memories for use in quantum computation, communication, and networking.[19, 29, 40]

In this work, we identify that the difficulty in creating high-efficiency, broadband atomic-ensemble-based photonic quantum memories stems from the mismatch between broad photon bandwidths and narrow homogeneous atomic linewidths. We demonstrate a generic and scalable approach to overcome this problem,

[1] Preprint material appears in this section. Bibliographic information for this material is as follows: K. Shinbrough, T. Loveridge, B. D. Hunt, S. Park, K. Oolman, T. O. Reboli, J. G. Eden, V. O. Lorenz, "High-Efficiency, high-speed, and low-noise photonic quantum memory," arXiv:2309. 00969 (2023). No permissions are required by the preprint server for reuse. I gratefully acknowledge the coauthors listed above for their contributions to the text.

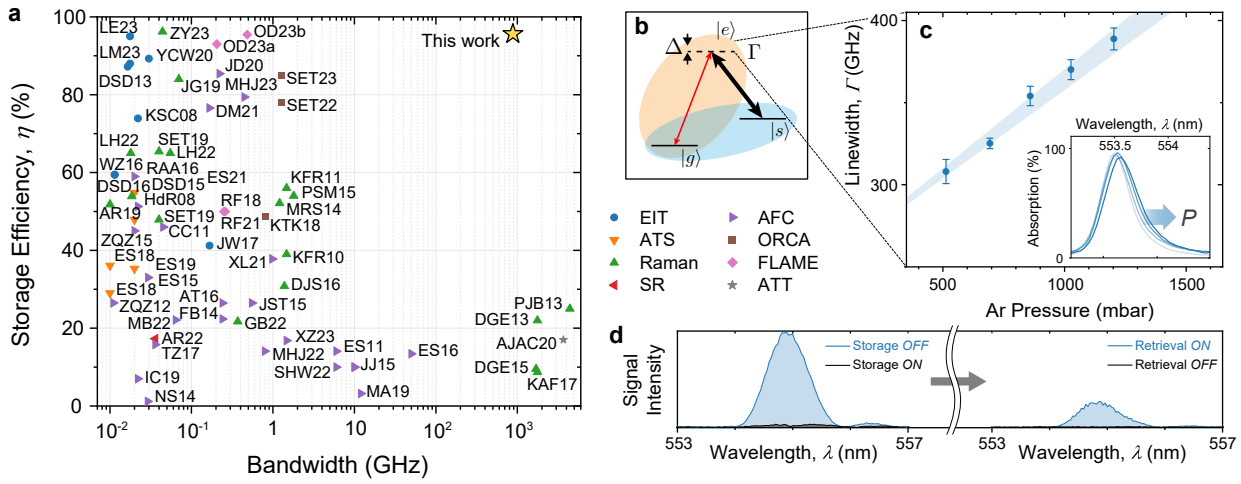

Figure 5.1: **Enhancement in memory bandwidth and efficiency due to collisional broadening. a**, Comparison of storage efficiencies and signal field bandwidths for atomic ensemble quantum memories in the broadband regime (> 10 MHz). References are specified by first author initials and publication year; for complete reference information see Supplementary Information. **b**, Atomic energy level structure for Λ-type quantum memory (Δ, detuning; Γ, excited state linewidth; thin red arrow, signal field; thick black arrow, control field). **c**, Measured collisionally broadened excited state linewidths for the $^1S_0 \rightarrow {}^1P_1$ ($|g\rangle \rightarrow |e\rangle$) transition in atomic barium as a function of argon (Ar) buffer gas pressure (inset: absorption spectra; bold arrow indicates the effect of increasing pressure, P, across the dataset). **d**, Spectral waveforms of the signal field before storage (light blue, left panel), after storage (dark grey, left panel), before retrieval (dark grey, right panel; at the noise floor), and after retrieval (light blue, right panel).

thereby enhancing the speed of atomic-vapor quantum memories by nearly three orders of magnitude relative to the state of the art. This demonstration is performed in a hitherto unused atomic species — neutral barium vapor — with a Λ-type internal level structure consisting of the $^1S_0$, $^1P_1$, and $^1D_2$ orbital levels. We present a comprehensive characterization of our system's performance in storing and retrieving weak coherent states with ≤ 1 average photon per pulse. This includes the measurement of memory efficiency, lifetime, noise level, and, for the first time, a complete reconstruction of the retrieved photon temporal amplitude and phase. Beyond the strong performance of the memory under these metrics, this characterization reveals a regime of operation for atomic ensemble memories we name Near-Off-Resonant Memory (NORM) operation, which leads to enhancements in total efficiency of around 5% in our system that we confirm via numerical simulation. Throughout, we highlight the unique advantages of our choice of atomic species, including the absence of four-wave mixing noise, the small collisional dephasing rate of the chosen storage state, and the telecom-compatibility of the excited–metastable transition.

5.1 Collisional broadening as a resource for speeding up ensemble memory

A limited set of resources have been identified for optimizing atomic-ensemble-based photonic quantum memories. For example, it is well known that the resonant optical depth of such memories, d, sets an upper bound on the maximum achievable storage efficiency of the form $\eta_{\text{opt}} \approx 1 - 2.9/d$ [66, 68, 118]. Optical depth, proportionate to atom number, is therefore a resource for increasing memory efficiency. Here we propose

another resource for atomic-ensemble quantum memories, this time for increasing memory bandwidth and speed: the intermediate-state homogeneous linewidth. This technique is in contrast to existing methods based on inhomogeneous broadening [169, 174, 424]. To illustrate this, we consider the memory protocol for which the value of this resource is most clear, the absorb-then-transfer (ATT) memory protocol, which has been explored in a variety of systems [31, 66, 141, 155–157]. In this protocol, shown schematically in Fig. 5.1b, resonant linear absorption maps a photonic qubit—the signal field—onto an atomic polarization of the form $P \sim \sum_{j=1}^{N} b_j e^{ik_s z_j} |g_1 \cdots e_i \cdots g_N\rangle$, where the sum runs over atoms 1 to N, each with a spatially dependent amplitude b_j and phase $k_s z_j$, where k_s is the k-vector of the signal field and z_j is the one-dimensional spatial position of the jth atom (orange shaded region in Fig. 5.1b). This collective Dicke state involving the ground state $|g\rangle$ and the excited state $|e\rangle$ is then mapped via a π-pulse optical control field onto a similar Dicke state with amplitudes c_j, $B \sim \sum_{j=1}^{N} c_j e^{i(k_s - k_c) z_j} |g_1 \cdots s_i \cdots g_N\rangle$, involving the storage state $|s\rangle$ and control field k-vector k_c, completing the quantum storage operation (blue shaded region in Fig. 5.1b). The protocol thus has two stages: resonant linear absorption, and π-pulse population transfer. The speed and efficiency of the second stage is ensured simply by accurate tuning of the control field timing and pulse area, but the speed of the first stage depends critically on both the resonant optical depth and the homogeneous linewidth of the $|g\rangle \rightarrow |e\rangle$ transition. A complete discussion of the dependence of linear absorption on these two memory parameters can be found in Ref. [31], but the fundamental physical intuition is clear: The transition linewidth sets an upper bound on the bandwidth of the signal field, as any significantly broader bandwidths possess frequency components that are not absorbed by the ensemble, and therefore contribute to memory inefficiency in the form of transmission loss. This loss can be compensated for by either decreasing the signal bandwidth (slowing down the memory), increasing the optical depth, or increasing the transition linewidth. For high-speed applications in which the first solution is not an option, increasing linewidth is significantly more effective than increasing optical depth [31]. A larger homogeneous linewidth is also a resource for the resonant protocols of electromagnetically induced transparency (EIT) and Autler-Townes Splitting (ATS), but whether a given memory is 'linewidth limited' or 'optical-depth limited' in general depends on the specific parameters of the signal field and the ensemble. Here we demonstrate experimentally a method to modify and control the homogeneous linewidth via collisional broadening with neutral rare-gas atomic perturbers, and, for the first time, harness this resource to increase the bandwidth of ensemble-based memory.

We summarize the key results of this demonstration in Fig. 5.1. Figure 5.1a presents a direct comparison of the storage efficiency and bandwidth achieved using our approach with the storage efficiencies and bandwidths achieved using existing techniques based on naturally broadened, Doppler-broadened, or inhomogeneously broadened three-level quantum memories. These existing techniques employ a variety of different storage protocols [colors, symbols in Fig. 5.1a], but in all cases the region of high-efficiency operation is limited to $\lesssim \mathcal{O}(1)$ GHz. In the ultra-broadband regime ($\sim$THz) investigated in this work, storage efficiencies have previously been limited to roughly 25% [92, 159–161]. We attribute the significant increase in storage efficiency demonstrated in this work to the use of a collisionally broadened linewidth [Fig. 5.1b-c], as described previously. Fig. 5.1c shows measured collisionally broadened linewidths in our system between 300 and 400 GHz, centered on the 553.5 nm ${}^1S_0 \rightarrow {}^1P_1$ ($|g\rangle \rightarrow |e\rangle$) transition in barium, that are linearly dependent upon argon (Ar) buffer gas pressure, as expected for collisional broadening. Fig. 5.1d shows the raw spectrally resolved storage and retrieval data for 0.9 THz photon bandwidth, from which we extract $95.6 \pm 0.3\%$ storage efficiency and $26 \pm 1\%$ total (end-to-end) efficiency near zero time delay. The uncertainty in these measurements is derived from Poissonian photon counting statistics. The total efficiency of our memory is limited by available control field power and can be improved significantly with improvements to the control

laser system. Our memory is also compatible with narrower signal field bandwidths (∼GHz), with suitable modifications to the control field. All experiments are performed in a home-built heat pipe oven vapor cell (described further in Methods). For quantum storage, we perform a modified version of the ATT protocol outlined above, where signal and control fields are both detuned $\Delta = 5\Gamma$ below resonance; this modification ensures less than 1% absorption of the signal field in the absence of the control field, such that when the control field is turned on, any increase in absorption is attributable to quantum storage.

5.2 Memory characterization and performance

In addition to the near-resonant storage and retrieval demonstrated in Fig. 5.1d, we characterize the performance of our ensemble as a photonic quantum memory with several experiments. First, we measure the dependence of the storage operation on control field pulse area. Shown in Fig. 5.2a, at 800 °C we observe a maximum in storage efficiency near π control field pulse area, as expected for the ATT protocol. At 900 °C, with higher optical depth and larger collisional broadening we are able to achieve larger control field pulse areas with the same total available control field power, and we observe an optimal control field pulse area of 1.25π. The experimental data in Fig. 5.2a are fit to a numerical model based on the Maxwell-Bloch equations (see Methods). The dashed horizontal lines represent the optimal bound on storage efficiency for a given temperature and independently measured optical depth (η_{opt}). We achieve near saturation of this bound after a half Rabi oscillation, confirming the coherence of the memory interaction, the applicability of the Maxwell-Bloch model, and the efficiency of our memory at high speeds.

Next, we turn to the coherence lifetime of our memory. In addition to collisional broadening of the intermediate excited state linewidth, the presence of noble gas perturbers also leads to collisional broadening of the metastable or storage state linewidth. As the linewidth of this state determines the coherence time of our memory, in principle a tradeoff exists between increasing memory efficiency and maintaining a long coherence time. In practice, due to an asymmetry in the relevant collisional cross-sections in barium, our memory is not limited by this tradeoff (see Methods). We measure the coherence lifetime of our memory as a function of argon buffer gas pressure, shown in Fig. 5.2b. The horizontal lines in Fig. 5.2b represent the limit to memory lifetime imposed by Doppler broadening at each temperature, due to the thermal motion of barium atoms, which decoheres the spatially varying phase of the atomic excitation. We observe qualitatively different behavior for the two vapor cell temperatures investigated in this work. At 800 °C, we observe a short memory lifetime at low argon pressure, which then increases to a maximum around 200 mbar before decaying according to an inverse model indicative of collisional broadening. At low pressures (<200 mbar), we believe the memory lifetime may be reduced due to the formation of a sub-ensemble of weakly bound barium-argon molecules [425–427], but further work is needed to investigate this effect. At 900 °C, we observe a memory lifetime that asymptotes to the Doppler limit at low pressure and that follows the expected collisional model for increasing argon pressure. We measured a maximum memory lifetime of 0.46 ± 0.05 ns. As the memory efficiency is unchanged for this range of argon pressures, we are able to achieve Doppler-limited memory lifetimes while still benefiting from the enhancement to memory efficiency due to collisional broadening. Importantly, the memory lifetimes demonstrated in this work are already a factor of ∼2 longer than previous ultra-broadband photonic quantum memories [92, 159–161], but in addition to this, the long radiative lifetime of the $^1D_2$ state in the bare atom (0.25 sec) [289] leaves significant room for improvement of our memory lifetime using recently developed dephasing-protection techniques [56].

We also measure the wavelength dependence of our memory. Keeping the signal and control fields in

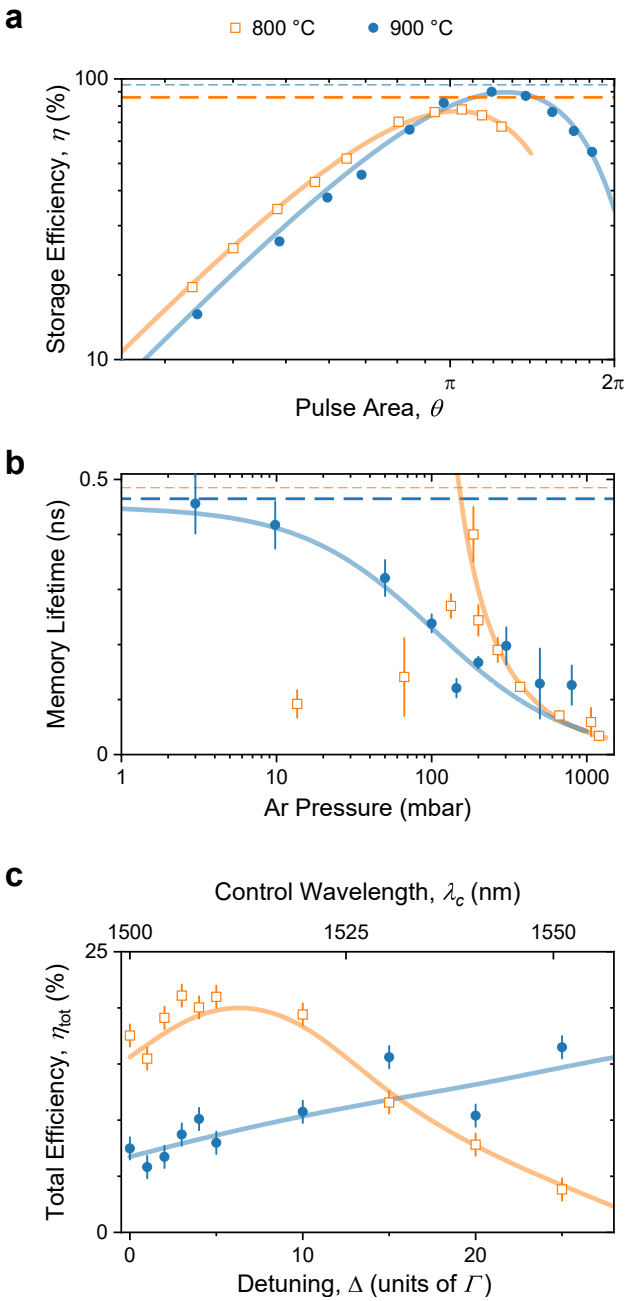

Figure 5.2: **Memory characterization and telecom compatibility. a**, Storage efficiency as a function of control field pulse area at 800 °C (orange squares) and 900 °C (blue circles). Horizontal lines represent the theoretical optimal bound on storage efficiency at each temperature (orange, dashed, 800 °C; blue, dotted, 900 °C). Statistical errors are smaller than the marker size. Solid curves are numerical fits based on the Maxwell-Bloch equations (see Methods). **b**, Memory lifetime as a function of argon (Ar) buffer gas pressure. Horizontal lines represent the limit on memory lifetime set by Doppler, or motional dephasing at each temperature (orange, dashed, 800 °C; blue, dotted, 900 °C). Error bars represent statistical error propagated through a decay model fit (see Methods). Solid curves are fits to an inverse function representing collisional broadening. **c**, Total (end-to-end) memory efficiency measured as a function of detuning, showing the behavior of near-off-resonant memory (NORM) operation. Error bars represent random uncertainty due to control field power variation. Solid curves: numerical fit to Maxwell-Bloch model (see Methods).

two-photon resonance, we vary the detuning, Δ, shown in Fig. 5.1b, and measure the total, end-to-end efficiency of our memory. At both temperatures we observe a maximum total efficiency at non-zero detuning, an effect we name Near-Off-Resonant Memory (NORM) operation (see Methods). This operation regime has been observed experimentally in previous work [53, 142], but we explore the effect theoretically for the first time, and offer an intuitive explanation in the Methods section. Our model fit is in good agreement with the data in Fig. 5.2c, where we observe an optimal detuning around $\Delta = 5\Gamma$ at 800 °C (190 mbar) and $\Delta \approx 25\Gamma$ at 900 °C (270 mbar). At 900 °C and 1550 nm control field wavelength, the total memory efficiency is 16 ± 1% (limited by available control field power), which highlights the telecom-compatibility of this memory; with optical pumping of the initial population into the storage state, we can implement storage and retrieval at 1550 nm signal field wavelength.

5.3 Single-photon-level retrieval with full amplitude and phase reconstruction

We now turn to the noise performance of our memory. Most Λ-type quantum memories are limited in noise performance by four-wave mixing (FWM) noise, wherein the control field coupling the storage and excited states also acts off-resonantly along the ground-to-excited state transition, generating spurious photons that overlap with the retrieved signal field. Several techniques have been developed to mitigate FWM noise in Λ-type quantum memories [150, 152, 428, 429], typically at the expense of additional optical fields, cavities, or more complex beam routing. By contrast, our barium Λ-type quantum memory is intrinsically FWM-noise-free. This is due to the 340 THz splitting of the ground and storage states being much larger than the excited-storage state splitting (200 THz) that defines the control field frequency. Thus the control field does not possess sufficient energy per photon to excite FWM noise. In Fig. 5.3a we show the measured signal-to-noise ratio (SNR) of our memory as a function of the average input photon number of a weak coherent state. The SNR is defined as the ratio of the average retrieved signal field photon number to the average noise photon number. We fit the SNR data to a linear function in order to extract a signal-to-noise ratio of $\mathrm{SNR} = 1.8(1) \times 10^3$ at an average of 1 input photon per pulse. This represents a retrieved single-photon fidelity of $\mathcal{F} = 1 - 1/(\mathrm{SNR} + 1) = 0.99944 \pm 0.00003$, which is the highest noise-limited fidelity of any Λ-type quantum memory to date [31]. We believe the noise performance of our memory to be limited by two-photon absorption of our control field followed by fluorescence from either a high-lying atomic orbital or the silica windows of our heat pipe oven, both of which result in noise near the dark count rate of our detectors.

The excellent noise performance of our memory combined with its ultra-broad bandwidth allows us to perform a novel fidelity characterization experiment. In Figs. 5.3b and 5.3c we show the predicted and reconstructed amplitude and phase of our output signal field. The predicted amplitude and phase is generated via integration of the Maxwell-Bloch equations with an input signal field obtained via the Fourier transform of our measured signal spectrum assuming a flat spectral phase (see Methods). The output field has two components, the field transmitted after the storage control field pulse, and the field retrieved via the retrieval pulse. The amplitude and phase in Fig. 5.3c are reconstructed from measured spectral interferograms between the output field and a known reference (see Methods). The agreement between the output field amplitude and phase in Figs. 5.3b and 5.3c is imperfect due to the limited stability and acquisition time of our interferometer, the assumption of a flat input phase, and the resolution of our spectrometer, but the agreement is sufficient to accurately extract linear and quadratic components of the retrieved signal field temporal phase, which are necessary for the spectral-temporal compression and shaping of the retrieved field required for some

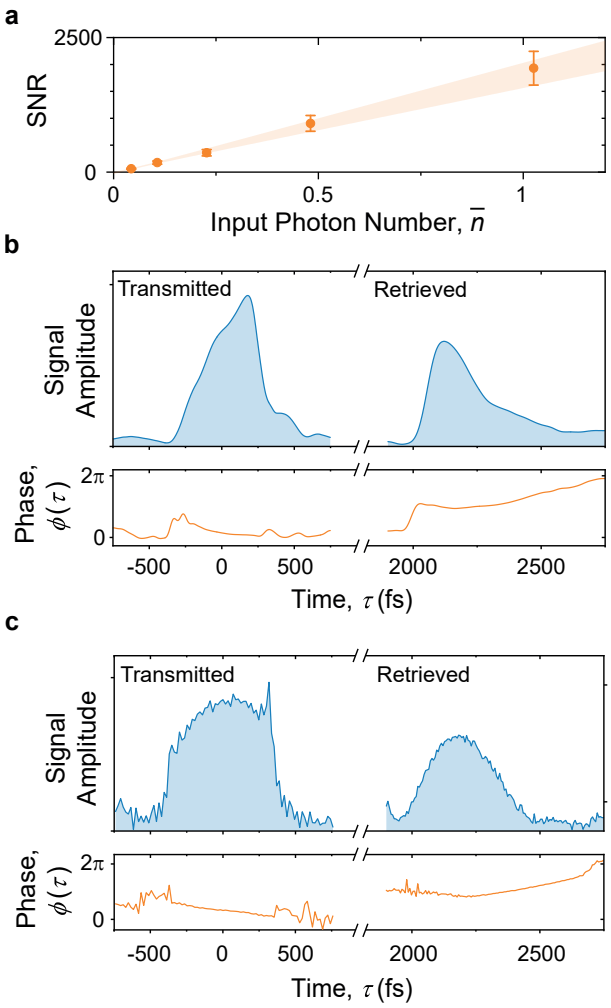

Figure 5.3: **Noise performance and full signal field amplitude and phase reconstruction.** **a**, Measured ratio of average retrieved photon number to average noise photon number (signal-to-noise ratio, SNR) **b**, Predicted amplitude (top panel) and phase (bottom panel) of photonic field after the memory, including transmitted (left) and retrieved (right) components. **c**, Experimental amplitude and phase of the photonic field after the memory, reconstructed from spectral interference with a known reference.

applications.

5.4 Discussion

In this work, we have demonstrated a novel and scalable approach to enhancing atomic-vapor quantum memory bandwidth and efficiency via tunable collisional broadening. This approach overcomes the trade-off between memory bandwidth and storage efficiency present in the literature, constituting a significant advance in photonic quantum memory performance. Our barium-based quantum memory exhibits simultaneously near optimal storage efficiency, a lifetime that is a factor of two longer than the state of the art, a telecom-wavelength control field, and the highest noise-limited fidelity of any Λ-type quantum memory to date. Our memory operates in a near-off-resonant regime, which balances resonant reabsorption loss and weak off-resonant light-matter coupling. The absence of four-wave mixing noise combined with the broad bandwidth

of our signal field allows for full amplitude and phase reconstruction of the output signal field via spectral interference. Taken as a whole, this performance makes our memory a promising candidate for applications in quantum communication, multiphoton state preparation, and local quantum processing, but further work is needed to transform our memory into a practically useable device. We discuss these limitations and future improvements here.

The most important bottleneck for broadband ensemble-based quantum memories lies in their limited storage lifetime [31]. A common figure of merit often quoted for ensemble-based memories is the time-bandwidth product — TBP $= T \times BW$, where T is the $1/e$ memory lifetime and BW is the signal field bandwidth. TBP represents the memory lifetime in multiples of the pulse duration, and is therefore a rough estimate of how many operations could be performed in a photonic quantum processor during the storage time at a clock rate comparable to the signal bandwidth. The time-bandwidth product in this work of is 980, which is comparable to the state of the art for broadband ensemble memories [91, 117, 161, 419], but this simple calculation conceals the fact that clock rates beyond a few GHz are not compatible with contemporary fast electronics and electro-optics, and may not be usable in a practical device. To elucidate this difference, we define the time-clock-rate product TRP $= T \times R$, which represents the number of clock cycles for which a quantum memory can store a photonic qubit. The TRP of our memory is only ~ 1 for a standard 2 GHz CPU clock, and is even lower for most quantum photon pair source repetition rates, which are typically in the MHz range (often limited by detector saturation) [430–432]. Nevertheless, a TRP equal to (but ideally much greater than) 1 is a prerequisite for a useful memory device, and our memory is the first in the ultra-broadband regime to meet this threshold. Furthermore, as noted in Sec. 5.2, our memory has significant room for improvement in memory lifetime (T), and therefore in TRP; if our memory lifetime could saturate the bound set by the bare atom radiative lifetime (0.25 sec [289]), this would bring the 2-GHz TRP of our memory to a bound of 5×10^8.

Acknowledgments

This work was supported by NSF grant Nos. 1205812, 1540513, 1521110, 1640968, 1806572, and 2207822; and NSF Award DMR1747426. We thank Andrey Mironov and Kavita Desai for helpful discussion related to barium-argon molecule formation; Ran Finkelstein, Eilon Poem, and Ofer Firstenberg for helpful discussion related to mitigation of Doppler dephasing; Donny R. Pearson Jr., Yujie Zhang, and Dong Beom Kim for helpful discussion related to the apparatus and measurement; Bin Fang, Shuai Dong, Seth Meiselman, and Offir Cohen to significant contributions at early stages of the project; and Ernest Northern and Jim Brownfield for expert machining of the heat-pipe oven.

Author Contributions

V.O.L. conceived the research. V.O.L. and J.G.E. led the research. K.B.S., T.L., and K.O. performed the experiments and analyzed the data. K.B.S., B.D.H., S.P., and T.O.R. characterized the home built heat pipe oven and performed initial laser alignment and spectroscopy. K.B.S. performed the numerical modelling. K.B.S. and V.O.L. wrote the manuscript, which all authors discussed.

Data Availability

The datasets generated during and/or analyzed during the current study are available from the corresponding authors on reasonable request.

Competing Interests

The authors declare no competing interests.

Methods

Barium heat pipe oven

We employ a home-built stainless steel heat pipe oven [197–199] to generate a neutral ensemble of atomic barium in the presence of controllable argon buffer gas pressure (0-1333 mbar). The heat pipe is loaded with natural abundance solid barium metal fragments (American Elements) at room temperature under argon atmosphere, which melt and vaporize when the heat pipe is brought to 800-900 °C (Ba melting point: 727 °C [433]) via an external resistive heater. A stainless steel mesh wick is inserted into the main chamber of the heat pipe to ensure convective flow and to prevent "hot spots." The two regions of the chamber before the windows are water cooled to 18 °C, and two 1/4 inch diameter apertures are inserted into the chamber, one on each end, to reduce flow and deposition of barium vapor on the windows, which is often a source of transmission loss. The heated region of the oven is 12 inches in length, and is surrounded by three clamshell resistive heaters. Two heaters with power consumption of 218 W heat the top of the heat pipe, and one heater with 600 W power consumption heats the bottom of the heat pipe.

Experimental setup

We provide a simplified experimental diagram in Extended Data Fig. 5.4. We employ an $\mathcal{O}(1)$ mJ pulse energy, $\mathcal{O}(100)$ fs, 1 kHz repetition rate, 800 nm Ti:Sapphire amplified laser system (Ti:sapph OPA; Spectra-Physics) cascaded with a tunable white-light seeded amplified wavelength converter (WL-OPA; Light Conversion) to produce $\mathcal{O}(10)$ uJ control field pulses between 1400 and 1700 center wavelength. We use a frequency-resolved optical gating (FROG) device (Mesa Photonics) to verify our control field pulses are Fourier-transform limited (group delay dispersion $<$100 fs^2). A small fraction of this control field is split off and used to generate our signal field via sum-frequency generation with an 877 nm continuous wave diode laser [AlGaAs Fabry-Perot, $\mathcal{O}(100)$ GHz linewidth; Thorlabs] in a room-temperature 1.2 mm β-barium-borate (BBO) crystal (Newlight Photonics). The phasematching function of the sum-frequency generation process sets the signal field spectrum and 880 GHz full-width at half-maximum (FWHM) bandwidth (500 fs Fourier-limited FWHM duration). The control field is split into two pulses with controllable delay (retrieval delay in Extended Data Fig. 5.4) before being focused and overlapped with the signal field on a dichroic mirror (Semrock). The signal field is also split into two pulses, one of which is sent to the heat pipe while one is reserved to act as a reference for the spectral interference measurements. The signal and control field waist radii in the center of the heat pipe oven are 110(10) and 250(10) μm, respectively. After the heat pipe, the signal field is split from the control field with a dichroic mirror and 4 cascaded interference filters (Semrock), each with $>$93% transmission at the signal field wavelength, before being recombined with the reference field and coupled into

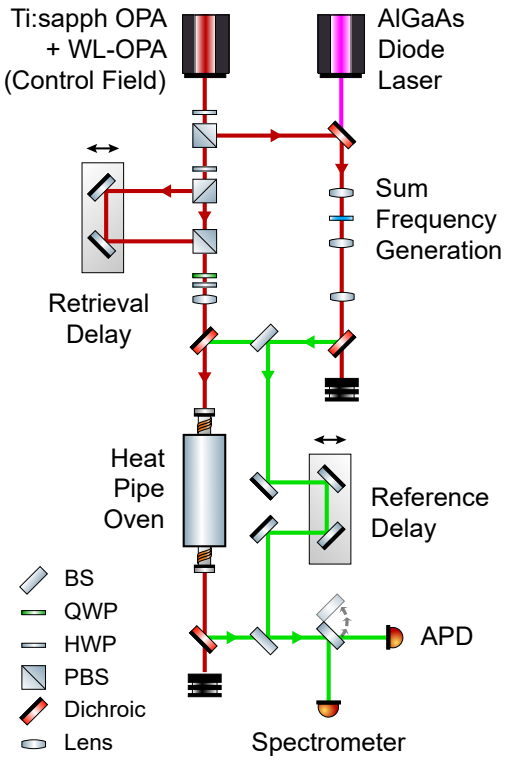

Figure 5.4: **Experimental schematic.** Simplified diagram of the barium quantum memory experiment. BS: Beam Splitter; QWP: Quarter Wave Plate; HWP: Half Wave Plate; PBS: Polarizing Beam Splitter; APD: Avalanche Photodiode.

single-mode fiber. The in-fiber signal field is sent to either a high-quantum-efficiency spectrometer (Oxford Instruments, Andor; >85% QE at 553.5 nm; $f/6.5$ aperture) or a Si avalanche photodiode (Excelitas) and time-to-digital converter (ID Quantique).

Collisionally broadened $^1P_1$ state linewidth measurements

We perform three separate spectroscopic measurements of the $^1S_0$ to $^1P_1$ transition at varying temperature and argon buffer gas pressure: white-light spectroscopy, scanning narrowband spectroscopy [$\mathcal{O}(10)$ GHz bandwidth, 3 ns probe], and coherent femtosecond spectroscopy (4.4 THz bandwidth, 100 fs probe). The optical depth and collisionally broadened linewidth extracted from each method agree within measurement error with each other and with previous work [434]. The measured peak optical depths range from 25 to 50, depending on the heat pipe temperature. The measured $^1P_1$ state linewidth is $\mathcal{O}(100)$ GHz, and depends linearly on argon buffer gas pressure, as shown in Fig. 5.1c. The equivalent optical depth of our system in a natural-linewidth ($\Gamma_{\text{nat}} = 120$ MHz [435]) atomic ensemble (the so-called 'cold OD') is roughly $d\Gamma/\Gamma_{\text{nat}} = 10^5$.

From kinetic theory [436, 437] and the Van der Waals radii of barium and argon, we calculate the barium-barium and barium-argon diffusion coefficients, mean free path, and mean time between collisions for varying argon pressure and system temperature. For the experimental settings in this work (argon pressures between 1-1000 mbar and temperatures 800-900 °C), the expected mean time between collisions is $\mathcal{O}(1-10)$ ns. At longer timescales, measured via white light spectroscopy and scanning narrowband spectroscopy, we probe the impact broadening regime, where phase discontinuities in the time-domain emission (or absorption)

of the radiating dipoles accounts for the broadened spectral line. For shorter timescales, measured via coherent femtosecond spectroscopy, we probe the quasistatic broadening regime, where the presence of many perturbers leads to an averaging over the atom-perturber potential energy surface, and therefore line broadening [284, 425–427, 438, 439].

$^1D_2$ coherence lifetime measurements

In Extended Data Fig. 5.5, we provide the data and model fit used to extract the maximum memory lifetime shown in Fig. 5.2b. Each lifetime measurement in Fig. 5.2b is performed by increasing the argon buffer gas pressure inside the heat pipe to a target setpoint and measuring the total (end-to-end) memory efficiency as a function of retrieval delay (see Extended Data Fig. 5.4). We fit each set of data to either a single exponential or single Gaussian decay function, depending on whether the argon pressure is above or below a cutoff of 25 mbar. Above this threshold, the experimental data are well described by exponential decay, and below this threshold, the experimental data are better fit to a Gaussian decay function characteristic of Doppler dephasing. The error bars in Extended Data Fig. 5.5 represent random uncertainty due to control field power and beam pointing fluctuations, and the propagated error in Fig. 5.2b represents the fitting uncertainty in the presence of this random error.

In general, the approach we introduce in this work based on controllable collisional broadening may also reduce memory lifetime, as the storage-ground state transition may also undergo collisional broadening beyond its Doppler linewidth. In our experiment, however, the collisional cross-section of the atoms in the storage state is roughly an order of magnitude smaller than the atoms in the excited state. As the collisional cross-section of an atomic state i is $\sigma_c \sim \pi\langle r_i\rangle^2$, where $\langle r_i\rangle$ is the expectation value of the outermost electron radius, and lower energy atomic states tend to have smaller effective radii, we anticipate this asymmetry in collisional cross-section to be a general feature of Λ-type level structures. Experimentally, we are able to demonstrate Doppler-limited memory lifetimes while simultaneously taking advantage of large collisionally broadened excited state linewidths; that is, the collisional (Γ_s^{coll}) and Doppler (Γ_s^{dop}) decay rates of the storage state obey $\Gamma_s^{\text{coll}} < \Gamma_s^{\text{dop}}$, while the exited state collisional (Γ_e^{coll}) and Doppler (Γ_e^{dop}) decay rates simultaneously obey $\Gamma_e^{\text{coll}} > \Gamma_e^{\text{dop}}$. In general, the introduction of collisional broadening does place an upper limit on the memory lifetime, set by the asymmetry in collisional cross-sections and the required broadening of the ground-excited state transition.

Maxwell-Bloch equations

We model our experiment using the well-known Maxwell-Bloch equations [66, 68, 69, 141, 440]:

$$\partial_z A(z,\tau) = -\sqrt{d}P(z,\tau) \tag{5.1}$$

$$\partial_\tau P(z,\tau) = -\bar{\gamma}P(z,\tau) + \sqrt{d}A(z,\tau) - i\frac{\Omega(\tau)}{2}B(z,\tau) \tag{5.2}$$

$$\partial_\tau B(z,\tau) = -\gamma_B B(z,\tau) - i\frac{\Omega^*(\tau)}{2}P(z,\tau), \tag{5.3}$$

where z represents the one-dimensional spatial coordinate of the atomic ensemble normalized to the ensemble length [i.e., $z = 0$ ($z = 1$) represents the beginning (end) of the ensemble]; $\tau = t - z/c$ represents time measured in the comoving frame of the signal photon (t represents time in the lab frame) normalized to

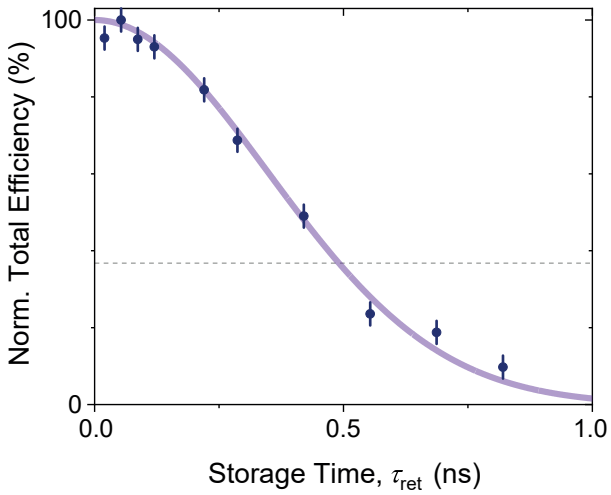

Figure 5.5: **Coherence lifetime.** Coherence lifetime measurement for the barium $^1S_0$–$^1D_2$ ensemble superposition state at 900 °C and 139.5 torr Ar pressure. Measured efficiencies are normalized to a maximum value of 100%. Storage time refers to the time delay between storage and retrieval control field pulses, set by the retrieval delay (τ_{ret}) in Extended Data Fig. 5.4. Solid curve is a fit to Gaussian decay. Dotted horizontal line denotes the $1/e$ point for total efficiency.

the excited-state coherence decay rate $\gamma = \Gamma/2$ (Γ is the total excited-state population decay rate, or the linewidth of the $|g\rangle \leftrightarrow |e\rangle$ transition); $A(z,\tau)$ is the spatially and temporally dependent signal photonic field; $P(z,\tau)$ and $B(z,\tau)$, referred to as the atomic polarization and spin wave fields, respectively, are macroscopic field operators representing the atomic coherences $|g\rangle \leftrightarrow |e\rangle$ and $|g\rangle \leftrightarrow |s\rangle$, which are delocalized across the length of the medium and are shown in Fig. 5.1b as orange and blue shaded regions, respectively; d is the resonant optical depth of the memory; $\bar{\gamma} = (\gamma - i\Delta)/\gamma$ is the normalized complex detuning, where the detuning Δ is shown schematically in Fig. 5.1b; and $\Omega(\tau)$ is the control field Rabi frequency coupling the $|e\rangle$ and $|s\rangle$ states. All atomic population is assumed to start in the ground state, and the metastable storage state is assumed to have a coherence decay rate γ_B that is much smaller than the excited state decay rate ($\gamma_B \ll 1$, in normalized units).

The set of equations (5.1)-(5.3) define a map between the input photonic field $A(z=0,\tau)$ and either the output spin-wave field $B(z,\tau\to\infty)$, in the case of the quantum storage operation, or the output photonic field $A(z=1,\tau)$, in the case of storage and retrieval operations. In quantum storage, the storage efficiency is defined as $\eta = \int_0^1 dz|B(z,\infty)|^2 / \int_{-\infty}^{\infty} d\tau|A(0,\tau)|^2$, which is well-approximated by $\eta \approx \int_{-\infty}^{\infty} d\tau|A(1,\tau)|^2 / \int_{-\infty}^{\infty} d\tau|A(0,\tau)|^2$ when all of the signal field population entering the atomic system is transferred into the storage state (i.e., no spontaneous emission loss). This condition is met, for example, in the absorb-then-transfer protocol when there is unit efficiency transfer between P and B fields (ensured by a π-pulse-area control field) and no excited-state decay during the storage operation (ensured when the storage-control-field delay $\Delta\tau^{\text{ctrl}}$ is much shorter than the decay time, Γ, which is trivially the case in the broadband regime when the pulse duration $\tau_{\text{FWHM}} \ll 1/\Gamma$ and $\Delta\tau^{\text{ctrl}} \sim \tau_{\text{FWHM}}$). This condition is also met in the idealized EIT regime with complete adiabatic elimination of the atomic polarization field, and in the off-resonant regime when the detuning is sufficiently large that no linear absorption takes place in the absence of the control field, and the presence of the control field maps population only to the storage state. This approximation to η is useful as it allows for measurement of storage efficiency through photon counting alone.

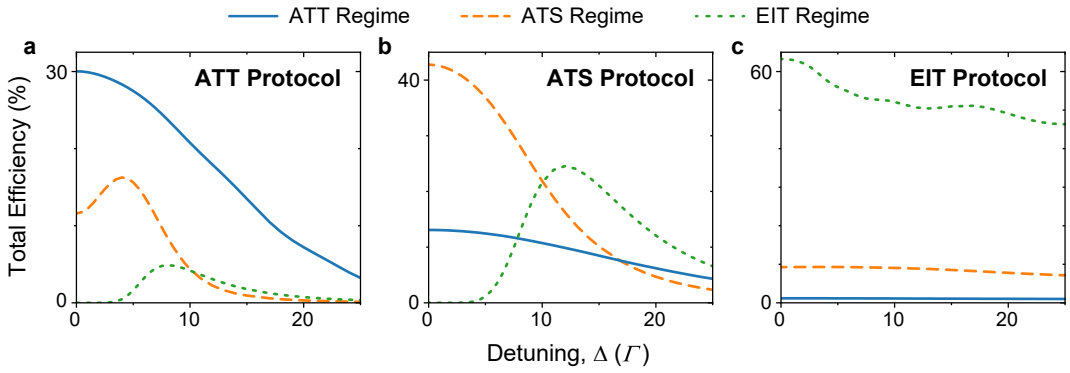

Figure 5.6: **Simulations of near-off-resonant-memory operation. a-c**, Total memory efficiencies plotted as a function of detuning for the absorb-then-transfer (ATT) (**a**), Autler-Townes splitting (ATS) (**b**), and electromagnetically induced transparency (EIT) (**c**) protocols. Solid curves show the memory efficiencies for each protocol when applied in the ATT (blue), ATS (orange), and EIT (green) memory parameter regimes (see Methods section 5.4). Maximal efficiency occurs at non-zero detuning when the memory adiabaticity (dependent on memory regime) is larger than the effective adiabaticity for a particular control field (dependent on memory protocol).

After storage and retrieval, the total efficiency $\eta_{\text{tot}} = \int_{-\infty}^{\infty} d\tau |A(1, \tau > \tau_{\text{ret}})|^2 / \int_{-\infty}^{\infty} d\tau |A(0,\tau)|^2$, where τ_{ret} is the retrieval delay or storage time, can also be measured via photon counting by subtracting the photon counts corresponding to transmission during the storage operation ('leaked' photons) from the total output photon counts.

Eq. (5.1)-(5.3) can also be used as a numerical fitting function. The fits performed in Fig. 5.2a and 5.2c assume Fourier-limited signal and control fields with experimentally measured bandwidth, control field power, signal–control-field delay, detuning, and waist radii; literature values for the control field transition dipole matrix element, and the signal and control field center frequencies; and use the optical depth and excited-state coherence decay rate as fit parameters.

Near-Off-Resonant Memory (NORM) operation

It may be unexpected *a priori* that an atomic-ensemble quantum memory with a given optical depth, linewidth, and control field parameters possesses a finite, non-zero optimal detuning. Especially in the ultra-broadband regime considered in this work, where we employ the absorb-then-transfer protocol that is limited in memory efficiency by linear absorption, one would naïvely expect the maximal memory efficiency always occurs on resonance, where linear absorption is maximized. Here we aim to provide some physical intuition as to why this is not the case.

Our intuition relies on understanding the control fields used in ensemble-based memory to possess their own adiabaticity, distinct from the memory adiabaticity. As in the rest of the literature, we define the free-space memory adiabaticity as $\chi = d\tau_{\text{FWHM}}\gamma$ [66, 68, 69], and gives an indication of how slowly varying the signal field is relative to the response of the medium defined by d and γ. As in Refs. [141, 441], we define the memory parameters $\mathcal{M} \equiv (d, \tau_{\text{FWHM}}\gamma)$, and for simplicity we limit our analysis to the case of Gaussian control fields, where the optimal Gaussian control field for a given set of memory parameters is uniquely defined by $\mathcal{G}(\mathcal{M})$. For a given control field, we can invert this function and find the corresponding optimal memory parameters $\mathcal{M}'(\mathcal{G}) = (d', \tau_{\text{FWHM}}\gamma')$ and effective adiabaticity for a particular control field χ'. When $\chi' < \chi$ (the control-field adiabaticity is less than the memory adiabaticity) we observe NORM operation — a

maximal total memory efficiency at finite, non-zero detuning. In this case, the memory's linear absorption is stronger than what is optimal for the control field being used, and it is beneficial to increase the detuning slightly to effectively reduce the linear absorption of the memory.

Another way to explain this behavior is in terms of reabsorption loss. In optically thick atomic ensembles, some fraction of the retrieved signal field must propagate through the atomic ensemble before reaching the free-space output port of the memory. This propagation introduces additional loss to the memory operation, as the retrieved signal field has some probability of being re-absorbed by the ensemble. This is a well-known source of memory inefficiency [121], and is strongest on resonance where the signal field overlaps with the absorption spectrum of the ensemble. It is therefore often beneficial to detune from resonance to avoid reabsorption loss, but increasing the detuning without increasing the control field strength can also decrease the light-matter coupling and therefore the memory efficiency. A tradeoff between these two effects leads to a maximal memory efficiency at non-zero two-photon detuning. We note, however, that this explanation is incomplete as it does not account for a control field sufficiently strong that it opens a transparency window at the signal frequency and eliminates reabsorption loss. The description above in terms of memory and control-field adiabaticities is more general and complete.

In Extended Data Fig. 5.6, we numerically simulate several combinations of memory parameters and control field parameters that elucidate NORM operation and verify our intuition. We choose three sets of memory parameters that correspond to the three resonant memory regimes: $\mathcal{M} = (5, 0.1)$, $(7.5, 0.4)$, and $(50, 1.5)$ for the ATT, ATS, and EIT regimes, respectively. For each set of memory parameters, we find the three sets of unique, optimal Gaussian control field parameters $\mathcal{G}(\mathcal{M}) = \left(\theta, \Delta\tau^{\text{ctrl}}, \tau^{\text{ctrl}}_{\text{FWHM}}\right)$, where θ is the control field pulse area (units of π), $\Delta\tau^{\text{ctrl}}$ is the control field delay relative to the signal field (units of τ_{FWHM}), and $\tau^{\text{ctrl}}_{\text{FWHM}}$ is the control field duration (intensity FWHM, units of τ_{FWHM}). As the control field parameters define the memory protocol, each $\mathcal{G}(\mathcal{M})$ constitutes a different memory protocol; we use $\mathcal{G}(\mathcal{M}) = (1.1, 0.8, 0.5)$, $(2.6, -0.2, 1.2)$, and $(10.1, -0.5, 1.3)$ for the ATT, ATS, and EIT protocols, respectively. Extended Data Fig 5.6a shows numerical applications of the ATT protocol in the ATT (blue), ATS (orange), and EIT (green) regimes, and Extended Data Fig 5.6b and c show the same for the ATS and EIT protocols, respectively. Clear near-off-resonant-memory operation occurs in Extended Data Fig 5.6a and b when applying a less adiabatic memory protocol in a more adiabatic memory regime. In some cases, e.g., when using the ATT and ATS protocols in the EIT regime, the memory efficiency is near zero on resonance and only increases to appreciable values for near-resonant detunings. As one would expect, each memory protocol is most efficient in its respective regime.

The experiment reported in this work and the data shown in Fig. 5.2c are most similar to the ATS regime in Extended Data Fig. 5.6a, where we employ the ATT protocol (due to the available control field power and pulse duration) in a regime more suitable to the ATS (or a mixed ATT-ATS) protocol.

Amplitude and phase reconstruction via spectral interferometry

In order to reconstruct the retrieved signal field amplitude and phase from spectral interference measurements, we first consider the general case of two ultrafast pulses with electric fields $A_1(\tau)$ $[A_1(\omega)]$ and $A_2(\tau)$ $[A_2(\omega)]$ in the temporal (spectral) domain. We take $A_1(\tau)$ to be a reference pulse with known amplitude and phase and $A_2(\tau)$ to be a modified pulse similar in spectral bandwidth to $A_1(\tau)$ but with differing amplitude $|A_2(\tau)|$ and temporal phase $\phi_2(\tau)$, which we aim to measure. If we combine $A_1(\tau)$ and $A_2(\tau)$ on a beamsplitter with time delay $\Delta\tau$, the resulting interference spectrum in one output port of the beamsplitter can be recorded on a spectrometer and used to reconstruct $A_2(\tau)$. The details of this process are as follows.

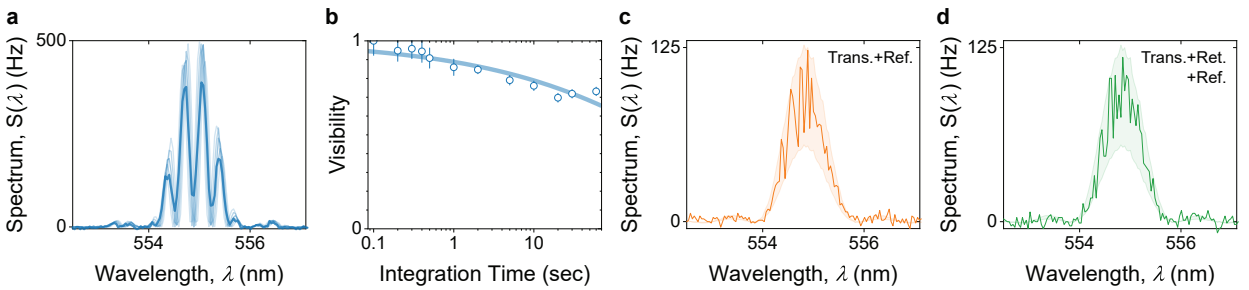

Figure 5.7: **Spectral Interferometry. a**, Non-unit visibility measured spectral interference between the two interferometer paths with the memory off (solid blue curve) occurs at finite integration time due to averaging of many short-duration interference spectra with varying phase (shaded blue curves). **b**, Measured spectral interference visiblity (markers) as a function of spectrometer integration time. Error bars represent statistical error from photon counting statistics propagated through a sinusoidal fit. Solid curve is a fit to the data based on a time-varying Gaussian phase distribution (see Methods). **c**-**d**, Spectral interference between the transmitted and reference (**c**), and transmitted, retrieved, and reference (**d**) pulses with the memory on. Shaded regions designate the expected bounds for non-unit interference visiblity according to our model (see Methods).

The Fourier decomposition of $A_j(\tau)$ (for $j = 1, 2$) is given by $A_j(\tau) = \frac{1}{\sqrt{2\pi}} \int_{-\infty}^{\infty} d\omega \, |A_j(\omega)| e^{i[\omega\tau + \phi_j(\omega)]}$, where $A_j(\omega) = |A_j(\omega)| e^{i\phi_j(\omega)}$. The Fourier decomposition of the signal impinging on the spectrometer is therefore: $\frac{1}{2\sqrt{\pi}} \int_{-\infty}^{\infty} d\omega \left[i|A_1(\omega)| e^{i\phi_1(\omega)} + |A_2(\omega)| e^{i[\omega\Delta\tau + \phi_2(\omega)]} \right] e^{i\omega\tau}$, where we have assumed (without loss of generality) that $A_1(\tau)$ is reflected at the beamsplitter and $A_2(\tau)$ is transmitted. The spectrometer detects the spectral intensity of the signal impinging on it:

$$S(\omega) = |A_1(\omega)|^2 + |A_2(\omega)|^2 + 2|A_1(\omega)||A_2(\omega)| \sin\left[\omega\Delta\tau + \phi_{\text{dif}}(\omega)\right], \tag{5.4}$$

where $\phi_{\text{dif}}(\omega) = \phi_2(\omega) - \phi_1(\omega)$. Both $|A_1(\omega)|^2$ and $|A_2(\omega)|^2$ (and therefore $|A_1(\omega)|$ and $|A_2(\omega)|$ by applying the square root) can be measured trivially by blocking the opposite input port of the beamsplitter and recording the single-path spectrum. If $\Delta\tau$ is known, and is smaller than the inverse of the spectrometer resolution, everything in Eq. (5.4) is known except for $\phi_{\text{dif}}(\omega)$. We can therefore measure the interferogram $S(\omega)$, fit to Eq. (5.4), extract $\phi_{\text{dif}}(\omega)$ [and therefore $\phi_2(\omega)$ for known $\phi_1(\omega)$], and reconstruct $A_2(\omega)$ and $A_2(\tau)$ using the relations above.

In experiment, we follow this procedure by splitting the signal field as generated via sum-frequency generation (see Sec. 5.4) into two paths; one path is sent to the barium heat pipe quantum memory for storage and retrieval, and the other path propagates in free space and acts as a reference. The two paths are recombined on a beamsplitter before being sent to a single-photon-level spectrometer with ∼0.04 nm resolution. With the memory off (heat pipe at 20 °C, where the number density of gas-phase barium atoms is negligible), we observe spectral interference between the two paths as shown in Extended Data Fig. 5.7a. At spectrometer integration times less than 0.1 sec we achieve near unit visibility spectral interference, but the statistical error due to photon counting statistics is significant and makes spectral reconstruction of the signal field with the memory on impossible. We must therefore use longer spectrometer integration times, where the interference visibility is significantly below unity. Measured interference visibilities as a function of spectrometer integration time are shown in Extended Data Fig. 5.7b, along with a model fit derived from first principles: We define the time-averaged visibility $\overline{V} = (\overline{I_{\text{max}}} - \overline{I_{\text{min}}})/(\overline{I_{\text{max}}} + \overline{I_{\text{min}}})$ in terms of the time-averaged maximum and minimum intensities, $\overline{I_{\text{max}}}$ and $\overline{I_{\text{min}}}$, respectively. We assume that one

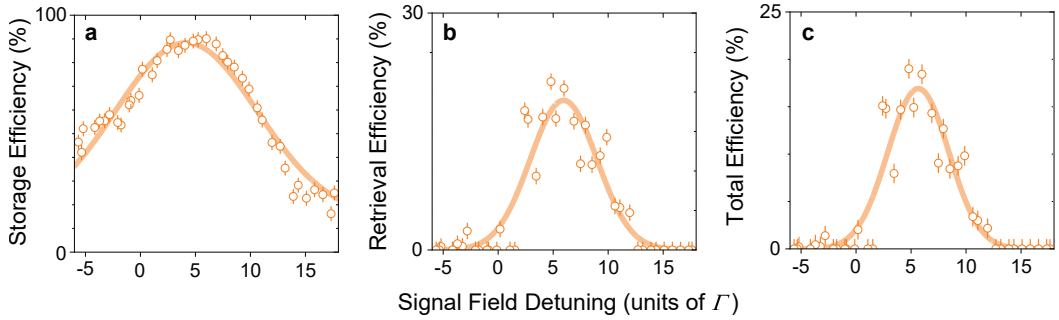

Figure 5.8: **Signal field frequency dependence. a-c**, Measured storage (**a**), retrieval (**b**), and total (**c**) efficiencies as a function of signal field center frequency, written as the detuning from resonance. Solid lines are fits representative of the light-matter coupling due to the Gaussian control field centered near a detuning of 5Γ. Error bars represent random uncertainty due to control field power variation.

can convert the spectral interference in, e.g., Extended Data Fig. 5.7a into a purely sinusoidal interference spectrum and an envelope function (which, in experiment, we measure by blocking one interferometer path at a time and summing the resulting single-path spectra). In this case, the time-averaged maximum and minimum sinusoid intensities are $\overline{I_{\max}} = \int d\phi\, P(\phi,t)\sin^2(\phi+\pi/2)$ and $\overline{I_{\min}} = \int d\phi\, P(\phi,t)\sin^2(\phi)$, for a phase distribution $P(\phi,t)$ at integration time t. For a Gaussian phase distribution, $P(\phi,t) \sim e^{-\phi^2/[2\sigma(t)^2]}$, the time-dependence is contained solely in the parameter $\sigma(t)$, and leads to an time-averaged visibility $\overline{V} = e^{-2\sigma(t)^2}$. The exact time dependence of $\sigma(t)$ depends on the specific experimental apparatus. We achieve reasonable agreement with experimental data using the general form $\sigma(t) = f_1 t^{f_2}$ for fit parameters f_1 and f_2, which evaluate to $f_1 = 0.06$ and $f_2 = 0.3$ in our experiment, as shown in Extended Data Fig. 5.7b. Using this model for non-unit visibility interference, along with the measured spectral intensities of the transmitted, retrieved, and reference fields, we estimate the expected upper and lower bounds for non-unit visibility spectral interference shown in Extended Data Fig. 5.7c and d.

Extended Data Fig. 5.7c shows the measured interference spectrum after combining the transmitted and reference pulses on a beamsplitter after the memory. We isolate the transmitted pulse from the retrieved pulse experimentally by blocking the retrieval control field. The interference spectrum shows significantly asymmetrical visibility, as expected for a transmitted pulse with linear temporal phase relative to the reference pulse. When unblocking the retrieval control field, we observe the interference spectrum in Extended Data Fig. 5.7d, which again has an asymmetrical interference visibility, but with a significantly more complicated interference pattern. We use the method described above to reconstruct the amplitude and phase (relative to the reference pulse) of the transmitted and retrieved signal field pulses, leading to the results shown in Fig. 5.3c.

Signal-field frequency dependence

As a further characterization step, we measure the signal-field frequency dependence of our memory. We keep the center frequency of our control field fixed at around 5Γ off resonance and vary the center frequency of our signal field, scanning over the range of near-resonant coupling due to our Gaussian control field. In Extended Data Fig. 5.8 we report the measured storage, retrieval, and total memory efficiencies along with fits to independent Gaussian functions. The storage efficiency spectrum is approximately a factor of $\sqrt{2}$ wider than the retrieval and total efficiency spectra as the storage operation requires the action of a single control

field pulse, whereas the retrieval (and therefore total) operation requires the action of two control field pulses.

Supplemental: Broadband quantum memory literature review

Here we provide the full citation information used to generate Fig. 5.1a, which includes, to the best of our knowledge, every quantum memory demonstration with signal field bandwidths (intensity full-width at half-maximum) greater than 10 MHz:

Abbreviation	Citation
AJAC20	A. J. A. Carvalho, *et al.*, Phys. Rev. A **101**, 053426 (2020).
AR19	A. Rastogi, *et al.*, Physical Review A **100**, 012314 (2019).
AR22	A. Rastogi, *et al.*, Physical Review Letters **129**, 120502 (2022).
AT16	A. Tiranov, *et al.*, Physical Review Letters **117**, 240506 (2016).
CC11	C. Clausen, *et al.*, Nature **469**, 508 (2011).
DCL22	D.-C. Liu, *et al.*, Physical Review Letters **129**, 210501 (2022).
DGE13	D. G. England, *et al.*, Physical Review Letters **111**, 243601 (2013).
DGE15	D. G. England, *et al.*, Physical Review Letters **114**, 053602 (2015).
DJS16	D. J. Saunders, *et al.*, Physical Review Letters **116**, 090501 (2016).
DM21	D. Main, *et al.*, Optics Letters **46**, 2960 (2021).
DSD13	D.-S. Ding, *et al.*, Nature Communications **4**, 2527 (2013).
DSD15	D.-S. Ding, *et al.*, Nature Photonics **9**, 332 (2015).
DSD16	D.-S. Ding, *et al.*, Light Science & Applications **5**, e16157 (2016).
ES11	E. Saglamyurek, *et al.*, Nature **469**, 512 (2011).
ES15	E. Saglamyurek, *et al.*, Nature Photonics **9**, 83 (2015).
ES16	E. Saglamyurek, *et al.*, Nature Communications **7**, 11202 (2016).
ES18	E. Saglamyurek, *et al.*, Nature Photonics **12**, 774 (2018).
ES19	E. Saglamyurek, *et al.*, Physical Review Research **1**, 022004(R) (2019).
ES21	E. Saglamyurek, *et al.*, New Journal of Physics **23**, 043028 (2021).
FB14	F. Bussieres, *et al.*, Nature Photonics **8**, 775 (2014).
GB22	G. Buser, *et al.*, PRX Quantum **3**, 020349 (2022).
HdR08	H. de Riedmatten, *et al.*, Nature **456**, 773 (2008).
IC19	I. Craiciu, *et al.*, Physical Review Applied **12**, 024062 (2019).
JD20	J. Davidson, *et al.*, Physical Review A **101**, 042333 (2020).
JG19	J. Guo, *et al.*, Nature Communications **10**, 148 (2019).
JJ15	J. Jin, *et al.*, Physical Review Letters **115**, 140501 (2015).
JST15	J.-S. Tang, *et al.*, Nature Communications **6**, 8652 (2015).
JW17	J. Wolters, *et al.*, Physical Review Letters **119**, 060502 (2017).
KAF17	K. A. Fisher, *et al.*, Physical Review A **96**, 012324 (2017).
KFR10	K. F. Reim, *et al.*, Nature Photonics **4**, 218 (2010).
KFR11	K. F. Reim, *et al.*, Physical Review Letters **107**, 053603 (2011).
KSC08	K. S. Choi, *et al.*, Nature **452**, 67 (2008).

Table 5.1: (cont.)

Abbreviation	Citation
KTK18	K.T. Kaczmarek, *et al.*, Physical Review A **97**, 042316 (2018).
LE23	L. Esguerra, *et al.*, Phys. Rev. A **107**, 042607 (2023).
LH22	L. Heller, *et al.*, Physical Review Applied **18**, 024036 (2022).
LM23	L. Meßner, *et al.*, Opt. Express **31**, 10150 (2023).
MA19	M. Askarani, *et al.*, Physical Review Applied **11**, 054056 (2019).
MB22	M. Businger, *et al.*, Nature Communications **13**, 6438 (2022).
MHJ22	M.-H. Jiang, *et al.*, arXiv:2212.12898v1 [quant-ph] (2022).
MHJ23	M.-H. Jiang, *et al.*, Nat. Commun. **14**, 6995 (2023).
MRS14	M. R. Sprague, *et al.*, Nature Photonics **8**, 287 (2014).
NS14	N. Sinclair, *et al.*, Physical Review Letters **113**, 053603 (2014).
OD23a	O. Davidson, *et al.*, Commun. Phys. **6**, 131 (2023).
OD23b	O. Davidson, *et al.*, Phys. Rev. Lett. **131**, 033601 (2023).
PJB13	P. J. Bustard, *et al.*, Physical Review Letters **111**, 083901 (2013).
PSM15	P. S. Michelberger, *et al.*, New Journal of Physics **17**, 043006 (2015).
RAA16	R. A. Akhmedzhanov, *et al.*, Laser Physics Letters **13**, 015202 (2016).
RF18	R. Finkelstein, *et al.*, Science Advances **4**, eaap8598 (2018).
RF21	R. Finkelstein, *et al.*, Physical Review X **11**, 011008 (2021).
SET19	S. E. Thomas, *et al.*, Physical Review A **100**, 033801 (2019).
SET22	S. E. Thomas, *et al.*, arXiv 2211.04415v1 (2022).
SET23	S. E. Thomas, *et al.*, Phys. Rev. Appl. **19**, L031005 (2023).
SHW22	S.-H. Wei, *et al.*, arXiv:2209.00802 [quant-ph] (2022).
TZ17	T. Zhong, *et al.*, Science **357**, 1392 (2017).
WZ16	W. Zhang, *et al.*, Nature Communications **7**, 13514 (2016).
XL21	X. Liu, *et al.*, Nature **594**, 41 (2021).
XZ23	X. Zhang, *et al.*, Sci. Adv. **9**, eadf4587 (2023).
YCW20	Y.-C. Wei, *et al.*, Physical Review A **102**, 063720 (2020).
ZQZ12	Z.-Q. Zhou, *et al.*, Physical Review Letters **108**, 190505 (2012).
ZQZ15	Z.-Q. Zhou, *et al.*, Physical Review Letters **115**, 070502 (2015).
ZY23	Z. Yu, *et al.*, Phys. Rev. Lett **131**, 150804 (2023).

Table 5.1: **Citation information.** Full citation information for Figure 1a, sorted by abbreviation (first and last initial of the first author, then two-digit year). For first authors with multiple publications in a single year, we append a lowercase letter (a, b, ...) to the abbreviation.

Chapter 6

Conclusions and Future Work

6.1 Summary

We have covered a considerable amount of intellectual ground in this thesis. As a brief summary, the material covered is as follows:

- We have discussed the underpinning motivation of this work in layman's terms, reviewing the key distinctions between classical and quantum information theory, the motivation behind using single photons as the quantum particle of choice for quantum technological applications, and the open challenges to the development of large-scale, fault-tolerant quantum technology based on the photonic platform. We have discussed the DLCZ protocol, and how it may be reformulated in a heralded single-photon generation framework. We have covered the basics of atomic-ensemble-based photonic quantum memory, its motivation, the protocols and hardware used for this task, the underlying quantum mechanical theory, and the state of the art in broadband quantum memory, which foreshadow our contributions in the later chapters of this thesis.

- We have provided a theoretical description of photon-phonon quantum correlations in spontaneous Stokes Raman scattering, including the effects of chromatic dispersion, finite phonon lifetime, and three-dimensional Stokes photon collection geometry. This theoretical framework predicts a maximum in Stokes photon quantum state purity (i.e., a minimum in photon-phonon correlations) at a distinct optimal pump bandwidth, which we verify experimentally for the case of bulk optical phonons in single-crystal sapphire. Furthermore, we predict significant collection-geometry dependence of the Stokes photon purity, which we verify experimentally by comparing measured photon purities at various angles near the forward and backward scattered geometries. This work develops valuable physical intuition for these quantum correlations, which are critical to understand for high-purity, high-indistinguishability single-photon generation based on the DLCZ protocol.

- We have discussed the optimization of Λ-type atomic-ensemble quantum memory by way of optimized control field pulses with Gaussian temporal envelope and arbitrary envelope. We describe the numerical solution of the Maxwell-Bloch equations governing atomic-ensemble memory, and how the efficiency of this process can be optimized directly in the resonant and off-resonant regime with simple numerical tools. This direct optimization reveals a continuous and unique map between the *memory* parameters of an atomic ensemble (its optical depth and linewidth) and the optimal *control* parameters, $\mathcal{M} \rightarrow \mathcal{G}_{\text{opt}}$.

Moreover, in the resonant case, three distinct regions of memory parameter space correspond to three distinct physical memory protocols, and the map we develop reveals a continuous transformation connecting these three protocols. This continuous transformation allows for near-optimal efficiencies in the mixed regions of memory parameter space not previously well understood.

- With the map $\mathcal{M} \to \mathcal{G}_{\text{opt}}$ in hand, one can start to investigate the sensitivity of Λ-type quantum memory to perturbations in $\mathcal{M}$ and $\mathcal{G}$. We perform such an investigation, considering shot-to-shot fluctuations in $\mathcal{M}$, and longer-timescale drift in $\mathcal{G}$, each of which are realistic sources of error in Λ-type quantum memory experiments. We find that, in fact, all resonant Λ-type quantum memory protocols are robust to $\mathcal{M}$ fluctuations, insofar as the relative fluctuations in memory efficiency are always smaller than the relative fluctuations in $\mathcal{M}$ causing them, i.e., Λ-type quantum memory is inherently noise-robust an non-amplifying. This being said, we find the Electromagnetically Induced Transparency (EIT) protocol is the most robust to this type of perturbation, and is approximately three times less sensitive (i.e., more robust) than the Autler-Townes Splitting (ATS) protocol and approximately four times less sensitive than the Absorb-Then-Transfer (ATT) protocol. With respect to drift in the control field parameters, we find that the type of drift is quite important, and which memory protocol is most robust depends in general on the type of control field drift, with some important physical intuition for each case of drift.

- We have presented our experimental work on high-efficiency, broadband, and low-noise photonic quantum memory in neutral barium vapor, which exhibits state-of-the-art and best-in-class memory efficiency, bandwidth, and noise performance simultaneously. This experiment is at the extremes of high temperature, high pressure, high pulse energy, and ultrabroad bandwidth. We demonstrate theoretically and experimentally that collisional broadening of an atomic ensemble with noble gas perturbers is a resource for broadband memory operation, not a necessarily parasitic dephasing mechanism, as previously thought. We fully characterize the performance of our memory as a function of buffer gas pressure, control field pulse area, two-photon detuning, and single-photon detuning. Moreover, we perform a fundamentally new characterization technique enabled by the ultra-low noise in our system by reconstructing the amplitude and phase of our broadband signal field after the memory via spectral interferometry with a known reference. We discuss the future promise of this memory before moving on to supplementary information, including a novel theoretical description of the two-photon detuning dependence of our memory efficiency that we name Near-Off-Resonant Memory (NORM) operation. This NORM operation is explained by use of the same map between memory and control parameters developed previously, this time inverted as $\mathcal{G} \to \mathcal{M}_{\text{opt}}$; contrary to the non-inverted map, this map is not guaranteed to exist or to be unique, but for the well-behaved $\mathcal{G}$ typically used in experiment we are able to use it to develop physical intuition for NORM behavior.

There are several possible extensions to the work performed in this thesis, particularly for the experimental work, which we discuss in the next sections.

6.2 Increasing memory lifetime

If there is one drawback to the experiment described in Chapter 5, it is the memory lifetime. As shown in Section 1.3.4, the memory lifetime of our experiment is no particularly bad relative to the trend set by the rest of the literature, but in absolute terms, and relative to the repetition rate of our laser, it is small. Fortunately, several dephasing-protection techniques exist that can serve to improve the lifetime of our memory (see,

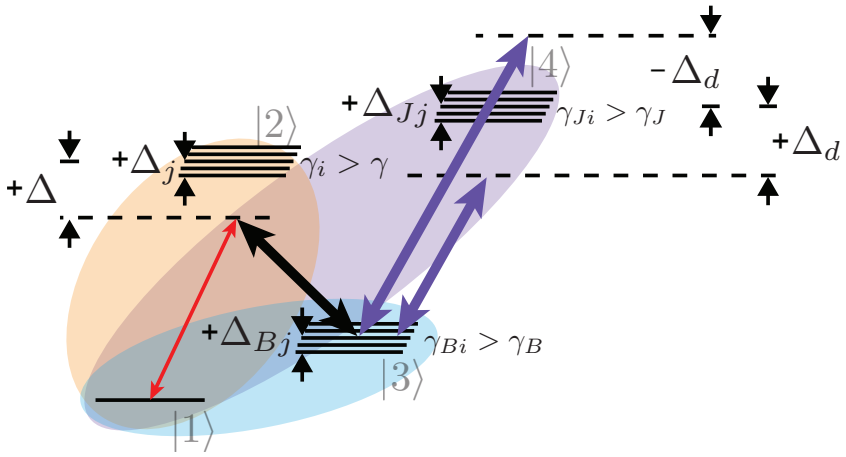

Figure 6.1: N-type energy level structure.

e.g., Ref. [56]). What follows is a brief theoretical description of a novel dephasing-protection technique, which preliminary results indicate may increase the lifetime of our memory by more than a factor of $10X$ at moderate laser power.

Consider the level structure shown in Fig. 6.1 with $\Delta_d = 0$ and a single dressing field (purple, thick arrows in Fig. 6.1). The multiple levels in state $|2\rangle$, $|3\rangle$, and $|4\rangle$ represent inhomogeneous broadening of these states with inhomogeneous coherence decay rates γ_i, γ_{Bi}, and γ_{Ji}, respectively. We consider the memory interaction governed by the following extended Maxwell-Bloch equations:

$$\partial_z A(z,\tau) = -\sqrt{d}\sum_j \sqrt{p_j} P_j(z,\tau) \tag{6.1}$$

$$\partial_\tau P_j(z,\tau) = -\gamma P_j(z,\tau) + i(\Delta + \Delta_j) P_j(z,\tau) + \sqrt{d}\sqrt{p_j} A(z,\tau) - i\Omega(\tau) B_j(z,\tau) \tag{6.2}$$

$$\partial_\tau B_j(z,\tau) = -\gamma_B B_j(z,\tau) + i\Delta_{Bj} B_j(z,\tau) - i\Omega^*(\tau) P_j(z,\tau) - i\Omega_d^*(\tau) J_j(z,\tau) \tag{6.3}$$

$$\partial_\tau J_j(z,\tau) = -\gamma_J J_j(z,\tau) + i\Delta_{Jj} J_j(z,\tau) - i\Omega_d(\tau) B_j(z,\tau), \tag{6.4}$$

where, in addition to the treatments of Chapters 1 and 3-5, we introduce the inhomogeneously distributed sensor fields $J_j \propto \sum_{\beta(\mathbf{r})} \tilde{\sigma}_{14}^{j(\beta)} e^{i\Delta_{Jj}\tau}$ that couple to the spin wave fields B_j via the many-photon, classical dressing field Ω_d. In this definition of J_j, $\beta(\mathbf{r})$ is an index that runs over all atoms in an infinitesimal cyclindrical volume located at position z along the optic axis of the signal field, and $\tilde{\sigma}_{14}$ is the flip operator $\tilde{\sigma}_{14} = |4\rangle\langle 1| e^{i\omega_{14}\tau}$ under the rotating wave approximation for transition frequency ω_{14} between levels $|1\rangle$ and $|4\rangle$.

In the trivial case, when $s = \gamma_{Ji}/\gamma_{Bi} = 1$, after storage of a single-photon-level signal field in the spin wave field B, a dressing field with constant Rabi frequency $\Omega_d(\tau) = \Omega_d^0$ induces unit-visibility Rabi oscillations between spin wave and sensor fields, where any inhomogeneous dephasing accrued in the spin wave is canceled by rephasing in the sensor field. This is the conventional continuous wave dynamical decoupling sequence [442].

For $s \neq 0$, we can approximate this same behavior by requiring sequential π pulses with durations $\delta\tau_\pi$ that vary by $1/s$, i.e.:

$$\delta\tau_{\pi,2} = \delta\tau_{\pi,1}/s \tag{6.5}$$

$$\vdots$$

$$\delta\tau_{\pi,n+1} = \delta\tau_{\pi,n}/s, \tag{6.6}$$

where

$$\delta\tau_{\pi,n} = \tau_n - \tau_{n-1}, \tag{6.7}$$

which enforces

$$\tau_n = \sum_{m=1}^{n} \frac{\tau_1}{s^{m-1}}, \tag{6.8}$$

for arbitrary τ_1. The condition that the dressing field implements a π-pulse over each $\delta\tau_{\pi,n}$ is

$$\int_{\tau_{n-1}}^{\tau_n} d\tau\, \Omega_d(\tau) = \pi, \tag{6.9}$$

which does not uniquely define $\Omega_d(\tau)$; many different functional forms, including discontinuous stepwise functions, satisfy this constraint. In order to ease experimental implementation, we find the following smooth function that satisfies condition (6.9):

$$\Omega_d^{\text{opt}}(\tau) = \frac{f\pi/\ln s}{s/(s-1) - f(\tau - \Delta\tau_d)}, \tag{6.10}$$

where f scales the duration of the first π pulse and $\Delta\tau_d$ controls its group delay relative to the signal field. This optimal dressing field increases rapidly as the sequential π pulses comprising it become shorter in duration, and this poses a challenge for physical dressing fields with finite power. Fortunately, this challenge can be overcome by limiting the function only to the first two π pulses, and repeating the pulse sequence in a continuous fashion. This leads to an optimal quasi-CW dressing field with a sawtooth shape, which ought to be experimentally realizable with acousto- or electro-optic modulation of a CW field.

6.3 Optical pumping for telecom storage and retrieval

A key selling point of the memory described in Chapter 5 is its compatibility with tecommuncations (telcom) wavelengths, most notably 1550 nm. Given the Λ-type level structure with 340 THz ground-storage state splitting and the 800-900 °C vapor temperature, all of the atomic population begins in the $^1S_0$ ground state to an excellent approximation. This implies that the signal field must be in the optical domain, near 550 nm (553.5 nm, for resonant operation), and only the control field can be in the 1500 - 1600 nm telecom range. This is a far less desirable situation than the inverse, where the signal field is in the telecom range and the control field is optical. Fortunately, we can achieve this arrangement if we can optically pump the atomic

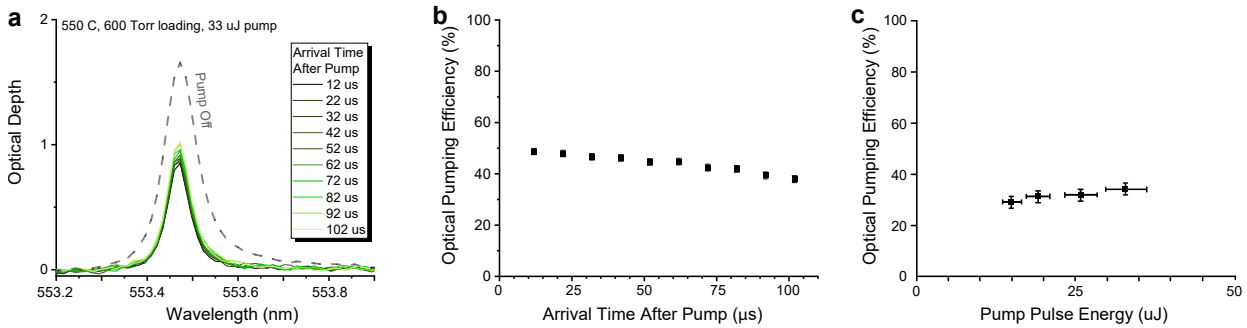

Figure 6.2: **Preliminary optical pumping measurements.** **a** Time-resolved spectroscopic data, **b** extracted maximal optical pumping efficiency as a function of pump pulse energy, and **c** scaling of maximal optical pumping efficiency with pulse energy.

population into the metastable $^1D_2$ level before the storage operation.

We have performed preliminary optical pumping measurements on a significantly smaller barium heat pipe oven and at significantly lower temperatures than the oven used in the experiments of Chapter 5, which provides a smaller atom number and optical depth and facilitates measurement of optical pumping efficiency. The results of these preliminary measurements are provided in Figure 6.2. We employ a ns duration pump pulse at 553.5 nm that counterpropagates relative to a white light probe beam. We measure the absorption spectrum of the probe beam with the pump beam off (grey dashed trace in Fig. 6.2a), and with the pump beam on at variable temporal delays. This latter set of measurements allows us to estimate the lifetime of the $^1D_2$ level at these lower temperatures, and allows us to extrapolate a maximal optical pumping efficiency at arrival time zero. (Direct measurement of the optical pumping efficiency at time zero is made impossible by strong scattering of the pump pulse into the fiber collecting the white light beam.) The time dependence of the optical pumping efficiency measured in this way are given in Fig. 6.2b. The measurements in Fig. 6.2a and b are performed at the highest available pump pulse energy, 33 uJ. We measure the maximal optical pumping efficiency at varying pump pulse energy and present the results in Fig. 6.2c. The pump pulse energy dependence in this case is not favorable—a more promising path forward for optical pumping in this experiment would be to use a longer duration pump pulse.

References

[1]M. Born, A. Einstein, H. Born, and B. Russell, *Albert einstein, hedwig und max born: briefwechsel 1916-1955; geleitwort von bertrand russell* (Nymphenburger, 1969).

[2]P. W. Shor, "Algorithms for quantum computation: discrete logarithms and factoring", in Proceedings 35th annual symposium on foundations of computer science (Ieee, 1994), pp. 124–134.

[3]D. Coppersmith, "Modifications to the number field sieve", Journal of Cryptology **6**, 169–180 (1993).

[4]R. L. Rivest, A. Shamir, and L. Adleman, "A method for obtaining digital signatures and public-key cryptosystems", Communications of the ACM **21**, 120–126 (1978).

[5]E. Martin-Lopez, A. Laing, T. Lawson, R. Alvarez, X.-Q. Zhou, and J. L. O'brien, "Experimental realization of shor's quantum factoring algorithm using qubit recycling", Nature Photonics **6**, 773–776 (2012).

[6]M. Amico, Z. H. Saleem, and M. Kumph, "Experimental study of shor's factoring algorithm using the ibm q experience", Physical Review A **100**, 012305 (2019).

[7]C. Gidney and M. Ekera, "How to factor 2048 bit rsa integers in 8 hours using 20 million noisy qubits", Quantum **5**, 433 (2021).

[8]E. Gouzien and N. Sangouard, "Factoring 2048-bit rsa integers in 177 days with 13 436 qubits and a multimode memory", Physical Review Letters **127**, 140503 (2021).

[9]S. McArdle, S. Endo, A. Aspuru-Guzik, S. C. Benjamin, and X. Yuan, "Quantum computational chemistry", Reviews of Modern Physics **92**, 015003 (2020).

[10]Y. Cao, J. Romero, and A. Aspuru-Guzik, "Potential of quantum computing for drug discovery", IBM Journal of Research and Development **62**, 6–1 (2018).

[11]R. Orus, S. Mugel, and E. Lizaso, "Quantum computing for finance: overview and prospects", Reviews in Physics **4**, 100028 (2019).

[12]M. Suchara, Y. Alexeev, F. Chong, H. Finkel, H. Hoffmann, J. Larson, J. Osborn, and G. Smith, "Hybrid quantum-classical computing architectures", in Proceedings of the 3rd international workshop on post-moore era supercomputing, 2018. (2018).

[13]A. Callison and N. Chancellor, "Hybrid quantum-classical algorithms in the noisy intermediate-scale quantum era and beyond", Physical Review A **106**, 010101 (2022).

[14]P. Kok, W. J. Munro, K. Nemoto, T. C. Ralph, J. P. Dowling, and G. J. Milburn, "Linear optical quantum computing with photonic qubits", Reviews of Modern Physics **79**, 135 (2007).

[15]G. Wendin, "Quantum information processing with superconducting circuits: a review", Reports on Progress in Physics **80**, 106001 (2017).

[16]H. Häffner, C. F. Roos, and R. Blatt, "Quantum computing with trapped ions", Physics reports **469**, 155–203 (2008).

[17]V. Schafer, C. Ballance, K. Thirumalai, L. Stephenson, T. Ballance, A. Steane, and D. Lucas, "Fast quantum logic gates with trapped-ion qubits", Nature **555**, 75–78 (2018).

[18]M. A. Nielsen and I. L. Chuang, *Quantum computation and quantum information* (Cambridge university press, 2010).

[19]E. Knill, R. Laflamme, and G. J. Milburn, "A scheme for efficient quantum computation with linear optics", nature **409**, 46–52 (2001).

[20]J. Nunn, N. Langford, W. Kolthammer, T. Champion, M. Sprague, P. Michelberger, X.-M. Jin, D. England, and I. Walmsley, "Enhancing multiphoton rates with quantum memories", Physical Review Letters **110**, 133601 (2013).

[21]K. C. Cox, P. Bienias, D. H. Meyer, D. P. Fahey, P. D. Kunz, and A. V. Gorshkov, "Spin-wave quantum computing with atoms in a single-mode cavity", Physical Review Research **4**, 033149 (2022).

[22]P. G. Kwiat, K. Mattle, H. Weinfurter, A. Zeilinger, A. V. Sergienko, and Y. Shih, "New high-intensity source of polarization-entangled photon pairs", Physical Review Letters **75**, 4337 (1995).

[23]F. Kaneda and P. G. Kwiat, "High-efficiency single-photon generation via large-scale active time multiplexing", Science Advances **5**, eaaw8586 (2019).

[24]U. Sinha, S. N. Sahoo, A. Singh, K. Joarder, R. Chatterjee, and S. Chakraborti, "Single-photon sources", Optics and Photonics News **30**, 32–39 (2019).

[25]E. Meyer-Scott, N. Montaut, J. Tiedau, L. Sansoni, H. Herrmann, T. J. Bartley, and C. Silberhorn, "Limits on the heralding efficiencies and spectral purities of spectrally filtered single photons from photon-pair sources", Physical Review A **95**, 061803 (2017).

[26]E. Meyer-Scott, C. Silberhorn, and A. Migdall, "Single-photon sources: approaching the ideal through multiplexing", Review of Scientific Instruments **91**, 041101 (2020).

[27]E. Meyer-Scott, N. Prasannan, I. Dhand, C. Eigner, V. Quiring, S. Barkhofen, B. Brecht, M. B. Plenio, and C. Silberhorn, "Scalable generation of multiphoton entangled states by active feed-forward and multiplexing", Physical Review Letters **129**, 150501 (2022).

[28]S. Ramelow, A. Mech, M. Giustina, S. Gröblacher, W. Wieczorek, J. Beyer, A. Lita, B. Calkins, T. Gerrits, S. W. Nam, et al., "Highly efficient heralding of entangled single photons", Optics express **21**, 6707–6717 (2013).

[29]L.-M. Duan, M. D. Lukin, J. I. Cirac, and P. Zoller, "Long-distance quantum communication with atomic ensembles and linear optics", Nature **414**, 413–418 (2001).

[30]N. Sangouard, C. Simon, H. De Riedmatten, and N. Gisin, "Quantum repeaters based on atomic ensembles and linear optics", Reviews of Modern Physics **83**, 33 (2011).

[31]K. Shinbrough, D. R. Pearson Jr., B. Fang, E. A. Goldschmidt, and V. O. Lorenz, "Broadband quantum memory in atomic ensembles", Advances in Atomic, Molecular, and Optical Physics, 297 (2023).

[32]W. K. Wootters and W. H. Zurek, "A single quantum cannot be cloned", Nature **299**, 802–803 (1982).

[33]S. Muralidharan, L. Li, J. Kim, N. Lütkenhaus, M. D. Lukin, and L. Jiang, "Optimal architectures for long distance quantum communication", Scientific reports **6**, 1–10 (2016).

[34]J. Kitching, "Chip-scale atomic devices", Applied Physics Reviews **5**, 031302 (2018).

[35]L. Lu, X. Zheng, Y. Lu, S. Zhu, and X.-S. Ma, "Advances in chip-scale quantum photonic technologies", Advanced Quantum Technologies **4**, 2100068 (2021).

[36]L. Bremer, S. Fischbach, S.-I. Park, S. Rodt, J.-D. Song, T. Heindel, and S. Reitzenstein, "Cesium-vapor-based delay of single photons emitted by deterministically fabricated quantum dot microlenses", Advanced Quantum Technologies **3**, 1900071 (2020).

[37]J. Maisch, H. Vural, M. Jetter, P. Michler, I. Gerhardt, and S. L. Portalupi, "Controllable delay and polarization routing of single photons", Advanced Quantum Technologies **3**, 1900057 (2020).

[38]J. D. Siverns, J. Hannegan, and Q. Quraishi, "Demonstration of slow light in rubidium vapor using single photons from a trapped ion", Science Advances **5**, eaav4651 (2019).

[39]N. Akopian, L. Wang, A. Rastelli, O. G. Schmidt, and V. Zwiller, "Hybrid semiconductor-atomic interface: slowing down single photons from a quantum dot", Nature Photonics **5**, 230–233 (2011).

[40]H. J. Kimble, "The quantum internet", Nature **453**, 1023–1030 (2008).

[41]W. Tittel, J. Brendel, H. Zbinden, and N. Gisin, "Violation of bell inequalities by photons more than 10 km apart", Physical Review Letters **81**, 3563 (1998).

[42]J.-W. Pan, D. Bouwmeester, H. Weinfurter, and A. Zeilinger, "Experimental entanglement swapping: entangling photons that never interacted", Physical Review Letters **80**, 3891 (1998).

[43]D. Bouwmeester, J.-W. Pan, K. Mattle, M. Eibl, H. Weinfurter, and A. Zeilinger, "Experimental quantum teleportation", Nature **390**, 575–579 (1997).

[44]P. W. Shor and J. Preskill, "Simple proof of security of the bb84 quantum key distribution protocol", Physical Review Letters **85**, 441 (2000).

[45]D. Gottesman, T. Jennewein, and S. Croke, "Longer-baseline telescopes using quantum repeaters", Physical Review Letters **109**, 070503 (2012).

[46]G. Campbell, O. Pinel, M. Hosseini, T. C. Ralph, B. Buchler, and P. K. Lam, "Configurable unitary transformations and linear logic gates using quantum memories", Physical Review Letters **113**, 063601 (2014).

[47]D. Kielpinski, V. Meyer, M. Rowe, C. A. Sackett, W. M. Itano, C. Monroe, and D. J. Wineland, "A decoherence-free quantum memory using trapped ions", Science **291**, 1013–1015 (2001).

[48]Y. Wang, M. Um, J. Zhang, S. An, M. Lyu, J.-N. Zhang, L.-M. Duan, D. Yum, and K. Kim, "Single-qubit quantum memory exceeding ten-minute coherence time", Nature Photonics **11**, 646–650 (2017).

[49]S. Yang, Y. Wang, D. B. Rao, T. Hien Tran, A. S. Momenzadeh, M. Markham, D. Twitchen, P. Wang, W. Yang, R. Stöhr, et al., "High-fidelity transfer and storage of photon states in a single nuclear spin", Nature Photonics **10**, 507–511 (2016).

[50]M. K. Bhaskar, R. Riedinger, B. Machielse, D. S. Levonian, C. T. Nguyen, E. N. Knall, H. Park, D. Englund, M. Loncar, D. D. Sukachev, et al., "Experimental demonstration of memory-enhanced quantum communication", Nature **580**, 60–64 (2020).

[51]A. Reiserer and G. Rempe, "Cavity-based quantum networks with single atoms and optical photons", Reviews of Modern Physics **87**, 1379–1418 (2015).

[52]K. Shinbrough and V. O. Lorenz, "Variance-based sensitivity analysis of Λ-type quantum memory", arXiv preprint arXiv:2210.05530 (2022).

[53]R. Finkelstein, E. Poem, O. Michel, O. Lahad, and O. Firstenberg, "Fast, noise-free memory for photon synchronization at room temperature", Science Advances **4**, eaap8598 (2018).

[54]K. Kaczmarek, P. Ledingham, B. Brecht, S. Thomas, G. Thekkadath, O. Lazo-Arjona, J. Munns, E. Poem, A. Feizpour, D. Saunders, et al., "High-speed noise-free optical quantum memory", Physical Review A **97**, 042316 (2018).

[55]S. Thomas, S. Sagona-Stophel, Z. Schofield, I. Walmsley, and P. Ledingham, "A single-photon-compatible telecom-c-band quantum memory in a hot atomic gas", arXiv preprint arXiv:2211.04415 (2022).

[56]R. Finkelstein, O. Lahad, I. Cohen, O. Davidson, S. Kiriati, E. Poem, and O. Firstenberg, "Continuous protection of a collective state from inhomogeneous dephasing", Physical Review X **11**, 011008 (2021).

[57]O. Davidson, O. Yogev, E. Poem, and O. Firstenberg, "Fast, noise-free atomic optical memory with 35% end-to-end efficiency", arXiv preprint arXiv:2212.04263 (2022).

[58]T. H. Qiu, H. Li, M. Xie, Q. Liu, and H. Y. Ma, "Coherent generation and manipulation of entangled stationary photons based on a multiple degrees of freedom quantum memory", Opt. Express **27**, 27477–27487 (2019).

[59]P. Li, Y. Gu, K. Wang, and Q. Gong, "Dark-state polaritons for quantum memory in a five-level M-type atomic ensemble", Phys. Rev. A **73**, 032343 (2006).

[60]B. S. Ham, "A wavelength-convertible quantum memory: controlled echo", Scientific Reports **8**, 10675 (2018).

[61]G. Hétet, J. J. Longdell, A. L. Alexander, P. K. Lam, and M. J. Sellars, "Electro-optic quantum memory for light using two-level atoms", Phys. Rev. Lett. **100**, 023601 (2008).

[62]Y.-C. Wei, S.-X. Lin, P.-J. Tsai, and Y.-C. Chen, "Memory-based optical polarization conversion in a double-Λatomic system with degenerate zeeman states", Scientific Reports **10**, 13990 (2020).

[63]K. Jensen, W. Wasilewski, H. Krauter, T. Fernholz, B. M. Nielsen, M. Owari, M. B. Plenio, A. Serafini, M. M. Wolf, and E. S. Polzik, "Quantum memory for entangled continuous-variable states", Nature Physics **7**, 13–16 (2011).

[64]F. Arecchi and R. Bonifacio, "Theory of optical maser amplifiers", IEEE Journal of Quantum Electronics **1**, 169–178 (1965).

[65]A. V. Gorshkov, A. André, M. D. Lukin, and A. S. Sørensen, "Photon storage in Λ-type optically dense atomic media. i. cavity model", Physical Review A **76**, 033804 (2007).

[66]A. V. Gorshkov, A. André, M. D. Lukin, and A. S. Sørensen, "Photon storage in Λ-type optically dense atomic media. ii. free-space model", Physical Review A **76**, 033805 (2007).

[67]A. V. Gorshkov, A. André, M. D. Lukin, and A. S. Sørensen, "Photon storage in Λ-type optically dense atomic media. iii. effects of inhomogeneous broadening", Physical Review A **76**, 033806 (2007).

[68]A. V. Gorshkov, A. André, M. Fleischhauer, A. S. Sørensen, and M. D. Lukin, "Universal approach to optimal photon storage in atomic media", Physical Review Letters **98**, 123601 (2007).

[69]J. Nunn, "Quantum memory in atomic ensembles", PhD thesis (St. John's College, Oxford University, 2008).

[70]M. Bouillard, G. Boucher, J. F. Ortas, B. Pointard, and R. Tualle-Brouri, "Quantum storage of single-photon and two-photon fock states with an all-optical quantum memory", Physical Review Letters **122**, 210501 (2019).

[71]T. Pittman, B. Jacobs, and J. Franson, "Single photons on pseudodemand from stored parametric down-conversion", Physical Review A **66**, 042303 (2002).

[72]F. Kaneda, B. G. Christensen, J. J. Wong, H. S. Park, K. T. McCusker, and P. G. Kwiat, "Time-multiplexed heralded single-photon source", Optica **2**, 1010–1013 (2015).

[73]C. Xiong, X. Zhang, Z. Liu, M. J. Collins, A. Mahendra, L. Helt, M. J. Steel, D.-Y. Choi, C. Chae, P. Leong, et al., "Active temporal multiplexing of indistinguishable heralded single photons", Nature Communications **7**, 1–6 (2016).

[74]K. Makino, Y. Hashimoto, J.-i. Yoshikawa, H. Ohdan, T. Toyama, P. van Loock, and A. Furusawa, "Synchronization of optical photons for quantum information processing", Science Advances **2**, e1501772 (2016).

[75]T. Pittman and J. Franson, "Cyclical quantum memory for photonic qubits", Physical Review A **66**, 062302 (2002).

[76]X.-L. Pang, A.-L. Yang, J.-P. Dou, H. Li, C.-N. Zhang, E. Poem, D. J. Saunders, H. Tang, J. Nunn, I. A. Walmsley, et al., "A hybrid quantum memory–enabled network at room temperature", Science Advances **6**, eaax1425 (2020).

[77]S. Clemmen, A. Farsi, S. Ramelow, and A. L. Gaeta, "All-optically tunable buffer for single photons", Optics Letters **43**, 2138–2141 (2018).

[78]A. G. Magnoni, I. H. López Grande, L. T. Knoll, and M. A. Larotonda, "Performance of a temporally multiplexed single-photon source with imperfect devices", Quantum Information Processing **18**, 1–13 (2019).

[79]P. J. Bustard, K. Bonsma-Fisher, C. Hnatovsky, D. Grobnic, S. J. Mihailov, D. England, and B. J. Sussman, "Toward a quantum memory in a fiber cavity controlled by intracavity frequency translation", Physical Review Letters **128**, 120501 (2022).

[80]Y.-W. Cho, G. Campbell, J. Everett, J. Bernu, D. Higginbottom, M. Cao, J. Geng, N. Robins, P. Lam, and B. Buchler, "Highly efficient optical quantum memory with long coherence time in cold atoms", Optica **3**, 100–107 (2016).

[81]G. P. Agrawal, *Fiber-optic communication systems* (John Wiley & Sons, 2012).

[82]M. R. Sprague, D. G. England, A. Abdolvand, J. Nunn, X.-M. Jin, W. S. Kolthammer, M. Barbieri, B. Rigal, P. S. Michelberger, T. F. Champion, et al., "Efficient optical pumping and high optical depth in a hollow-core photonic-crystal fibre for a broadband quantum memory", New Journal of Physics **15**, 055013 (2013).

[83]M. Sprague, P. Michelberger, T. Champion, D. England, J. Nunn, X.-M. Jin, W. Kolthammer, A. Abdolvand, P. S. J. Russell, and I. Walmsley, "Broadband single-photon-level memory in a hollow-core photonic crystal fibre", Nature Photonics **8**, 287–291 (2014).

[84]T. Peters, T.-P. Wang, A. Neumann, L. S. Simeonov, and T. Halfmann, "Single-photon-level narrowband memory in a hollow-core photonic bandgap fiber", Optics Express **28**, 5340–5354 (2020).

[85]M. Bajcsy, S. Hofferberth, V. Balic, T. Peyronel, M. Hafezi, A. S. Zibrov, V. Vuletic, and M. D. Lukin, "Efficient all-optical switching using slow light within a hollow fiber", Physical Review Letters **102**, 203902 (2009).

[86]B. Gouraud, D. Maxein, A. Nicolas, O. Morin, and J. Laurat, "Demonstration of a memory for tightly guided light in an optical nanofiber", Physical Review Letters **114**, 180503 (2015).

[87]K. Heshami, D. G. England, P. C. Humphreys, P. J. Bustard, V. M. Acosta, J. Nunn, and B. J. Sussman, "Quantum memories: emerging applications and recent advances", Journal of modern optics **63**, 2005–2028 (2016).

[88]A. K. Patnaik, J. Liang, and K. Hakuta, "Slow light propagation in a thin optical fiber via electromagnetically induced transparency", Physical Review A **66**, 063808 (2002).

[89]K. F. Reim, J. Nunn, X.-M. Jin, P. Michelberger, T. Champion, D. G. England, K. Lee, W. Kolthammer, N. Langford, and I. Walmsley, "Multipulse addressing of a raman quantum memory: configurable beam splitting and efficient readout", Physical Review Letters **108**, 263602 (2012).

[90]E. Saglamyurek, T. Hrushevskyi, A. Rastogi, K. Heshami, and L. J. LeBlanc, "Coherent storage and manipulation of broadband photons via dynamically controlled autler–townes splitting", Nature Photonics **12**, 774–782 (2018).

[91]L. Heller, J. Lowinski, K. Theophilo, A. Padrón-Brito, and H. de Riedmatten, "Raman storage of quasideterministic single photons generated by rydberg collective excitations in a low-noise quantum memory", Physical Review Applied **18**, 024036 (2022).

[92]D. G. England, K. A. Fisher, J.-P. W. MacLean, P. J. Bustard, R. Lausten, K. J. Resch, and B. J. Sussman, "Storage and retrieval of thz-bandwidth single photons using a room-temperature diamond quantum memory", Physical Review Letters **114**, 053602 (2015).

[93]K. A. Fisher, D. G. England, J.-P. W. MacLean, P. J. Bustard, K. J. Resch, and B. J. Sussman, "Frequency and bandwidth conversion of single photons in a room-temperature diamond quantum memory", Nature Communications **7**, 1–6 (2016).

[94]P. J. Bustard, D. G. England, K. Heshami, C. Kupchak, and B. J. Sussman, "Quantum frequency conversion with ultra-broadband tuning in a raman memory", Physical Review A **95**, 053816 (2017).

[95]E. Saglamyurek, N. Sinclair, J. A. Slater, K. Heshami, D. Oblak, and W. Tittel, "An integrated processor for photonic quantum states using a broadband light–matter interface", New Journal of Physics **16**, 065019 (2014).

[96]N. N. Oza, Y.-P. Huang, and P. Kumar, "Entanglement-preserving photonic switching: full cross-bar operation with quantum data streams", IEEE Photonics Technology Letters **26**, 356–359 (2013).

[97]U. Purakayastha, C. P. Lualdi, and P. G. Kwiat, "Ultrafast all-optical switching of telecom single photons", in Frontiers in optics (Optica Publishing Group, 2022), FTu6B–1.

[98]A. Alarcon, P. González, J. Cariñe, G. Lima, and G. B. Xavier, "Polarization-independent single-photon switch based on a fiber-optical sagnac interferometer for quantum communication networks", Optics Express **28**, 33731–33738 (2020).

[99]M. A. Hall, J. B. Altepeter, and P. Kumar, "Ultrafast switching of photonic entanglement", Physical Review Letters **106**, 053901 (2011).

[100]D. England, F. Bouchard, K. Fenwick, K. Bonsma-Fisher, Y. Zhang, P. J. Bustard, and B. J. Sussman, "Perspectives on all-optical kerr switching for quantum optical applications", Applied Physics Letters **119**, 160501 (2021).

[101]C. Kupchak, J. Erskine, D. England, and B. Sussman, "Terahertz-bandwidth switching of heralded single photons", Optics Letters **44**, 1427–1430 (2019).

[102]T. Volz, A. Reinhard, M. Winger, A. Badolato, K. J. Hennessy, E. L. Hu, and Imamoglu, "Ultrafast all-optical switching by single photons", Nature Photonics **6**, 605–609 (2012).

[103]C. Kupchak, P. J. Bustard, K. Heshami, J. Erskine, M. Spanner, D. G. England, and B. J. Sussman, "Time-bin-to-polarization conversion of ultrafast photonic qubits", Physical Review A **96**, 053812 (2017).

[104]S. Friberg, Y. Silberberg, M. Oliver, M. Andrejco, M. Saifi, and P. Smith, "Ultrafast all-optical switching in a dual-core fiber nonlinear coupler", Applied Physics Letters **51**, 1135–1137 (1987).

[105]V. R. Almeida, C. A. Barrios, R. R. Panepucci, and M. Lipson, "All-optical control of light on a silicon chip", Nature **431**, 1081–1084 (2004).

[106]K. Nozaki, T. Tanabe, A. Shinya, S. Matsuo, T. Sato, H. Taniyama, and M. Notomi, "Sub-femtojoule all-optical switching using a photonic-crystal nanocavity", Nature Photonics **4**, 477–483 (2010).

[107]H. Kanbara, H. Kobayashi, T. Kaino, T. Kurihara, N. Ooba, and K. Kubodera, "Highly efficient ultrafast optical kerr shutters with the use of organic nonlinear materials", Josa B **11**, 2216–2223 (1994).

[108]L. S. Costanzo, A. S. Coelho, D. Pellegrino, M. S. Mendes, L. Acioli, K. N. Cassemiro, D. Felinto, A. Zavatta, and M. Bellini, "Zero-area single-photon pulses", Physical Review Letters **116**, 023602 (2016).

[109]K. Shinbrough, B. D. Hunt, S. Park, K. Oolman, T. Loveridge, J. G. Eden, and V. O. Lorenz, "Broadband quantum memory in atomic barium vapor with 95% storage efficiency", in Conference on lasers and electro-optics (cleo) (Optica Publishing Group, 2023).

[110]K. Shinbrough, B. D. Hunt, S. Park, K. Oolman, J. G. Eden, and V. O. Lorenz, "Efficient thz-bandwidth quantum memory in atomic barium", in Frontiers in optics + laser science 2022 (fio, ls) (Optica Publishing Group, 2022), FTh3C.7.

[111]K. Reim, J. Nunn, V. Lorenz, B. Sussman, K. Lee, N. Langford, D. Jaksch, and I. Walmsley, "Towards high-speed optical quantum memories", Nature Photonics **4**, 218–221 (2010).

[112]A. S. Cacciapuoti, M. Caleffi, F. Tafuri, F. S. Cataliotti, S. Gherardini, and G. Bianchi, "Quantum internet: networking challenges in distributed quantum computing", IEEE Network **34**, 137–143 (2019).

[113]D. England, P. Michelberger, T. Champion, K. Reim, K. Lee, M. Sprague, X. Jin, N. Langford, W. Kolthammer, J. Nunn, et al., "High-fidelity polarization storage in a gigahertz bandwidth quantum memory", Journal of Physics B: Atomic, Molecular and Optical Physics **45**, 124008 (2012).

[114]Q. He, M. Reid, E. Giacobino, J. Cviklinski, and P. Drummond, "Dynamical oscillator-cavity model for quantum memories", Physical Review A **79**, 022310 (2009).

[115]Y.-H. Chen, M.-J. Lee, I.-C. Wang, S. Du, Y.-F. Chen, Y.-C. Chen, and A. Y. Ite, "Coherent optical memory with high storage efficiency and large fractional delay", Physical Review Letters **110**, 083601 (2013).

[116]Y. Wang, J. Li, S. Zhang, K. Su, Y. Zhou, K. Liao, S. Du, H. Yan, and S.-L. Zhu, "Efficient quantum memory for single-photon polarization qubits", Nature Photonics **13**, 346–351 (2019).

[117]Y.-C. Wei, B.-H. Wu, Y.-F. Hsiao, P.-J. Tsai, and Y.-C. Chen, "Broadband coherent optical memory based on electromagnetically induced transparency", Physical Review A **102**, 063720 (2020).

[118]J. Nunn, K. Reim, K. Lee, V. Lorenz, B. Sussman, I. Walmsley, and D. Jaksch, "Multimode memories in atomic ensembles", Physical Review Letters **101**, 260502 (2008).

[119]K. Surmacz, J. Nunn, K. Reim, K. Lee, V. Lorenz, B. Sussman, I. Walmsley, and D. Jaksch, "Efficient spatially resolved multimode quantum memory", Physical Review A **78**, 033806 (2008).

[120]Y. Pu, N. Jiang, W. Chang, H. Yang, C. Li, and L. Duan, "Experimental realization of a multiplexed quantum memory with 225 individually accessible memory cells", Nature Communications **8**, 1–6 (2017).

[121]M. Afzelius, C. Simon, H. De Riedmatten, and N. Gisin, "Multimode quantum memory based on atomic frequency combs", Physical Review A **79**, 052329 (2009).

[122]N. Sinclair, E. Saglamyurek, H. Mallahzadeh, J. A. Slater, M. George, R. Ricken, M. P. Hedges, D. Oblak, C. Simon, W. Sohler, et al., "Spectral multiplexing for scalable quantum photonics using an atomic frequency comb quantum memory and feed-forward control", Physical Review Letters **113**, 053603 (2014).

[123]G. Teja and S. K. Goyal, "Studying the effect of fluctuating environment on intra-atomic frequency comb based quantum memory", Scientific Reports **11**, 1–9 (2021).

[124]I. M. Sobol, "Global sensitivity indices for nonlinear mathematical models and their monte carlo estimates", Mathematics and Computers in Simulation **55**, 271–280 (2001).

[125]I. Sobol and S. Kucherenko, "On global sensitivity analysis of quasi-monte carlo algorithms", Monte Carlo Methods and Applications **11**, 83–92 (2005).

[126]I. M. Sobol, "Sensitivity analysis for non-linear mathematical models", Mathematical Modelling and Computational Experiment **1**, 407–414 (1993).

[127]T. Miya, Y. Terunuma, T. Hosaka, and T. Miyashita, "Ultimate low-loss single-mode fibre at 1.55? m", Electronics Letters **4**, 106–108 (1979).

[128]A. C. Leung, W. Lau, A. D. Tranter, K. V. Paul, M. Rambach, B. C. Buchler, P. K. Lam, A. G. White, and T. J. Weinhold, "Efficient, ever-ready quantum memory at room temperature for single photons", arXiv preprint arXiv:2203.12108 (2022).

[129]M. Fleischhauer, A. Imamoglu, and J. P. Marangos, "Electromagnetically induced transparency: optics in coherent media", Reviews of Modern Physics **77**, 633 (2005).

[130]M. Fleischhauer and M. D. Lukin, "Quantum memory for photons: dark-state polaritons", Physical Review A **65**, 022314 (2002).

[131]M. Fleischhauer and M. D. Lukin, "Dark-state polaritons in electromagnetically induced transparency", Physical Review Letters **84**, 5094 (2000).

[132]D. F. Phillips, A. Fleischhauer, A. Mair, R. L. Walsworth, and M. D. Lukin, "Storage of light in atomic vapor", Physical Review Letters **86**, 783 (2001).

[133]A. I. Lvovsky, B. C. Sanders, and W. Tittel, Nature Photonics **3**, 706–714 (2009).

[134]A. Rastogi, E. Saglamyurek, T. Hrushevskyi, S. Hubele, and L. J. LeBlanc, "Discerning quantum memories based on electromagnetically-induced-transparency and autler-townes-splitting protocols", Physical Review A **100**, 012314 (2019).

[135]L. Ma, O. Slattery, and X. Tang, "Optical quantum memory based on electromagnetically induced transparency", Journal of Optics **19**, 043001 (2017).

[136]X. Lei, L. Ma, J. Yan, X. Zhou, Z. Yan, and X. Jia, "Electromagnetically induced transparency quantum memory for non-classical states of light", Advances in Physics: X **7**, 2060133 (2022).

[137]I. Novikova, R. L. Walsworth, and Y. Xiao, "Electromagnetically induced transparency-based slow and stored light in warm atoms", Laser & Photonics Reviews **6**, 333–353 (2012).

[138]Y.-F. Hsiao, P.-J. Tsai, H.-S. Chen, S.-X. Lin, C.-C. Hung, C.-H. Lee, Y.-H. Chen, Y.-F. Chen, A. Y. Ite, and Y.-C. Chen, "Highly efficient coherent optical memory based on electromagnetically induced transparency", Physical Review Letters **120**, 183602 (2018).

[139]Y. Dudin, L. Li, and A. Kuzmich, "Light storage on the time scale of a minute", Physical Review A **87**, 031801 (2013).

[140]G. Heinze, C. Hubrich, and T. Halfmann, "Stopped light and image storage by electromagnetically induced transparency up to the regime of one minute", Physical Review Letters **111**, 033601 (2013).

[141]K. Shinbrough, B. D. Hunt, and V. O. Lorenz, "Optimization of broadband Λ-type quantum memory using gaussian pulses", Physical Review A **103**, 062418 (2021).

[142]J. Wolters, G. Buser, A. Horsley, L. Béguin, A. Jöckel, J.-P. Jahn, R. J. Warburton, and P. Treutlein, "Simple atomic quantum memory suitable for semiconductor quantum dot single photons", Physical Review Letters **119**, 060502 (2017).

[143]A. Rastogi, E. Saglamyurek, T. Hrushevskyi, and L. J. LeBlanc, "Superradiance-mediated photon storage for broadband quantum memory", Physical Review Letters **129**, 120502 (2022).

[144]E. Saglamyurek, T. Hrushevskyi, A. Rastogi, L. W. Cooke, B. D. Smith, and L. J. LeBlanc, "Storing short single-photon-level optical pulses in bose–einstein condensates for high-performance quantum memory", New Journal of Physics **23**, 043028 (2021).

[145]N. B. Phillips, A. V. Gorshkov, and I. Novikova, "Light storage in an optically thick atomic ensemble under conditions of electromagnetically induced transparency and four-wave mixing", Physical Review A **83**, 063823 (2011).

[146]N. Lauk, C. O'Brien, and M. Fleischhauer, "Fidelity of photon propagation in electromagnetically induced transparency in the presence of four-wave mixing", Physical Review A **88**, 013823 (2013).

[147]J. Geng, G. Campbell, J. Bernu, D. Higginbottom, B. Sparkes, S. Assad, W. Zhang, N. Robins, P. K. Lam, and B. Buchler, "Electromagnetically induced transparency and four-wave mixing in a cold atomic ensemble with large optical depth", New Journal of Physics **16**, 113053 (2014).

[148]L. Ma, O. Slattery, and X. Tang, "Noise reduction in optically controlled quantum memory", Modern Physics Letters B **32**, 1830001 (2018).

[149]K. Zhang, J. Guo, L. Chen, C. Yuan, Z. Ou, and W. Zhang, "Suppression of the four-wave-mixing background noise in a quantum memory retrieval process by channel blocking", Physical Review A **90**, 033823 (2014).

[150]J. Nunn, J. Munns, S. Thomas, K. T. Kaczmarek, C. Qiu, A. Feizpour, E. Poem, B. Brecht, D. Saunders, P. M. Ledingham, et al., "Theory of noise suppression in Λ-type quantum memories by means of a cavity", Physical Review A **96**, 012338 (2017).

[151]M. Dabrowski, R. Chrapkiewicz, and W. Wasilewski, "Hamiltonian design in readout from room-temperature raman atomic memory", Optics Express **22**, 26076–26091 (2014).

[152]S. E. Thomas, T. M. Hird, J. H. Munns, B. Brecht, D. J. Saunders, J. Nunn, I. A. Walmsley, and P. M. Ledingham, "Raman quantum memory with built-in suppression of four-wave-mixing noise", Physical Review A **100**, 033801 (2019).

[153]N. E. Rehler and J. H. Eberly, "Superradiance", Physical Review A **3**, 1735 (1971).

[154]S. Roof, K. Kemp, M. Havey, and I. Sokolov, "Observation of single-photon superradiance and the cooperative lamb shift in an extended sample of cold atoms", Physical Review Letters **117**, 073003 (2016).

[155]S. A. Moiseev and S. Kröll, "Complete reconstruction of the quantum state of a single-photon wave packet absorbed by a doppler-broadened transition", Physical Review Letters **87**, 173601 (2001).

[156]V. C. Vivoli, N. Sangouard, M. Afzelius, and N. Gisin, New Journal of Physics **15**, 095012 (2013).

[157]A. Carvalho, R. Moreira, J. Ferraz, S. Vianna, L. Acioli, and D. Felinto, "Enhanced absorption of weak ultrashort light pulses by a narrowband atomic medium", Physical Review A **101**, 053426 (2020).

[158]J. Nunn, I. Walmsley, M. Raymer, K. Surmacz, F. Waldermann, Z. Wang, and D. Jaksch, "Mapping broadband single-photon wave packets into an atomic memory", Physical Review A **75**, 011401 (2007).

[159]K. A. Fisher, D. G. England, J.-P. W. MacLean, P. J. Bustard, K. Heshami, K. J. Resch, and B. J. Sussman, "Storage of polarization-entangled thz-bandwidth photons in a diamond quantum memory", Physical Review A **96**, 012324 (2017).

[160]D. England, P. Bustard, J. Nunn, R. Lausten, and B. Sussman, "From photons to phonons and back: a thz optical memory in diamond", Physical Review Letters **111**, 243601 (2013).

[161]P. J. Bustard, R. Lausten, D. G. England, and B. J. Sussman, "Toward quantum processing in molecules: a thz-bandwidth coherent memory for light", Physical Review Letters **111**, 083901 (2013).

[162]G. Campbell, K. Ferguson, M. Sellars, B. Buchler, and P. Lam, "Echo-based quantum memory", arXiv preprint arXiv:1902.04313 (2019).

[163]N. Sangouard, C. Simon, M. Afzelius, and N. Gisin, "Analysis of a quantum memory for photons based on controlled reversible inhomogeneous broadening", Physical Review A **75**, 032327 (2007).

[164]B. Kraus, W. Tittel, N. Gisin, M. Nilsson, S. Kröll, and J. I. Cirac, "Quantum memory for nonstationary light fields based on controlled reversible inhomogeneous broadening", Physical Review A **73**, 020302 (2006).

[165]C. Simon, M. Afzelius, J. Appel, A. Boyer de La Giroday, S. Dewhurst, N. Gisin, C. Hu, F. Jelezko, S. Kröll, J. Müller, et al., "Quantum memories", The European Physical Journal D **58**, 1–22 (2010).

[166]D. L. McAuslan, P. M. Ledingham, W. R. Naylor, S. E. Beavan, M. P. Hedges, M. J. Sellars, and J. J. Longdell, "Photon-echo quantum memories in inhomogeneously broadened two-level atoms", Physical Review A **84**, 022309 (2011).

[167]S. Moiseev, "Photon-echo-based quantum memory of arbitrary light field states", Journal of Physics B: Atomic, Molecular and Optical Physics **40**, 3877 (2007).

[168]J. J. Longdell, G. Hetet, P. K. Lam, and M. Sellars, "Analytic treatment of controlled reversible inhomogeneous broadening quantum memories for light using two-level atoms", Physical Review A **78**, 032337 (2008).

[169]M. P. Hedges, J. J. Longdell, Y. Li, and M. J. Sellars, "Efficient quantum memory for light", Nature **465**, 1052–1056 (2010).

[170]B. Lauritzen, J. Minář, H. De Riedmatten, M. Afzelius, N. Sangouard, C. Simon, and N. Gisin, "Telecommunication-wavelength solid-state memory at the single photon level", Physical Review Letters **104**, 080502 (2010).

[171]A. C. Leung, K. S. I. Melody, A. D. Tranter, K. V. Paul, G. T. Campbell, P. K. Lam, and B. C. Buchler, "Observation of cross phase modulation in cold atom gradient echo memory", New Journal of Physics **24**, 093011 (2022).

[172]B. M. Sparkes, J. Bernu, M. Hosseini, J. Geng, Q. Glorieux, P. A. Altin, P. K. Lam, N. P. Robins, and B. C. Buchler, "An ultra-high optical depth cold atomic ensemble for quantum memories", Journal of Physics: Conference Series **467**, 012009 (2013).

[173]B. M. Sparkes, M. Hosseini, G. Hétet, P. K. Lam, and B. C. Buchler, "Ac stark gradient echo memory in cold atoms", Physical Review A **82**, 043847 (2010).

[174]H. De Riedmatten, M. Afzelius, M. U. Staudt, C. Simon, and N. Gisin, "A solid-state light–matter interface at the single-photon level", Nature **456**, 773–777 (2008).

[175]E. Saglamyurek, M. Grimau Puigibert, Q. Zhou, L. Giner, F. Marsili, V. B. Verma, S. Woo Nam, L. Oesterling, D. Nippa, D. Oblak, et al., "A multiplexed light-matter interface for fibre-based quantum networks", Nature Communications **7**, 11202 (2016).

[176]M. Bonarota, V. Damon, T. Chanelière, J.-L. Le Gouët, and M. Pascual-Winter, "Revival of silenced echo for optical quantum memories: efficiency and noise level", in Quantum information and measurement (Optica Publishing Group, 2012), Qw2a–6.

[177]J. Ruggiero, J.-L. Le Gouët, C. Simon, and T. Chaneliere, "Why the two-pulse photon echo is not a good quantum memory protocol", Physical Review A **79**, 053851 (2009).

[178]J. Dajczgewand, J.-L. L. Gouët, A. Louchet-Chauvet, and T. Chanelière, "Large efficiency at telecom wavelength for optical quantum memories", Optics Letters **39**, 2711–2714 (2014).

[179]V. Damon, M. Bonarota, A. Louchet-Chauvet, T. Chaneliere, and J.-L. Le Gouët, "Revival of silenced echo and quantum memory for light", New Journal of Physics **13**, 093031 (2011).

[180]M. Bonarota, J. Dajczgewand, A. Louchet-Chauvet, J.-L. Le Gouët, and T. Chanelière, "Photon echo with a few photons in two-level atoms", Laser Physics **24**, 094003 (2014).

[181]M. Minnegaliev, K. Gerasimov, T. Sabirov, R. Urmancheev, and S. Moiseev, "Implementation of an optical quantum memory protocol in the 167er3+: y2sio5 crystal", JETP Letters **115**, 720–727 (2022).

[182]M. Minnegaliev, K. Gerasimov, R. Urmancheev, and S. Moiseev, "Experimental realization of revival of silenced echo memory protocol in optical cavity", in Epj web of conferences, Vol. 190 (EDP Sciences, 2018), p. 03007.

[183]K. Gerasimov, M. Minnegaliev, S. Moiseev, R. Urmancheev, T. Chanelière, and A. Louchet-Chauvet, "Quantum memory in an orthogonal geometry of silenced echo retrieval", Optics and Spectroscopy **123**, 211–216 (2017).

[184]M. Minnegaliev, K. Gerasimov, R. Urmancheev, A. Zheltikov, and S. Moiseev, "Linear stark effect in y3al5o12:tm3 crystal and its application in the addressable quantum memory protocol", Physical Review B **103**, 174110 (2021).

[185]S. Jiang, X.-M. Luo, L.-Q. Chen, B. Ning, S. Chen, J.-Y. Wang, Z.-P. Zhong, and J.-W. Pan, "Observation of prolonged coherence time of the collective spin wave of an atomic ensemble in a paraffin-coated r 87 b vapor cell", Physical Review A **80**, 062303 (2009).

[186]J. Guo, X. Feng, P. Yang, Z. Yu, L. Q. Chen, C.-H. Yuan, and W. Zhang, "High-performance raman quantum memory with optimal control in room temperature atoms", Nature Communications **10**, 148 (2019).

[187]S. Brandt, A. Nagel, R. Wynands, and D. Meschede, "Buffer-gas-induced linewidth reduction of coherent dark resonances to below 50 hz", Physical Review A **56**, R1063 (1997).

[188]S. Manz, T. Fernholz, J. Schmiedmayer, and J.-W. Pan, "Collisional decoherence during writing and reading quantum states", Physical Review A **75**, 040101 (2007).

[189]W. Happer, "Optical pumping", Reviews of Modern Physics **44**, 169 (1972).

[190]M. Bouchiat and J. Brossel, "Relaxation of optically pumped rb atoms on paraffin-coated walls", Physical Review **147**, 41 (1966).

[191]D. Rousseau, G. Patterson, and P. Williams, "Resonance raman scattering and collision-induced redistribution scattering in i 2", Physical Review Letters **34**, 1306 (1975).

[192]B. Zhao, Y.-A. Chen, X.-H. Bao, T. Strassel, C.-S. Chuu, X.-M. Jin, J. Schmiedmayer, Z.-S. Yuan, S. Chen, and J.-W. Pan, "A millisecond quantum memory for scalable quantum networks", Nature Physics **5**, 95–99 (2009).

[193]D. Main, T. Hird, S. Gao, E. Oguz, D. Saunders, I. Walmsley, and P. Ledingham, "Preparing narrow velocity distributions for quantum memories in room-temperature alkali-metal vapors", Physical Review A **103**, 043105 (2021).

[194]J. Appel, E. Figueroa, D. Korystov, M. Lobino, and A. Lvovsky, "Quantum memory for squeezed light", Physical Review Letters **100**, 093602 (2008).

[195]H. P. Specht, C. Nölleke, A. Reiserer, M. Uphoff, E. Figueroa, S. Ritter, and G. Rempe, "A single-atom quantum memory", Nature **473**, 190–193 (2011).

[196]L. Tian, S. Li, Z. Zhang, and H. Wang, "Suppressing decoherence of spin waves in a warm atomic vapor by applying a guiding magnetic field", Journal of Physics B: Atomic, Molecular and Optical Physics **48**, 035506 (2015).

[197]C. Vidal and J. Cooper, "Heat-pipe oven: a new, well-defined metal vapor device for spectroscopic measurements", Journal of Applied Physics **40**, 3370–3374 (1969).

[198]C. Vidal and F. Haller, "Heat pipe oven applications. i. isothermal heater of well defined temperature. ii. production of metal vapor-gas mixtures", Review of Scientific Instruments **42**, 1779–1784 (1971).

[199]C. Vidal, "Vapor cells and heat pipes", Experimental methods in the physical sciences **29**, 67–83 (1996).

[200]S. Hendrickson, M. Lai, T. Pittman, and J. Franson, "Observation of two-photon absorption at low power levels using tapered optical fibers in rubidium vapor", Physical Review Letters **105**, 173602 (2010).

[201]S. Ghosh, A. R. Bhagwat, C. K. Renshaw, S. Goh, A. L. Gaeta, and B. J. Kirby, "Low-light-level optical interactions with rubidium vapor in a photonic band-gap fiber", Physical Review Letters **97**, 023603 (2006).

[202]W. Yang, D. B. Conkey, B. Wu, D. Yin, A. R. Hawkins, and H. Schmidt, "Atomic spectroscopy on a chip", Nature Photonics **1**, 331–335 (2007).

[203]E. Alexandrov, M. Balabas, D. Budker, D. English, D. Kimball, C.-H. Li, and V. Yashchuk, "Light-induced desorption of alkali-metal atoms from paraffin coating", Physical Review A **66**, 042903 (2002).

[204]T. Karaulanov, M. Graf, D. English, S. Rochester, Y. Rosen, K. Tsigutkin, D. Budker, E. Alexandrov, M. Balabas, D. J. Kimball, et al., "Controlling atomic vapor density in paraffin-coated cells using light-induced atomic desorption", Physical Review A **79**, 012902 (2009).

[205]E. Talker, P. Arora, R. Zektzer, Y. Sebbag, M. Dikopltsev, and U. Levy, "Light-induced atomic desorption in microfabricated vapor cells for demonstrating quantum optical applications", Physical Review Applied **15**, L051001 (2021).

[206]R. Kalish, "Diamond as a unique high-tech electronic material: difficulties and prospects", Journal of Physics D: Applied Physics **40**, 6467 (2007).

[207]D. G. England, K. A. G. Fisher, J.-P. W. MacLean, P. J. Bustard, K. Heshami, K. J. Resch, and B. J. Sussman, "Phonon-mediated nonclassical interference in diamond", Physical Review Letters **117**, 073603 (2016).

[208]K. Lee, B. Sussman, M. Sprague, P. Michelberger, K. Reim, J. Nunn, N. Langford, P. Bustard, D. Jaksch, and I. Walmsley, "Macroscopic non-classical states and terahertz quantum processing in room-temperature diamond", Nature Photonics **6**, 41–44 (2012).

[209]E. Poem, C. Weinzetl, J. Klatzow, K. Kaczmarek, J. Munns, T. Champion, D. Saunders, J. Nunn, and I. Walmsley, "Broadband noise-free optical quantum memory with neutral nitrogen-vacancy centers in diamond", Physical Review B **91**, 205108 (2015).

[210]K. Heshami, C. Santori, B. Khanaliloo, C. Healey, V. M. Acosta, P. E. Barclay, and C. Simon, "Raman quantum memory based on an ensemble of nitrogen-vacancy centers coupled to a microcavity", Physical Review A **89**, 040301 (2014).

[211]A. Kalachev, A. Berezhnoi, P. Hemmer, and O. Kocharovskaya, "Raman quantum memory based on an ensemble of silicon-vacancy centers in diamond", Laser Physics **29**, 104001 (2019).

[212]C. Li and P. Cappellaro, "Telecom photon interface of solid-state quantum nodes", Journal of Physics Communications **3**, 095016 (2019).

[213]N. Ohlsson, R. K. Mohan, and S. Kröll, "Quantum computer hardware based on rare-earth-ion-doped inorganic crystals", Optics Communications **201**, 71–77 (2002).

[214]J. H. Wesenberg, K. Mølmer, L. Rippe, and S. Kröll, "Scalable designs for quantum computing with rare-earth-ion-doped crystals", Physical Review A **75**, 012304 (2007).

[215]V. Hizhnyakov, V. Boltrushko, H. Kaasik, and Y. Orlovskii, "Rare earth ions doped mixed crystals for fast quantum computers with optical frequency qubits", Optics Communications **485**, 126693 (2021).

[216]I. Roos and K. Mølmer, "Quantum computing with an inhomogeneously broadened ensemble of ions: suppression of errors from detuning variations by specially adapted pulses and coherent population trapping", Physical Review A **69**, 022321 (2004).

[217]A. Walther, L. Rippe, Y. Yan, J. Karlsson, D. Serrano, A. Nilsson, S. Bengtsson, and S. Kröll, "High-fidelity readout scheme for rare-earth solid-state quantum computing", Physical Review A **92**, 022319 (2015).

[218]R. Ahlefeldt, M. Pearce, M. R. Hush, and M. Sellars, "Quantum processing with ensembles of rare-earth ions in a stoichiometric crystal", Physical Review A **101**, 012309 (2020).

[219]M. Grimm, A. Beckert, G. Aeppli, and M. Müller, "Universal quantum computing using electronuclear wavefunctions of rare-earth ions", Physical Review X Quantum **2**, 010312 (2021).

[220]C. W. Thiel, T. Böttger, and R. Cone, "Rare-earth-doped materials for applications in quantum information storage and signal processing", Journal of Luminescence **131**, 353–361 (2011).

[221]T. Zhong, J. M. Kindem, J. Rochman, and A. Faraon, "Interfacing broadband photonic qubits to on-chip cavity-protected rare-earth ensembles", Nature Communications **8**, 1–7 (2017).

[222]A. Arcangeli, R. M. Macfarlane, A. Ferrier, and P. Goldner, "Temperature dependence of nuclear spin coherence in e u 3+: y 2 si o 5", Physical Review B **92**, 224401 (2015).

[223]T. Böttger, C. Thiel, R. Cone, and Y. Sun, "Effects of magnetic field orientation on optical decoherence in er 3+: y 2 sio 5", Physical Review B **79**, 115104 (2009).

[224]M. Zhong, M. P. Hedges, R. L. Ahlefeldt, J. G. Bartholomew, S. E. Beavan, S. M. Wittig, J. J. Longdell, and M. J. Sellars, "Optically addressable nuclear spins in a solid with a six-hour coherence time", Nature **517**, 177–180 (2015).

[225]G. Liu and B. Jacquier, *Spectroscopic properties of rare earths in optical materials*, Vol. 83 (Springer Science & Business Media, 2006).

[226]R. Ahlefeldt et al., "Evaluation of a stoichiometric rare earth crystal for quantum computing", PhD thesis (The Australian National University, 2013).

[227]N. Kunkel and P. Goldner, "Recent advances in rare earth doped inorganic crystalline materials for quantum information processing", Zeitschrift für anorganische und allgemeine Chemie **644**, 66–76 (2018).

[228]S. Hastings-Simon, B. Lauritzen, M. U. Staudt, J. L. M. van Mechelen, C. Simon, H. de Riedmatten, M. Afzelius, and N. Gisin, "Zeeman-level lifetimes in er 3+: y 2 sio 5", Physical Review B **78**, 085410 (2008).

[229]W. Yen, R. Greene, W. Scott, and D. Huber, "Optical linewidth and line-shape studies of energy transfer mechanisms between rare-earth impurity ions", Physical Review **140**, A1188 (1965).

[230]A. Kinos, L. Rippe, A. Walther, and S. Kröll, "Microscopic treatment of instantaneous spectral diffusion and its effect on quantum gate fidelities in rare-earth-ion-doped crystals", Physical Review A **105**, 032608 (2022).

[231]Z.-Q. Zhou, Y. Ma, T. Tu, P.-Y. Li, Z.-F. Li, C. Liu, P.-J. Liang, X. Liu, Y.-L. Hua, T.-S. Yang, et al., "Probing the collective dynamics of nuclear spin bath in a rare-earth ion doped crystal", arXiv preprint arXiv:1803.03075 (2018).

[232]E. Fraval, M. Sellars, and J. Longdell, "Method of extending hyperfine coherence times in pr3", Physical Review Letters **92**, 077601 (2004).

[233]J. Longdell, A. Alexander, and M. Sellars, "Characterization of the hyperfine interaction in europium-doped yttrium orthosilicate and europium chloride hexahydrate", Physical Review B **74**, 195101 (2006).

[234]D. McAuslan, J. Bartholomew, M. Sellars, and J. J. Longdell, "Reducing decoherence in optical and spin transitions in rare-earth-metal-ion–doped materials", Physical Review A **85**, 032339 (2012).

[235]S. Beavan, E. Fraval, M. Sellars, and J. J. Longdell, "Demonstration of the reduction of decoherent errors in a solid-state qubit using dynamic decoupling techniques", Physical Review A **80**, 032308 (2009).

[236]M. Hain, M. Stabel, and T. Halfmann, "Few-photon storage on a second timescale by electromagnetically induced transparency in a doped solid", New Journal of Physics **24**, 023012 (2022).

[237]M. Pascual-Winter, R.-C. Tongning, T. Chaneliere, and J.-L. Le Gouët, "Spin coherence lifetime extension in tm3 through dynamical decoupling", Physical Review B **86**, 184301 (2012).

[238]M. Lovrić, D. Suter, A. Ferrier, and P. Goldner, "Faithful solid state optical memory with dynamically decoupled spin wave storage", Physical Review Letters **111**, 020503 (2013).

[239]E. Fraval, M. J. Sellars, and J. J. Longdell, "Dynamic decoherence control of a solid-state nuclear-quadrupole qubit", Physical Review Letters **95**, 030506 (2005).

[240]R. Macfarlane, A. Cassanho, and R. Meltzer, "Inhomogeneous broadening by nuclear spin fields: a new limit for optical transitions in solids", Physical Review Letters **69**, 542 (1992).

[241]E. Lafitte-Houssat, A. Ferrier, S. Welinski, L. Morvan, M. Afzelius, P. Berger, and P. Goldner, "Optical and spin inhomogeneous linewidths in 171yb3+: y2sio5", Optical Materials: X **14**, 100153 (2022).

[242]C. Thiel, R. Macfarlane, T. Böttger, Y. Sun, R. Cone, and W. Babbitt, "Optical decoherence and persistent spectral hole burning in er3+: linbo3", Journal of Luminescence **130**, 1603–1609 (2010).

[243]C. W. Thiel, N. Sinclair, W. Tittel, and R. L. Cone, "Tm3 materials for spectrally multiplexed quantum memories", Physical Review Letters **113**, 160501 (2014).

[244]A. Tiranov, A. Ortu, S. Welinski, A. Ferrier, P. Goldner, N. Gisin, and M. Afzelius, "Spectroscopic study of hyperfine properties in yb 3+ 171: y 2 sio 5", Physical Review B **98**, 195110 (2018).

[245]Y. Sun, C. Thiel, and R. Cone, "Optical decoherence and energy level structure of 0.1% tm3:linbo3", Physical Review B **85**, 165106 (2012).

[246]M. Sellars, E. Fraval, and J. Longdell, "Investigation of static electric dipole–dipole coupling induced optical inhomogeneous broadening in eu3+: y2sio5", Journal of Luminescence **107**, 150–154 (2004).

[247]R. L. Ahlefeldt, M. R. Hush, and M. J. Sellars, "Ultranarrow optical inhomogeneous linewidth in a stoichiometric rare-earth crystal", Physical Review Letters **117**, 250504 (2016).

[248]R. Equall, R. Cone, and R. Macfarlane, "Homogeneous broadening and hyperfine structure of optical transitions in pr 3+: y 2 sio 5", Physical Review B **52**, 3963 (1995).

[249]J. Karlsson, N. Kunkel, A. Ikesue, A. Ferrier, and P. Goldner, "Nuclear spin coherence properties of 151eu3+ and 153eu3+ in a y2o3 transparent ceramic", Journal of Physics: Condensed Matter **29**, 125501 (2017).

[250]P. Goldner and O. Guillot-Noël, "Magnetic interactions in pr3+: liyf4 for quantum manipulation: search for an efficient three-level Λ system", Molecular physics **102**, 1185–1192 (2004).

[251]I. Nakamura, T. Yoshihiro, H. Inagawa, S. Fujiyoshi, and M. Matsushita, "Spectroscopy of single pr3+ ion in laf3 crystal at 1.5 k", Scientific Reports **4**, 7364 (2014).

[252]A. Louchet, Y. Le Du, T. Brouri, F. Bretenaker, T. Chanelière, F. Goldfarb, I. Lorgeré, and J.-L. Le Gouët, "Optical investigation of nuclear spin coherence in tm:yag", Solid State Sciences **10**, 1374–1378 (2008).

[253]H. Fan, K. H. Kagalwala, S. V. Polyakov, A. L. Migdall, and E. A. Goldschmidt, "Electromagnetically induced transparency in inhomogeneously broadened solid media", Physical Review A **99**, 053821 (2019).

[254]J. M. Kindem, J. G. Bartholomew, P. J. Woodburn, T. Zhong, I. Craiciu, R. L. Cone, C. W. Thiel, and A. Faraon, "Characterization of yb 3+ 171: yvo 4 for photonic quantum technologies", Physical Review B **98**, 024404 (2018).

[255]S. Probst, H. Rotzinger, A. Ustinov, and P. Bushev, "Microwave multimode memory with an erbium spin ensemble", Physical Review B **92**, 014421 (2015).

[256]A. Ortu, A. Tiranov, S. Welinski, F. Fröwis, N. Gisin, A. Ferrier, P. Goldner, and M. Afzelius, "Simultaneous coherence enhancement of optical and microwave transitions in solid-state electronic spins", Nature Materials **17**, 671–675 (2018).

[257]S. Welinski, P. J. T. Woodburn, N. Lauk, R. L. Cone, C. Simon, P. Goldner, and C. W. Thiel, "Electron spin coherence in optically excited states of rare-earth ions for microwave to optical quantum transducers", Physical Review Letters **122**, 247401 (2019).

[258]E. Z. Cruzeiro, A. Tiranov, J. Lavoie, A. Ferrier, P. Goldner, N. Gisin, and M. Afzelius, "Efficient optical pumping using hyperfine levels in 145nd3+: y2sio5 and its application to optical storage", New Journal of Physics **20**, 053013 (2018).

[259]E. Z. Cruzeiro, A. Tiranov, I. Usmani, C. Laplane, J. Lavoie, A. Ferrier, P. Goldner, N. Gisin, and M. Afzelius, "Spectral hole lifetimes and spin population relaxation dynamics in neodymium-doped yttrium orthosilicate", Physical Review B **95**, 205119 (2017).

[260]D. Hashimoto and K. Shimizu, "Coherent raman beat analysis of the hyperfine sublevel coherence properties of 167er3+ ions doped in an y2sio5 crystal", Journal of Luminescence **171**, 183–190 (2016).

[261]M. Rančić, M. P. Hedges, R. L. Ahlefeldt, and M. J. Sellars, "Coherence time of over a second in a telecom-compatible quantum memory storage material", Nature Physics **14**, 50–54 (2018).

[262]S. Welinski, A. Tiranov, M. Businger, A. Ferrier, M. Afzelius, and P. Goldner, "Coherence time extension by large-scale optical spin polarization in a rare-earth doped crystal", Physical Review X **10**, 031060 (2020).

[263]N. Timoney, I. Usmani, P. Jobez, M. Afzelius, and N. Gisin, "Single-photon-level optical storage in a solid-state spin-wave memory", Physical Review A **88**, 022324 (2013).

[264]K. Kutluer, M. F. Pascual-Winter, J. Dajczgewand, P. M. Ledingham, M. Mazzera, T. Chanelière, and H. de Riedmatten, "Spectral-hole memory for light at the single-photon level", Physical Review A **93**, 040302 (2016).

[265]J. S. Stuart, M. Hedges, R. Ahlefeldt, and M. Sellars, "Initialization protocol for efficient quantum memories using resolved hyperfine structure", Physical Review Research **3**, L032054 (2021).

[266]T. Zhong, J. M. Kindem, J. G. Bartholomew, J. Rochman, I. Craiciu, E. Miyazono, M. Bettinelli, E. Cavalli, V. Verma, S. W. Nam, et al., "Nanophotonic rare-earth quantum memory with optically controlled retrieval", Science **357**, 1392–1395 (2017).

[267]E. Saglamyurek, N. Sinclair, J. Jin, J. A. Slater, D. Oblak, F. Bussieres, M. George, R. Ricken, W. Sohler, and W. Tittel, "Broadband waveguide quantum memory for entangled photons", Nature **469**, 512–515 (2011).

[268]A. Seri, A. Lenhard, D. Rieländer, M. Gündoğan, P. M. Ledingham, M. Mazzera, and H. de Riedmatten, "Quantum correlations between single telecom photons and a multimode on-demand solid-state quantum memory", Physical Review X **7**, 021028 (2017).

[269]F. Bussières, C. Clausen, A. Tiranov, B. Korzh, V. B. Verma, S. W. Nam, F. Marsili, A. Ferrier, P. Goldner, H. Herrmann, et al., "Quantum teleportation from a telecom-wavelength photon to a solid-state quantum memory", Nature Photonics **8**, 775–778 (2014).

[270]D. Rieländer, K. Kutluer, P. M. Ledingham, M. Gündoğan, J. Fekete, M. Mazzera, and H. de Riedmatten, "Quantum storage of heralded single photons in a praseodymium-doped crystal", Physical Review Letters **112**, 040504 (2014).

[271]T.-X. Zhu, C. Liu, M. Jin, M.-X. Su, Y.-P. Liu, W.-J. Li, Y. Ye, Z.-Q. Zhou, C.-F. Li, and G.-C. Guo, "On-demand integrated quantum memory for polarization qubits", Physical Review Letters **128**, 180501 (2022).

[272]A. Seri, G. Corrielli, D. Lago-Rivera, A. Lenhard, H. de Riedmatten, R. Osellame, and M. Mazzera, "Laser-written integrated platform for quantum storage of heralded single photons", Optica **5**, 934–941 (2018).

[273]A. Seri, D. Lago-Rivera, A. Lenhard, G. Corrielli, R. Osellame, M. Mazzera, and H. de Riedmatten, "Quantum storage of frequency-multiplexed heralded single photons", Physical Review Letters **123**, 080502 (2019).

[274]M. Gündoğan, P. M. Ledingham, A. Almasi, M. Cristiani, and H. De Riedmatten, "Quantum storage of a photonic polarization qubit in a solid", Physical Review Letters **108**, 190504 (2012).

[275]X. Liu, J. Hu, Z.-F. Li, X. Li, P.-Y. Li, P.-J. Liang, Z.-Q. Zhou, C.-F. Li, and G.-C. Guo, "Heralded entanglement distribution between two absorptive quantum memories", Nature **594**, 41–45 (2021).

[276]C. Clausen, I. Usmani, F. Bussieres, N. Sangouard, M. Afzelius, H. de Riedmatten, and N. Gisin, "Quantum storage of photonic entanglement in a crystal", Nature **469**, 508–511 (2011).

[277]J. V. Rakonjac, D. Lago-Rivera, A. Seri, M. Mazzera, S. Grandi, and H. de Riedmatten, "Entanglement between a telecom photon and an on-demand multimode solid-state quantum memory", Physical Review Letters **127**, 210502 (2021).

[278]D. Lago-Rivera, J. V. Rakonjac, S. Grandi, and H. de Riedmatten, "Long-distance multiplexed quantum teleportation from a telecom photon to a solid-state qubit", arXiv preprint arXiv:2209.06249 (2022).

[279]D. Lago-Rivera, S. Grandi, J. V. Rakonjac, A. Seri, and H. de Riedmatten, "Telecom-heralded entanglement between multimode solid-state quantum memories", Nature **594**, 37–40 (2021).

[280]Y. Ma, Y.-Z. Ma, Z.-Q. Zhou, C.-F. Li, and G.-C. Guo, "One-hour coherent optical storage in an atomic frequency comb memory", Nature Communications **12**, 1–6 (2021).

[281]I. Craiciu, M. Lei, J. Rochman, J. M. Kindem, J. G. Bartholomew, E. Miyazono, T. Zhong, N. Sinclair, and A. Faraon, "Nanophotonic quantum storage at telecommunication wavelength", Physical Review Applied **12**, 024062 (2019).

[282]M. F. Askarani, T. Lutz, V. B. Verma, M. D. Shaw, S. W. Nam, N. Sinclair, D. Oblak, W. Tittel, et al., "Storage and reemission of heralded telecommunication-wavelength photons using a crystal waveguide", Physical Review Applied **11**, 054056 (2019).

[283]J. H. Davidson, P. Lefebvre, J. Zhang, D. Oblak, and W. Tittel, "Improved light-matter interaction for storage of quantum states of light in a thulium-doped crystal cavity", Physical Review A **101**, 042333 (2020).

[284]A. Corney, *Atomic and laser spectroscopy* (Clarendon Press Oxford, 1978).

[285]N. B. Phillips, A. V. Gorshkov, and I. Novikova, "Optimal light storage in atomic vapor", Physical Review A **78**, 023801 (2008).

[286]I. Novikova, A. V. Gorshkov, D. F. Phillips, A. S. Sørensen, M. D. Lukin, and R. L. Walsworth, "Optimal control of light pulse storage and retrieval", Physical Review Letters **98**, 243602 (2007).

[287]M. Bonarota, J. Ruggiero, J.-L. Le Gouët, and T. Chanelière, "Efficiency optimization for atomic frequency comb storage", Physical Review A **81**, 033803 (2010).

[288][1] E. Saglamyurek, *et al.*, Nature Photonics **12**, 774 (2018).
[2] A. Rastogi, *et al.*, Physical Review A **100**, 012314 (2019).
[3] E. Saglamyurek, *et al.*, Physical Review Research **1**, 022004(R) (2019).
[4] E. Saglamyurek, *et al.*, New Journal of Physics **23**, 043028 (2021).
[5] D. G. England, *et al.*, Physical Review Letters **114**, 053602 (2015).
[6] K. A. Fisher, *et al.*, Physical Review A **96**, 012324 (2017).
[7] D. G. England, *et al.*, Physical Review Letters **111**, 243601 (2013).
[8] P. J. Bustard, *et al.*, Physical Review Letters **111**, 083901 (2013).
[9] E. Saglamyurek, *et al.*, Nature **469**, 512 (2011).
[10] P. S. Michelberger, *et al.*, New Journal of Physics **17**, 043006 (2015).
[11] M. R. Sprague, *et al.*, Nature Photonics **8**, 287 (2014).
[12] K. F. Reim, *et al.*, Nature Photonics **4**, 218 (2010).
[13] K. F. Reim, *et al.*, Physical Review Letters **107**, 053603 (2011).
[14] R. A. Akhmedzhanov, *et al.*, Laser Physics Letters **13**, 015202 (2016).
[15] Z.-Q. Zhou, *et al.*, Physical Review Letters **115**, 070502 (2015).
[16] S. E. Thomas, *et al.*, Physical Review A **100**, 033801 (2019).
[17] D.-S. Ding, *et al.*, Light Science & Applications **5**, e16157 (2016).
[18] K.T. Kaczmarek, *et al.*, Physical Review A **97**, 042316 (2018).
[19] R. Finkelstein, *et al.*, Science Advances **4**, eaap8598 (2018).
[20] D. J. Saunders, *et al.*, Physical Review Letters **116**, 090501 (2016).
[21] J. Guo, *et al.*, Nature Communications **10**, 148 (2019).
[22] Y.-C. Wei, *et al.*, Physical Review A **102**, 063720 (2020).
[23] R. Finkelstein, *et al.*, Physical Review X **11**, 011008 (2021).
[24] G. Buser, *et al.*, PRX Quantum **3**, 020349 (2022).
[25] C. Clausen, *et al.*, Nature **469**, 508 (2011).
[26] L. Heller, *et al.*, Physical Review Applied **18**, 024036 (2022).
[27] J. Wolters, *et al.*, Physical Review Letters **119**, 060502 (2017).
[28] I. Craiciu, *et al.*, Physical Review Applied **12**, 024062 (2019).
[29] S. E. Thomas, *et al.*, arXiv 2211.04415v1 (2022).
[30] K. Shinbrough, *et al.*, in Conference on Lasers and Electro-Optics (CLEO) (Optica Publishing Group, 2023).
[31] A. Rastogi, *et al.*, Physical Review Letters **129**, 120502 (2022).
[32] N. Sinclair, *et al.*, Physical Review Letters **113**, 053603 (2014).
[33] T. Zhong, *et al.*, Science **357**, 1392 (2017).
[34] H. de Riedmatten, *et al.*, Nature **456**, 773 (2008).
[35] Z.-Q. Zhou, *et al.*, Physical Review Letters **108**, 190505 (2012).
[36] M. Askrani, *et al.*, Physical Review Applied **11**, 054056 (2019).

[37] J. Davidson, *et al.*, Physical Review A **101**, 042333 (2020).
[38] M. Businger, *et al.*, Nature Communications **13**, 6438 (2022).
[39] X. Liu, *et al.*, Nature **594**, 41 (2021).
[40] K. S. Choi, *et al.*, Nature **452**, 67 (2008).
[41] M.-H. Jiang, *et al.*, arXiv:2212.12898v1 [quant-ph] (2022).
[42] D. Main, *et al.*, Optics Letters **46**, 2960 (2021).
[43] D.-S. Ding, *et al.*, Nature Photonics **9**, 332 (2015).
[44] D.-S. Ding, *et al.*, Nature Communications **4**, 2527 (2013).
[45] W. Zhang, *et al.*, Nature Communications **7**, 13514 (2016).
[46] O. Davidson, *et al.*, arXiv:2212.04263 [quant-ph] (2022).
[47] J. Jin, *et al.*, Physical Review Letters **115**, 140501 (2015).
[48] E. Saglamyurek, *et al.*, Nature Communications **7**, 11202 (2016).
[49] F. Bussieres, *et al.*, Nature Photonics **8**, 775 (2014).
[50] J.-S. Tang, *et al.*, Nature Communications **6**, 8652 (2015).
[51] A. Tiranov, *et al.*, Physical Review Letters **117**, 240506 (2016).
[52] S.-H. Wei, *et al.*, arXiv:2209.00802 [quant-ph] (2022).
[53] E. Saglamyurek, *et al.*, Nature Photonics **9**, 83 (2015).
[54] D.-C. Liu, *et al.*, Physical Review Letters **129**, 210501 (2022).
[55] P. J. Bustard, *et al.*, Physical Review Letters **128**, 120501 (2022).
[56] M. Bouillard, *et al.*, Physical Review Letters **122**, 210501 (2019).
[57] T. B. Pittman, *et al.*, Physical Review A **66**, 042303 (2002).
[58] F. Kaneda, *et al.*, Optica **2**, 1010 (2015).
[59] F. Kaneda, P. G. Kwiat, Science Advances **5**, eaaw8586 (2019).
[60] C. Xiong, *et al.*, Nature Communications **7**, 10853 (2016).
[61] K. Makino, *et al.*, Science Advances **2**, e1501772 (2016).
[62] S. Clemmen, *et al.*, Optics Letters **43**, 2138 (2018).
[63] T. B. Pittman, *et al.*, Physical Review A **66**, 062302 (2002).
[64] X.-L. Pang, *et al.*, Science Advances **6**, eaax1425 (2020).
[65] E. Meyer-Scott, *et al.*, Physical Review Letters **129**, 150501 (2022).

[289] J. Migdalek and W. Baylis, "Multiconfiguration dirac-fock calculations of two electric quadrupole transitions in neutral barium", Physical Review A **42**, 6897 (1990).

[290] K. Shinbrough, Y. Teng, B. Fang, V. O. Lorenz, and O. Cohen, "Photon-matter quantum correlations in spontaneous raman scattering", Physical Review A **101**, 013415 (2020).

[291] M. G. Raymer, I. A. Walmsley, J. Mostowski, and B. Sobolewska, "Quantum theory of spatial and temporal coherence properties of stimulated raman scattering", Phys. Rev. A **32**, 332–344 (1985).

[292] M. G. Raymer and J. Mostowski, "Stimulated Raman scattering: Unified treatment of spontaneous initiation and spatial propagation", Phys. Rev. A **24**, 1980–1993 (1981).

[293] M. G. Raymer, Z. W. Li, and I. A. Walmsley, "Temporal quantum fluctuations in stimulated raman scattering: coherent-modes description", Phys. Rev. Lett. **63**, 1586–1589 (1989).

[294] W. Wasilewski and M. G. Raymer, "Pairwise entanglement and readout of atomic-ensemble and optical wave-packet modes in traveling-wave raman interactions", Phys. Rev. A **73**, 063816 (2006).

[295]M. G. Raymer, K. Rzazewski, and J. Mostowski, "Pulse-energy statistics in stimulated raman scattering", Opt. Lett. **7**, 71–73 (1982).

[296]I. A. Walmsley and M. G. Raymer, "Observation of macroscopic quantum fluctuations in stimulated raman scattering", Phys. Rev. Lett. **50**, 962–965 (1983).

[297]N. N. Bogolubov, A. S. Shumovsky, and T. Quang, "Collective effects in resonant raman scattering of intense optical waves", J. Phys. B **20**, 629–637 (1987).

[298]N. Fabricius, K. Nattermann, and D. von der Linde, "Macroscopic manifestation of quantum fluctuations in transient stimulated raman scattering", Phys. Rev. Lett. **52**, 113–116 (1984).

[299]M. O. Scully and M. S. Zubairy, *Quantum optics* (Cambridge University Press, Cambridge, 1997), pp. 271–290.

[300]M. G. Raymer, "Quantum state entanglement and readout of collective atomic-ensemble modes and optical wave packets by stimulated raman scattering", J. Mod. Opt. **51**, 1739–1759 (2004).

[301]L.-M. Duan, M. Lukin, J. Cirac, and P. Zoller, Nature **414**, 413–418 (2001).

[302]H. J. Kimble, "The quantum internet", Nature **453**, 1023–1030 (2008).

[303]N. Gisin, G. Ribordy, W. Tittel, and H. Zbinden, "Quantum cryptography", Rev. Mod. Phys. **74**, 145–195 (2002).

[304]W. P. Grice and I. A. Walmsley, Phys. Rev. A **56**, 1627–1634 (1997).

[305]K. Garay-Palmett, H. J. McGuinness, O. Cohen, J. S. Lundeen, R. Rangel-Rojo, A. B. U'Ren, M. G. Raymer, C. J. McKinstrie, S. Radic, and I. A. Walmsley, "Photon pair-state preparation with tailored spectral properties by spontaneous four-wave mixing in photonic-crystal fiber", En, Opt. Express **15**, 14870–14886 (2007).

[306]K. C. Lee, B. J. Sussman, M. R. Sprague, P. Michelberger, K. F. Reim, J. Nunn, N. K. Langford, P. J. Bustard, D. Jaksch, and I. A. Walmsley, Nat. Photonics **6**, 41–44 (2011).

[307]K. C. Lee, M. R. Sprague, B. J. Sussman, J. Nunn, N. K. Langford, X.-M. Jin, T. Champion, P. Michelberger, K. F. Reim, D. England, D. Jaksch, and I. A. Walmsley, Science **334**, 1253–1256 (2011).

[308]T. Chanelière, D. N. Matsukevich, S. D. Jenkins, S.-Y. Lan, T. A. B. Kennedy, and A. Kuzmich, Nature **438**, 833–836 (2005).

[309]J.-P. Dou, A.-L. Yang, M.-Y. Du, D. Lao, H. Li, X.-L. Pang, J. Gao, L.-F. Qiao, H. Tang, and X.-M. Jin, "Direct observation of broadband nonclassical states in a room-temperature light–matter interface", npj Quantum Information **4**, 31 (2018).

[310]K. F. Reim, P. Michelberger, K. C. Lee, J. Nunn, N. K. Langford, and I. A. Walmsley, Phys. Rev. Lett. **107**, 053603 (2011).

[311]D. Matsukevich and A. Kuzmich, Science **306**, 663–666 (2004).

[312]H. de Riedmatten, M. Afzelius, M. U. Staudt, C. Simon, and N. Gisin, Nature **456**, 773–777 (2008).

[313]K. F. Reim, J. Nunn, V. O. Lorenz, B. J. Sussman, K. C. Lee, N. K. Langford, D. Jaksch, and I. A. Walmsley, Nat. Photonics **4**, 218–221 (2010).

[314]C. Simon, *et al.*, Eur. Phys. J. D **58**, 1–22 (2010).

[315]M. Kasperczyk, A. Jorio, E. Neu, P. Maletinsky, and L. Novotny, Opt. Lett. **40**, 2393–2396 (2015).

[316]M. Parniak, M. Dabrowski, M. Mazelanik, A. Leszczynski, M. Lipka, and W. Wasilewski, Nat. Commun. **8**, 2140 (2017).

[317]R. Chrapkiewicz and W. Wasilewski, Opt. Express **20**, 29540–29552 (2012).

[318]R. Chrapkiewicz, M. Dabrowski, and W. Wasilewski, Phys. Rev. Lett. **118**, 063603 (2017).

[319]M. Rosenau da Costa, A. O. Caldeira, S. M. Dutra, and H. Westfahl, "Exact diagonalization of two quantum models for the damped harmonic oscillator", Phys. Rev. A **61**, 022107 (2000).

[320]S. Mukamel, *Principles of nonlinear optical spectroscopy*, Vol. 29 (Oxford University Press, New York, 1995).

[321]M. G. Raymer and I. A. Walmsley, Prog. Opt. **28**, 182–270 (1990).

[322]U. Fano, "Effects of configuration interaction on intensities and phase shifts", Phys. Rev. **124**, 1866–1878 (1961).

[323]K. Rzazewski, M. G. Raymer, and R. W. Boyd, "Delay-time statistics of cooperative emission in the presence of homogeneous line broadening", Phys. Rev. A **39**, 5785–5790 (1989).

[324]C. K. Hong, Z. Y. Ou, and L. Mandel, "Measurement of subpicosecond time intervals between two photons by interference", Phys. Rev. Lett. **59**, 2044–2046 (1987).

[325]M. Ashkin, J. Parker Jr., and D. Feldman, Solid State Comm. **6**, 343–346 (1968).

[326]G. Pezzotti and W. Zhu, "Resolving stress tensor components in space from polarized raman spectra: polycrystalline alumina", Phys. Chem. Chem. Phys. **17**, 2608–2627 (2015).

[327]M. J. Dodge, *Handbook of laser science and technology, optical materials: part 2*, Vol. IV (CRC Press, Boca Raton, 1986), p. 30.

[328]Y. Yu, F. Ma, X.-Y. Luo, B. Jing, P.-F. Sun, R.-Z. Fang, C.-W. Yang, H. Liu, M.-Y. Zheng, X.-P. Xie, et al., "Entanglement of two quantum memories via metropolitan-scale fibers", arXiv preprint arXiv:1903.11284 (2019).

[329]L. .-. Duan, J. I. Cirac, and P. Zoller, "Three-dimensional theory for interaction between atomic ensembles and free-space light", Phys. Rev. A **66**, 023818 (2002).

[330]J. Mostowski and B. Sobolewska, "Transverse effects in stimulated raman scattering", Phys. Rev. A **30**, 610–612 (1984).

[331]W. Mauerer, M. Avenhaus, W. Helwig, and C. Silberhorn, Phys. Rev. A **80**, 053815 (2009).

[332]A. Christ, K. Laiho, A. Eckstein, K. N. Cassemiro, and C. Silberhorn, "Probing multimode squeezing with correlation functions", New J. Phys. **13**, 033027 (2011).

[333]P. Kok, W. J. Munro, K. Nemoto, T. C. Ralph, J. P. Dowling, and G. J. Milburn, "Linear optical quantum computing with photonic qubits", Rev. Mod. Phys. **79**, 135–174 (2007).

[334]J. Nunn, N. K. Langford, W. S. Kolthammer, T. F. M. Champion, M. R. Sprague, P. S. Michelberger, X.-M. Jin, D. G. England, and I. A. Walmsley, "Enhancing multiphoton rates with quantum memories", Phys. Rev. Lett. **110**, 133601 (2013).

[335]F. Kaneda and P. G. Kwiat, "High-efficiency single-photon generation via large-scale active time multiplexing", Science Advances **5**, eaaw8586 (2019).

[336]N. Sangouard, C. Simon, H. de Riedmatten, and N. Gisin, "Quantum repeaters based on atomic ensembles and linear optics", Rev. Mod. Phys. **83**, 33–80 (2011).

[337]E. Knill, R. Laflamme, and M. G., Nature **409**, 46–52 (2001).

[338]Y.-C. Wei, B.-H. Wu, Y.-F. Hsiao, P.-J. Tsai, and Y.-C. Chen, "Broadband coherent optical memory based on electromagnetically induced transparency", Phys. Rev. A **102**, 063720 (2020).

[339]I. Novikova, A. V. Gorshkov, D. F. Phillips, A. S. Sørensen, M. D. Lukin, and R. L. Walsworth, "Optimal control of light pulse storage and retrieval", Phys. Rev. Lett. **98**, 243602 (2007).

[340]A. V. Gorshkov, A. André, M. Fleischhauer, A. S. Sørensen, and M. D. Lukin, "Universal approach to optimal photon storage in atomic media", Phys. Rev. Lett. **98**, 123601 (2007).

[341]A. V. Gorshkov, A. André, M. D. Lukin, and A. S. Sørensen, "Photon storage in Λ-type optically dense atomic media. ii. free-space model", Phys. Rev. A **76**, 033805 (2007).

[342]A. V. Gorshkov, T. Calarco, M. D. Lukin, and A. S. Sørensen, "Photon storage in Λ-type optically dense atomic media. iv. optimal control using gradient ascent", Phys. Rev. A **77**, 043806 (2008).

[343]H. Nakao and N. Yamamoto, "Optimal control for perfect state transfer in linear quantum memory", J. Phys. B **50**, 065501 (2017).

[344]J. Nunn, "Quantum memory in atomic ensembles", English, PhD thesis (University of Oxford, 2008).

[345]I. Novikova, N. B. Phillips, and A. V. Gorshkov, "Optimal light storage with full pulse-shape control", Phys. Rev. A **78**, 021802 (2008).

[346]N. B. Phillips, A. V. Gorshkov, and I. Novikova, "Optimal light storage in atomic vapor", Phys. Rev. A **78**, 023801 (2008).

[347]J. Guo, X. Feng, P. Yang, Z. Yu, L. Q. Chen, C.-H. Yuan, and W. Zhang, Nat. Commun. **10**, 148 (2019).

[348]M. Hosseini, B. Sparkes, G. Campbell, P. Lam, and B. Buchler, Nat. Commun. **2**, 174 (2011).

[349]Y.-H. Chen, M.-J. Lee, I.-C. Wang, S. Du, Y.-F. Chen, Y.-C. Chen, and I. A. Yu, "Coherent optical memory with high storage efficiency and large fractional delay", Phys. Rev. Lett. **110**, 083601 (2013).

[350]Y.-W. Cho, G. T. Campbell, J. L. Everett, J. Bernu, D. B. Higginbottom, M. T. Cao, J. Geng, N. P. Robins, P. K. Lam, and B. C. Buchler, "Highly efficient optical quantum memory with long coherence time in cold atoms", Optica **3**, 100–107 (2016).

[351]Y.-F. Hsiao, P.-J. Tsai, H.-S. Chen, S.-X. Lin, C.-C. Hung, C.-H. Lee, Y.-H. Chen, Y.-F. Chen, I. A. Yu, and Y.-C. Chen, "Highly efficient coherent optical memory based on electromagnetically induced transparency", Phys. Rev. Lett. **120**, 183602 (2018).

[352]Y. Wang, J. Li, S. Zhang, K. Su, Y. Zhou, K. Liao, S. Du, H. Yan, and S.-L. Zhu, Nat. Phys. **13**, 346–351 (2019).

[353]D. G. England, P. J. Bustard, J. Nunn, R. Lausten, and B. J. Sussman, "From photons to phonons and back: a thz optical memory in diamond", Phys. Rev. Lett. **111**, 243601 (2013).

[354]P. J. Bustard, R. Lausten, D. G. England, and B. J. Sussman, "Toward quantum processing in molecules: a thz-bandwidth coherent memory for light", Phys. Rev. Lett. **111**, 083901 (2013).

[355]D. G. England, K. A. G. Fisher, J.-P. W. MacLean, P. J. Bustard, R. Lausten, K. J. Resch, and B. J. Sussman, "Storage and retrieval of thz-bandwidth single photons using a room-temperature diamond quantum memory", Phys. Rev. Lett. **114**, 053602 (2015).

[356]P. S. Michelberger, T. F. M. Champion, M. R. Sprague, K. T. Kaczmarek, M. Barbieri, X. M. Jin, D. G. England, W. S. Kolthammer, D. J. Saunders, J. Nunn, and I. A. Walmsley, New J. Phys. **17**, 043006 (2015).

[357]S. E. Thomas, J. H. D. Munns, K. T. Kaczmarek, C. Qiu, B. Brecht, A. Feizpour, P. M. Ledingham, I. A. Walmsley, J. Nunn, and D. J. Saunders, New J. Phys. **19**, 063034 (2017).

[358]E. Saglamyurek, N. Sinclair, J. Jin, J. A. Slater, D. Oblak, F. Bussières, M. George, R. Ricken, W. Sohler, and W. Tittel, Nature **469**, 512–515 (2011).

[359]K. A. G. Fisher, D. G. England, J.-P. W. MacLean, P. J. Bustard, K. Heshami, K. J. Resch, and B. J. Sussman, "Storage of polarization-entangled thz-bandwidth photons in a diamond quantum memory", Phys. Rev. A **96**, 012324 (2017).

[360]K. T. Kaczmarek, P. M. Ledingham, B. Brecht, S. E. Thomas, G. S. Thekkadath, O. Lazo-Arjona, J. H. D. Munns, E. Poem, A. Feizpour, D. J. Saunders, J. Nunn, and I. A. Walmsley, "High-speed noise-free optical quantum memory", Phys. Rev. A **97**, 042316 (2018).

[361]B. Fang, S. Dong, S. Meiselman, O. Cohen, and V. O. Lorenz, "Storage of ultra-broadband pulses in hot atomic barium vapor", in Conference on lasers and electro-optics (2017), Fm2e.3.

[362]D.-S. Ding, W. Zhang, Z.-Y. Zhou, S. Shi, B.-S. Shi, and G.-C. Guo, Nat. Photonics **9**, 332–338 (2015).

[363]E. Saglamyurek, T. Hrushevskyi, A. Rastogi, K. Heshami, and L. J. LeBlanc, Nat. Photonics **12**, 774–782 (2018).

[364]A. Rastogi, E. Saglamyurek, T. Hrushevskyi, S. Hubele, and L. J. LeBlanc, "Discerning quantum memories based on electromagnetically-induced-transparency and autler-townes-splitting protocols", Phys. Rev. A **100**, 012314 (2019).

[365]E. Saglamyurek, T. Hrushevskyi, L. Cooke, A. Rastogi, and L. J. LeBlanc, "Single-photon-level light storage in cold atoms using the autler-townes splitting protocol", Phys. Rev. Research **1**, 022004 (2019).

[366]E. Saglamyurek, T. Hrushevskyi, A. Rastogi, L. W. Cooke, B. D. Smith, and L. J. LeBlanc, *Storing short single-photon-level optical pulses in bose-einstein condensates for high-performance quantum memory*, 2020.

[367]V. C. Vivoli, N. Sangouard, M. Afzelius, and N. Gisin, "High-bandwidth quantum memory protocol for storing single photons in rare-earth doped crystals", New J. Phys. **15**, 095012 (2013).

[368]S. A. Moiseev and S. Kröll, "Complete reconstruction of the quantum state of a single-photon wave packet absorbed by a doppler-broadened transition", Phys. Rev. Lett. **87**, 173601 (2001).

[369]A. J. A. Carvalho, R. S. N. Moreira, J. Ferraz, S. S. Vianna, L. H. Acioli, and D. Felinto, "Enhanced absorption of weak ultrashort light pulses by a narrowband atomic medium", Phys. Rev. A **101**, 053426 (2020).

[370]M. Fleischhauer and M. D. Lukin, "Quantum memory for photons: dark-state polaritons", Phys. Rev. A **65**, 022314 (2002).

[371]D. F. Phillips, A. Fleischhauer, A. Mair, R. L. Walsworth, and M. D. Lukin, "Storage of light in atomic vapor", Phys. Rev. Lett. **86**, 783–786 (2001).

[372]A. I. Lvovsky, B. C. Sanders, and W. Tittel, Nat. Photonics **3**, 706–714 (2009).

[373]M. O. Scully and M. S. Zubairy, *Quantum optics* (Cambridge University Press, 1997).

[374]L. S. Costanzo, A. S. Coelho, D. Pellegrino, M. S. Mendes, L. Acioli, K. N. Cassemiro, D. Felinto, A. Zavatta, and M. Bellini, "Zero-area single-photon pulses", Phys. Rev. Lett. **116**, 023602 (2016).

[375]J. E. Rothenberg, D. Grischkowsky, and A. C. Balant, "Observation of the formation of the 0π pulse", Phys. Rev. Lett. **53**, 552–555 (1984).

[376]J. Miná ř, N. Sangouard, M. Afzelius, H. de Riedmatten, and N. Gisin, "Spin-wave storage using chirped control fields in atomic frequency comb-based quantum memory", Phys. Rev. A **82**, 042309 (2010).

[377]G. Demeter, "Coherence rephasing combined with spin-wave storage using chirped control pulses", Phys. Rev. A **89**, 063806 (2014).

[378]X. Zhang, A. Kalachev, and O. Kocharovskaya, "All-optical quantum storage based on spatial chirp of the control field", Phys. Rev. A **90**, 052322 (2014).

[379]A. V. Gorshkov, A. André, M. D. Lukin, and A. S. Sørensen, "Photon storage in Λ-type optically dense atomic media. iii. effects of inhomogeneous broadening", Phys. Rev. A **76**, 033806 (2007).

[380]S. A. Moiseev and S. Kröll, "Complete reconstruction of the quantum state of a single-photon wave packet absorbed by a doppler-broadened transition", Phys. Rev. Lett. **87**, 173601 (2001).

[381]M. Nilsson and S. Kröll, "Solid state quantum memory using complete absorption and re-emission of photons by tailored and externally controlled inhomogeneous absorption profiles", Optics Communications **247**, 393–403 (2005).

[382]W. Tittel, M. Afzelius, T. Chaneliére, R. Cone, S. Kröll, S. Moiseev, and M. Sellars, "Photon-echo quantum memory in solid state systems", Laser & Photonics Reviews **4**, 244–267 (2010).

[383]M. Afzelius, C. Simon, H. de Riedmatten, and N. Gisin, "Multimode quantum memory based on atomic frequency combs", Phys. Rev. A **79**, 052329 (2009).

[384]C. H. Bennett and G. Brassard, "Quantum cryptography: public key distribution and coin tossing", Proc. IEEE Int. Conf. Comp., Sys., and Signal Proc., 175–179 (1984).

[385]R. Raussendorf and H. J. Briegel, "A one-way quantum computer", Phys. Rev. Lett. **86**, 5188–5191 (2001).

[386]K. Makino, Y. Hashimoto, J.-i. Yoshikawa, H. Ohdan, T. Toyama, P. van Loock, and A. Furusawa, "Synchronization of optical photons for quantum information processing", Science Advances **2**, e1501772 (2016).

[387]N. Sangouard, C. Simon, B. Zhao, Y.-A. Chen, H. de Riedmatten, J.-W. Pan, and N. Gisin, "Robust and efficient quantum repeaters with atomic ensembles and linear optics", Phys. Rev. A **77**, 062301 (2008).

[388]H.-J. Briegel, W. Dür, J. Cirac, and P. Zoller, Phys. Rev. Lett. **81**, 5932–5935 (1998).

[389]C. H. Bennett, G. Brassard, C. Crépeau, R. Jozsa, A. Peres, and W. K. Wootters, "Teleporting an unknown quantum state via dual classical and einstein-podolsky-rosen channels", Phys. Rev. Lett. **70**, 1895–1899 (1993).

[390]L. Ma, O. Slattery, and X. Tang, "Optical quantum memory based on electromagnetically induced transparency", J. Opt. **19**, 043001 (2017).

[391]A. V. Gorshkov, A. André, M. Fleischhauer, A. S. Sørensen, and M. D. Lukin, "Universal approach to optimal photon storage in atomic media", Phys. Rev. Lett. **98**, 123601 (2007).

[392]A. V. Gorshkov, A. André, M. D. Lukin, and A. S. Sørensen, "Photon storage in Λ-type optically dense atomic media. i. cavity model", Phys. Rev. A **76**, 033804 (2007).

[393]A. V. Gorshkov, A. André, M. D. Lukin, and A. S. Sørensen, "Photon storage in Λ-type optically dense atomic media. ii. free-space model", Phys. Rev. A **76**, 033805 (2007).

[394]A. V. Gorshkov, A. André, M. D. Lukin, and A. S. Sørensen, "Photon storage in Λ-type optically dense atomic media. iii. effects of inhomogeneous broadening", Phys. Rev. A **76**, 033806 (2007).

[395]A. V. Gorshkov, T. Calarco, M. D. Lukin, and A. S. Sørensen, "Photon storage in Λ-type optically dense atomic media. iv. optimal control using gradient ascent", Phys. Rev. A **77**, 043806 (2008).

[396]J. Nunn, I. A. Walmsley, M. G. Raymer, K. Surmacz, F. C. Waldermann, Z. Wang, and D. Jaksch, "Mapping broadband single-photon wave packets into an atomic memory", Phys. Rev. A **75**, 011401 (2007).

[397]G. P. Teja and S. K. Goyal, "Studying the effect of fluctuating environment on intra-atomic frequency comb based quantum memory", Scientific Reports **11**, 11439 (2021).

[398]M. Otten, K. Kapoor, A. B. Ozguler, E. T. Holland, J. B. Kowalkowski, Y. Alexeev, and A. L. Lyon, "Impacts of noise and structure on quantum information encoded in a quantum memory", Phys. Rev. A **104**, 012605 (2021).

[399]D. G. Cacuci, *Sensitivity & uncertainty analysis, volume 1: theory*, Vol. 1 (CRC press, 2003).

[400]E. Castillo, R. Minguez, and C. Castillo, "Sensitivity analysis in optimization and reliability problems", Reliability Engineering & System Safety **93**, 17th European Safety and Reliability Conference, 1788–1800 (2008).

[401]A. Saltelli, P. Annoni, I. Azzini, F. Campolongo, M. Ratto, and S. Tarantola, "Variance based sensitivity analysis of model output. design and estimator for the total sensitivity index", Computer Physics Communications **181**, 259–270 (2010).

[402]I. M. Sobol', "Global sensitivity indices for nonlinear mathematical models and their monte carlo estimates", Mathematics And Computers In Simulation **55**, 271–280 (2001).

[403]I. M. Sobol', "Sensitivity analysis for non-linear mathematical models", Mathematical modelling and computational experiment **1**, 407–414 (1993).

[404]K. Pearson, *On the general theory of skew correlation and non-linear regression*, 14 (Dulau and Company, 1905).

[405]A. Saltelli, K. Aleksankina, W. Becker, P. Fennell, F. Ferretti, N. Holst, S. Li, and Q. Wu, "Why so many published sensitivity analyses are false: a systematic review of sensitivity analysis practices", Environmental Modelling & Software **114**, 29–39 (2019).

[406]A. Saltelli, M. Ratto, T. Andres, F. Campolongo, J. Cariboni, D. Gatelli, M. Saisana, and S. Tarantola, *Global sensitivity analysis: the primer* (John Wiley & Sons, 2008).

[407]K. Shinbrough, B. D. Hunt, and V. O. Lorenz, "Optimization of broadband Λ-type quantum memory using gaussian pulses", Phys. Rev. A **103**, 062418 (2021).

[408]M. R. Sprague, P. S. Michelberger, T. F. M. Champion, D. G. England, J. Nunn, X. .-. Jin, W. S. Kolthammer, A. Abdolvand, P. S. J. Russell, and I. A. Walmsley, "Broadband single-photon-level memory in a hollow-core photonic crystal fibre", Nature Photonics **8**, 287–291 (2014).

[409]M. R. Sprague, D. G. England, A. Abdolvand, J. Nunn, X.-M. Jin, W. S. Kolthammer, M. Barbieri, B. Rigal, P. S. Michelberger, T. F. M. Champion, P. S. J. Russell, and I. A. Walmsley, "Efficient optical pumping and high optical depth in a hollow-core photonic-crystal fibre for a broadband quantum memory", New Journal of Physics **15**, 055013 (2013).

[410]K. T. Kaczmarek, P. M. Ledingham, B. Brecht, S. E. Thomas, G. S. Thekkadath, O. Lazo-Arjona, J. H. D. Munns, E. Poem, A. Feizpour, D. J. Saunders, J. Nunn, and I. A. Walmsley, "High-speed noise-free optical quantum memory", Phys. Rev. A **97**, 042316 (2018).

[411]R. Finkelstein, O. Lahad, I. Cohen, O. Davidson, S. Kiriati, E. Poem, and O. Firstenberg, "Continuous protection of a collective state from inhomogeneous dephasing", Phys. Rev. X **11**, 011008 (2021).

[412]I. M. Sobol´ and S. Kucherenko, "On global sensitivity analysis of quasi-monte carlo algorithms", Monte Carlo Methods Appl. **11**, 83–92 (2005).

[413]C. Liu, Z. Dutton, C. H. Behroozi, and L. V. Hau, "Observation of coherent optical information storage in an atomic medium using halted light pulses", Nature **409**, 490–493 (2001).

[414]K. Shinbrough, T. Loveridge, B. D. Hunt, S. Park, K. Oolman, T. O. Reboli, J. G. Eden, and V. O. Lorenz, "High-efficiency, high-speed, and low-noise photonic quantum memory", arXiv preprint arXiv:2309.00969 (2023).

[415]Y. Yu, F. Ma, X.-Y. Luo, B. Jing, P.-F. Sun, R.-Z. Fang, C.-W. Yang, H. Liu, M.-Y. Zheng, X.-P. Xie, et al., "Entanglement of two quantum memories via fibres over dozens of kilometres", Nature **578**, 240–245 (2020).

[416]H.-S. Zhong, H. Wang, Y.-H. Deng, M.-C. Chen, L.-C. Peng, Y.-H. Luo, J. Qin, D. Wu, X. Ding, Y. Hu, et al., "Quantum computational advantage using photons", Science **370**, 1460–1463 (2020).

[417]Y.-A. Chen, Q. Zhang, T.-Y. Chen, W.-Q. Cai, S.-K. Liao, J. Zhang, K. Chen, J. Yin, J.-G. Ren, Z. Chen, et al., "An integrated space-to-ground quantum communication network over 4,600 kilometres", Nature **589**, 214–219 (2021).

[418]L. S. Madsen, F. Laudenbach, M. F. Askarani, F. Rortais, T. Vincent, J. F. Bulmer, F. M. Miatto, L. Neuhaus, L. G. Helt, M. J. Collins, et al., "Quantum computational advantage with a programmable photonic processor", Nature **606**, 75–81 (2022).

[419]K. Reim, P. Michelberger, K. Lee, J. Nunn, N. Langford, and I. Walmsley, "Single-photon-level quantum memory at room temperature", Physical Review Letters **107**, 053603 (2011).

[420]O. Davidson, O. Yogev, E. Poem, and O. Firstenberg, "Single-photon synchronization with a room-temperature atomic quantum memory", Phys. Rev. Lett. **131**, 033601 (2023).

[421]S. Thomas, S. Sagona-Stophel, Z. Schofield, I. Walmsley, and P. Ledingham, "Single-photon-compatible telecommunications-band quantum memory in a hot atomic gas", Physical Review Applied **19**, L031005 (2023).

[422]X.-L. Wang, L.-K. Chen, W. Li, H.-L. Huang, C. Liu, C. Chen, Y.-H. Luo, Z.-E. Su, D. Wu, Z.-D. Li, et al., "Experimental ten-photon entanglement", Physical Review Letters **117**, 210502 (2016).

[423]T. Jennewein, C. Simon, G. Weihs, H. Weinfurter, and A. Zeilinger, "Quantum cryptography with entangled photons", Physical Review Letters **84**, 4729 (2000).

[424]M. Afzelius, I. Usmani, A. Amari, B. Lauritzen, A. Walther, C. Simon, N. Sangouard, J. Minář, H. De Riedmatten, N. Gisin, et al., "Demonstration of atomic frequency comb memory for light with spin-wave storage", Physical Review Letters **104**, 040503 (2010).

[425]E. Czuchaj, F. Rebentrost, H. Stoll, and H. Preuss, "Calculation of ground-and excited-state potential energy curves for barium-rare gas complexes in a pseudopotential approach", Theoretical Chemistry Accounts **100**, 117–123 (1998).

[426]D. S. Bezrukov, N. N. Kleshchina, I. S. Kalinina, and A. A. Buchachenko, "Ab initio interaction potentials of the ba, ba+ complexes with ar, kr, and xe in the lowest excited states", The Journal of Chemical Physics **150** (2019).

[427]A. A. Buchachenko and L. A. Viehland, "Interaction potentials and transport properties of ba, ba+, and ba2+ in rare gases from he to xe", The Journal of Chemical Physics **148** (2018).

[428]P. J. Bustard, D. G. England, K. Heshami, C. Kupchak, and B. J. Sussman, "Reducing noise in a raman quantum memory", Optics Letters **41**, 5055–5058 (2016).

[429]E. Saglamyurek, T. Hrushevskyi, L. Cooke, A. Rastogi, and L. J. LeBlanc, "Single-photon-level light storage in cold atoms using the autler-townes splitting protocol", Physical Review Research **1**, 022004 (2019).

[430]B. Lounis and M. Orrit, "Single-photon sources", Reports on Progress in Physics **68**, 1129 (2005).

[431]M. D. Eisaman, J. Fan, A. Migdall, and S. V. Polyakov, "Invited review article: single-photon sources and detectors", Review of scientific instruments **82**, 071101 (2011).

[432]C. Couteau, S. Barz, T. Durt, T. Gerrits, J. Huwer, R. Prevedel, J. Rarity, A. Shields, and G. Weihs, "Applications of single photons to quantum communication and computing", Nature Reviews Physics, 1–13 (2023).

[433]D. R. Lide, *Crc handbook of chemistry and physics*, Vol. 85 (CRC press, 2004).

[434]E. Ehrlacher and J. Huennekens, "Noble-gas broadening rates for the 6 s 2 1 s 0 → 6s6p 1, 3 p 1 resonance and intercombination lines of barium", Physical Review A **47**, 3097 (1993).

[435]V. Dzuba and J. Ginges, "Calculations of energy levels and lifetimes of low-lying states of barium and radium", Physical Review A **73**, 032503 (2006).

[436]J. Crank, *The mathematics of diffusion* (Oxford university press, 1979).

[437]J. O. Hirschfelder, C. F. Curtiss, and R. B. Bird, "Molecular theory of gases and liquids", Molecular theory of gases and liquids (1964).

[438]A.-R. Allouche, M. Aubert-Frécon, G. Nicolas, and F. Spiegelmann, "Theoretical study of the electronic structure of the ba2 molecule", Chemical physics **200**, 63–77 (1995).

[439]M. Lebeault, J. Viallon, V. Boutou, and J. Chevaleyre, "Vibrational structure of the (2) 1Σ+ u–x (1) 1Σ+ transition of the ba2 molecule", Journal of molecular spectroscopy **192**, 179–182 (1998).

[440]M. O. Scully and M. S. Zubairy, *Quantum optics* (Cambridge University Press, 1997).

[441]K. Shinbrough and V. O. Lorenz, "Variance-based sensitivity analysis of Λ-type quantum memory", Physical Review A **107**, 033703 (2023).

[442]L. Viola, E. Knill, and S. Lloyd, "Dynamical decoupling of open quantum systems", Physical Review Letters **82**, 2417 (1999).

[443]S. Harilal, G. Miloshevsky, P. Diwakar, N. LaHaye, and A. Hassanein, "Experimental and computational study of complex shockwave dynamics in laser ablation plumes in argon atmosphere", Physics of Plasmas **19** (2012).

[444]S. C. Reddy and L. N. Trefethen, "Stability of the method of lines", Numerische Mathematik **62**, 235–267 (1992).

[445]E. Hinnov and W. Ohlendorf, "Measurement of barium vapor density", The Journal of Chemical Physics **50**, 3005–3010 (1969).

[446]A. Laubereau, D. Von der Linde, and W. Kaiser, "Decay time of hot to phonons in diamond", Physical Review Letters **27**, 802 (1971).

[447]V. Ivady, J. Davidsson, N. T. Son, T. Ohshima, I. A. Abrikosov, and A. Gali, "Identification of si-vacancy related room-temperature qubits in 4 h silicon carbide", Physical Review B **96**, 161114 (2017).

[448]P. Friedrichs, T. Kimoto, L. Ley, and G. Pensl, *Silicon carbide, volume 1: growth, defects, and novel applications* (John Wiley & Sons, 2011).

Appendix A

Laser ablation of barium under argon atmosphere

In an effort to work toward a room-temperature, optically mediated mechanism for generating a dense ensemble of neutral barium atoms, we have taken preliminary data on laser ablation of barium in Ar buffer gas. Optical pulses between 10-40 mJ from a frequency-doubled Nd:YAG laser at 532 nm were focused onto barium pellets with a spot size of approximately 1 mm through the top window of a 6-sided vacuum chamber. Two windows on opposite sides of the vacuum chamber allowed for white-light spectroscopy of the resulting barium plume, with the remaining vacuum ports used for loading buffer gas and monitoring pressure.

The results of time resolved white-light spectroscopy at varying ablation pulse energy are provided in Fig. A.1(a). We believe the characteristic 'double-peak' in the time-resolved optical depth at high ablating pulse energy corresponds to the arrival of fast barium atoms from the initial ejection of laser-ablated atoms, and the subsequent arrival of a slow, dense shockwave of atoms as seen in other studies of laser ablation in Ar atmosphere [443]. Figure A.1(b)-(g) shows select absorption spectra at indicated times following the 40 mJ laser ablation pulse. Optical depths of $\sim$1.1 and linewidths of $\sim$0.75 nm are readily achievable with a single ablation pulse, without significant optimization.

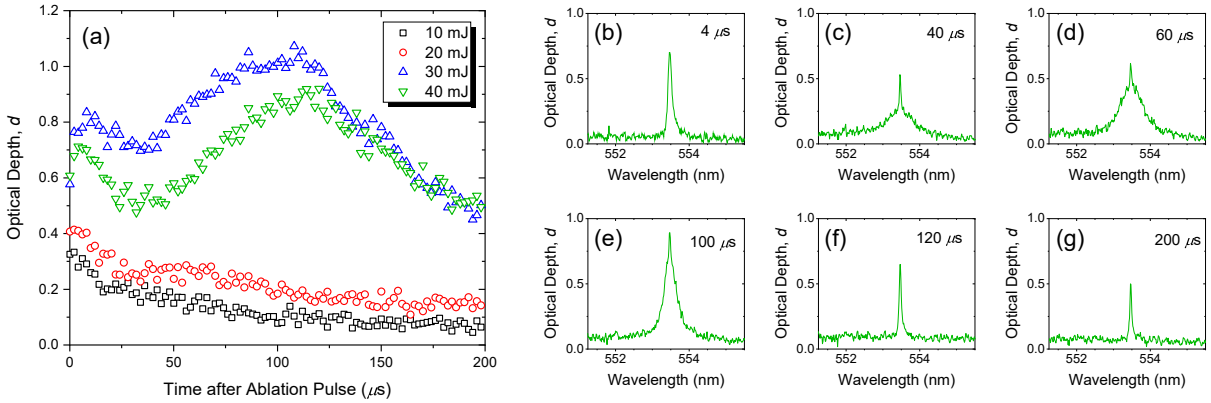

Figure A.1: **Preliminary laser ablation measurements. a** Peak optical depths extracted from time-resolved white-light spectroscopy of a barium plume after ablation at varying pulse energies (markers). **b-g** Select example absorption spectra at varying times after a 40 mJ ablation pulse.

Appendix B

Fourier transform of Maxwell-Bloch equations and numerical solution

As described in Ch. 3-5, the dimensionless, normalized Maxwell-Bloch equations of motion for quantum storage, including decay of the spin-wave, in (z, τ) space are:

$$\partial_z A(z,\tau) = -\sqrt{d}P(z,\tau) \tag{B.1}$$

$$\partial_\tau P(z,\tau) = -\tilde{\gamma}P(z,\tau) + \sqrt{d}A(z,\tau) - i\Omega(\tau)B(z,\tau) \tag{B.2}$$

$$\partial_\tau B(z,\tau) = -\gamma_B B(z,\tau) - i\Omega^*(\tau)P(z,\tau), \tag{B.3}$$

for photonic mode $A(z,\tau)$, atomic polarization $P(z,\tau)$, and spin wave mode $B(z,\tau)$. In Eq. (B.2), $\tilde{\gamma} = (\gamma - i\Delta)/\gamma$ is the normalized complex detuning, and γ_B is the decay rate of the spin wave, in units of γ. Taking the Fourier transform of both sides of each equation, we find:

$$\partial_z \tilde{A}(z,\omega) = -\sqrt{d}\tilde{P}(z,\omega) \tag{B.4}$$

$$i\omega\tilde{P}(z,\omega) = -\tilde{\gamma}\tilde{P}(z,\omega) + \sqrt{d}\tilde{A}(z,\omega) - \frac{i}{2\pi}\tilde{\Omega}(\omega) * \tilde{B}(z,\omega) \tag{B.5}$$

$$i\omega\tilde{B}(z,\omega) = -\gamma_B\tilde{B}(z,\omega) - \frac{i}{2\pi}\tilde{\Omega}^*(-\omega) * \tilde{P}(z,\omega), \tag{B.6}$$

where we have used the fact that the Fourier transform of the product of two functions is the convolution of the two Fourier transforms, and that the Fourier transform of a conjugated function is the conjugate of the function's Fourier transform reflected about $\omega = 0$. We have used "$*$" to express the convolution of two functions, e.g.:

$$\tilde{\Omega}(\omega) * \tilde{B}(z,\omega) = \int_{-\infty}^{\infty} du\, \tilde{\Omega}(\omega - u)\tilde{B}(z,u). \tag{B.7}$$

Rearranging terms, we have:

$$\partial_z \tilde{A}(z,\omega) = -\sqrt{d}\tilde{P}(z,\omega) \tag{B.8}$$

$$[1 + i(\omega - \Delta)]\tilde{P}(z,\omega) + \frac{i}{2\pi}\tilde{\Omega}(\omega) * \tilde{B}(z,\omega) = \sqrt{d}\tilde{A}(z,\omega) \tag{B.9}$$

$$\frac{i}{2\pi}\tilde{\Omega}^*(-\omega) * \tilde{P}(z,\omega) + (i\omega + \gamma_B)\tilde{B}(z,\omega) = 0. \tag{B.10}$$

Before describing the technique we use to numerically solve these equations, we first note that taking the Fourier transform of Eqs. (B.1)-(B.3) has reduced a system of 3 coupled PDEs to a single PDE [Eq. (B.4)] and a linear system 2 of algebraic equations [Eqs. (B.5) and (B.6)], which allows for a significant computational speedup. At first sight, the fact that a convolution enters the transformed equations of motion does not bode well for their numerical solution however—it would appear that in order to solve the system of equations in Eq. (B.5) and (B.6) for $\tilde{B}$ and $\tilde{P}$ at a given z and ω, we need foreknowledge of all of $\tilde{B}(z,u)$ along u in order to compute the convolution in Eq. (B.6) [and all of $\tilde{P}(z,u)$ to compute the convolution in Eq. (B.5)]. This is indeed a problem if we wish to implement an iterative scheme, wherein, for fixed $z^{(n)}$, we iterate through $\omega^{(m)} \in [\omega^{\text{lim-}}, \omega^{\text{lim+}}]$ and attempt to solve Eqs. (B.9) and (B.10) for $\tilde{P}(z^{(n)}, \omega^{(m)})$ and $\tilde{B}(z^{(n)}, \omega^{(m)})$. Instead, we may circumvent this problem by employing the Method of Lines [444], similar to the usual numerical solution of Eqs. (B.1)-(B.3) in (z,t) space [344], where we will solve for all ω at the same time, for a given z. The general idea is that, for a given $z = z^{(n)}$, assuming we have $\tilde{A}(z^{(n)}, \omega)$ in hand, we have a linear system of two equations for $\tilde{P}(z^{(n)}, \omega)$ and $\tilde{B}(z^{(n)}, \omega)$. If ω, $\tilde{P}(z^{(n)}, \omega)$, and $\tilde{B}(z^{(n)}, \omega)$ are each vectors of length M, we thus have $2M$ equations, which we can solve to find the $2M$ unknowns corresponding to the elements of the vectors $\tilde{P}(z^{(n)}, \omega)$ and $\tilde{B}(z^{(n)}, \omega)$. We then iterate through $z^{(n)} \in [0,1]$ to produce $\tilde{P}(z,\omega)$ and $\tilde{B}(z,\omega)$ for all z and ω.

The algorithm we have in mind thus takes the form

For $z^{(n)} \in [0,1]$:

1. Euler step $\tilde{A}(z^{(n)}, \omega)$ forward for all ω at once, using $\partial_z \tilde{A}$ from equation (B.8) evaluated at previous value of $z^{(n)}$ [for the first discretized z position, $z^{(1)}$, use initial conditions $\tilde{A}_{\text{in}} = \tilde{A}(0,\omega)$ and $\tilde{P}(0,\omega) = 0$].
2. Set up and solve the system of $2M$ equations in Eqs. (B.9) and (B.10) for $\omega^{(m)} \in [\omega^{\text{lim-}}, \omega^{\text{lim+}}]$, all at once.

The linear system to be solved in this case is:

$$\begin{pmatrix} & & \\ M_1 & M_2 & \\ & & \\ M_3 & M_4 & \\ & & \end{pmatrix} \cdot \begin{pmatrix} \tilde{P}(z^{(n)},\omega^{(1)}) \\ \vdots \\ \tilde{P}(z^{(n)},\omega^{(M/2)}) \\ \vdots \\ \tilde{P}(z^{(n)},\omega^{(M)}) \\ \tilde{B}(z^{(n)},\omega^{(1)}) \\ \vdots \\ \tilde{B}(z^{(n)},\omega^{(M/2)}) \\ \vdots \\ \tilde{B}(z^{(n)},\omega^{(M)}) \end{pmatrix} = \begin{pmatrix} \sqrt{d}\tilde{A}(z^{(n)},\omega^{(1)}) \\ \vdots \\ \sqrt{d}\tilde{A}(z^{(n)},\omega^{(M/2)}) \\ \vdots \\ \sqrt{d}\tilde{A}(z^{(n)},\omega^{(M)}) \\ 0 \\ \vdots \\ 0 \\ \vdots \\ 0 \end{pmatrix}, \tag{B.11}$$

where $\omega^{(1)} = \omega^{\text{lim-}}$ and $\omega^{(M)} = \omega^{\text{lim+}}$, and where the block matrices are:

$$M_1 = \begin{pmatrix} [1+i(\omega^{(1)}-\Delta)] & 0 & \dots & 0 \\ 0 & [1+i(\omega^{(2)}-\Delta)] & \dots & 0 \\ \vdots & & \ddots & \\ 0 & 0 & \dots & [1+i(\omega^{(M)}-\Delta)] \end{pmatrix}, \tag{B.12}$$

$$M_2 = \begin{pmatrix} \frac{i}{2\pi}\tilde{\Omega}(\omega^{(M/2)}) & \frac{i}{2\pi}\tilde{\Omega}(\omega^{(M/2-1)}) & \frac{i}{2\pi}\tilde{\Omega}(\omega^{(M/2-2)}) & \dots & 0 \\ \frac{i}{2\pi}\tilde{\Omega}(\omega^{(M/2+1)}) & \frac{i}{2\pi}\tilde{\Omega}(\omega^{(M/2)}) & \frac{i}{2\pi}\tilde{\Omega}(\omega^{(M/2-1)}) & \dots & 0 \\ \vdots & & & \ddots & \\ \frac{i}{2\pi}\tilde{\Omega}(\omega^{(M)}) & \frac{i}{2\pi}\tilde{\Omega}(\omega^{(M-1)}) & \frac{i}{2\pi}\tilde{\Omega}(\omega^{(M-2)}) & \dots & \frac{i}{2\pi}\tilde{\Omega}(\omega^{(1)}) \\ 0 & \frac{i}{2\pi}\tilde{\Omega}(\omega^{(M)}) & \frac{i}{2\pi}\tilde{\Omega}(\omega^{(M-1)}) & \dots & \frac{i}{2\pi}\tilde{\Omega}(\omega^{(2)}) \\ \vdots & & & \ddots & \\ 0 & 0 & 0 & \dots & \frac{i}{2\pi}\tilde{\Omega}(\omega^{(M/2)}) \end{pmatrix}, \tag{B.13}$$

$$M_3 = \begin{pmatrix} \frac{i}{2\pi}\tilde{\Omega}^*(\omega^{(M/2)}) & \frac{i}{2\pi}\tilde{\Omega}^*(\omega^{(M/2+1)}) & \frac{i}{2\pi}\tilde{\Omega}^*(\omega^{(M/2+2)}) & \dots & 0 \\ \frac{i}{2\pi}\tilde{\Omega}^*(\omega^{(M/2-1)}) & \frac{i}{2\pi}\tilde{\Omega}^*(\omega^{(M/2)}) & \frac{i}{2\pi}\tilde{\Omega}^*(\omega^{(M/2+1)}) & \dots & 0 \\ \vdots & & & \ddots & \\ \frac{i}{2\pi}\tilde{\Omega}^*(\omega^{(1)}) & \frac{i}{2\pi}\tilde{\Omega}^*(\omega^{(2)}) & \frac{i}{2\pi}\tilde{\Omega}^*(\omega^{(3)}) & \dots & \frac{i}{2\pi}\tilde{\Omega}^*(\omega^{(M)}) \\ 0 & \frac{i}{2\pi}\tilde{\Omega}^*(\omega^{(1)}) & \frac{i}{2\pi}\tilde{\Omega}^*(\omega^{(2)}) & \dots & \frac{i}{2\pi}\tilde{\Omega}^*(\omega^{(M-1)}) \\ \vdots & & & \ddots & \\ 0 & 0 & 0 & \dots & \frac{i}{2\pi}\tilde{\Omega}^*(\omega^{(M/2)}) \end{pmatrix} = J_N(-M_2^*)J_N, \tag{B.14}$$

$$M_4 = \begin{pmatrix} (i\omega^{(1)}+\gamma_B) & 0 & \dots & 0 \\ 0 & (i\omega^{(2)}+\gamma_B) & \dots & 0 \\ \vdots & & \ddots & \\ 0 & 0 & \dots & (i\omega^{(M)}+\gamma_B) \end{pmatrix}, \tag{B.15}$$

where J_N is the $N \times N$ exchange matrix, or anti-diagonal identity matrix. This linear system of equations can be solved through any number of numerical methods (Gaussian elimination, least squares optimization, etc.).

A few practical notes on this technique:

- The Euler step in algorithmic step (1) can unproblematically be replaced with RK2 or RK4, depending on the convergence and numerical accuracy required.
- The linear system in (2) is of the form $Ax = B$; we note that only x and B change with $z^{(n)}$, and this means we can decompose A once and reuse the result at each solution of the linear system, which provides a significant speedup.
- Importantly, the convolution 'moves' at the intrinsic speed of the grid, and the convolution has its largest amplitude at grid point $O/2$ where O is the size of the grid.
- The form of M_3 in eq. (B.14) assumes a frequency domain centered around $\omega = 0$—that is, $\tilde{\Omega}^*(-\omega^{(j)}) = \tilde{\Omega}^*(\omega^{(M-j+1)})$ [e.g. $\tilde{\Omega}^*(-\omega^{(1)}) = \tilde{\Omega}^*(\omega^{(M)})$].

Appendix C

Barium-Argon Gas Mixture Diffusion Coefficients

As described in Ch. 5, the natural lifetime of the $6s5d\ ^1D_2$ state of neutral barium is 0.25 sec [289]. Without collisions, a barium atom moving ballistically at average thermal velocity (∼350 m/s) at 800 C takes 2.5 ns to traverse one spin wavelength (0.877 um). Including collisions with argon atoms, the motion of a given barium atom is diffusive; the barium atom takes a random walk across the spin wavelength, which in general takes longer than ballistic transport. From the collisional cross sections of barium and argon, we can calculate an average barium atom's diffusion coefficient, mean free path, spin wavelength transit time, average number of collisions during a random walk across one spin wavelength, mean time between collisions, etc. A few of these parameters are shown as a function of temperature and pressure for both Ba-Ba collisions and Ba-Ar collisions in Figure C.1. These parameters fully describe the kinetic evolution of barium and argon atoms in the gaseous mixtures relevant to the experiments in Ch. 5.

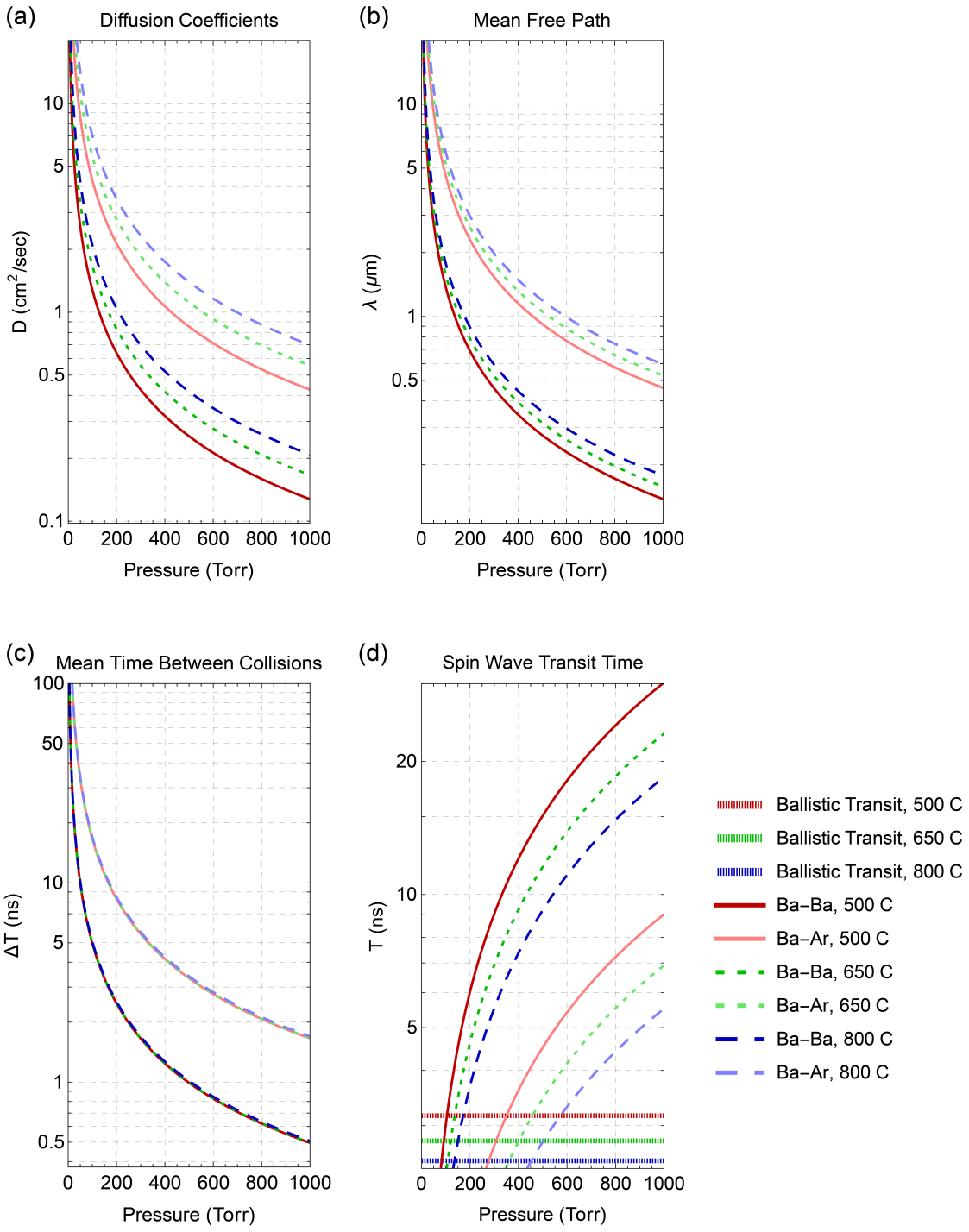

Figure C.1: **Barium-Barium and Barium-Argon diffusion parameters.** **a** Diffusion coefficients, **b** mean free paths, **c** mean times between collisions, and **d** spin wave transit times assuming a diffusive random walk for barium vapor and barium-argon gas mixtures at varying temperatures and pressures.

Appendix D

Black-body radiation noise from high-temperature quantum memories

The high temperatures used in the experimental results of Ch. 5 lead to a new source of noise for atomic quantum memories not previously well-characterized: blackbody radiation from the heat pipe oven overlapping with the signal field. Figure D.1 shows the relevant experimental geometries for this kind of blackbody noise. The heat pipe used in Ch. 5 has a $a = 1/4$ inch aperture limiting diffusion of barium atoms towards the heat pipe windows, which also serves to constrain the emission of blackbody radiation. The signal field represented in red in Fig. D.1 is overlapped with the collection mode of the experiment (backward propagated through the experimental apparatus from the fiber collection mode), which has a characteristic mode diameter $w \approx 3$ mm. The collection optics are placed a distance $D \approx 1$ m away from the aperture of the heat pipe oven. For the experiments in Ch. 5, in addition to the spatial filtering imposed by coupling the signal field into single mode fiber, we also filter the signal field in the spectral domain with a stack of 5 interference filters that have a combined transmission bandwidth between 553.8 nm and 555.8 nm (for a typical near-off-resonant signal field wavelength of 554.8 nm). From Planck's law, we take the blackbody spectral density to be

$$B(\lambda, T) = \frac{2hc^2}{\lambda^5} \frac{1}{e^{hc/(\lambda k_B T)} - 1}. \tag{D.1}$$

For a heat pipe temperature of 900 °C, radiating in the geometry of Fig. D.1(a), we calculate the blackbody radiation entering the collection mode to be:

$$\begin{aligned} &\pi(a/2)^2 \int_{\Omega_{\text{col}}} d\Omega \int_{553.8\,\text{nm}}^{555.8\,\text{nm}} d\lambda\, B(\lambda, 1173\text{K}) \cos\theta \\ &\qquad = \pi(a/2)^2 \int_0^{\arctan(w/2D)} d\theta \int_0^{2\pi} d\phi\, \sin\theta \cos\theta \int_{553.8\,\text{nm}}^{555.8\,\text{nm}} d\lambda\, B(\lambda, 1173\text{K}) \\ &\qquad = \mathcal{O}(0.3\text{ pW}) \\ &\qquad = \mathcal{O}(7 \times 10^5\text{ photons/sec}) \end{aligned} \tag{D.2}$$

where $d\Omega = \sin\theta d\theta d\phi$ is the infinitesimal solid angle integrated over the collected solid angle Ω_{col}, for zenith angle θ and azimuthal angle ϕ in spherical coordinates oriented along the optic axis of the collection mode. This calculation makes a few assumptions, namely that $D \gg w$ and $D \gg a$, which implies that the bounds

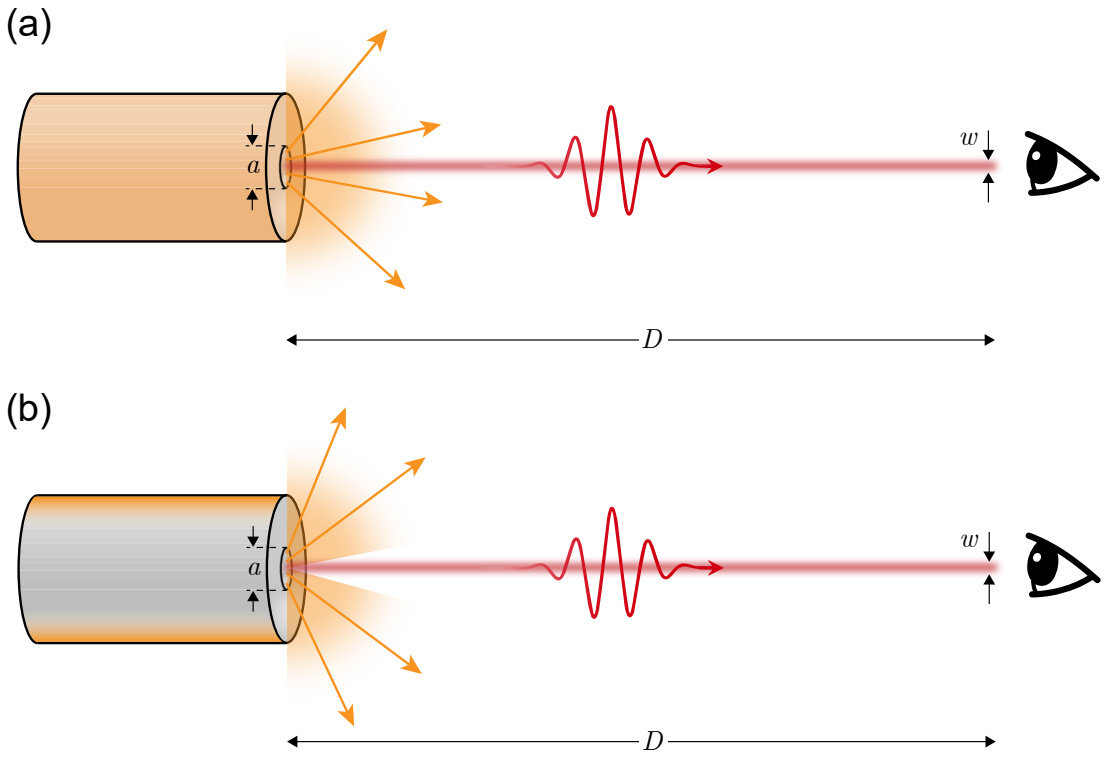

Figure D.1: **Blackbody radiation noise.** Schematic of the experimental geometries used to calculate blackbody radiation noise. Orange diffuse emission represents blackbody radiation; red collimated spatial mode represents the detection mode, which is backward propagated from the fiber collection mode.

of integration over Ω_{col} are not affected by the point of emission inside the area $\pi(a/2)^2$, and that the collection mode is well-approximated by cylinder (as opposed to, e.g., a Gaussian collection mode), which would necessitate including a factor of $G(\Omega)$ in the integration over Ω. Neither of these factors are important for the order of magnitude estimate above, nor for the physical intuition one can glean from Eq. (D.2), namely that one can in principle reduce blackbody radiation noise below any arbitrary threshold by increasing D and a or decreasing w. This simple calculation indicates that blackbody radiation can, in general, be a significant source of noise for quantum applications at typical length scales. The number of photons entering the collection mode in Eq. (D.2) does not agree with the noise level measured in Ch. 5, however. We believe the discrepancy, which serves to significantly limit the number of blackbody noise photons detected in experiment, is due to the assumption that the whole aperture area $\pi(a/2)^2$ acts as a blackbody emitter. In practice, only the walls of the heat pipe oven act as blackbody radiators, as shown in Fig. D.1(b), which prevents leakage of blackbody noise into the collection mode. The $\sim$1 atm of buffer gas inside the cell can only emit radiation along electronic transitions in the atoms (or the rotational, vibrational, electronic transitions of weakly bound molecules), and thus the radiation coming from the gas along the optic axis not governed by the Planck distribution; instead, the most detrimental kind of thermal radiation from the gas is thermal excitation of the barium atoms to the $^1P_1$ state and subsequent spontaneous decay. The fraction of thermally excited barium atoms in this state is given by the Boltzmann distribution

$$p_i = \frac{e^{-E_{ig}/k_B T}}{\sum_{j=1}^{\infty} e^{-E_{jg}/k_B T}}, \tag{D.3}$$

where p_i represents the probability of finding a given barium atom in state i, with energy relative to the ground state g of E_{ig}, when the gas is at a temperature T. Given the large energy separations between the low-lying levels of neutral barium, we truncate the sum in the denominator of Eq. (D.3) after the $^1P_1$ level. In principle, this overestimates the probability of finding a given barium atom in $^1P_1$; even with this overestimate, for $i =^1 P_1$ and $T = 1173$ K, we find $p_i \approx 2 \times 10^{-10}$. From measurements of the peak optical depth of the homogeneously broadened $^1S_0$ to $^1P_1$ transition of $d = 50$, we estimate that at 900 °C the density of barium atoms is $n \approx 4 \times 10^1 3$ cm^{-3}. For a loosely focused signal field with waist radius of 100μm and a 12 inch heated region of the heat pipe oven, this leads to an estimate of 4×10^{11} barium atoms overlapping with the optic axis. This implies that in thermal equilibrium, $p_i 4 \times 10^{11} = 80$ barium atoms along the optic axis are thermally excited into the $^1P_1$ state. Each of these 80 atoms spontaneously decays over a timescale defined by the natural decay rate of the $^1P_1$ state, ~ 100 MHz into the collected solid angle $\Omega_{\text{col}} \approx 10^{-4}\Omega_{\text{tot}}$, which leaves around 8×10^4 photons emitted per second into the collection mode. Again this may not be negligible, however, the atoms that are emitting into the collection mode are uniformly distributed along the length of the atomic cloud. This means that in order for an atom near the input port of the cloud to spontaneously emit a noise photon that makes it past the output port and on to the detector, the emitted photon must propagate through a resonant cloud of atoms with optical depth $d = 50$ without being absorbed ($e^{-50} \approx 10^{-22}$).

Appendix E

Heat-pipe pressure-temperature relation

In this appendix we aim to find the pressure-temperature relation in the atomic barium heat pipe of Ch. 5. The heat pipe body is made of 1/8th inch thick stainless steel tube, with windows attached on either end. The heat pipe body is connected to the argon buffer gas loading system with 1/2 inch diameter orbital welded stainless steel piping. The heat pipe is brought to temperature with a custom double-clamshell heater, that heats volume V_1 to temperature T_1, while keeping volume V_2 at temperature $T_2 = T_i = 273$ K as shown in Figure E.1.

Initially, the system is loaded to a pressure P_{load} of argon buffer gas at room temperature, when all barium is in the solid phase. In this initial step, the ideal gas law gives the following number of argon atoms in each volume:

$$n_1 = \frac{P_{\text{load}} V_1}{k_B T_i}, \qquad n_2 = \frac{P_{\text{load}} V_2}{k_B T_i}. \tag{E.1}$$

The system is then sealed, and the temperature of volume V_1 is increased to T_1. After the system reaches thermal equilibrium, we have the two volumes at different temperatures, and we aim to find the common system pressure P.

As a zeroth-order solution, we again we use the ideal gas law to find the number of argon atoms in each volume:

$$n_1' = \frac{P V_1}{k_B T_1}, \qquad n_2' = \frac{P V_2}{k_B T_i}. \tag{E.2}$$

As the system was sealed, we can equate the number of argon atoms in each case and solve for the common pressure as a function of T_1:

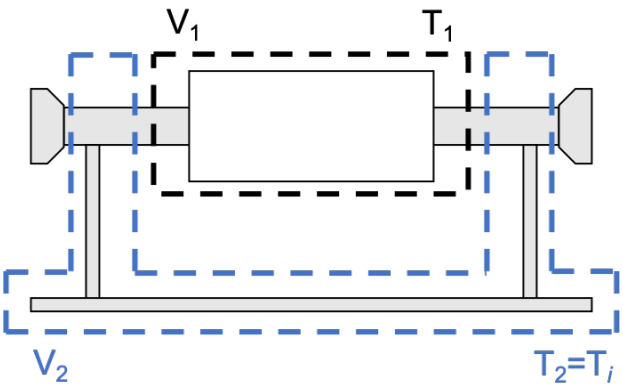

Figure E.1: **Barium heat pipe volumes and temperatures.** A schematic of the home-built barium heat pipe oven.

$$n_1 + n_2 = n_1' + n_2' \tag{E.3}$$

$$\frac{P_{\text{load}}}{k_B T_i}(V_1 + V_2) = \frac{P}{k_B}\left(\frac{V_1}{T_1} + \frac{V_2}{T_i}\right) \tag{E.4}$$

$$P = \frac{P_{\text{load}}(V_1 + V_2)}{T_i\left(\frac{V_1}{T_1} + \frac{V_2}{T_i}\right)}. \tag{E.5}$$

In principle, once we measure a set of correlated pressure and temperature data, at this point we can fit those data and extract an estimate for V_1 and V_2. This zeroth-order treatment ignores however the evaporation of barium atoms, which increases the effective atom number in V_1, and increases the total pressure significantly after T_1 exceeds the melting point of barium. To account for this, as a first-order solution we simply add the predicted barium vapor pressure in volume V_1 from the Nesmeyanov equations to the argon pressure in V_1 calculated above. We call P in Eq. (E.5) $P^{(0)}$ such that the solution including this first-order correction is

$$P = P^{(0)} + P^{(1)} \tag{E.6}$$

$$= \frac{P_{\text{load}}(V_1 + V_2)}{T_i\left(\frac{V_1}{T_1} + \frac{V_2}{T_i}\right)} + A_0 \frac{400}{3} 10^{6.80 - 8800/T_1}, \tag{E.7}$$

where the factor of 400/3 converts from Torr to Pa, the factors 6.80 and -8800 come from Ref. [445], and where A_0 is a loading-pressure dependent scaling factor that determines how much influence the barium evaporation has on the final pressure. Given correlated pressure and temperature data, one can fit to Eq. (E.7) to extract A_0, V_1, and V_2. This information can be very useful if, for example, a thermocouple attached to the heat pipe oven breaks and one must infer the heat pipe temperature from the measured pressure.

Appendix F

Scanning absorption spectroscopy with an intermediate-bandwidth source

In this appendix, we aim to describe spectral measurement of an atomic transition with a laser source that is neither broadband or narrowband relative to the transition linewidth, γ. For low optical depths, white light absorption spectroscopy is typically the simplest and most reliable method to determine the the optical depth and lineshape of a particular atomic transition, but for larger optical depths ($d \gtrsim 10$) the absorption of most white light sources become saturated. As an alternative, one can measure the absorption profile and optical depth using a narrowband laser that is scanned across the absorption feature in frequency. In the limit where the laser bandwidth (δ) is much smaller than the absorption linewidth, $\delta \ll \gamma$, the absorption profile and optical depth can be acquired directly by measuring the pulse energy (if pulsed) or optical power of the narrowband laser with and without atoms present at the scanning frequencies. The opposite limit, $\delta \gg \gamma$, is quantitatively identical to the white light absorption spectroscopy case. In the intermediate case, $\delta \sim \gamma$, one can repeat the same scanning absorption measurements (as for $\delta \ll \gamma$), but the measurements correspond to a convolution of the absorption feature with the laser bandwidth. Here we describe a method to deconvolve such data.

A picture of the case at hand is provided in Fig. F.1. The scanning laser spectra are given by $G_n(x)$, and are measured with a spectrometer. Despite setting the center wavelength of the scanning laser at regular intervals, one may measure spectra that do not in general have regular center wavelength separation. The measured center wavelengths, and the center wavelengths where the absorption is measured, are written as x_n. In the general case, each $G_n(x)$ may possess a different amplitude; this can be measured trivially by means of a power meter or energy meter at each laser setpoint. The absorption lineshape, which here we give in terms of the transmission coefficient (ranging from 0 to 1) at each wavelength, is $S(x)$. The separation between center wavelengths is $\Delta\lambda_n$. If there are insufficient data points in the region of the transmission profile where transmission is unity (insufficient for the numerical extraction described below), one can add padding points (orange in Fig. 1) sufficiently far from the absorption feature where the transmission is assumed to be unity.

We model the absorption (transmission) process in terms of the linear algebra problem

$$G * S = P \tag{F.1}$$

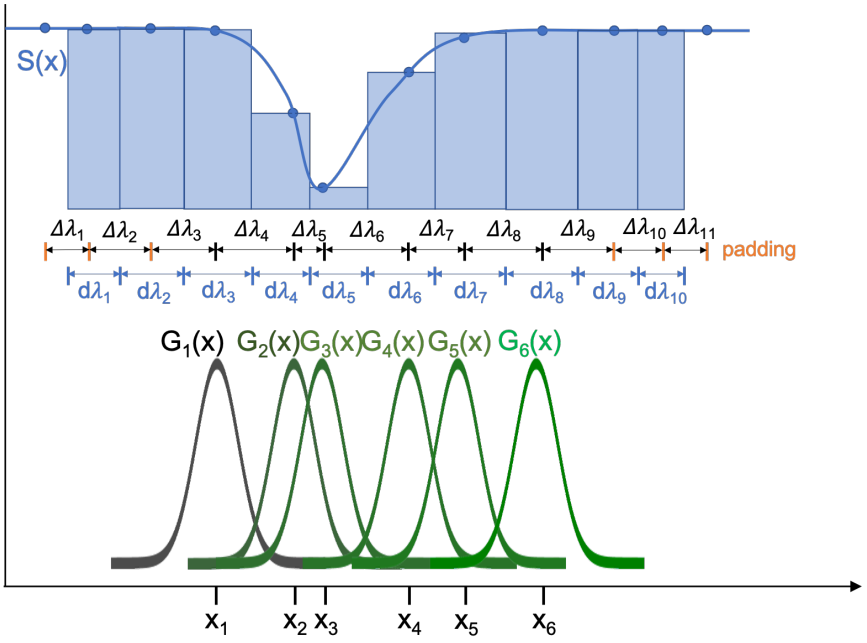

Figure F.1: **Schematic of intermediate-bandwidth scanning absorption spectroscopy.** See text for symbol definitions.

$$\begin{bmatrix} \int_{d\lambda_1} dx\, G_1(x) & \int_{d\lambda_2} dx\, G_1(x) & \dots & \int_{d\lambda_n} dx\, G_1(x) \\ \int_{d\lambda_1} dx\, G_2(x) & \int_{d\lambda_2} dx\, G_2(x) & \dots & \int_{d\lambda_n} dx\, G_2(x) \\ \vdots & & \ddots & \\ \int_{d\lambda_1} dx\, G_n(x) & \int_{d\lambda_2} dx\, G_n(x) & \dots & \int_{d\lambda_n} dx\, G_n(x) \end{bmatrix} * \begin{bmatrix} S(x_1) \\ S(x_2) \\ \vdots \\ S(x_n) \end{bmatrix} = \begin{bmatrix} P(x_1) \\ P(x_2) \\ \vdots \\ P(x_n) \end{bmatrix}, \tag{F.2}$$

where each probe laser spectrum $[G_n(x)]$ is integrated over the intervals shown in Fig. F.1, and P represents the transmission of the probe laser measured at each center frequency with atoms present. For known $G_n(x)$, $d\lambda_n$, and $P(x_n)$, we can solve for $S(x_n)$, which represents the transmission profile of the atomic transition, using any number of known linear algebra techniques (Gaussian elimination, LU factorization, etc.). As shown in Fig. F.1, this amounts to approximating the transmission profile by a series of constant scaling factors over the intervals $d\lambda_n$, similar to a Riemann sum. The resolution of this technique thus scales with the center frequency separation, as expected.

Once the transmission spectrum $S(x)$ is found, the linewidth can be calculated trivially, and the optical depth can be calculated as $d(x) = -\ln[S(x)]$.

Appendix G

All-optical defect emission engineering at room temperature via phonon pumping

This appendix details a proposal for the spectral engineering of single-photon emission from point defects in solids using an all-optical method compatible with room-temperature operation. This is a particularly useful idea, as point defects in solids are excellent single-photon sources, but typically require cryogenic operation and/or integration into a nanophotonic cavity to generate spectrally indistinguishable photons. The following proposal aims to relax these experimental constraints, while retaining high indistinguishability, in principle.

Optically-active point defects in solids are an important resource for quantum applications in communication, cryptography, measurement, and computation, but despite major progress in the field, realization of a defect-based source of high-purity single photons at room temperature remains an outstanding challenge. Optical emission from point defects is useful chiefly because single defects emit photons with exquisite single-photon purity. Two major, and related, challenges for this platform however are the spectral distribution and quantum state purity of the emitted photons. In the typical scheme depicted in Fig. G.1(a), after off-resonant excitation of the well-isolated two-level system comprised of the defect's electronic ground ($|g\rangle$) and excited ($|e\rangle$) states, the point defect can decay either through emission of a photon with energy equal to the ground-excited state splitting—the so-called zero-phonon line (ZPL) emission—or via emission of a photon and an accompanying phonon through the phonon sideband (PSB). Since the PSB is composed of all acoustic and optical phonons that couple to the defect, at room temperature many of these phonon modes (particularly at low frequency, ν) have appreciable thermal population and the defect's photoluminescence spectrum is dominated by the PSB. In general, this PSB emission is undesirable; the large phonon density of states populated at room temperature results in an extremely broad emission spectrum (typically of order ~ 100 nm), which makes spectral synchronization of multiple defects (e.g., for use in defect spin state teleportation or interfacing with a narrowband quantum memory) impossible. In addition, as the broad linewidths of low frequency acoustic phonon modes overlap significantly, and emission of a photon into the PSB at a particular frequency often corresponds to the creation of a phonon that could exist in several physically distinct but spectrally indistinguishable modes; this leads to emitted photons that are projected onto mixed quantum states that are not useful for most quantum applications.

These, among others, are known problems with point defect emission at room temperature, and their solution to date has relied on cooling of the defects and their host lattice to cryogenic temperatures—such that the phonon density of states is reduced until the majority of emission occurs in the ZPL—the use of high-finesse photonic cavities that suppress emission at the PSB frequencies, and/or exotic solutions relying on phononic structures that mitigate the phonon DOS through other means. These solutions have been sufficient for several important experimental achievements, but may not represent a fundamentally scalable approach for the use of point defect emission in quantum applications. Here we propose an alternative, all-optical scheme, which allows for single photon defect emission in pure quantum states at room temperature. Our approach is depicted schematically in (b)-(d) of Fig. G.1. In our proposed technique, instead of mitigating emission into the PSB, we *enhance* emission into the PSB, but only in a particular phonon mode. Insofar as we can selectively populate a well-isolated phononic mode, upon emission the photon bandwidth will be reduced dramatically, and the quantum state purity of the photon will be improved. In practice, we plan to selectively populate a certain Raman-active phononic mode through off-resonant stimulated Raman scattering via optical pump and Stokes fields described by Rabi frequencies $\Omega_p(t)$ and $\Omega_s(t)$ shown in Fig. G.1(c). Off-resonant stimulated Raman scattering of this form has routinely been shown to produce large phononic populations in particular, optically-addressable phonon modes (see, e.g., Ref [446]). This process, which only relies on the parameters of the host crystal lattice, is mediated by an intermediate excited state with two-photon detuning Δ. The resulting photoluminescence (PL) spectrum with this enhancement is shown schematically in Fig. G.1(d).

We propose to initially study this approach for room temperature, all-optical defect emission engineering in the negatively charged, h-site Si vacancy (SiV) defect in silicon carbide (SiC), with ZPL emission at 862.2 nm [447]. Silicon carbide is an attractive medium for this study due to its wide use and stability in mechanical, electrical, and thermophysical applications, its wide bandgap and transparency region ($E_g = 3.05$ eV), and its well-studied phononic behavior, with a particularly well-isolated and optically-addressable phonon mode at 785 cm^{-1} [448]. In addition, the SiV defect emission considered here is compatible with conventional near-IR

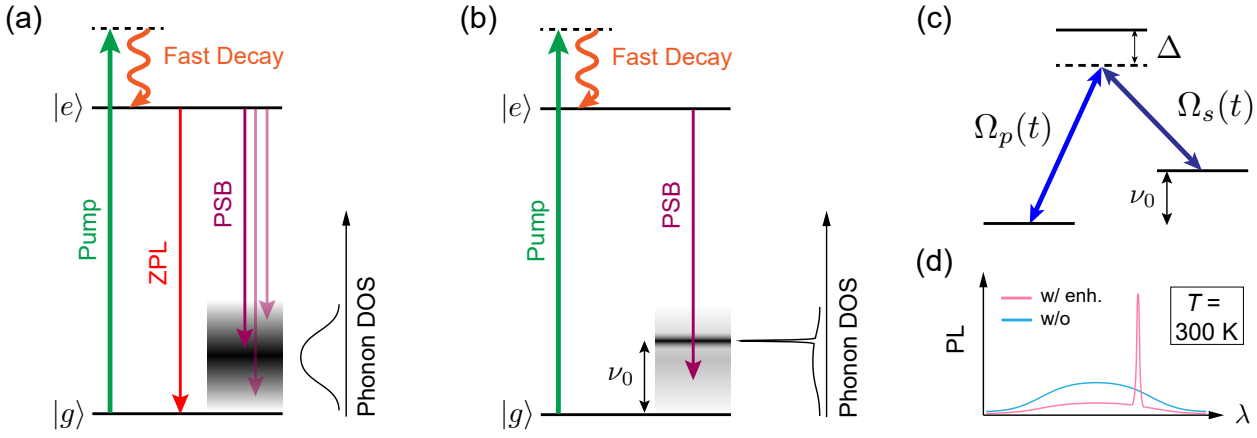

Figure G.1: (a) Typical single-defect level structure and photoluminescence (PL) contributions at room temperature, where the zero-phonon line (ZPL) is dominated by the phonon sideband (PSB) emission caused by the broad phonon density of states (DOS). (b) Scheme for enhancing emission into a particular phonon mode inside the PSB, where the phonon mode is brought to have a large occupation by (c) stimulated Raman scattering with optical pump and Stokes fields with Rabi frequencies $\Omega_p(t)$, $\Omega_s(t)$, respectively. (d) Our scheme promises a large enhancement (enh.) of the PL emission into a particular, tunable phonon mode in the PSB, at room temperature.

photodetectors.

In order to investigate the dependence of single-photon and state-purity on a number of salient parameters, photons created through a Raman-mediated process are detected by two avalanche photodiode (APD) detectors in a Hanbury Brown-Twiss interferometric configuration, which allows for measurement of the second-order autocorrelation function

$$g^{(2)}(t_1, t_2) = \frac{\langle : \hat{n}_1(t_1)\hat{n}_2(t_2) : \rangle}{\langle \hat{n}_1(t_1) \rangle \langle \hat{n}_2(t_2) \rangle}, \tag{G.1}$$

expressed in terms of time-dependent photon number operators $\hat{n_i} = \hat{a_i}^\dagger(t)\hat{a_i}(t)$ in arms 1 and 2 of the interferometer at times t_1 and t_2, where $\langle :: \rangle$ indicates normal ordering. In the case of an ensemble of defects, multiple photons can be emitted simultaneously and this second-order autocorrelation, normalized at time zero, can be shown to be identical to $1 + P$, where P is the Stokes photon quantum state purity [290]. Measurement of single-photon purity can be accomplished with a nearly-identical experimental setup, wherein instead of measuring two-fold coincidences between APDs, the single-photon $g^2(0)$ is measured via three-fold coincidence between both APDs as well as an electronic trigger produced by the pump laser at its repetition rate. In combination with conventional spectroscopy, these measurements allow for full characterization of the photonic states produced through the process proposed above. In addition, with sufficient brightness, single photons from two sequential pulse sequences can be overlapped on a beamsplitter in a time-delay interferometer to measure photon indistinguishability via Hong-Ou-Mandel interference, which provides a highly-sensitive, unconditional measurement of photon indistinguishability.

This trailblazing research constitutes a significant step towards feasible quantum technologies relying on room-temperature sources of pure single photons, with potential for growth beyond the laboratory. We anticipate these sources will open up new capabilities in quantum communication, while engineered emission into a specific PSB mode may also significantly enhance the SNR for quantum sensing applications.